Experimentelle Physik

Measurement of Semi-Electronic Beauty-Hadron Decays via their Impact Parameter in pp Collisions in ALICE

Inauguraldissertation

zur Erlangung des Doktorgrades

der Naturwissenschaften im Fachbereich Physik

der Mathematisch-Naturwissenschaftlichen Fakultät

der Westfälischen Wilhelms-Universität Münster

Vorgelegt von

Markus Ansgar Heide

aus Cloppenburg

— 2014 —

Dekan: Prof. Dr. M. Donath
Erster Gutachter: Prof. Dr. J. P. Wessels
Zweiter Gutachter: PD Dr. S. Masciocchi

Tag der Disputation: 23.06.2014
Tag der Promotion: 23.06.2014

Contents

1 Introduction

There are two major points of interest in the measurement of beauty production in proton-proton collisions at the Large Hadron Collider (LHC). The first one is the test of theoretical predictions of particle production in hard scatterings under unprecedented conditions. The LHC allows for the analysis of beauty production in a new energy domain, and the mass of the b quark is significantly larger than those of all other elementary particles produced in comparable abundance.

The second point of interest lies in the fact that the measurement of beauty production in pp collisions is an essential reference for the comparison to the corresponding measurement in Pb-Pb collisions at the LHC, where a hot and dense state of matter, the Quark-Gluon Plasma, is created that presumably existed during the first 10^{-5} s after the big bang. Beauty quarks are produced at the earliest stage of heavy-ion collisions and experience the whole evolution of the plasma. Therefore, they can be used as a probe for the energy loss of particles passing through this medium. Chapter 2 of this thesis gives an overview over the predictions made by Quantum Chromodynamics in the context of both points, as well as over the preceding measurements of open heavy flavour production and the questions that arise from them.

ALICE, whose name is an acronym for "A Large Ion Collider Experiment", is one of the four large experiments at the LHC. As its name suggests, it is primarily designed for the analysis of heavy-ion collisions. There are, however, several advantageous features that make ALICE measurements particularly interesting for the analysis of beauty production in proton-proton collisions. Its tracking and particle identification capabilities allow ALICE to measure particle spectra down to very low transverse momenta, and therefore effectively constrain theoretical predictions for total particle production cross sections. The experimental setup of the LHC in general and of ALICE in particular will be described in Chapter 3.

In the analysis approach for a beauty production measurement followed in this work, explained in detail in Chapter 4, the measured and identified particles are electrons from the decays of hadrons containing a single beauty quark. The overall branching ratio of such hadrons to electronic decays amounts to approximately 10%. With the high beauty production rates at LHC energies, this promises a sufficient electron yield for statistically significant measurements in a wide transverse momentum range. Owing to the long lifetime and the decay kinematics of beauty hadrons, the tracks of their daughter electrons have on average a particularly large distance to the primary vertex. Using the good tracking resolution provided by the ALICE

Inner Tracking System, they can therefore be separated from background electrons on a statistical basis.

The results of the analysis described in this work, the p_{T}-differential cross sections of electrons from beauty-hadron decays for proton-proton collisions at centre-of-mass energies of 7 TeV and 2.76 TeV, as well as the total beauty production cross sections at both energies, are presented and compared to theoretical predictions in Chapter 5.

As an outlook on the upcoming challenges of the corresponding analysis for Pb-Pb collisions at a centre-of-mass energy per nucleon of 2.76 TeV, some preparatory work based on simulated Pb-Pb events is presented in Chapter 6, as a first step of an analysis that may extend our knowledge about the energy-loss mechanisms in the Quark-Gluon Plasma.

2 Quantum Chromodynamics

The Standard Model of particle physics, which to current knowledge describes very successfully three of the four fundamental forces (strong, electromagnetic, and weak interaction), attributes to each of them one or more particles that transmit the interaction. These particles have an integer spin quantum number and are called *gauge bosons*. While the weak interaction is mediated by the massive $W^{\pm}$ and Z bosons, the electromagnetic force is transmitted via photon exchange. The gauge bosons of the strong interaction, most relevant for the scope of this thesis, are the massless gluons. They permit the exchange of the so-called *colour charge* between quarks, the constituents of nuclear matter. Quarks can assume three different colour states (green, red, blue) or, in the case of anti-quarks, their counterparts, the respective anti-colours. It is an experimentally established fact that free particles composed of quarks, called *hadrons*, are always neutral with respect to their overall colour charge. They consist either of three quarks with colours green, red, and blue (or their respective anti-colours) or of a quark-anti-quark pair carrying a colour and its anti-colour. In the first case, the composite particles are referred to as *baryons*, in the second as *mesons*. Recent experimental results [Liu13, Abl13] hint to the formation of *tetraquarks*, combinations of two quarks and two antiquarks, while the existence of *pentaquarks* consisting of three quarks of all different colours and a quark-antiquark pair is a subject of theoretical and experimental research to this date.

Corresponding to the central concept of colour, the quantum field theory that describes the strong interaction between quarks and gluons is called *quantum chromodynamics* (QCD; from Ancient Greek: $\chi\rho\bar{\omega}\mu\alpha$ = colour). It is based on the non-abelian gauge group SU(3). One can show that, as a consequence of the requirement for local gauge invariance, the QCD Lagrangian must include a term that corresponds to the interaction of gluons among each other, and even with themselves.

Just like the quarks between which they transmit interactions, gluons carry colour charge – a feature that distinguishes them from the photon, the electrically neutral gauge boson of the electromagnetic interaction in quantum electrodynamics. The gluon charge always consists of components of colour and anti-colour. From group-theoretical considerations, it can be concluded that there is an octet of colour/anti-colour constellations which correspond to eight different possible gluon states.

2.1 Confinement and Asymptotic Freedom

The constraint for quarks to be always bound in combinations of at least two is known as *confinement*. Phenomenologically, the potential between a quark and an anti-quark can be described as

$$V_S = -\frac{4}{3}\frac{\alpha_\mathrm{S}}{r} + kr \qquad , \tag{2.1}$$

with the distance r between quark and anti-quark, and the coupling constant α_S of the strong interaction. The constant $k \approx 1$ GeV/fm is also called *string tension*, since the lines of the colour field between both quarks are restricted to a string-like shape by gluon-gluon interactions [Per00].

The potential exhibits a remarkable behaviour for small values of r on the one hand, and for large values of r on the other. The linear increase of the second term with r means that a complete separation of both particles ($r \to \infty$) would require an infinite amount of energy. However, once the energy inside the field between both is sufficiently large, a new pair of quarks can be produced, each one combining with one or two of the surrounding particles. As a result, quarks always stay confined in hadrons.

At small distances r, corresponding to interactions with a large momentum transfer Q^2, the first term of Equation 2.1 becomes dominant. Its dependence on r suggests a potential shape similar to that of the Coulomb potential. However, α_S depends strongly on the value of Q^2. For very large Q^2, perturbative calculations can be applied, where in a first-order approximation, the coupling constant behaves like [Pov09]

$$\alpha_\mathrm{S}(Q^2) = \frac{12\pi}{(33 - 2N_\mathrm{f}) \cdot \ln \frac{Q^2}{\lambda^2_\mathrm{QCD}}} \qquad , \tag{2.2}$$

with the number of energetically accessible quark flavours $N_\mathrm{f} \leq 6$ and the QCD scale parameter $\lambda_\mathrm{QCD} \approx 250$ MeV/c. For a very large momentum transfer $Q^2 \to \infty$, α_S approaches 0. As a consequence, the quarks behave like free particles – a phenomenon called *asymptotic freedom*. While the shape of the scale dependence of α_S can be predicted by QCD, the value of α_S for a given energy has to be determined from experiment. To make experimental results obtained at different Q^2 comparable, they are by convention scaled to their corresponding value $\alpha_\mathrm{S}(M_{\mathrm{Z}^0})$ at a momentum transfer equal to the Z^0 mass, as expected according to the predicted energy dependence. In Figure 2.1, the dependence of α_S on Q is shown, based on the available measurements and calculations as of 2012. The value of $\alpha_\mathrm{S}(M_{\mathrm{Z}^0})$ has recently been updated by *Pich* to $\alpha_\mathrm{S}(M_{\mathrm{Z}^0}) = 0.1186 \pm 0.0007$ [Pic12].

As will be explained in the next section, hard processes with a large momentum transfer between partons are accessible to a description via perturbative calculations. For soft processes, predictions from first principles are more complicated. An

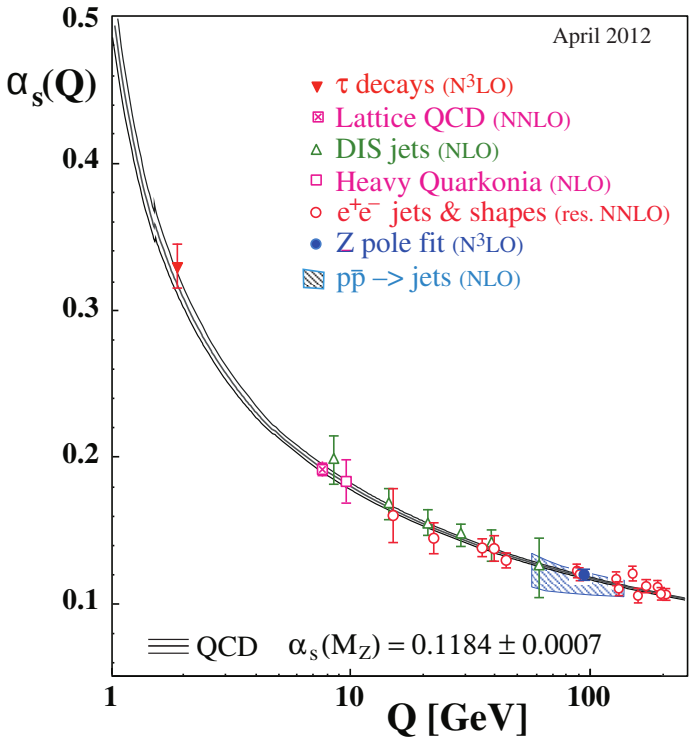

Figure 2.1: Dependence of the coupling constant α_S on the energy scale Q [Beh12]. The curves represent the QCD shape-dependence prediction and its uncertainties for the combined world average value of $\alpha_S(M_{Z^0})$. Symbols correspond to different types of measurements and one lattice QCD calculation. The degree of perturbation theory for extraction of experimental results is given as: NLO (next-to-leading order); NNLO (next-to-next-to-leading-order); res. NNLO (next-to-next-to-leading order with resummed next-to-leading logarithmic terms; N^{3}LO: next-to-NNLO.

instrument that has been applied successfully in this context is provided by Lattice QCD (LQCD) [Wil74], which replaces the continuum field theory of QCD by calculations on a grid with discrete intervals in the dimensions time and space. However, its application is still challenging for systems with baryon densities $\mu_b > 0$.

2.2 Beauty Production and Perturbative Quantum Chromodynamics

In the following, a short overview will be given over the theoretical treatment of beauty production in hadronic collisions. Most of the considerations presented in this chapter apply to heavy quarks in general and are therefore equally or similarly valid for charm production.

Owing to their large mass, beauty quarks are exclusively produced in the hard

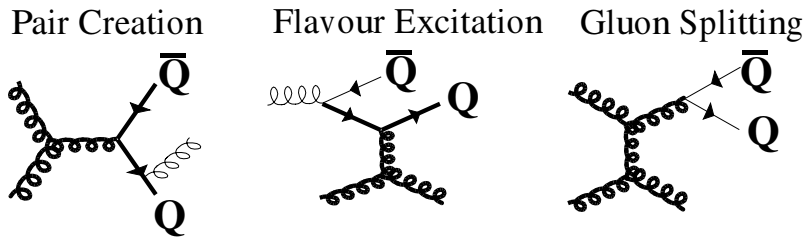

Figure 2.2: b-quark production mechanisms. Thick lines represent hard processes [Dai03].

parton scattering processes at the initial stage of hadronic collisions. A successful instrument for calculating partonic cross sections of such processes has been established in perturbative quantum chromodynamics (pQCD). As the momentum transfer Q^2 is high for the case of $b\bar{b}$ pair production, the coupling constant α_{S} becomes very small (see Equation 2.2). If one expands the production cross section for $b\bar{b}$ pairs in orders of α_{S}, contributions become negligible at a finite order. Therefore, perturbative calculations can produce reliable predictions concerning beauty quark production from hard partonic scatterings.

The relevant production mechanisms are, at leading order (corresponding to α_{S}^2), gluon fusion ($gg \rightarrow b\bar{b}$) and annihilation of light quarks ($q\bar{q} \rightarrow b\bar{b}$) [Fie02, Vog02]. For LHC collision energies, gluon fusion is the dominant contribution. At next-to-leading order, corresponding to α_{S}^3, more complex processes have to be taken into account (see Figure 2.2). Among these are gluon splitting ($g \rightarrow b\bar{b}$) in the final state and flavour excitation - the scattering of an initial-state beauty sea quark from gluon splitting into the final state.

The partonic hard-scattering cross section can be described perturbatively in terms of the dimensionless scaling functions $f_{ij}^{(k,l)}$, which only depend on the parameter $\xi = \hat{s}/4m_b^2 - 1$ [Vog02]:

$$\hat{\sigma}_{ij}(\hat{s}, m_b^2, \mu_{\mathrm{F}}^2, \mu_{\mathrm{R}}^2) = \frac{\alpha_{\mathrm{S}}^2(\mu_{\mathrm{R}})}{m_b^2} \sum_{k=0}^{\infty} (4\pi\alpha_{\mathrm{S}}(\mu_{\mathrm{R}}))^k \sum_{l=0}^{k} f_{ij}^{(k,l)}(\xi) \ln^l\left(\frac{\mu_{\mathrm{F}}^2}{m_b^2}\right) \quad . \tag{2.3}$$

$\hat{s}$ stands for the partonic centre-of-mass energy squared, while m_b is the b-quark mass, μ_{F} the factorization scale, and μ_{R} the renormalization scale.

Perturbative calculations are adequate for the case of hard partonic scatterings. However, the particles observed in experiments are not the produced quarks themselves. For the measurements described in this thesis, predictions have to be made for p_{T}-differential spectra of electrons from the decay of the hadrons into which the beauty quarks have fragmented. The initial hadron structure, the hadronization process in the final state, and the properties of the subsequent weak decay cannot be described via pQCD and have to be determined experimentally. For this reason, and since the relevant scales for these processes are different, they have to be treated separately. The factorization theorem [Col98] offers a solution to this

problem. By convoluting the terms corresponding to the different perturbative and non-perturbative quantities, one obtains [Cac12]:

$$\mathrm{d}\sigma_e = \mathrm{d}\sigma^{b\bar{b}}_{\mathrm{AB}} \otimes D^{\mathrm{NP}}_{b\to H_b} \otimes g^{\mathrm{weak}}_{H_b\to e} \qquad , \tag{2.4}$$

where $\mathrm{d}\sigma_e$ is the cross section for electron production from the decay of a given beauty hadron H_b ($B^{+/-/0}$, B_s, Υ, or a beauty baryon, e.g. Λ_b), as a differential in transverse momentum p_{T}, pseudorapidity η, or rapidity y. $D^{\mathrm{NP}}_{b\to H_b}$ is the non-perturbative fragmentation function which describes the formation of the respective hadron. $g^{\mathrm{weak}}_{H_b\to e}$ describes the weak decay into electrons, taking into account the branching ratio and shape of the electron spectrum, known from experiment. The total beauty-quark production cross section $\sigma^{b\bar{b}}_{\mathrm{AB}}$ for the collision between hadronic objects A and B (where A, B are either p or Pb at the LHC) is calculated as a convolution of the partonic cross section $\hat{\sigma}_{ij}$ with the parton distribution functions for the colliding particles, F^A_i and F^B_i [Vog02]:

$$\sigma^{b\bar{b}}_{\mathrm{AB}}(s, m_b^2) = \sum_{i,j=q,\bar{q},g} \int_{\frac{4m_Q^2}{s}}^{1} \frac{d\tau}{\tau} \delta(x_1 x_2 - \tau) F^A_i(x_1, \mu^2) F^B_j(x_2, \mu^2) \hat{\sigma}_{ij}(\tau, m_b^2, \mu^2) \qquad . \tag{2.5}$$

τ is defined as $\hat{s}/s$ and the sum is over all massless partons i and j, which carry the fractional momenta x_1 and x_2.

Predictions for the hadronic cross section and the resulting electron spectrum from beauty-hadron decays at the LHC have been made using the FONLL (fixed-order plus next-to-leading logarithmic terms [Cac12]) and the GM-VFNS (general-mass-variable-flavour-number-scheme [Bol13]) frameworks, as well as the k_{T}-factorization approach [Mac11, Mac13b]. The results of the respective calculations will be compared to the measurements treated in this thesis in Chapter 5.

The FONLL and GM-VFNS approaches aim at mending a weakness of the NLO calculations that have been used for predictions for a long time: they are either accurate for $p_{\mathrm{T}} \gg m_b$ (in the case of the zero-mass-variable-flavour-number scheme (ZM-VFNS), assuming a massless b quark) or for $p_{\mathrm{T}} \leq m_b$ (fixed-flavour-number scheme or "massive scheme" (FFNS), assuming four light flavours in the initial state, adding a massive b quark only in the final state) [Kni08]. The transition region between both regimes, of high importance for the RHIC and LHC experiments, is not covered reliably.

The FONLL calculation of $\frac{\mathrm{d}\sigma^{b\bar{b}}_{\mathrm{AB}}}{\mathrm{d}p_{\mathrm{T}}}$ starts from a fixed-order NLO calculation of the FFNS, combining it with an all-order resummation up to next-to-leading logarithms[1], for the limit of $p_{\mathrm{T}} \gg m_b$ [Cac98] [Cac12].

As its name suggests, the GM-VFN scheme is conceptually closer to the ZM-VFNS approach, starting from the assumption of $p_{\mathrm{T}} \ll m_b$, but taking into account a heavy

[1]The terms considered for resummation are the leading logarithms (LL) of the order $\alpha_{\mathrm{S}}^2(\alpha_{\mathrm{S}} \ln(p_{\mathrm{T}}/m_b))^n$ and the next-to-leading logarithms (NLL) of the order $\alpha_{\mathrm{S}}^3(\alpha_{\mathrm{S}} \ln(p_{\mathrm{T}}/m_b))^n$.

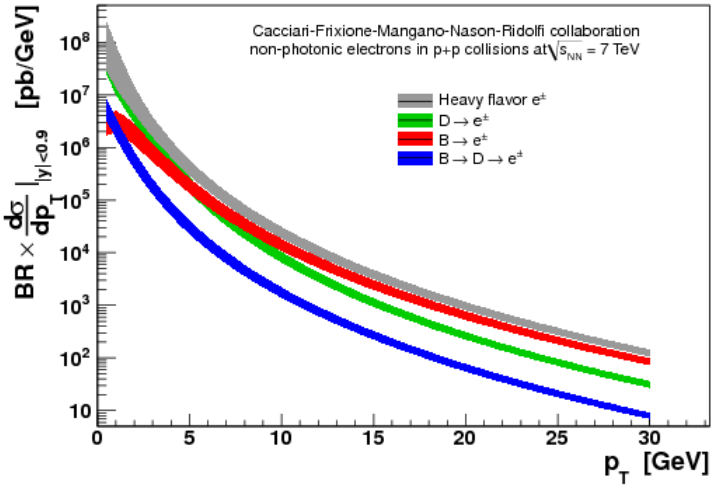

Figure 2.3: Predictions for p_{T}-differential production cross sections of electrons from direct and indirect decays of B mesons and from D-meson decays for pp collisions at $\sqrt{s} = 7$ TeV (taken from [Fas12], therein based on [Cac98]).

b quark besides four massless quarks. Here, the occurring large terms $\ln(\mu_{\mathrm{F}}/m_b)^2$ are absorbed into the parton distribution function of the initial-state hadrons and the fragmentation function for the hadronization of b quarks, while all m^2/p_{T} power terms, neglected in the ZM-VFN scheme, are included for the hard-scattering cross section calculation [Kni08].

In contrast to the two approaches described above, the k_{T}-factorization scheme is based on the unintegrated gluon distribution functions (UGDFs, [Kim01]) of the protons, which depend on the transverse momenta k_{T} of the initial partons. It starts from the assumption that at LHC energies, gluon splitting is by far dominant over quark-antiquark annihilation for heavy-flavour production. By design, it also includes some contributions from NLO processes and from partons carrying low momentum fractions x of the protons. Since at LHC energies, low x can correspond to rather high absolute momenta, and thus to equivalently hard parton scatterings, the low-x domain is of some importance for the prediction of charm production in ALICE [Mac13b].

In the calculations described above, the dominant uncertainties arise from the choice of renormalization and factorization scales and from variation of the charm and beauty-quark masses, the latter point being neglected in the GM-VFN scheme.

Figure 2.3 shows FONLL predictions for the production of electrons from B-meson and D-meson decays, as well as for the indirect decays $B \to D \to e$ in pp collisions at the LHC energy of 7 TeV. The B-decay contribution to the heavy-flavour electron yield is expected to become dominant with respect to electrons from D decays towards high p_{T}, while the total electron cross section from heavy-flavour hadron decays is dominated by the D decays at low p_{T}.

2.2.1 Open Heavy-Flavour Production Cross Section in pp and p$\bar{\text{p}}$ Collisions: Preceding Measurements

In the pre-LHC era, numerous heavy-flavour measurements have been performed in hadron collisions at RHIC[2] by the PHENIX[3] and STAR[4] experiment and at the Tevatron by the CDF[5] and D0 experiments.

PHENIX [Ada06b] and STAR [Aga11] measured the p_{T}-differential production cross section of electrons from inclusive heavy-flavour hadron decays in pp collisions at $\sqrt{s} = 200$ GeV at rapidities of $|y| < 0.35$ and $|y| < 0.7$, respectively. FONLL predictions tend to slightly lower values than the measurements, but are still in agreement within the theoretical and experimental uncertainties. A measurement of muons from heavy-flavour decays at forward rapidity for 1 GeV/$c < p_{\mathrm{T}} < 3$ GeV/c at PHENIX lies significantly above the FONLL values [Adl07b].

Separate measurements of the production of charm and beauty-decay electrons have been performed at STAR [Aga11] and PHENIX [Ada09] by exploiting the different kinematics of beauty and charm decays to determine their relative contributions to the inclusive heavy-flavour electron spectrum. STAR analysed azimuthal angular electron-hadron correlations [Agg10], while PHENIX, whose result is comparable, but has far larger uncertainties, measured the invariant-mass distributions of electon-hadron pairs [Ada09]. The relative number of charm and beauty decays in both measurements was determined by comparison of the angular and invariant-mass distributions to those obtained from simulations. By combination with their respective measurements of inclusive heavy-flavour electrons, both experiments have extracted p_{T}-differential production cross sections of electrons from charm decays and from beauty decays, which agree with FONLL calculations within uncertainties. The results from STAR are presented in Figure 2.4.

The CDF and D0 collaboration at the Tevatron measured heavy-flavour production at p$\bar{\text{p}}$ collision energies of 1.8 TeV and 1.96 TeV. The analyses of exclusive hadronic charm-decay channels performed by CDF hinted to an underprediction of D-meson production at mid-rapidity by NLO pQCD calculations. However, the predictions were still compatible with the experimental results within uncertainties [Aco03].

First results of beauty production measurements at the Tevatron for $\sqrt{s} = 1.8$ TeV showed a more significant deviation from theoretical expectations: CDF analyses of the decays $B^0 \to J/\psi K^*$ and $B^+ \to J/\psi K^+$ found an excess of beauty production of a factor 3 as compared to NLO pQCD predictions [Aco02] that was confirmed by measurements of muonic decays from the D0 collaboration [Abb00]. After a detector upgrade that, among other aspects, enabled triggering on displaced vertices, CDF measurements of $B \to J/\psi$ decays on a data set from p$\bar{\text{p}}$ collisions

[2]Relativistic Heavy Ion Collider
[3]Pioneering High Energy Nuclear Interactions eXperiment
[4]Solenoidal Tracker At RHIC
[5]Collider Detector at Fermilab

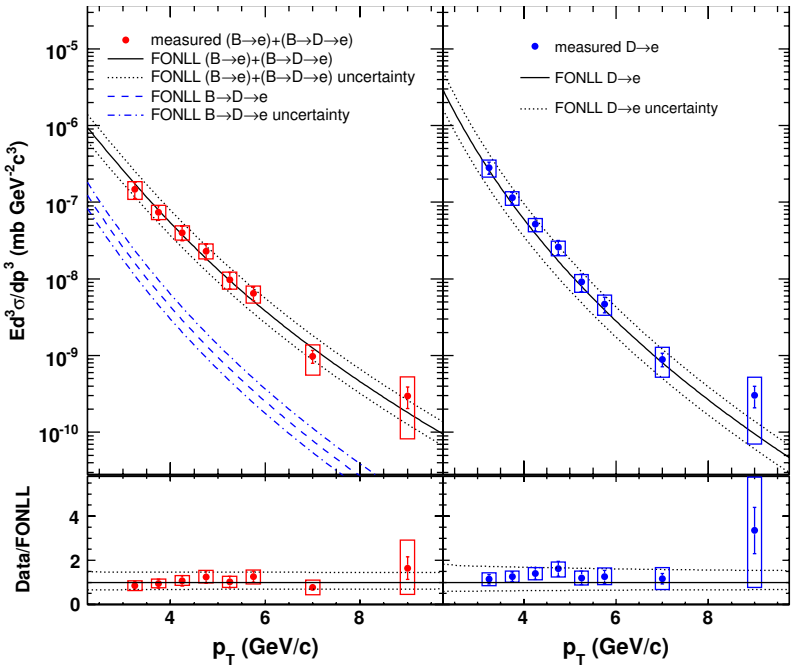

Figure 2.4: STAR measurements of the production cross section of electrons from beauty (upper left) and charm (upper right) decays [Aga11], compared to FONLL predictions. For beauty decays, FONLL curves for the indirect decay $B \to D \to e$ are represented in blue. The lower panels show the ratios of the measurements to the corresponding FONLL calculations.

at $\sqrt{s} = 1.96$ TeV [Aco05] could reconcile theoretical predictions (this time already based on FONLL) and experimental results, mostly owing to important improvements of the experimental inputs used by predictions [Man05].

More recently, a large number of measurements of open heavy flavour production have been performed at the LHC for the pp centre-of-mass energies of 7 TeV and 2.76 TeV. Results include p_{T}-differential production cross sections of exclusive D-meson decays [Abe12e, Abe12a, Abe12c] measured with ALICE at mid-rapidity and with LHCb at forward rapidity [Aai13b], and of muons from inclusive heavy-flavour hadron decays at forward rapidity at ALICE [Abe12b, Abe12k] and ATLAS [Aad12b]. The ALICE analyses of the semi-muonic decay channels are complementary to mid-rapidity measurements of semi-electronic decays of heavy-flavour hadrons for 0.5 GeV/c $< p_{\mathrm{T}} <$ 8 GeV/c [Abe12g, Ave13b], which are closely related to the analysis treated in this thesis, and whose results will be referred to in Chapter 5. ATLAS measurements for 7 GeV/c $< p_{\mathrm{T}} <$ 26 GeV/c [Aad12b] extend the p_{T} range of LHC results for heavy-flavour electrons and are in good agreement with the ALICE results. A combined representation of the inclusive heavy-flavour electron spectrum for $\sqrt{s} = 7$ TeV by ALICE and the corresponding spectrum by ATLAS is given in the left panel of Figure 2.5.

All measurements agree with FONLL and, where available, GM-VFNS predic-

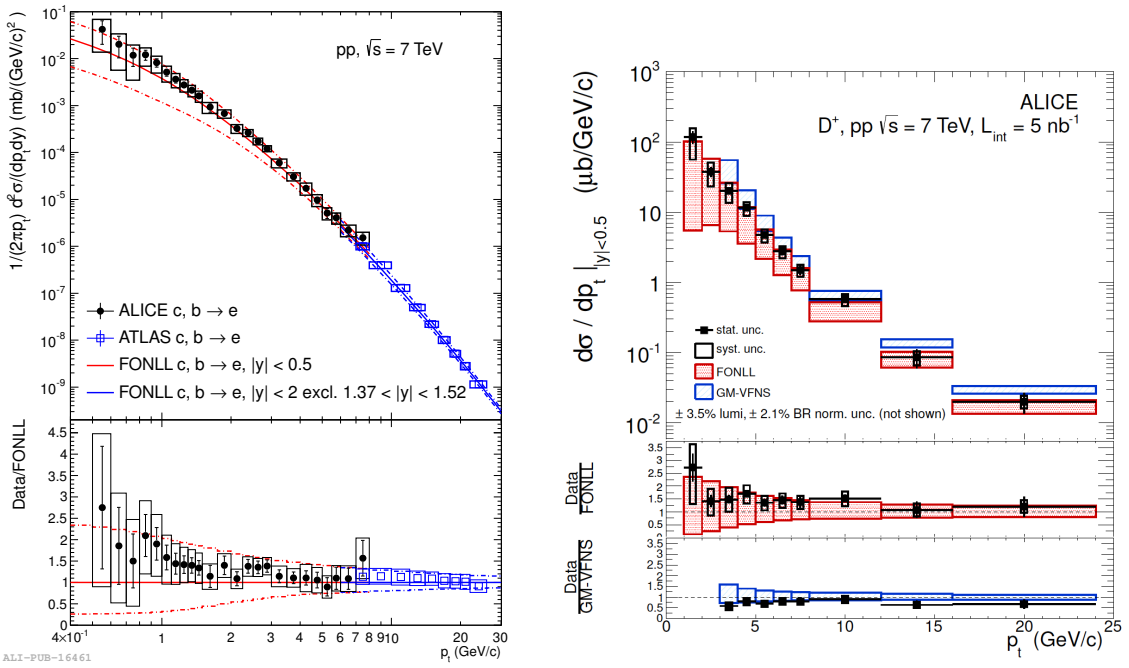

Figure 2.5: Left: p_{T}-differential production cross section of electrons from inclusive heavy-flavour hadron decays, measured by ALICE (black) and ATLAS (blue) [Abe12g], compared to a FONLL prediction. Right: p_{T}-differential production cross section of D^+ mesons at mid-rapidity, measured with ALICE at $\sqrt{s} = 7$ TeV, and calculations by FONLL and GM-VFNS (upper panel) [Abe12e]. The lower panels of both plots show the ratios between measurements and theoretical predictions.

tions within uncertainties. In the case of exclusive D-meson decays, shown in the right panel of Figure 2.5 for D^+, the measured points are close to the upper limit of FONLL predictions, which, in turn, is close to the lower limit of GM-VFNS predictions.

Dedicated analyses of decays of hadrons containing beauty have been performed by the ATLAS and LHCb collaborations for $\sqrt{s} = 7$ TeV. At ATLAS, the p_{T}-differential cross sections of b-hadron and B^+ production for $p_{\mathrm{T}} > 9$ GeV/c have been measured at mid-rapidity [Aad12a, Aad13], while LHCb analysed exclusive decays of $B^{+/-}$, B^0, and B_s^0 for 0-40 GeV/c at forward rapidity [Aai12, Aai13a] (see Figure 2.6, left, for the case of D^+). All results could be described by theoretical predictions within uncertainties.[6]

Analyses of beauty production via measurements of non-prompt J/ψ have been carried out by CMS and ALICE for $\sqrt{s} = 7$ TeV. CMS has measured the p_{T}-differential $B \to J/\psi$ cross section in different rapidity intervals around mid-rapidity,

[6] ATLAS results were compared to NLO QCD and, in the case of B^+, with FONLL calculations. Predictions for LHCb measurements were provided by FONLL calculations.

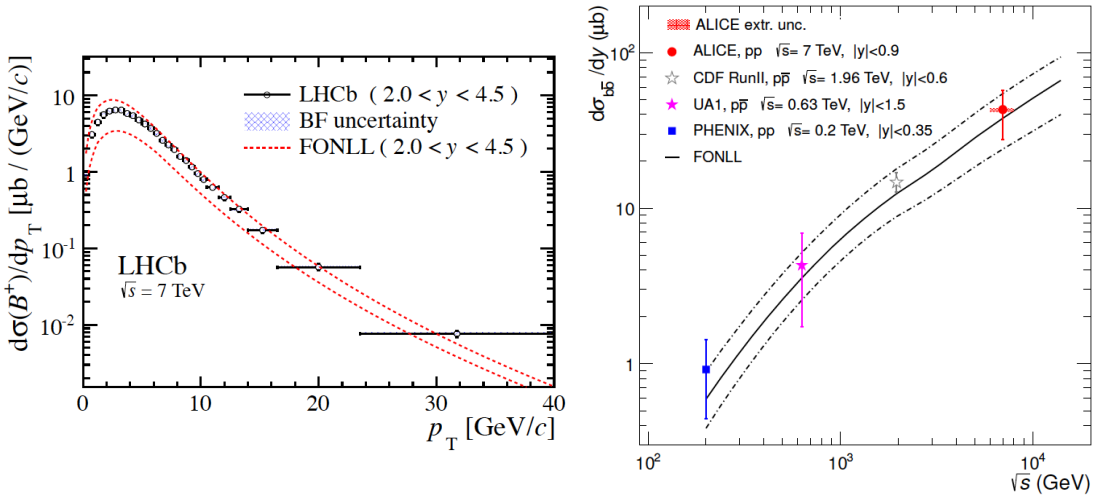

Figure 2.6: Left: p_{T}-differential production cross section of B^+ mesons at mid-rapidity, measured by LHCb at $\sqrt{s} = 7$ TeV, compared to FONLL calculations [Aai13a]. Blue-shaded areas represent the uncertainty from the D^+ branching fraction. Right: total beauty-hadron production cross section for pp collisions at different centre-of-mass energies [Abe12i]. Measurements from PHENIX, the UA1 experiment at the SPS, CDF, and ALICE are compared to FONLL predictions.

where results are well described by FONLL predictions [Kha11a], while ALICE has been able to extract the total beauty-hadron production cross section from non-prompt J/ψ measurements at mid-rapidity [Abe12i] (see Figure 2.6, right).

2.3 Heavy-Ion Collisions and the Quark-Gluon Plasma

One important purpose of the measurements in pp collisions treated in this thesis is to provide a reference for comparison with the electron spectra from beauty-hadron decays in Pb-Pb collisions, which are expected to be modified by the interaction between the beauty quarks and the hot and dense medium produced in heavy-ion collisions at the LHC. ALICE is the LHC experiment dedicated to measurements in heavy-ion collisions. A particular advantage of using reference measurements from the same experiment is the possible cancellation of a series of systematic uncertainties that are common to pp and Pb-Pb measurements, resulting in a high significance of the comparison between both results.

The conditions for the generation of the medium generated in Pb-Pb collisions, the so-called *Quark-Gluon Plasma* (QGP), can be qualitatively predicted by effective models emulating QCD, e.g. *bag models* [Tak87,Sav91] or models taking into account purely thermodynamical considerations [Han01, Pes94]. The existence of strongly

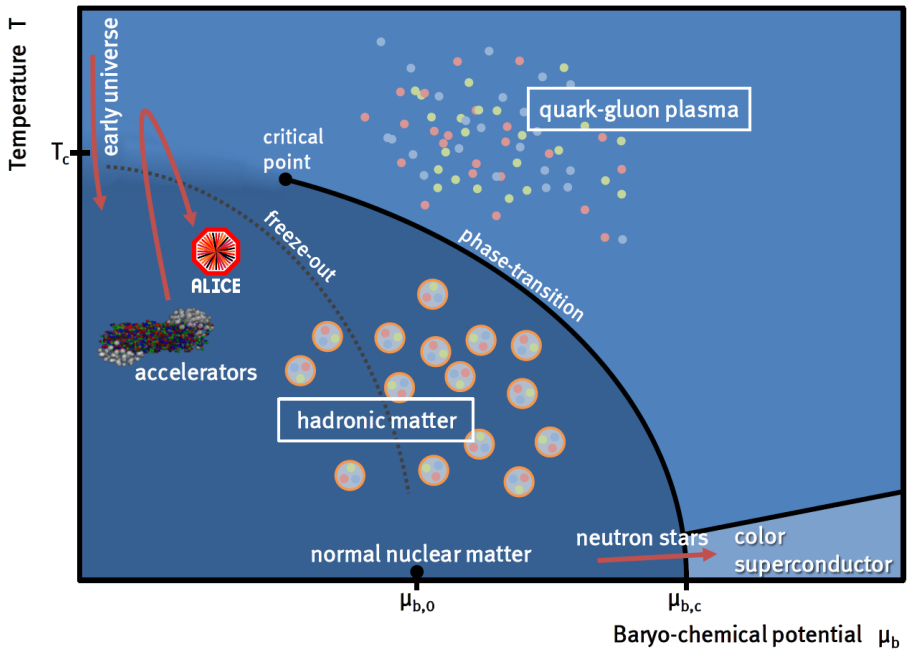

Figure 2.7: Schematic representation of a possible phase diagram of strongly interacting matter in terms of temperature T and baryo-chemical potential μ_b, taken from [Bat12]. Thick lines indicate first-order phase transitions. At low μ_b, a gradual crossover between hadronic matter and Quark-Gluon Plasma is expected. For very strongly compressed systems, the formation of a colour superconductor is predicted.

interacting matter in different phases is suggested, depending on the temperature T and the baryo-chemical potential μ_b. Schematically, these phases are represented in Figure 2.7.

In a system of quarks and gluons, deconfinement can exist in the case of extremely high energy densities. These can be achieved by increasing the temperature of the system or its baryo-chemical potential μ_b, which is a measure of the baryon density.

At low temperatures and small values of μ_b, quarks and gluons are confined in hadronic matter, combining to colourless objects as in the common nuclear matter of our environment, indicated in Figure 2.7 at $\mu_{\mathrm{b},0}$. At high densities and low temperatures, an additional state of matter, the *colour superconductor*, is predicted to be created [Bla10], in which quarks and gluons form Colour Cooper pairs. This state could exist in the core of neutron stars, under extreme gravitational compression.

In ultra-relativistic heavy-ion collisions, where high temperatures are achieved at low μ_b, the energy density is high enough to produce additional hadrons and thereby increase the particle density of the generated medium. If the collision occurs at a sufficiently high energy, the distance between neighbouring quarks becomes so small that separate hadrons cease to exist, and no confining interaction among groups of two or three quarks occurs. Instead, quarks can move freely inside the created phase,

the Quark-Gluon Plasma - an effect that is called *deconfinement*. The conditions for creation of this state of matter were supposedly met during the first few microseconds of the existence of our universe. Today, a QGP can only be created at heavy-ion colliders operating at the highest achievable energies.

Quantitative predictions for the behaviour of quarks and gluons during the phase transition between hadronic matter and QGP can be made by lattice QCD for the case of $\mu_\mathrm{b} = 0$. Figure 2.8 shows the results of LQCD calculations for the dependence of the energy density ϵ, in terms of the variable ϵ/T^4, on the temperature T of the medium. The quick rise in ϵ that is observed at $T \approx 150$ MeV can be attributed to an increase of the degrees of freedom n_dof in the medium, since

$$\epsilon = n_\mathrm{dof} \frac{\pi^2}{30} T^4 \tag{2.6}$$

for an equilibrated ideal gas. With the transition from a confined to a deconfined phase, ϵ would rise as a consequence of additional colour and flavour degrees of freedom. However, the rise in energy density does not seem to have the character of a sharp first-order phase transition, like the melting or evaporation of water, but is rather a rapid, but smooth crossover to a new state of matter. The fact that the Stefan-Boltzmann limit for ideal relativistic gases, given by Equation 2.6, is not reached even for temperatures much higher than the transition region indicates that there are still significant interactions between the quarks and gluons at this stage. Therefore, one speaks of a *strongly interacting QGP* (sQGP).

For higher μ_b, the confined phase has generally been expected to be separated from the deconfined phase by a sharply defined first-order transition instead of a continuous crossover (cf. [Sto09] and references therein). This would imply the existence of a critical endpoint to the first-order phase transition line, as shown in Figure 2.7. At present, approximative LQCD calculations for the deconfinement phase boundary are available up to values of μ_b as high as 500 MeV. Unfortunately, results from different methods are still divergent, such that the existence of a critical point in this region could neither be proved nor excluded [Phi12].

It has further been observed in experiments at the *Relativistic Heavy Ion Collider* (RHIC) that for $\mu_\mathrm{b} \to 0$, transitions from a deconfined to a confined phase coincide with a hadro-chemical freeze-out, i.e. the point at which the multiplicities of different hadron species are no longer changed by inelastic interactions between particles of the medium. From measurements at lower collision energies, it has been concluded that for larger values of μ_b, the freeze-out happens at temperatures that are significantly below the ones at which confinement is expected to set in [Sto09]. The observed freeze-out curve is drawn in Figure 2.7. As a possible description of the behaviour of the medium from the onset of confinement to a hadro-chemical equilibrium at large μ_b, an intermediate *quarkyonic* QCD phase has been proposed by McLerran et al. [McL07], potentially involving a separation of the phase-transition lines of deconfinement and chiral symmetry restoration.

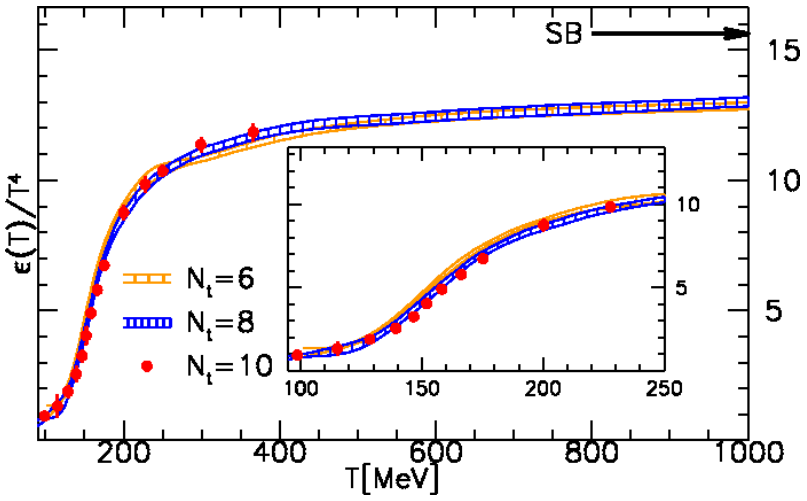

Figure 2.8: Energy density ϵ/T^4 as a function of temperature T. Curves and data points for $N_\mathrm{t} = 6$, 8, 10 correspond to the results of lattice QCD calculations with different lattice spacings, 10 being the finest one. Two light quarks with degenerate mass and one heavy strange quark (all with physical mass values) are assumed. The arrow on the upper right indicates the energy density at the Stefan-Boltzmann limit for ideal gases [Bor10].

2.3.1 Space-Time Dynamics of Heavy-Ion Collisions

In 2010 and 2011, collisions of lead nuclei have taken place at the LHC at centre-of-mass energies $\sqrt{s_\mathrm{NN}}$ per nucleon pair of 2.76 TeV. The maximal collision energy of $\sqrt{s_\mathrm{NN}} = 5.5$ TeV, for which the LHC has been designed, will prospectively be reached in 2015. In this highly relativistic system, Lorentz contraction makes both nuclei appear as thin discs to each other, as sketched in Figure 2.9. In most collisions, only some of the nucleons of each nucleus – the *participants* – interact with their counterparts. The rest of them, the *spectators*, continue their original trajectory without contributing to the processes in the so-called *fireball* which develops in the overlap zone between both nuclei. The size of this zone depends on the centrality of the collision, described by the *impact parameter*[7], which measures the distance of closest approach between the centres of the nuclei.

For LHC energies, the collisions are well described by the *Bjorken-McLerran model* [Bjo83], in which the nuclei are to a high degree transparent to each other, so that an interpenetration with a low energy loss through nuclear stopping takes place. In this scenario, extremely high temperatures at very low baryon densities are reached.

The lower panel of Figure 2.9 gives an overview of the space-time evolution of a heavy-ion collision. In the interactions at the very beginning of the collision, a non-equilibrated phase of highly excited matter is formed. Thermal equilibrium is

[7]This collisional impact parameter should not be confused with the transverse impact parameter of reconstructed electrons with respect to the primary vertex that appears in the title of this thesis, and which is described in Section 4.6.

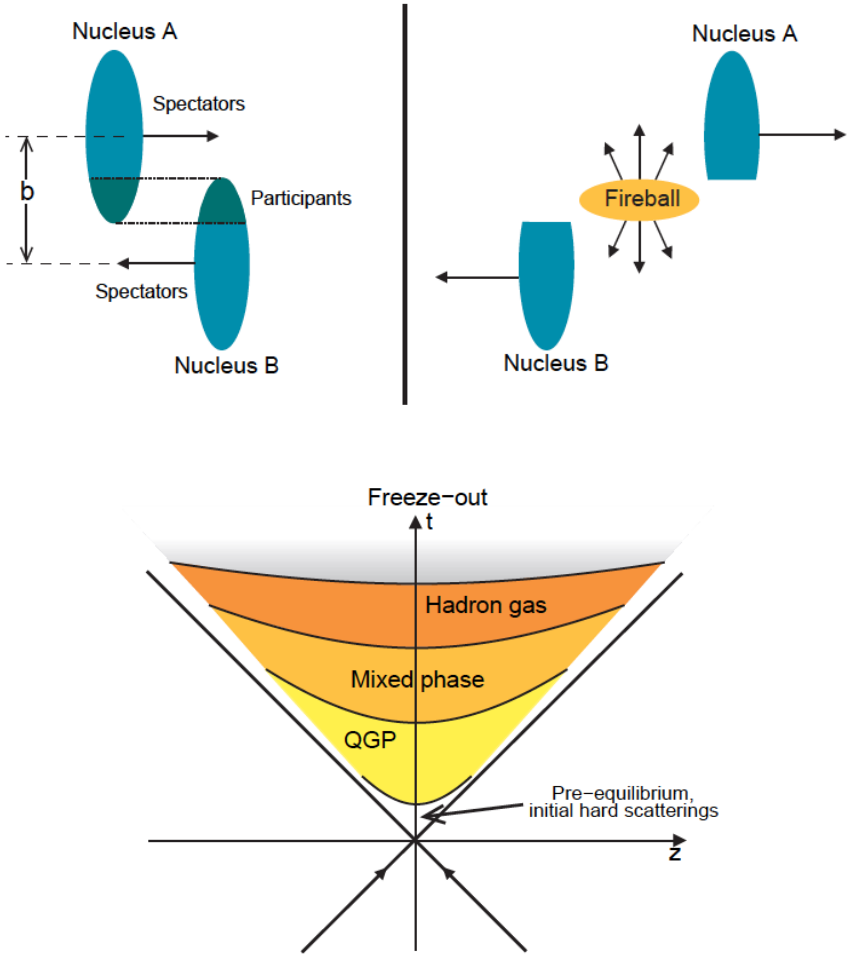

Figure 2.9: Upper panel: participant-spectator model of a nucleus-nucleus collision. The distance of closest approach between the centres of both nuclei, the impact parameter b, is a measure of the centrality of the collision. Nucleons in the overlapping parts of the nuclei are the *participants*, which form the expanding *fireball*. The remaining *spectators* are mostly unaffected. Lower panel: space-time dynamics of a central ultra-relativistic nucleus-nucleus collision. After an initial non-equilibrated phase of hard scatterings, the system thermalizes. If the energy density generated in the collision is sufficiently high, a Quark-Gluon Plasma is formed. During its expansion, the fireball cools down and a transition to a hadronic phase takes place, possibly passing through a stage of a mixed phase where regions of QGP and hadron gas exist simultaneously. When there are no more inelastic interactions between hadrons, the chemical freeze-out is reached. Both graphics taken from [Wil10], therein adapted from [Kle04].

expected to be reached after a short period of expansion of the fireball into the surrounding vacuum. In central collisions, which should produce a sufficiently high energy density at the LHC, a Quark-Gluon Plasma is formed. The hot and dense medium continues its expansion, during which it cools down until the energy density is low enough for matter to condensate into hadrons. Possibly, the system passes through a *mixed phase* of domains of hadrons and of QGP before turning into a hadron gas. The moment at which the amounts of particles of each species in the medium cease to change is called the *chemical freeze-out*. At a later stage, the density of the hadron gas has decreased to a level at which no momentum exchange between particles takes place anymore – the *thermal freeze-out* is reached. At this moment, all interactions between the constituents of the medium have stopped. Further changes in relative abundances of particle species and kinematical properties occur only through decay of unstable particles and interaction with the surrounding material of the experimental apparatus.

2.3.2 Signatures of the Quark-Gluon Plasma

The generation of a QGP in heavy-ion collisions cannot be proved by measuring one single signal, since each of the proposed candidates for a QGP signature may also be explained by models involving hadronic interactions. However, a combination of several of these signatures may provide sufficient evidence for deconfinement.

Harris and Müller [Har96] gave an overview of the numerous expected characteristic QGP signals, dividing them into several classes that form one of the most commonly used classification schemes until today:

- **Kinematic probes.** Among these are global observables that describe the overall behaviour of the particles produced in the collision. A phase transition between hadronic matter and Quark-Gluon Plasma would have an impact on the dependences between thermodynamical quantities like the pressure, energy density, entropy, or temperature of the system (see, e.g., Figure 2.8). Such quantities can be inferred from observables like charged particle multiplicity $\mathrm{d}N_{\mathrm{ch}}/\mathrm{d}y$ or transverse energy $\mathrm{d}E_{\mathrm{T}}/\mathrm{d}y$ per rapidity unit at mid-rapidity, and to some extent also from the average transverse momentum $\langle p_{\mathrm{T}} \rangle$ of the measured particles.

  As a result of the radially asymmetric shape of the overlap region of two colliding nuclei, anisotropic pressure gradients exist initially in the expanding system. These have an influence on the observed particle momenta at different emission angles, such that a collective anisotropic outward flow is generated, whose measurement can provide information about the hydrodynamical properties and the equation of state of the medium.

  Moreover, identical-particle interferometry (*Hanbury Brown and Twiss* or *HBT interferometry*) can be used to study the size and lifetime of the medium.

- **Electromagnetic probes.** Neither photons nor leptons take part in the strong interaction. Therefore, they can be used as probes for the development of the medium from the initial stages of the collision. Both are produced throughout the collision, although their prevalent production mechanisms change with the development of the expanding fireball.

  From photon measurements, the amount of thermal radiation, and thus the temperature of the medium, can be inferred, as described in [Wil14]. At LHC energies, a QGP with a temperature clearly exceeding the expected critical value of T_c is assumed to be produced, which should result in a correspondingly high yield of thermal radiation. ALICE measurements by M. Wilde [Wil13] showed that the shape of the p_T-differential spectrum of direct photons is consistent with a thermal photon spectrum, and that its contribution to the overall photon yield is substantial up to a transverse momentum of 4 GeV/c.

  Pairs of electrons or muons are produced in the QGP by annihilations of quarks and antiquarks; their production rate depends on the momentum distribution of the freely propagating quarks in the medium and can therefore yield valuable information about the thermodynamical properties of the system [Won94]. But lepton pairs can also arise from interactions of charged particles in a hadron gas (e.g. $\pi^+ + \pi^- \rightarrow l^+ + l^-$), or from the Drell-Yan process, in which a valence quark from one nucleon annihilates with a sea-antiquark of another one. A further source of dileptons are decays of short-living mesons, like π^0, η, ρ^0, ω, and ϕ, which can be identified via their invariant mass. Moreover, measurements of electrons and muons include signals from the semi-leptonic decays of heavy-flavoured hadrons, such as J/ψ, open charm and open beauty. The significance of the latter contribution as a probe for the QGP phase will be discussed in detail in the next section.

- **Probes of chiral symmetry restoration.** The onset of deconfinement is closely connected (but not necessarily simultaneous) to another type of phase transition, the restoration of chiral symmetry, which is expected in the QGP phase. The transition from the chirally symmetric phase of the QGP to a phase with broken chiral symmetry may produce domains of a so-called *disoriented chiral condensate* (DCC), which can be described as a coherently excited pion field. An expected signature of a DCC is a large event-by-event fluctuation of the ratio between charged and neutral pions, into which the condensate decays [Aba98].

  As will be discussed in Section 2.4, the masses of light quarks are affected by chiral symmetry restoration. A broadening and, to a lesser degree, a shift of the invariant-mass distributions measured via dileptonic decays of the vector mesons ρ, ω, and ϕ is predicted [Koc97].

- **Hard QCD probes.** Partons with a high p_T from hard scattering fragment into several hadrons that move in a similar direction. Groups of such particles

occurring in bunches around a leading high-p_T particle are called *jets*. When passing through a Quark-Gluon Plasma, their initial partons can suffer elastic energy loss by collision with other partons or radiative energy loss by the emission of gluons (for more details, see Section 2.4). These processes would result in a reduction of the measured yield of high-p_{T} particles in Pb-Pb collisions as compared to proton-proton collisions, the so-called *jet quenching*. Furthermore, correlations between jets emitted back-to-back from the same hard scattering process may be changed by the presence of a QGP.

- **Probes of deconfinement.** The presence of a deconfined medium is expected to influence the yields of *quarkonia*. These are the mesons J/ψ, Υ, and their excited states, which consist of a heavy quark and its antiquark and are produced in initial hard scatterings. In earlier predictions (cf. [Mat86,Har96]), a mere suppression of quarkonia in a QGP with respect to the corresponding yields in proton-(anti)proton collisions was proposed. It was argued that owing to the influence of the surrounding medium, many of the produced $c\bar{c}$ and $b\bar{b}$ pairs were unable to bind and rather formed D or B mesons with light quarks. More recent works [Gre04], [BM07] predict an interplay of two effects at least for the case of the J/ψ: in addition to the aforementioned suppression mechanism, random coalescence of independently produced c and $\bar{c}$ becomes effective at RHIC and LHC energies, as the amount of $c\bar{c}$ pairs produced in one central Pb-Pb collision is of the order of 100 at LHC. The consequence is an enhancement of the J/ψ yield. The comparison between results from ALICE and the PHENIX experiment at RHIC [Ars13] confirms this model and hints to a dominant J/ψ suppression mechanism that is substantially moderated by coalescence effects.

  In the next section, the energy loss of heavy quarks, and in particular the beauty quark, as another signature of a deconfined medium will be discussed.

The list of predicted QGP signatures as given above is far from being exhaustive. For more detailed descriptions of expected signatures of a QGP, see [Won94], [KY05].

2.4 Beauty Quarks as a Probe for the Quark-Gluon Plasma

The temporal and spatial scale for the production of heavy quarks is of the order of $1/Q$, where Q is the momentum transfer of the process. Since for beauty production, $Q_{\mathrm{min}} = 2\ m_b$, this corresponds to a narrow spatial constraint and very short production times $\Delta\tau \sim 0.02$ fm, as compared to the expected lifetime of the QGP phase at LHC, > 10 fm. Hence, beauty quarks experience the complete history from Quark-Gluon-Plasma formation to the chemical freeze-out and can be ideally used as probes for this phase.

The passage of heavy quarks through the strongly interacting medium influences the measured quantities related to them. Examples are transverse-momentum distributions of heavy-flavoured hadrons and of their decay products, but also angular distributions and correlations of particles from heavy-flavour decays. While all this is also true for quantities related to light quarks, differences between both can provide information about the specific mechanisms that become effective in the interactions between the probes and the medium.

One difference in this respect is the behaviour of light and heavy quarks in an environment where chiral symmetry is restored, as it is predicted for the QGP phase. Since the masses of the light up, down, and strange *constituent quarks* in baryons mostly arise from spontaneous chiral symmetry breaking in the QCD vacuum, the restoration of this symmetry reduces them to their much smaller *current quark masses* of only a few MeV, as illustrated in Figure 2.10. In contrast, the masses of charm, beauty, and top quarks are practically entirely generated by their coupling to the electroweak Higgs field. Therefore, heavy quarks remain heavy even in a QGP.

The large mass of a high-momentum b quark plays an important role for the difference of its energy loss in QCD matter compared to light quarks, as will be explained below. Moreover, the beauty current quark mass clearly exceeds the scale of the QGP temperatures that can be generated in heavy-ion collisions, so that the total amount of b quarks is not changed by thermal production and is thus conserved throughout the development of the system.

2.4.1 Energy Loss in the Quark-Gluon Plasma

Two sources of energy loss can be identified for a parton propagating through a QGP: a collisional contribution, caused by elastic scattering of the quark on partons of the medium, and a radiative energy loss by emission of gluon bremsstrahlung. Estimations of the relative contributions of these mechanisms have undergone significant changes throughout the past three decades. While first approaches to this problem, starting from work by J.D. Bjorken [Bjo82], focussed on a rather low collisional energy loss, later publications predicted a pQCD-based radiative energy loss to be clearly dominant over the collisional contributions at RHIC and LHC energies, so that the latter were neglected.

A formulation of this radiative approach by Baier, Dokshitzer, Mueller, Peigné and Schiff [Bai97a, Bai97b], named "BDMPS" after the initials of its authors, establishes a dependence of the average energy loss $\langle \Delta E \rangle$ on α_{S}, on the so-called *Casimir factor* C_{R}, on the transport coefficient $\hat{q}$ of the medium, and on the in-medium path length L of a parton, as

$$\langle \Delta E \rangle \sim \alpha_{\mathrm{S}} C_{\mathrm{R}} \hat{q} L^2 \quad . \tag{2.7}$$

A remarkable feature is the dependence on L^2, in contrast to $\langle \Delta E \rangle \sim L$ for QED bremsstrahlung. Furthermore, no explicit dependence of ΔE on E is given, apart

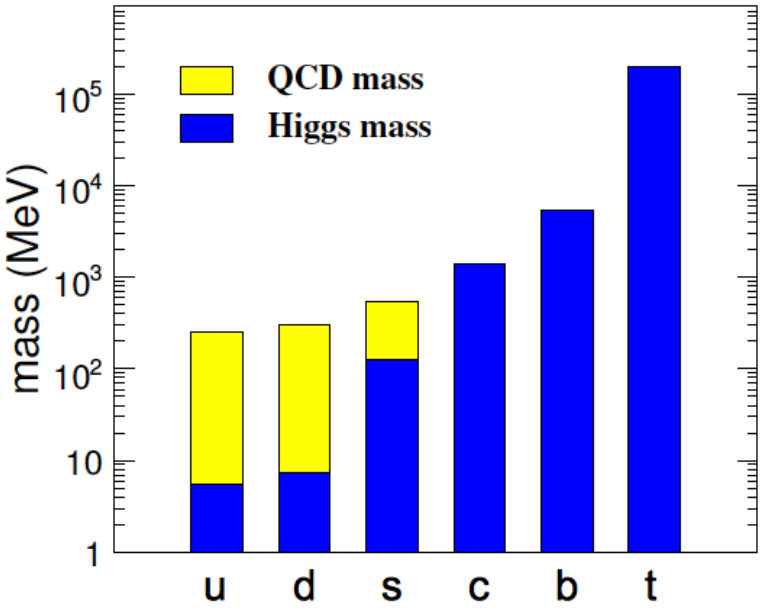

Figure 2.10: Contributions to the overall masses of different quark flavours: current quark masses from electroweak symmetry breaking are plotted in blue; constituent quark masses generated by chiral symmetry breaking in the QCD vacuum are represented in yellow. Adapted from [Mue05] and [Zha07].

from the obvious fact that the energy loss cannot exceed the overall kinetic energy of the parton.

The Casimir factor C_{R} describes the coupling strength of gluons to each other, where it takes on the value of 3, or between a quark and a gluon, where its value is 4/3. Since heavy-flavoured hadrons are mainly produced from quark jets, whereas light hadrons are generated from gluon jets, this difference should be reflected in the p_{T}-spectra of these hadrons and their decay products: the transverse momenta of heavy-flavoured particles should on average be reduced to a lesser degree than that of their light-flavoured counterparts.

Besides the influence of the Casimir factor, the so-called *dead-cone effect* is expected to cause a difference in radiative energy loss between light and heavy quarks. Dokshitzer et al. [Dok01] showed that the probability P of gluon emission off a heavy quark depends on the emission angle ϑ with respect to the direction of movement of a quark:

$$\mathrm{d}P = \frac{\alpha_{\mathrm{S}} C_{\mathrm{R}}}{\pi} \frac{\mathrm{d}\omega}{\omega} \frac{\mathrm{d}\vartheta}{\vartheta} \left(1 + \frac{\vartheta_0^2}{\vartheta^2}\right)^{-2} \quad , \tag{2.8}$$

where ω is the energy of the emitted gluon, and $\vartheta_0 = \frac{M}{E}$ is given by the ratio of the mass and kinetic energy of the quark. This means that for angles ϑ that are

small compared to this ratio, gluon emission by heavy quarks is suppressed, while for $\vartheta \gg \vartheta_0$, no difference between energy loss for light and heavy quarks exists.

As a consequence of the relations described by Equations 2.7 and 2.8, the overall energy loss by gluon radiation is predicted to be significantly lower for heavy quarks, and in particular for beauty quarks, whose large mass widens the dead cone considerably. Hence, the following energy-loss hierarchy is expected:

$$\Delta E_{\mathrm{gluon}} > \Delta E_{\mathrm{light-quark}} > \Delta E_{\mathrm{charm}} > \Delta E_{\mathrm{beauty}} \quad . \tag{2.9}$$

2.4.2 The Nuclear Modification Factor R_{AA}

For the quantification of the impact of energy-loss effects on the p_{T} distributions of the produced particles, one can refer to the respective calculations of the Glauber model [Gla70]. In this semi-classical description, a nucleus-nucleus collision is described as a superposition of inelastic binary nucleon-nucleon collisions, whose average number is $\langle N_{\mathrm{coll}} \rangle$ for a certain collision centrality, given by the impact parameter b (see Figure 2.9). Based on these considerations, a *nuclear modification factor* R_{AA} can be defined:

$$R_{\mathrm{AA}}(p_{\mathrm{T}}) = \frac{1}{\langle N_{\mathrm{coll}} \rangle} \frac{\mathrm{d}N_{\mathrm{AA}}/\mathrm{d}p_{\mathrm{T}}}{\mathrm{d}N_{\mathrm{pp}}/\mathrm{d}p_{\mathrm{T}}} \quad . \tag{2.10}$$

It establishes a relation between the measured p_{T}-differential yields in proton-proton and in nucleus-nucleus collisions, dN_{AA} and dN_{pp}, which are normalized to the number of expected inelastic binary nucleon-nucleon interactions in each collision of nuclei. In other words, the measured spectra are compared to the Glauber model assumption that on average, each of the $\langle N_{\mathrm{coll}} \rangle$ inelastic nucleon collisions of each heavy-ion collision produces the same amount of particles as a proton-proton collision, and that the kinematical properties of these particles are not altered by the presence of the surrounding nuclear or QCD matter. If these assumptions are correct, one finds $R_{\mathrm{AA}} = 1$.

In Pb-Pb collisions at the LHC, deviations from unity can be caused by several effects, depending on the transverse momentum and the mass of the produced partons. One important influence comes from the reduction of the transverse momenta of the measured particles via the energy-loss mechanisms discussed in Section 2.4.1. The aforementioned Casimir factor and the dead cone effect (see Equations 2.7 and 2.8) have an impact on the measured p_{T}-differential spectra of the decay products from heavy-flavoured hadrons. Owing to the predicted smaller energy loss in the QGP, their transverse momenta should suffer only a slight reduction. However, Horowitz [Hor13] points out that the energy-loss hierarchy given in Equation 2.9 does not immediately imply a certain ordering of the R_{AA} of the measured particles, since the nuclear modification factors are susceptible to the shapes of the quark production spectra, the fragmentation functions and, in the case of this analysis, the kinematics of decay into electrons. Despite this restriction, it has been

generally expected (e.g. [Ada07]) that electron yields from heavy-flavour decays for $p_{\mathrm{T}} < 10$ GeV/c should not be as strongly suppressed as, e.g., pions, the most frequent light-flavoured particles (see Section 2.4.4), and that the R_{AA} of beauty-decay electrons should be even closer to unity.

On the other hand, not every R_{AA} value of beauty quarks that exceeds the corresponding values for light quarks has to be interpreted in terms of differences in energy loss. For $p_{\mathrm{T}} \lesssim 2$ GeV/c, the nuclear modification factor for the production of light quarks would be expected to be smaller than the one for heavy quarks even in the absence of in-medium energy loss for all kinds of particles, since the scaling of particle production with the number of binary nucleon-nucleon collisions assumed in Equation 2.10 applies only to hard processes. While this assumption is valid for heavy-quark production at all momenta, light quarks at low p_{T} are mostly produced by soft scattering processes. As a consequence of the considerations discussed above, great care has to be taken in the interpretation of nuclear modification factors.

2.4.3 Cold Nuclear Matter Effects

While the nuclear modification factor can provide valuable information on the interactions between the probe particles and the QGP phase, it is important to note that also for $p_{\mathrm{T}} > 2$ GeV/c, not every deviation from $R_{\mathrm{AA}} = 1$ hints to deconfinement. There are so-called *cold nuclear matter effects* that have an impact on the particle spectra. They can be divided into initial state effects, which arise from the characteristics of the incoming colliding nuclei, and final state effects, which are caused by the hadronic matter that is produced in such a collision.

Examples of initial state effects are

- *nuclear shadowing and anti-shadowing*, modifications of the parton distribution functions inside the colliding nucleons that are initially bound in a nucleus [Bro90],
- the *Cronin effect*, an enhancement of particle yields at moderate transverse momenta [Cro73], generally attributed to multiple scattering of initial partons on the incoming opposite nucleus, by which these partons gain additional transverse momentum,
- energy loss of partons by initial state interactions [Vit07].

The most important final state effect is the absorption of particles produced in the collision by incoming nucleons [Acc07].

To distinguish these phenomena experimentally from the effects of QGP formation on the measured spectra, reference measurements with proton-nucleus or deuteron-nucleus collisions are needed, in which no deconfinement is expected to occur. In central d-Au collisions at RHIC, a strong Cronin enhancement of the p_{T}-differential spectra of protons in the region between 1 and 5 GeV/c was observed, while no

significant enhancement was found in the spectra of π^0, charged kaons and pions, and ϕ. The clear difference between protons and other particle species in this respect remains yet to be explained. For $p_{\mathrm{T}} < 1$ GeV/c, a suppression for all these particle spectra was observed, according to their generation in mostly soft processes [Ada12, Ada13, Ada06a].

The combined electron spectrum from D and B meson decays was found to be enhanced in the same p_{T} range as the proton spectrum, albeit to a lesser degree [Fra12]. Since D decays produce the dominant contribution to the heavy-flavour electron spectrum in this p_{T} region, the enhancement should originate mainly from this electron source. For the same reason, the behaviour for electrons from B decays remained unknown.

As in the case of the nuclear modification factor in Pb-Pb collisions, such observations have to be interpreted under careful consideration of various conditions. In the presence of a similar increase in p_{T}, electron spectra from heavy-flavour decays would have a less pronounced enhancement of the R_{AA} than light-hadron spectra, owing to their smaller spectral slope in p_{T}.

The relative importance of cold nuclear matter effects for beauty-related measurements at the LHC has yet to be clarified and requires dedicated analyses of data from p-Pb collisions, some of which are being carried out at the time of this thesis. At present, these effects are not expected to be very large for heavy-flavour production; however, the related predictions suffer from considerable uncertainties [Sal12].

2.4.4 Heavy-Quark Energy Loss in a Quark-Gluon Plasma: Conclusions from Previous Results and Open Questions

Measurements of the R_{AA} of electrons from heavy-flavour hadron decays have been presented at RHIC for Au-Au collisions at $\sqrt{s_{\mathrm{NN}}} = 200$ GeV by the PHENIX [Ada07] and STAR [Abe07, Abe11] collaboration, where the latter measurement suffers from large uncertainties. Panel (a) in Figure 2.11 shows the PHENIX result for the 0-10% most central events in comparison with the corresponding R_{AA} of neutral pions and with different theoretical predictions.

While the heavy-flavour decay electron R_{AA} for low p_{T} clearly exceeds the one of the π^0 measurements, both values become comparable at $p_{\mathrm{T}} > 4$ GeV/c. The latter observation is particularly surprising since at higher momenta, the electron contribution from beauty decays is expected to become more important (cf. Figure 2.3).

The predictions that are compared to the PHENIX measurements represent three different approaches: a pQCD prediction, combined with radiative energy loss in a strongly coupled medium ($\hat{q} = 14$ GeV^2/fm, curve I), a heavy-quark transport calculation including elastic scatterings whose cross section is enhanced by resonance excitation (curve II), and a model relating the diffusion coefficient of the medium to the collisional energy loss of the parton (curves III for two different coefficients).

A sound model of the physics in a QGP has to predict not only the p_{T}-dependent R_{AA} of different particles, but also consistently describe their elliptic flow v_2, de-

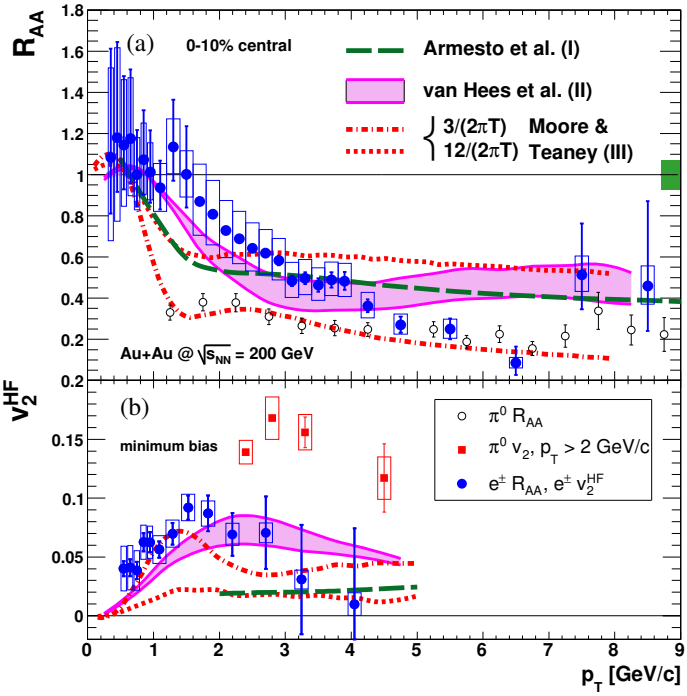

Figure 2.11: R_{AA} and v_2 of electrons from heavy-flavour decays in Au-Au collisions at 0-10% centrality and $\sqrt{s_{\mathrm{NN}}} = 200$ GeV, measured by the PHENIX collaboration at RHIC [Ada07]. For comparison, π^0 measurements and model calculations (see text) are shown.

picted in panel (b) of Figure 2.11 for electrons from heavy-flavour decays. Of the three predictions included in Figure 2.11, curve II comes closest to fulfilling this demand, while curve I, which only takes into account radiative energy loss, falls clearly short of describing the p_{T}-dependence of v_2. This hints to a need for additional contributions or different mechanisms of energy loss, which are subject to extensive discussion at the time of this thesis.

Recent preliminary results from ALICE for R_{AA} and v_2 of D mesons [Gre13,Caf13] and of heavy-flavour decay electrons [Sak13] have further inspired the development of model calculations, including the combination of radiative and collisional energy loss based on pQCD calculations (e.g. [Uph12], [Ren11]), new efforts on the enhancement of elastic scattering by excitation of heavy-flavour resonances [He12], and – with less success to this day – an approach relying on strong coupling among all quarks in the medium and the heavy-flavour probes [Hor13].

The availability of LHC data improves the possibilities of testing the proposed models: it adds to the challenge of describing both R_{AA} and v_2 the difficulty of doing so at the different collision energies of RHIC and LHC. So far, no model can fully satisfy this need. A separate measurement of the R_{AA} of beauty-decay electrons will help to further discriminate between different models by testing the accuracy of the predicted mass dependence of energy loss in the QGP. The only beauty-related

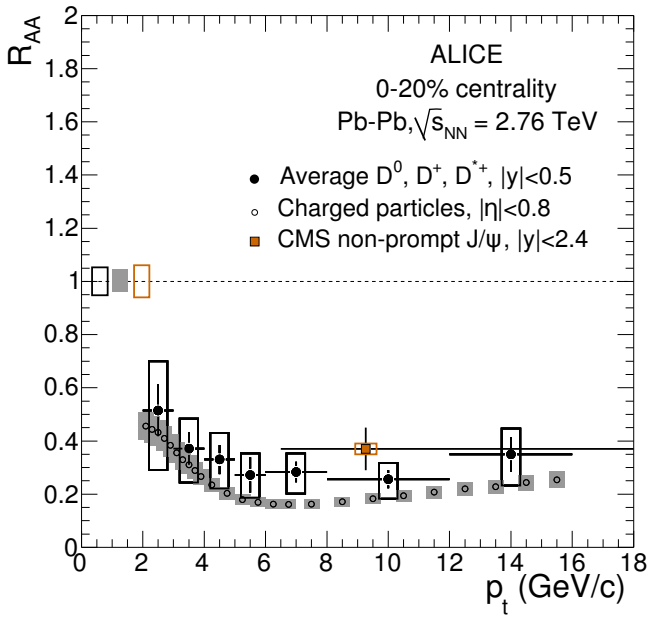

Figure 2.12: Comparison of R_{AA} in Pb-Pb collisions at 0-20% centrality and $\sqrt{s_{\mathrm{NN}}} = 2.76$ TeV, for D mesons and charged particles, measured with ALICE at mid-rapidity, and non-prompt J/ψ, measured with CMS at forward rapidity [Abe12l].

nuclear modification factor measurements already available from LHC are from non-prompt J/ψ analyses at forward rapidity from the CMS collaboration. They are limited to one data point in p_{T} at 0-20% centrality (see Figure 2.12, in comparison with charged hadrons and D mesons) and four data points in p_{T} integrating over all centralities, respectively [Cha12b, Jo13], and give only a slight hint to a less pronounced suppression of beauty with respect to charm and light flavours.

3 The LHC and ALICE

3.1 The Large Hadron Collider

With a circumference of 27 km and a nominal beam energy of 7 TeV for protons and 2.76 TeV per nucleon for lead nuclei, the Large Hadron Collider (LHC) at CERN is the world's largest and most powerful hadron accelerator [Eva08]. It is installed in a tunnel at 45 to 170 m under ground that was formerly used for the Large Electron Proton Collider (LEP), whose operation ended in the year 2000.

In two separate beam pipes, hadrons are accelerated in opposite directions, crossing at four colliding points at which the LHC experiments are installed. The accelerator is equipped with superconductive dipole magnets that generate magnetic fields up to 8.33 T for the nominal beam energy of 7 TeV. To establish the necessary conditions for superconductivity, the magnets are cooled down to 1.9 K by superfluid helium. Before injection into the LHC, the hadron beams are pre-accelerated in a series of smaller devices, the last two being the Proton Synchrotron (PS) and the Super Proton Synchrotron (SPS), while the first acceleration steps are different for protons and lead ions (see Figure 3.1). Lead nuclei are stripped of their electrons in three steps during this process.

By design, the LHC can achieve luminosities of 10^{34} cm^{-2}s^{-1} for pp collisions and 10^{27} cm^{-2}s^{-1} for Pb-Pb collisions, transporting 2802 bunches of $1.1 \cdot 10^{11}$ protons and 592 bunches of $7.0 \cdot 10^{7}$ lead nuclei at a time, respectively. ALICE is conceived for lower pp luminosities, with a maximum of 10^{30} cm^{-2}s^{-1}. Therefore, luminosity can be reduced for ALICE with respect to the other LHC experiments, e.g. by a displacement of the beams.

In November 2009, the first pp collisions were recorded at the LHC at a centre-of-mass energy of 900 GeV. In the subsequent runs from 2010 to 2012, the pp collision energy was raised to 7 TeV, with another increase to $\sqrt{s} = 8$ TeV in 2012 and a short period at $\sqrt{s} = 2.76$ TeV in April of 2011. Measurements at the latter energy are, above all, intended to be used as a reference for data taken during the Pb-Pb runs of the LHC in 2010 and 2011, with a centre-of-mass energy per nucleon $\sqrt{s_{\mathrm{NN}}}$ of 2.76 TeV. In addition, p-Pb collisions have taken place at the LHC at the end of 2012 and in the beginning of 2013 at $\sqrt{s_{\mathrm{NN}}} = 5.02$ TeV, enabling the experiments to investigate the impact of cold nuclear matter effects on the various QGP observables in Pb-Pb collisions (see Subsection 2.4.3). From March 2013 on, the LHC has been shut down in order to upgrade numerous detector systems and

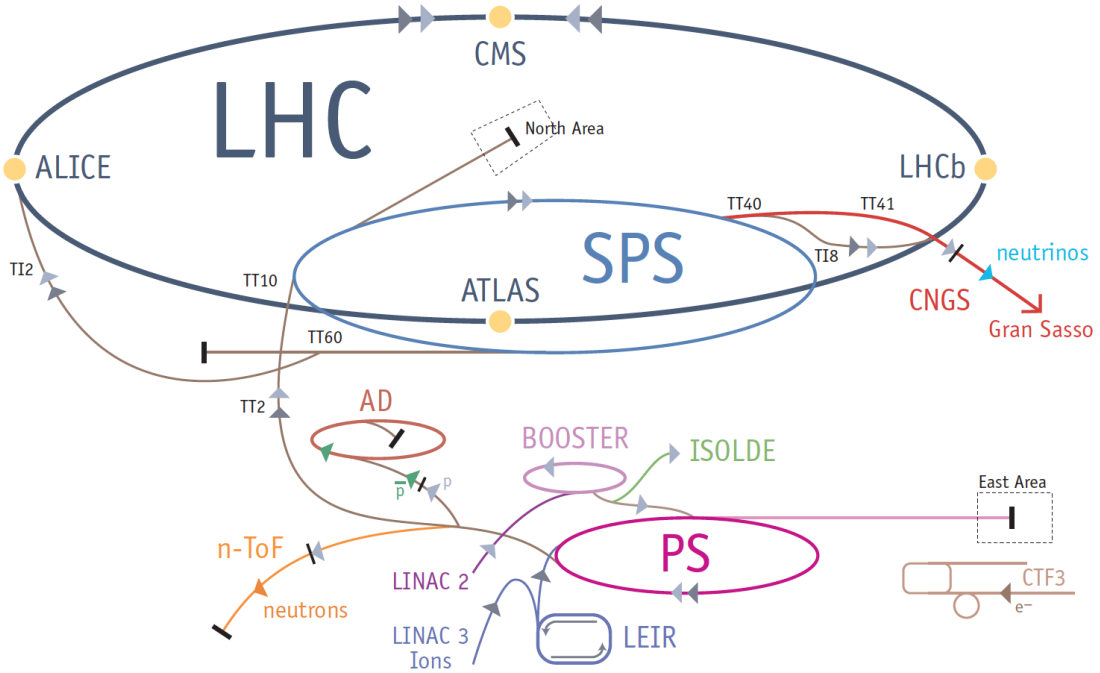

Figure 3.1: Schematic view of the accelerator system at CERN [CER08]. Pre-accelerators used for the LHC are PS and SPS, along with LEIR and LINAC 3 for ions or BOOSTER and LINAC 2 for protons.

to prepare the accelerator for running at its nominal energy of 7 TeV per beam. Operation is planned to be resumed at the beginning of 2015 [CER12]. For the present thesis, data sets from pp collisions at $\sqrt{s} = 7$ TeV taken in 2010, and at $\sqrt{s} = 2.76$ TeV taken in 2011 have been analysed.

The LHC hosts four major experiments, one at each of the four collision points. The two largest detector systems, A Toroidal LHC Apparatus (ATLAS) [Aad08] and Compact Muon Solenoid (CMS) [Cha08], have a wide range of applications and are conceived to provide mutually independent measurements concerning subjects like the characteristics of the Higgs boson and possible signatures of Supersymmetry (SUSY). The most remarkable success of these experiments so far was the discovery of a particle consistent with the Higgs boson predicted by the Standard Model in 2012 [Cha12a, Aad12c]. LHCb (LHC beauty experiment) [Alv08] focusses on the analysis of B-meson decays in search of indications for a CP violation. The ALICE experiment, which is the only experiment dedicated to the analysis of heavy-ion collisions for the exploration of the Quark-Gluon Plasma, will be described in detail in the next section.

3.2 ALICE

The ALICE detector setup is shown in Figure 3.2. The detector has an overall weight of about 10,000 t and a size of 16 × 16 × 26 m [ALI95, Aam08, Abe14d]. It provides excellent particle identification for charged hadrons and leptons over a wide p_{T} range and precise tracking for 0.1 GeV/$c \lesssim p_{\mathrm{T}} \lesssim$ 100 GeV/c. In order to extend the range of possible measurements to lowest p_{T}, the magnetic field of 0.5 T in the ALICE central barrel is smaller than for the CMS or ATLAS experiments. ALICE is specially designed for performing measurements in the high-multiplicity environment of Pb-Pb collisions, with up to 8000 charged particles per rapidity unit. Since it includes detectors whose signals depend on drift mechanisms, it is laid out for significantly smaller event rates than the other experiments at the LHC.

ALICE consists of three groups of detector modules: the so-called *central barrel*, covering a pseudorapidity range of $|\eta| < 0.9$ (Section 3.2.1), the muon arm, at $-2.5 < \eta < 4$ (Section 3.2.2), and a group of detectors at forward rapidity that are used for triggering and event characterization (Section 3.2.3).

3.2.1 The Central Barrel

The central barrel detectors are surrounded by a solenoid magnet that was formerly used for the L3 experiment at LEP. An exception is ACORDE, described further below, which is installed on top of the magnet. All detector systems that have full azimuthal acceptance are used for the measurement of charged particles and are disposed in cylindrical shapes in separate layers around the beam pipe. In the following, they will be listed from the innermost to the outermost device: the *Inner Tracking System* (ITS) is mainly used for tracking and vertex reconstruction. The *Time Projection Chamber* (TPC) is the main tracking and particle identification (PID) device. The *Transition Radiation Detector* (TRD) identifies electrons at $p_{\mathrm{T}} \gtrsim 1$ GeV/c, while the *Time of Flight* (TOF) detector is used for hadron identification at low momenta. Several additional detectors do not cover the full azimuth around the beam axis. The *Photon Spectrometer* (PHOS) and the *Electromagnetic Calorimeter* (EMCal) measure photons, neutral pions, and electrons; the *High Momentum Particle Identification Detector* (HMPID) is a ring-imaging Cherenkov device for hadron identification.

The Inner Tracking System

The Inner Tracking System consists of six layers around the beam pipe, composed of three different detector systems whose radii range from 3.7 cm to 44 cm [Del99a]. The *Silicon Pixel Detector* (SPD), the innermost ITS subsystem, includes two layers of fast-responding pixel detectors of high granularity and is of major importance for the reconstruction of primary and secondary vertices, as well as of the impact parameter of tracks with respect to the primary vertex. This last point is essential in

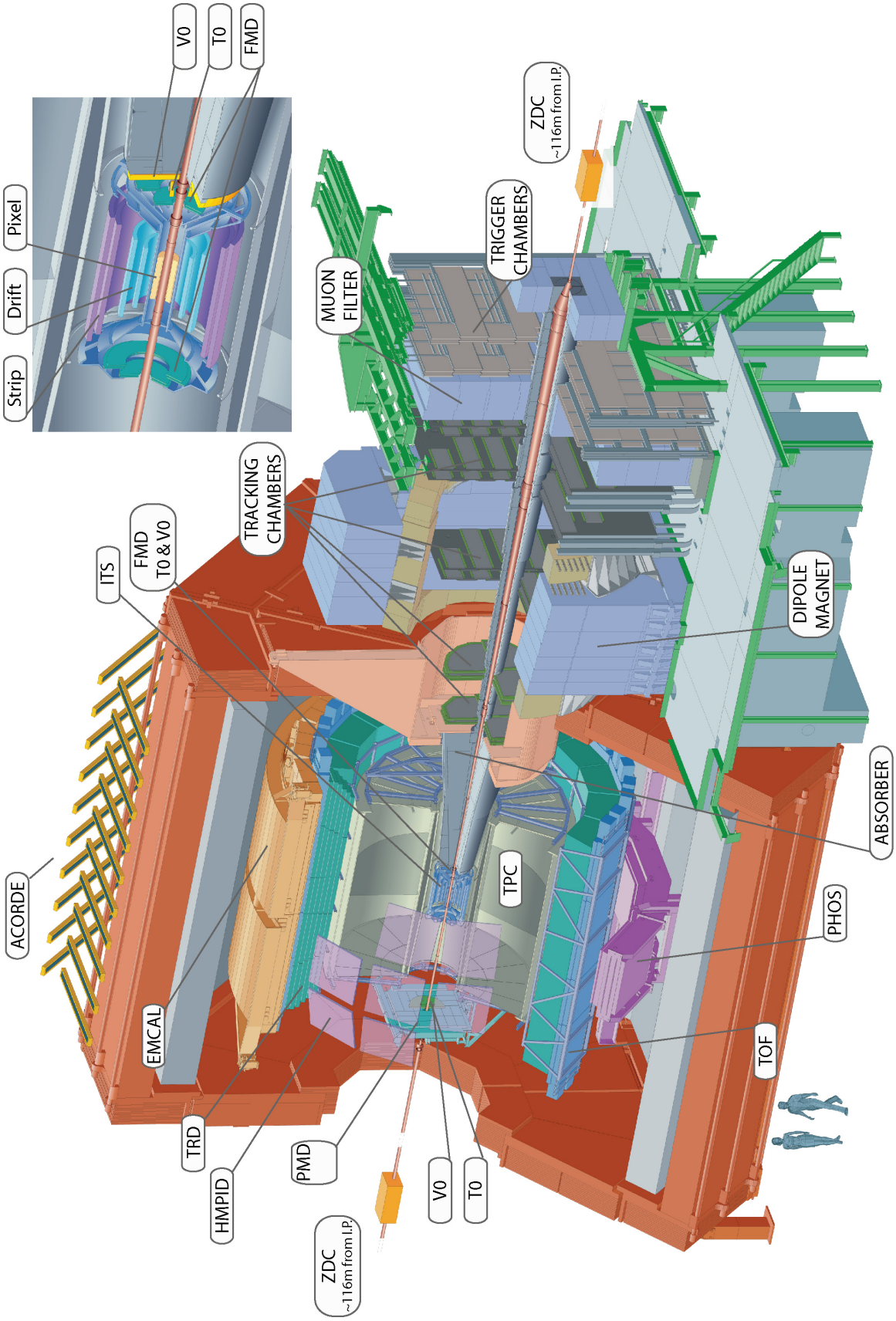

Figure 3.2: The ALICE detector setup [Aam08].

the context of this thesis, since it is the basis on which electrons from beauty-hadron decays are discriminated from other decays and primary tracks. Furthermore, the SPD is used for triggering on minimum-bias events in both pp and Pb-Pb collisions.

The two subdetector layers following further outside belong to the *Silicon Drift Detector* (SDD), which consists of modules divided into two drift regions in which crossing charged particles generate electron-hole pairs. The electrons drift to a cathode pad with a maximum drift collection time between 4.3 and 6.3 μs. The drift time, in combination with the spatial charge distribution, enables the localization of the particle crossing point. The amount of the collected charge, in turn, is proportional to the energy deposited by the particle and can be used for particle identification at low momenta.

The *Silicon Strip Detector* (SSD) forms the two outermost layers of the ITS and is therefore essential for the prolongation of tracks between ITS and TPC. Each of the two layers is composed of double-sided strip detectors, on each side of which the electron-hole pairs generated by crossing particles are collected. Just as in the SDD, the amount of the collected charge can be used for particle identification.

The Time Projection Chamber

ALICE has the largest Time Projection Chamber ever constructed, with a volume of 88 m^3, filled by a gas mixture of 85.7% Ne, 9.5% CO_2, and 4.8% N_2 [Aam11a], an inner and outer radius of 85 and 250 cm, respectively, and a length of 500 cm [Del00]. It is designed for a maximum of 20,000 simultaneous tracks in the TPC volume, which enables safe operation even in the high-multiplicity environment of Pb-Pb collisions. The readout rate is limited to 1 kHz, so that the luminosity for pp collisions in ALICE has to be reduced significantly in comparison with the other LHC experiments. The TPC covers a pseudorapidity region of $|\eta < 0.9|$ and is, along with the ITS, the main tracking device of the experiment, enabling track reconstruction with a good momentum resolution for p_{T} from 0.1 to 100 GeV/c. A high-voltage electrode at the centre at $\eta = 0$ divides the TPC cage in two sections, providing an axial drift field of 400 V/cm.

Charged particles that cross the TPC volume ionize gas molecules, producing free electrons which drift in the field towards the cathode pad planes at the end plates of the chamber, with a maximum drift time of 94 μs. The signal is read out in 159 radially oriented pad rows. While the radial and azimuthal coordinates of a tracking point can be determined by the position of the corresponding readout pad, the position along the beam axis (the z coordinate, see Appendix A) is calculated via the drift time.

In addition to its function as a tracking device, the TPC is also the most important PID detector in the ALICE central barrel. To identify the species of a particle, the energy loss per unit of length, $\mathrm{d}E/\mathrm{d}x$, which is proportional to the charge collected by the cathode pads, is compared to a Bethe-Bloch parameterization tuned on data.

The Time of Flight Detector

TOF is the outermost detector covering full azimuth, with a pseudorapidity acceptance of $|\eta| < 0.9$ and an inner radius of 3.7 m [TOF00, Cor02]. As its name suggests, it measures the time of flight of a detected particle, using the T0 signal (see below) as an additional input to determine the collision time. TOF consists of 18 supermodules of Multi-gap Resistive-Plate Chambers (MRPC) [Aam08]. The gaps between the glass plates which are installed in stacks in each MRPC are filled with a gas mixture of 90% CH_2F_4, 5% C_4H_{10}, and 5% SF_6. They have a width of only 250 μm, so that the drift time of electrons from the passage of ionizing radiation is negligible. Since the time of the collision can be determined more exactly for Pb-Pb collisions, the TOF resolution is better (85 ps) in this case, compared to the one in pp collisions (100 ps).

Particle identification by TOF is based on the fact that particles with different masses have a different velocity at a given momentum. With the momentum known from the curvature of the reconstructed track and the time of flight measured by TOF, an identification of kaons up to 1.5 GeV/c and of protons up to 3 GeV/c is possible. In the analyses presented in this thesis, TOF PID is used to reject protons and kaons from the electron-candidate sample selected by the TPC.

The Transition Radiation Detector

Situated between TPC and TOF, also the TRD covers the full azimuth and a pseudorapidity range of $|\eta| < 0.9$ [Cor01]. It is divided into 18 supermodules containing 522 individual chambers[1], organized in stacks of 6. At the beginning of LHC operation in 2009, 4 supermodules were installed, and a further 3 were included before the first long data-taking period in 2010. In the long shutdown before the 2012 LHC runs, the overall number of installed supermodules was increased to 13. The TRD setup will be finalized during the long maintenance shutdown of the LHC which started in the beginning of 2013.

Each TRD chamber consists of a radiator in which ultra-relativistic electrons produce transition radiation, and a multi-wire proportional chamber, filled with a mixture of Xenon and CO_2. Electrons can be distinguished from other particle species at $p_{\mathrm{T}} \gtrsim 1$ GeV/c, using the combined signal from the $\mathrm{d}E/\mathrm{d}x$ from the charged particle and the absorption of transition radiation in the gas volume. Besides the detected overall charge, the time distribution of the signal can be exploited for electron identification, since photons from transition radiation are usually absorbed shortly after entering the gas volume at a large distance to the read-out wires, hence generating a signal at late drift times.

Further applications of the TRD are the improvement of the ALICE tracking, as each of the TRD chambers reconstructs a space point with a resolution of 600 μm,

[1] In three supermodules, a stack at mid-rapidity is left out to minimize the radiation length in front of PHOS.

and its usage as a trigger for high-p_{T} hadrons or electrons.

For the present analyses, TRD PID has not been taken into account since the performance of the TPC and TOF PID has proved sufficient for this purpose and since the additional requirement of TRD PID would reduce the statistical basis of the measurements significantly (see Section 4.7).

Detectors with Partial Azimuthal Acceptance

Besides the detectors with full azimuthal coverage described above, there are three devices that cover smaller fractions of the central barrel acceptance, and which are not used for the analyses described in this thesis.

In its final form, PHOS [Man99] will cover an azimuthal range of 100° on the lower side of the central barrel and a pseudorapidity of $|\eta| < 0.12$. Three of its five modules are installed in ALICE at present. Each one consists of an electromagnetic calorimeter made of lead-tungstate crystal and a *Charged Particle Veto*, a multi-wire proportional chamber to reject charged particles.

The EMCal [Cor06] is a lead scintillator mounted on the central barrel side opposed to PHOS. It can provide a trigger for jets, photons, and electrons. While PHOS has a better energy resolution, the EMCal has a far larger acceptance, covering an azimuthal angle of 107° and a pseudorapidity of $|\eta| < 0.7$.

The HMPID [Piu98] consists of an array of ring-imaging Cherenkov counters and has an acceptance of 58° in azimuth and from -0.6 to 0.6 in η. It extends the hadron identification capabilities provided by TPC and TOF to higher momenta, discriminating kaons up to 3 GeV/c and protons up to 5 GeV/c. It can further be used for identification of light nuclei, like d, t, ^{3}He, and α.

ACORDE (ALICE Cosmic Ray Detector), an array of 60 plastic scintillator modules, is placed on top of the L3 magnet and is used as a trigger for cosmic ray events, which can be analysed using TPC, TRD, and TOF. Before the first LHC runs, it was used to calibrate the ALICE central barrel detectors, using cosmic radiation [Aam08].

Outside the central barrel acceptance, at large forward or backward rapidities, several further detectors with a wide range of applications are installed.

3.2.2 The Muon Spectrometer

The *Muon Spectrometer* [Muo99, Mua00, Mup96] is used for the reconstruction of high-momentum muon tracks ($p(\mu) \gtrsim 4$ GeV/c) at $-4 < \eta < -2.5$. It consists of ten layers of tracking chambers, four trigger chamber layers and three absorbers to reject background from hadrons, electrons, and low-momentum muons. At a distance of 7 m from the collision point, a dipole magnet provides a nominal field of 0.67 T. Besides performing measurements of dimuons from decays of light vector mesons and quarkonia, the Muon Spectrometer also measures single muons from

heavy-flavour decays and can therefore provide complementary measurements to the electron-based analyses of heavy-flavour decays (see Section 2.2.1).

3.2.3 Forward Rapidity Detectors

Among the remaining ALICE devices, the detector pairs of the *Zero Degree Calorimeter* (ZDC) [Gal99], *V0*, and *T0* are of some practical importance for this thesis. V0 and T0 have been described in a common technical design report, along with the FMD (see below) [Cor04].

ZDC and V0 are used to determine the centrality of Pb-Pb collisions. Furthermore, the V0 provides a minimum-bias trigger and is used for rejecting signals from beam-gas interactions. The ZDC detectors, which measure the kinetic energy of the spectator nucleons, are placed at distances of 116 m from the interaction point in both directions along the beam axis. Each one consists of a neutron and a proton calorimeter. The ZDC is complemented by two electromagnetic calorimeters at 7 m from the interaction point on the A side[2], opposite the Muon Spectrometer. The second device used for centrality determination, the V0, is a pair of scintillator counter arrays installed at 90 cm from the collision point on the C side and at 340 cm on the A side of ALICE.

The T0 detector, a combination of two arrays of Cherenkov counters, measures the time of the collision with a resolution of 50 ps and provides an important input for the TOF measurements. In addition, it can be used as a trigger and for estimation of the Pb-Pb event multiplicity. The two parts of the T0 are placed on either side of ALICE, at 72.7 cm and 375 cm on the C and A side, respectively.

The two last ALICE detectors to be mentioned are the *Photon Multiplicity Detector* (PMD) [Del99b, Fab03], measuring the photon distribution at forward rapidity, and the *Forward Multiplicity Detector* (FMD) [Cor04], which determines the charged particle multiplicity at forward and backward rapidity.

[2]For the definition of the A and C side of ALICE, see Appendix A.

4 Analysis

4.1 Analysis Strategy

The aim of the analyses described in this thesis is the measurement of the differential invariant production cross sections of electrons from beauty-hadron decays for pp collisions at centre-of-mass energies of 2.76 TeV and 7 TeV. In addition, an outlook will be given on the corresponding measurements for Pb-Pb collisions at $\sqrt{s_{\mathrm{NN}}} = 2.76$ TeV. To all of these three data sets, a mostly identical analysis procedure is applied that will be described in the following.

In a preselection step, a series of track quality criteria is applied (see Section 4.5) in order to assure that the measured signal corresponds to one single track from a particle which suffers neither strong scattering nor decay during its passage through the detector volume. Furthermore, only tracks are accepted whose measurement provides reliable information for further analysis.

To obtain a clean sample of electron tracks, electron identification requirements are applied subsequently, based on the signals from TOF and TPC (Section 4.7). A characteristic feature of the analysis strategy described in this thesis is the usage of the measurement of the transverse impact parameter d_0 of a track with respect to the primary vertex (Figure 4.1). B mesons have a larger mean lifetime than all other relevant particles that produce background electrons by their decays, and their daughter tracks have a particularly wide angular distribution. As will be explained in Section 4.6, the selection of tracks with a large value of d_0 exploits these properties in order to substantially increase the signal-to-background ratio of the selected sample. A requirement for tracks to produce a signal in the two innermost pixel layers of the SPD also excludes most conversion electrons with large impact parameters.

Despite the reduction of background electrons and hadrons, the resulting raw spectrum contains a considerable fraction of contamination from the decays of charmed and light-flavoured hadrons and from photon conversions. Their contributions have to be subtracted on a statistical basis. For this purpose, the selection efficiencies for the corresponding decays are determined via GEANT3 simulations [Goo95]. These, in turn, obtain as an input PYTHIA [Ben87] spectra which have been weighted according to a procedure described in Section 4.8, so as to represent the spectral shapes measured in other ALICE analyses.[1] From these calculations, estimations

[1] In the case of background electrons from Λ_c decays, the input spectrum has been determined based on results from ZEUS at HERA (see Section 4.8).

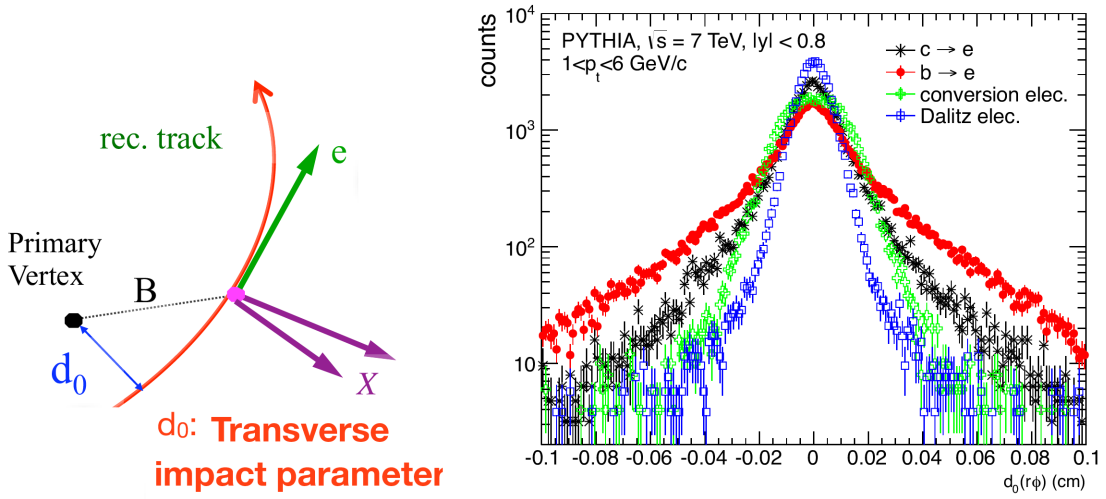

Figure 4.1: Definition of the transverse impact parameter d_0 (left) and transverse impact parameter distribution for electrons from different sources (right) in PYTHIA simulations of pp collisions at $\sqrt{s} = 7$ TeV [Ave12].

are obtained for the background electron spectra which remain after the impact parameter selection, and which are subtracted from the measured raw spectrum.

A further correction, based on the distribution of TPC signals in $\mathrm{d}E/\mathrm{d}x$, is applied for the contamination from hadrons misidentified as electrons (Section 4.7). The resulting raw spectrum of electrons from beauty-hadron decays is then corrected for the geometrical acceptance of the detectors, for the efficiency of the selection criteria, and for the effects of bremsstrahlung and p_{T} smearing by the track reconstruction. To infer from the p_{T}-dependent electron yield the p_{T}-differential cross section of beauty-decay electrons, the result is normalized by the number of minimum-bias collisions used for the measurement and by the total inelastic cross section of proton-proton collisions at the respective centre-of-mass energy (Section 4.9).

As an adaption to the particularities of each data set, slight changes in the analysis strategy have been necessary from the analysis for collisions at $\sqrt{s} = 7$ TeV to the one for collisions at 2.76 TeV, whose details will be discussed in the Subsections 4.4.1, 4.4.2, 4.7.1, and 4.7.2. Such specific changes will be even more significant when it comes to measurements for Pb-Pb collisions, for which an outlook will be presented in Chapter 6.

4.2 The ALICE Analysis Framework

The data taken by ALICE are analysed using a common software framework called AliRoot [ARO, ASV], an extension of the ROOT [ROO] framework, which is based on the object-oriented programming language C++. Since AliRoot is equally used

for the analysis of Monte Carlo simulations, it interfaces with several external event generators, such as PYTHIA [Ben87], HIJING [Gyu94], or PHOJET [Roe00], and with programs simulating the detector responses, like GEANT 3 [Goo95], GEANT 4 [Ago03], or FLUKA [Fas03]. For a description of the general features of simulation, alignment, calibration, reconstruction, and analysis with AliRoot, see [Aam08]. In the following, a short overview of the software structure used specifically for the analysis discussed in this thesis will be given.

The program for the analysis of beauty-hadron decays via displaced electrons makes use of the `HFE` software package [HFE] common to all analyses of the Heavy Flavour Electron working group, from which it takes its name. The software is composed of several modules [Fas12]:

- container classes,
- a track selection module,
- an electron identification module,
- an analysis task,
- a module for corrections of the electron spectrum for selection efficiency and acceptance,
- utility classes.

A basic ingredient of the `HFE` analysis package is the extensive usage of the AliRoot correction framework (`CORRFW`) [COR], which facilitates calculations of selection efficiency corrections in multiple dimensions and for several subsequent selection steps. A series of properties of tracks and particles are stored in so-called *containers*. Based on the `AliCFContainer` class defined in `CORRFW`, the class `AliHFEcontainer` has been introduced in the `HFE` package. It comprises the dimensions p_{T}, η, ϕ, Z, and *mother ID*. Z is the charge number of the particle whose track is measured, while *mother ID*, only filled in the analysis of simulated data, is a code for the species of the particle from whose decay the track originates. For simulated data, on which the efficiencies of most selection criteria are determined, only the information from true[2] electrons is stored. In order to quantify the distortive effects of bremsstrahlung and of the limited momentum resolution on the reconstructed spectra, information about the simulated and reconstructed values of p_{T} is stored separately for each simulated track.

The two following modules implement the track quality and electron identification selection steps which will be discussed in Sections 4.5 and 4.7. The track selection

[2] "True" means in this context that the original information stored during simulation identifies the corresponding particle as an electron, as a difference to the attribution of a particle species based on detector signals, as performed in the analysis of non-simulated data.

module uses selection criteria defined in the `CORRFW` or additional criteria implemented in the class `AliHFEextraCuts`, while the values to which all requirements are set are stored in the class `AliHFEcuts`.

In the module dedicated to electron identification, the class `AliHFEpidBase` steers the electron candidate selection by the different individual detectors that are employed in the analyses of the Heavy Flavour Electron group. These detector-specific requirements are handled in separate PID classes.

Selection steps and the filling of containers after each step are coordinated by the class `AliAnalysisTaskHFE`, while the correction module uses the information stored in the containers for different analysis steps to determine the overall amount of electrons before the application of all selection criteria. In the case of the analysis described here, the correction is done for electrons from beauty-hadron decays (see Section 4.9).

4.3 Track Reconstruction in ALICE

In order to describe the reconstruction of a track in the ALICE central barrel from signals in different detectors, it is necessary to introduce four basic concepts [Ale06]:

- A *digit* is a digitized signal delivered by a read-out pad of a detector.
- A *cluster* is a group of digits in neighbouring read-out pads and time bins that are exceeding a certain threshold value and are attributed to the same crossing particle.
- A reconstructed *space point* is the calculated position at which the particle generated the signal.
- A reconstructed *track* is a set of parameters describing the particle trajectory at a given space point, with the corresponding covariance matrix.

The reconstruction of tracks from charged particles is based on a Kalman filter approach [Bil84]. Track candidates are first reconstructed from clusters at the outer wall of the TPC inwards, continuing to the different layers of the ITS. In a second step, the tracking procedure is repeated starting from the ITS outwards to the TPC, from which tracks are extrapolated towards the outer detectors TOF, TRD, HMPID, and PHOS. Hits in those detectors are then associated to the tracks via geometrical matching [Ale06]. Finally, a Kalman filter refit is performed inwards through TPC and ITS.

4.4 Data Set and Event Selection

Many of the criteria applied in this analysis are based on previous work described in [Abe12g, Ave11a, Abe14b, Ave13b]. In this context, several important restrictions

for the event selection have been identified. First, a primary vertex has to be reconstructed using either the reconstructed tracks in the respective event or correlated hits in both SPD pixel layers. Second, the primary vertex position has to be within ± 10 cm in beam direction from the centre of the ALICE central barrel, in order to avoid effects from the edges of the detector acceptances. Beam-gas interaction background is rejected using information from VZERO and SPD, while pile-up events are excluded using the identification of further interaction vertices with at least three tracklets in the SPD. The remaining amount of pile-up events has been shown to be negligible for further analysis in pp collisions.

Apart from these requirements inherited from the inclusive heavy-flavour electron analysis, the beauty analysis has to take special care about the quality of the impact parameter reconstruction in each data set. This point will be discussed in detail in Section 4.6.1.

4.4.1 pp Collisions at $\sqrt{s} = 7$ TeV

For the collision energy of $\sqrt{s} = 7$ TeV, ALICE data from the so-called *pass2* reconstruction of run period LHC10d, recorded in 2010, were analysed. For the purpose of the present work, this data sample offers a clear advantage over samples from data-taking periods earlier in 2010: for the track reconstruction and for the calculation of the energy deposition per unit of length ($\mathrm{d}E/\mathrm{d}x$) in the TPC, also so-called *single-pad clusters* have been taken into account, i.e. clusters which have a signal exceeding the threshold value in only one read-out pad [Kal12]. This results in an improved hadron suppression for the electron identification method used in this analysis, and therefore in a reduction of contamination, in particular at high momenta [Ave12].

As pointed out in [Ave11a], only such runs can be considered in which all required detectors (ITS, TPC, TOF) were fully functional, and in which the collision rate was sufficiently low to avoid a large number of pile-up events. For the beauty analysis, 49 runs were accepted, which are listed in Appendix C. The total integrated luminosity of this data sample is 2.2 nb^{-1}.

For estimation of selection efficiencies, detector acceptance and reconstruction effects, two PYTHIA simulation samples were used: a minimum-bias event sample and a signal-enhanced sample which contains events enriched with heavy-flavour hadrons producing electrons through decays inside the ALICE central barrel acceptance. The software version used for this analysis was the AliRoot analysis tag v5-03-27-AN [Alia].

4.4.2 pp Collisions at $\sqrt{s} = 2.76$ TeV

The proton-proton collision data used for this part of the analysis have been taken during run period LHC11a in March 2011. As for $\sqrt{s} = 7$ TeV, the *pass2* reconstruction is used.

Some of the choices of requirements on the data set are due to the fact that the available sample is considerably smaller than the one used from the LHC10d period at 7 TeV; as a consequence, special efforts have been made to maximize the share of data used for the analysis.

Unlike in the analysis of 7 TeV collisions, the information from the Silicon Drift Detector (SDD) was not used for track and vertex reconstruction for 2.76 TeV collisions. The main reason for this decision is that during the LHC11a run, one readout partition excluded the relatively slow SDD, thus being able to take data at a much higher rate. It can also be shown that the impact parameter distribution of electrons from photon conversions is reproduced even more reliably when only SPD information is used.

In order to dispose of a sufficient sample size to extend the electron spectrum up to a transverse momentum of 8 GeV/c, electron identification from TOF will not be required for tracks with momenta higher than 2 GeV/c (see Section 4.7). Therefore, besides the eight runs available for measurements at lower transverse momenta, eight additional runs could be considered for analysis above this p_{T} value, in which no valid particle identification by TOF was provided. The corresponding runs and detector configurations are listed in Appendix C.

Overall, 33.8M events were analysed using TPC and TOF PID, for tracks in the p_{T} range of 1 GeV/c < 2 GeV/c, corresponding to a total integrated luminosity of 0.6 nb^{-1}. For momenta above 2 GeV/c, a total of 51.5M events, or 0.9 nb^{-1} were available.

The samples of simulated PYTHIA events used for this part of the analysis are similar to those described for the 7 TeV data sample. Besides a set of minimum-bias events, two different signal-enriched simulated samples are used. The first one contains large numbers of charm and beauty hadrons whose decays generate electrons inside the ALICE central barrel acceptance. In addition to these, the second sample is enriched with J/ψ, $B \to J/\psi$, π^0, and η. Further information on these Monte Carlo productions is given in [Ave13b].

The AliRoot analysis tag used for the analysis of pp collisions at $\sqrt{s} = 2.76$ TeV was v5-03-42-AN [Alib].

4.5 Track Reconstruction and Selection

Most criteria for track selection are identical for both analysed proton-proton collision energies. They have been directly adopted from the corresponding analyses for inclusive heavy-flavour electrons [Abe12g, Abe14b].

A successful track refit in the TPC and the ITS (see Section 4.3) is one criterion applied in this analysis to ensure that a track stems from one real, single, and adequately reconstructed particle trajectory. Other criteria are a minimum requirement on the number of ITS hits and a maximum constraint on the value of the χ^2 of the TPC track fit per TPC cluster that describes the quality of the fit, as well as the

Table 4.1: Track selection criteria.

Track property	Requirement	
	$\sqrt{s} = 7$ TeV	$\sqrt{s} = 2.76$ TeV
TPC and ITS refit	required	
Kink mothers and daughters	rejected	
Number of TPC clusters	≥ 120	≥ 110
Number of TPC clusters for $\mathrm{d}E/\mathrm{d}x$ calculation	≥ 80	
Ratio found/findable TPC clusters	> 0.6	
χ^2/TPC cluster	< 4	
Number of ITS hits	≥ 4	≥ 3
SPD layers in which a hit is requested	both	
Distance of Closest Approach in xy (cm)	< 1	
Distance of Closest Approach in z (cm)	< 2	

rejection of so-called kink candidates. The latter are tracks which are inconsistent with the hypothesis of a continuous particle trajectory. Instead, they show sudden directional changes, which can be caused by such effects as decay, bremsstrahlung, or scattering. In all these cases, the daughter tracks originating from the kink are of no interest for the analysis, as they do not represent anymore the properties of the original track coming from close to the primary vertex. It was, however, decided to reject also the tracks reconstructed up to the kink, since they have a worse $\mathrm{d}E/\mathrm{d}x$ resolution than regular tracks [Abe12g]. The minimal number of ITS hits required has changed from four hits in the 7 TeV analysis to three in the 2.76 TeV analysis, owing to the fact that the two SPD layers are not used in the latter.

A further group of track selection requirements sets constraints on the availability of clusters in the TPC and focusses not only on the quality of the track, but also of the particle identification provided by the TPC. From a maximum of 159 clusters that can be assigned to a track in the TPC, at least 120 were required for the 7 TeV analysis; this criterion has been loosened to 110 clusters for the 2.76 TeV analysis in order to maximize the data sample. It was found that by requiring such high numbers of clusters, the electron/pion separation of the TPC is improved: since electrons deposit significantly more energy than pions in the relevant momentum range (see Section 4.7), they are also less sensitive to threshold effects of the detector. Thus, they produce on average a higher number of clusters [Abe12g]. Additionally, a minimum ratio of 0.6 is required between the number of found TPC clusters and the maximal number of *findable* clusters that could have been produced, given the geometry of the TPC track.

In order to ensure a good quality of particle identification in the TPC, a separate minimal limit of 80 is set for the number of clusters used for the calculation of the $\mathrm{d}E/\mathrm{d}x$ value. This number differs from that of the TPC clusters for tracking since

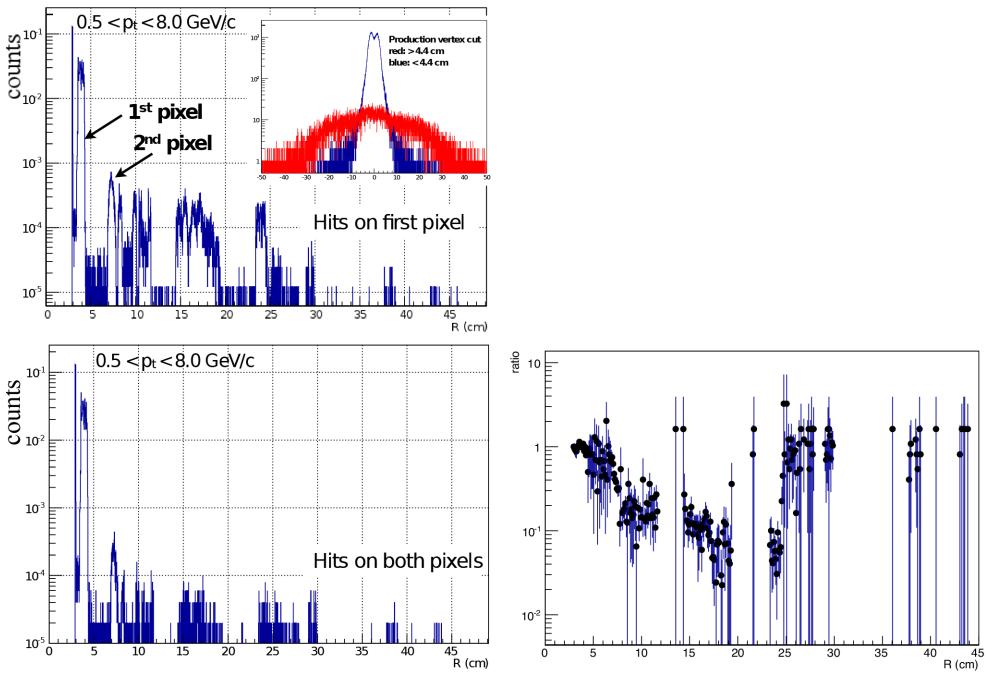

Figure 4.2: Left: distribution of the radial distance R of conversion vertices to the beam axis, requiring a hit in the first SPD layer only (upper panel) or hits in both SPD layers (lower left panel), both normalized to the number of events. Right: ratio of the lower left to the upper left graph. Both were produced with a minimum-bias simulation sample [Ave12]. Ratios above one are due to the fact that a smaller amount of events was analysed for the lower left plot.

clusters near the borders of TPC sectors are not taken into account for the $\mathrm{d}E/\mathrm{d}x$ calculation, owing to the low TPC gain in these areas [Kal12].

The remaining requirements for the track selection aim at the rejection of background decays or photon conversions. The distance of closest approach to the primary vertex was limited to a maximum of 2 cm in the beam direction and 1 cm in the transverse plane. As will be explained in Section 4.6, this analysis is based on the selection of tracks with a large transverse impact parameter. The aforementioned maximum limitation, however, is so large compared to the decay length of a B meson ($\approx 500\ \mu m$) that it rejects less than 1% of the signal electrons.

Finally, each track is required to produce hits in both SPD pixel layers. In the analysis of the inclusive heavy-flavour electron spectrum [Abe12g], only the innermost SPD layer had to provide a signal, so as to guarantee that only electrons from photon conversions happening in the beam pipe or the inner part of the first pixel layer contaminate the spectrum. While this measure is sufficient in the context of the inclusive HFE analysis, it turned out that the spectrum of displaced electrons

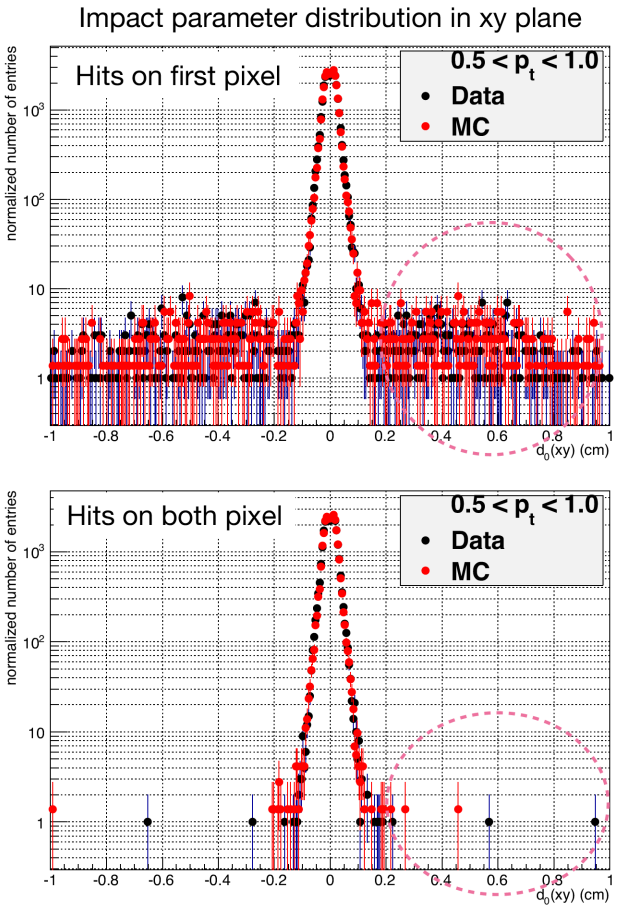

Figure 4.3: Transverse impact parameter distribution $d_0(xy)$ of electrons. In the upper panel, only a hit in the first SPD layer is required. The lower panel shows the suppression of tracks with large impact parameters when hits in both SPD layers are required [Ave12].

for the beauty-decay analysis suffered from contamination from conversions happening at larger transverse radii, whose electron tracks were erroneously combined with uncorrelated hits in the first SPD layer. Since these tracks have on average a much larger impact parameter than electrons from conversions occurring closer to the primary vertex, they are enhanced in the spectrum after the impact parameter selection. The upper panel of Figure 4.2 illustrates this fact: even after applying the requirement for a first pixel hit, a considerable amount of conversions is produced at transverse radii R larger than the 4.4 cm that correspond to the upper edge of the peak from the first pixel layer. The impact parameter distribution of these conversion electrons is clearly wider than that of conversions with $R < 4.4$ cm (plot included on the upper right in the same panel). As shown in the lower panels, a requirement for hits in both SPD layers reduces the respective contamination sig-

nificantly in the statistically relevant region of 4.4 cm $< R <$ 25 cm. Therefore, this criterion will be used for track selection in all analysed data sets. In Figure 4.3, the overall transverse impact parameter distributions (see Section 4.6) for both cases are presented for simulations and data from pp collisions at $\sqrt{s} = 7$ TeV in ALICE. In the case of the requirement for hits in both pixels, high values of $d_0(xy)$, which mostly correspond to conversions at large transverse radii, are strongly reduced.

All track selection criteria described in this section are listed in Table 4.1. The selection based on the impact parameter, which is applied exclusively in this analysis, will be discussed in Section 4.6.

4.6 The Impact Parameter Requirement

Two characteristic differences between the decays of beauty hadrons and other electron sources are relevant for the analysis described in this thesis. The first one is the particularly large decay length of the B meson (cf. Table 4.2). The second difference lies in the fact that, owing to the large B mass, daughter particles from B decays can have high momenta in the transverse direction with respect to the momentum of their mother particle and, therefore, a wide angular distribution. These considerations are also true for the decays of Λ_b baryons, whose contribution to the beauty-hadron decay spectrum is expected to be small.

The measurable quantity that is used to discriminate beauty-decay electrons from other electrons is the transverse track impact parameter with respect to the primary vertex, d_0, which is illustrated in the left panel of Figure 4.1. It can be described as the distance of closest approach of a reconstructed track to the reconstructed primary vertex in the plane perpendicular to the beam axis. d_0 is a signed quantity. For its calculation, a local right-handed cartesian coordinate system is defined whose axes will be named x', y', and z', to distinguish them from the axes x, y, and z of the global coordinate system. The x' axis points in the direction of the particle momentum projection in the global xy plane, while the z' axis coincides with the global z axis in beam direction, and the y' axis is perpendicular to both. The value of d_0 is now defined as the difference between the y' coordinates of the track and the primary vertex at the distance of closest approach between both in the transverse plane [Dai]. In this sense, the sign of d_0 indicates if the track passes the primary vertex in its own reference system to its left or to its right.

The impact parameter distributions of tracks at a given p_{T} from decays of different particle species are determined by a series of quantities [Völ12]:

- the decay length $c\tau$, where τ is the average lifetime of the mother particle,
- the mass of the mother particle,
- the contributing decay channels,
- the resolution of the impact parameter measurement.

Table 4.2: Decay lengths $c\tau$, mean path lengths L_{lab} in the laboratory frame at $p_{\mathrm{T}} = 3$ GeV/c, and masses m of the most relevant[3] electron sources [Beh12].

	decay length $c\tau$	$L_{lab}(p_{\mathrm{T}} = 3GeV/\mathrm{c})$	mass m
$B^{+/-}$	492.0 μm	280 μm	5279.26 ± 0.17 MeV
B^0	455.4 μm	259 μm	5279.58 ± 0.17 MeV
B_s^0	454.5 μm	254 μm	5366.77 ± 0.24 MeV
Λ_b^0	428 μm	228 μm	5619.4 ± 0.6 MeV
$D^{+/-}$	311.8 μm	500 μm	1869.62 ± 0.15 MeV
D^0	122.9 μm	198 μm	1864.86 ± 0.13 MeV
$D_s^{+/-}$	149.9 μm	228 μm	1968.50 ± 0.32 MeV
$\Lambda_c^{+/-}$	59.9 μm	78.6 μm	2286.46 ± 0.14 MeV
π^0	25.5 nm	567 nm	134.9766 ± 0.0006 MeV
η	0.15 nm	0.82 nm	547.862 ± 0.018 MeV
γ	∞ ; converts to $e^+ + e^-$ in matter		0

It is often argued (e.g. [Hei13][4]) that the decay length $c\tau$ is the determining factor for the large impact parameter of tracks from B-decay products. While it is true that without a long average lifetime ($\tau(B^{+/-}) = 1.64 \cdot 10^{-12}$s), the decays of B-mesons could not be separated from those of lighter hadrons by means of an impact parameter requirement, it has to be noted that the actual average decay distance from the primary vertex in the laboratory frame, $L_{lab} = \beta\gamma c\tau = p\tau/m$, is larger for charged D mesons than for any of the beauty hadrons at the same given hadron p_{T} (cf. Table 4.2). This indicates that the kinematical aspects which have to be taken into account are more complex.

First of all, the particles whose tracks are selected are the daughter electrons of the decaying hadrons. Electrons from the same decaying particle species and with the same given p_{T} may have mother particles with different values of p_{T}, and therefore with different expected path lengths. The probability for these p_{T} values depends on the species of the decaying particle. Furthermore, a significant amount of electrons considered for the measurement in this analysis originates from indirect decays of B via D mesons. The corresponding tertiary vertices are hence typically further displaced from the primary vertex than those from direct $B \to e$ or $D \to e$ decays. Finally, the angular distributions of daughter tracks from B decays have about twice the width of the distributions of D-meson daughter tracks – a feature that is used by dedicated analyses to determine the relative contribution of beauty-decay to inclusive heavy-flavour decay electrons (see Section 5.7). To take into account

[3] Relevance means in this context that these electron sources contribute significantly to the electron spectrum after impact parameter selection.

[4] cum vitiis convicium facio, in primis meis facio. *Seneca, De vita beata.*

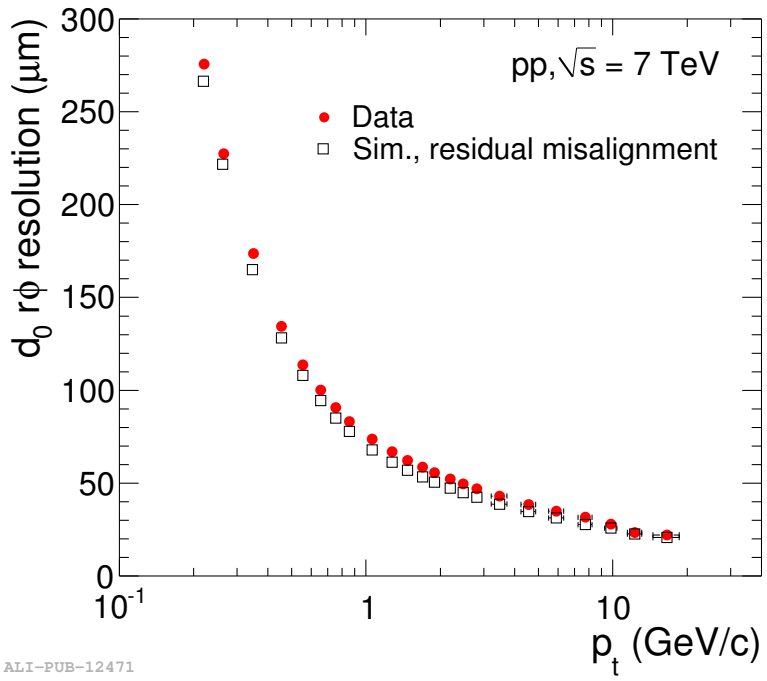

Figure 4.4: p_{T} dependence of the resolution of the transverse impact parameter d_0 for measured and simulated tracks [Abe12f].

all these influences on the d_0 distributions of electrons from different sources, the analysis of simulated particle decays is essential.

The right panel of Figure 4.1 shows reconstructed d_0 distributions of electrons from PYTHIA simulations of different particle decays. The relatively large decay length and wide angular distribution of heavy-flavour hadrons widen the beauty (red) and, to a lesser extent, the charm (black) decay distributions significantly. In contrast, the width of the d_0 distribution of Dalitz or di-electron decays of light mesons (blue, see Section 4.8) with a negligible decay length is dominated by the resolution of the measurement. Figure 4.4 shows the p_{T} dependence of this resolution for simulated and measured tracks.

Electrons from photon conversions, represented in green in Figure 4.1, have to be considered as a particular case. Unlike the electrons from the decays of massive particles, their production is not subject to an exponential decline with the radial distance from the primary vertex. Photon conversions require the presence of atomic nuclei for momentum conservation. Hence, they occur almost exclusively in the solid material of the detectors and the surrounding structures. The track requirements described in Section 4.5 assure that no particles produced outside the inner SPD pixel layer are accepted, so that most of the conversions whose electrons contribute to the selected particle sample come either from the beam pipe or from the first SPD layer.

As a consequence, the typical radial distance of the conversions to the primary

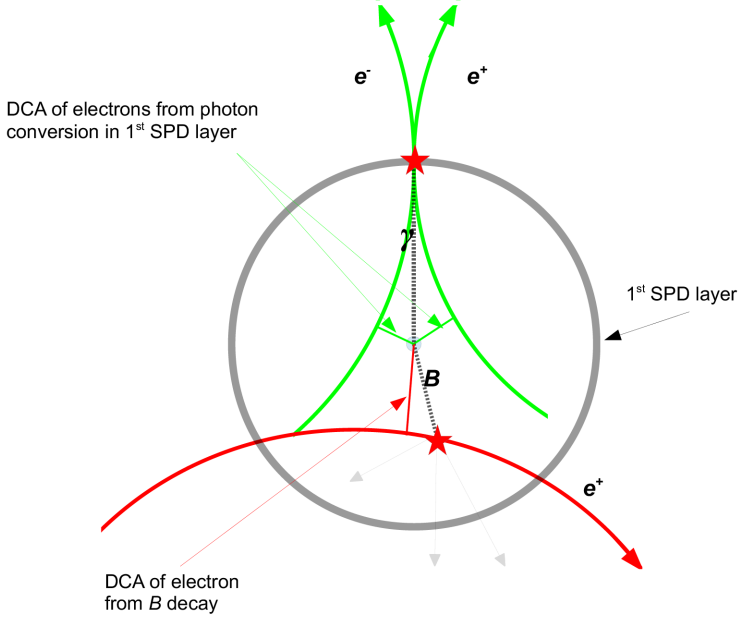

Figure 4.5: Schematic representation of the impact parameters of electrons from photon conversions and B-meson decays. Stars mark the conversion and decay point. Despite the shorter radial distance of the B decay, the resulting electron track in this example has a larger DCA with respect to the primary vertex, owing to the differences in B-decay and conversion kinematics. Decay topologies and SPD geometry are not to scale.

vertex is much larger than that of B-meson decays. Expectations might thus be that conversion electrons have a particularly large impact parameter and cannot be rejected by a requirement like the one applied in this analysis. Fortunately, there is another aspect of conversions which facilitates their distinction from B decays: as photons have no mass, the momenta of their daughter electrons at the conversion point do not have any transverse component with respect to the photon momentum – they point in a radial direction from the primary vertex, as represented in Figure 4.5. The magnitude of the distance of closest approach between the extrapolation of the reconstructed track and the primary vertex is therefore only due to the track curvature induced by the magnetic field and to the d_0 resolution, so that the transverse impact parameter is limited to rather small values.

The choice of a requirement on the impact parameter for the preferential selection of electrons from B decays has to take into account several aspects in order to achieve a result with an optimal significance. The signal efficiency should be large enough to guarantee statistically significant samples of signal electrons in each p_{T} bin within a

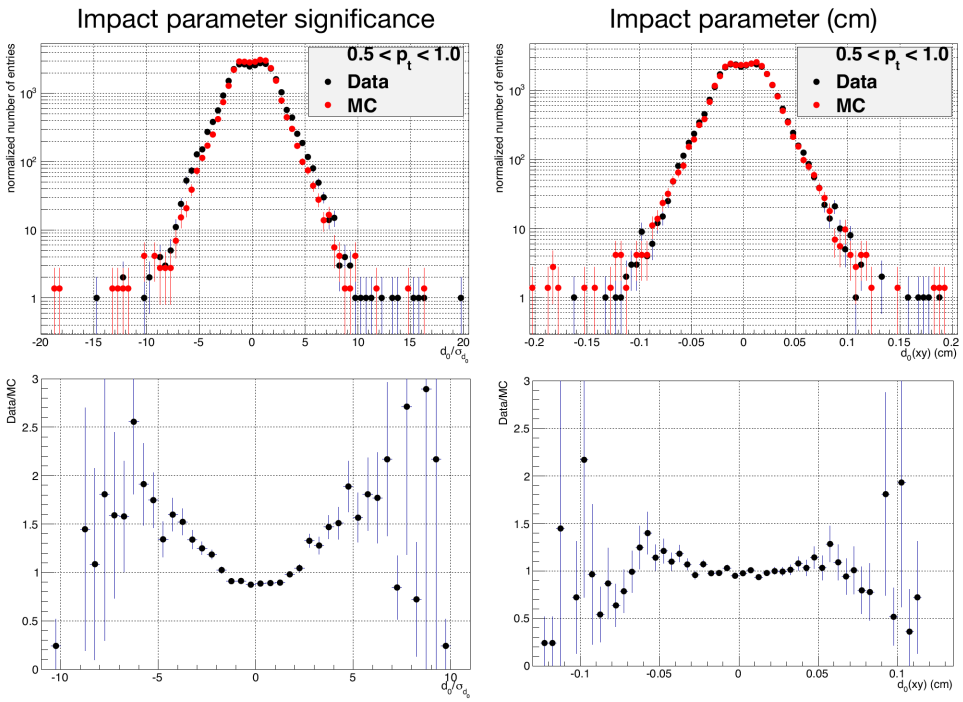

Figure 4.6: Left: comparison of the impact parameter significance distributions of measured and simulated electron tracks with $0.5 < p_{\mathrm{T}} < 1.0$ GeV/c in pp collisions at $\sqrt{s} = 7$ TeV. The lower panel shows the ratio between the distribution of measured and simulated tracks. Right: same, for the distributions of the impact parameter d_0 [Ave12].

wide transverse momentum range. On the other hand, the signal-to-background ratio should be as large as possible, in order to minimize the statistical and systematic uncertainties introduced by the background subtraction (see Section 4.8).

As shown in Figure 4.4, the d_0 resolution is best for high p_{T}, while at lower transverse momenta, it should significantly widen the d_0 distribution of electrons, above all for light-meson decays and conversions. The signal-to-background ratio in the electron sample before impact parameter selection becomes small towards low p_{T} (see Figure 2.3 and Section 4.8). Owing to these circumstances, an impact parameter criterion is needed that is severe at low p_{T} and becomes less strict for higher p_{T}. Given the p_{T} dependence of the d_0 resolution, an alternative approach has been considered in which the significance of the d_0 measurement, $d_0/\sigma(d_0)$, is used as a selection criterion.

The efficiency of the impact parameter selection is determined by Monte Carlo simulations. In order to reduce statistical uncertainties, minimum-bias samples have been combined with signal-enhanced samples for these calculations (see Section 4.4). While decay length and mass of the mother particle are well known, it is not obvious that the resolution of the d_0 measurement is precisely reproduced by simulations.

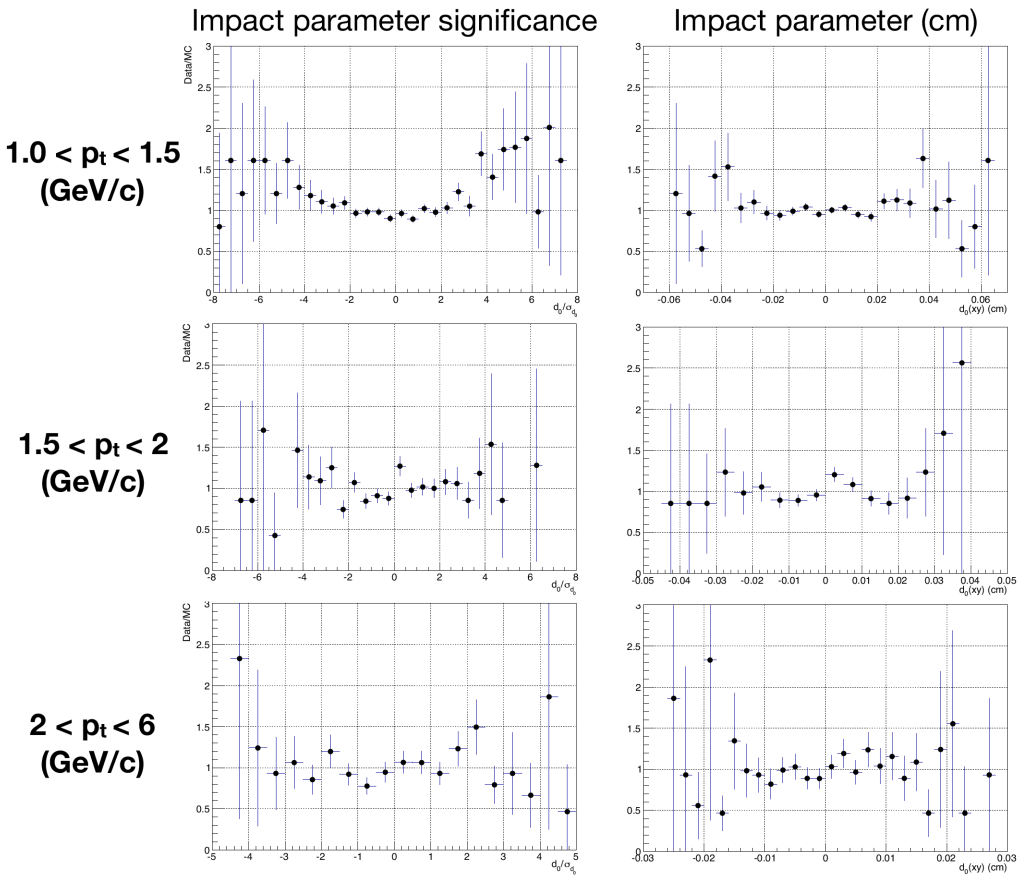

Figure 4.7: Ratio of impact parameter (right) and impact parameter significance (left) distributions between measured and simulated electrons from photon conversions, shown for three different p_{T} ranges in pp collisions at $\sqrt{s} = 7$ TeV [Ave12].

Therefore, the transverse impact parameter distributions of a pure sample of conversion electrons from ALICE measurements[5] and PYTHIA simulations have been compared.

The results of this check for pp collisions at $\sqrt{s} = 7$ TeV are shown in Figures 4.6 to 4.8: the upper panels of Figure 4.6 present the distributions of $d_0/\sigma(d_0)$ (left) and d_0 (right) of conversion electrons with 0.5 GeV/c $< p_{\mathrm{T}} <$ 1.0 GeV/c from a measured (black) and simulated data sample (red), normalized to the overall number of tracks in the sample. The ratios between the respective measured and simulated distribution are plotted in the lower panels. A clear dependence on the absolute value of $d_0/\sigma(d_0)$ is visible in the ratio for the impact parameter signif-

[5]The sample consists of electrons from fully reconstructed photon conversions, identified via requirements on the invariant mass and topology of electron pairs from a common reconstructed vertex.

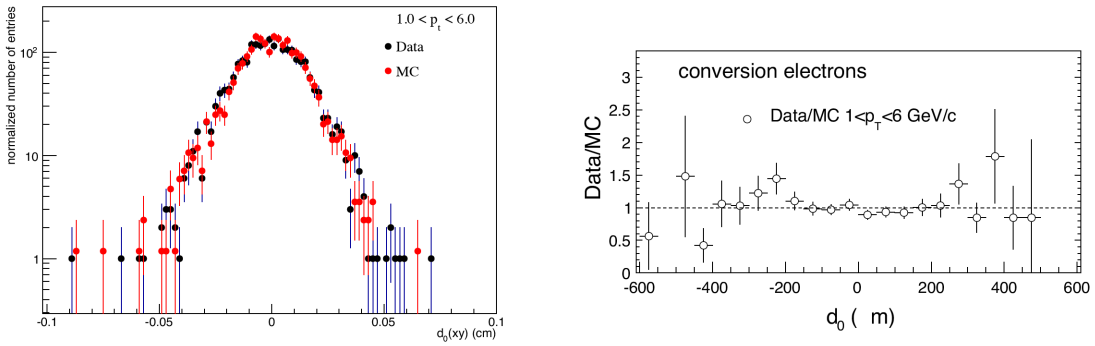

Figure 4.8: Impact parameter distributions of electrons tracks with 1.0 GeV/c < p_{T} < 6 GeV/c from photon conversions in measured data and in simulations at $\sqrt{s}$ = 2.76 TeV (left) and the ratio of both distributions (right) [Ave13a].

icance, while there are only moderate deviations from unity in the ratio for d_0. Figure 4.7 shows the same ratios for three higher transverse momentum regions. Despite increasing statistical uncertainties, an improvement of the situation is visible for the $d_0/\sigma(d_0)$ ratios for higher p_{T}, while the d_0 ratio remains stable and close to unity. For reasons explained in Section 4.8, this analysis is limited to tracks with $p_{\mathrm{T}} > 1.0$ GeV/c. It has, however, been decided to select electron tracks based on the d_0 value without consideration of its significance, since the measured ratio of $d_0/\sigma(d_0)$ for 1.0 GeV/c < p_{T} < 1.5 GeV/c still hints to a deviation from unity with a similar tendency as in Figure 4.6.

An analogous check has been performed for pp collisions at $\sqrt{s}$ = 2.76 TeV, for which a comparison and the ratio between the simulated and measured d_0 distribution is shown in Figure 4.8 for tracks with 1 GeV/c < p_{T} < 6 GeV/c. Both distributions are found to be in good mutual agreement within statistical uncertainties.

Figure 4.9 and Table 4.9 show the p_{T}-dependent parameterization of the applied requirements for both pp collision energies, with the additional parameterizations used to determine the systematic uncertainties of this criterion, as described in Section 4.10. The reference parameterization has been chosen to provide an optimal significance for the beauty-decay electron measurement after the impact parameter requirement. For the analysis of pp collisions at $\sqrt{s}$ = 2.76 TeV, the available data sets differ for the p_{T} regions below and above 2 GeV/c, as explained in Sections 4.4 and 4.7. Therefore, two different parameterizations have been used for these two cases.

While the impact parameter requirements are strict for low p_{T}, the average path length $L_{lab} = c\tau\beta\gamma$ of a B-meson decay with proper decay time τ decreases on average towards lower transverse momenta, which results in a decrease of the electron

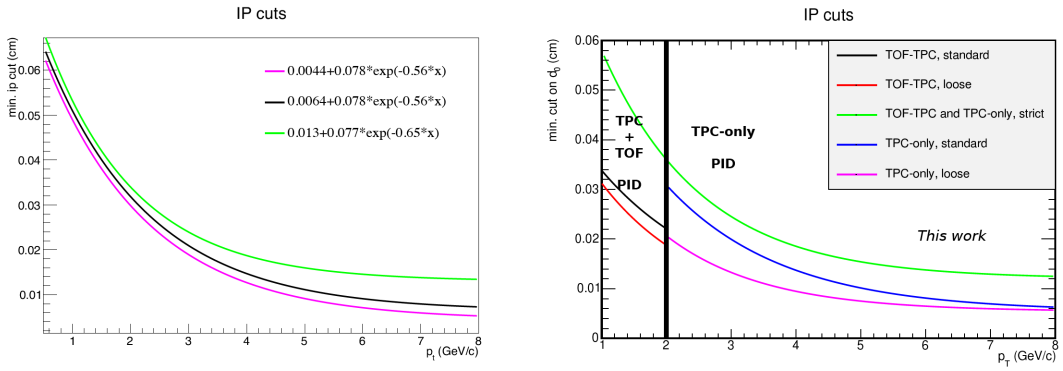

Figure 4.9: Parameterizations of the p_{T}-dependent impact parameter requirement for pp collisions at $\sqrt{s} = 7$ TeV (left, [Ave12]) and 2.76 TeV (right). On the left, the black line represents the standard requirement, while the additional two lines show the deviating parameterizations used to determine the systematic uncertainties. For $\sqrt{s} = 2.76$ TeV, two different sets of standard requirements plus deviating parameterizations exist: one for the momentum region 1 GeV/c $< p_{\mathrm{T}} <$ 2 GeV/c, where TPC and TOF are used for electron identification, and one for $p_{\mathrm{T}} > 2$ GeV/c, where only TPC is used.

track impact parameter and leads to a particularly low signal efficiency at low p_{T}, as shown in Figure 4.10. As the same dependence holds true for all background electron sources except for photon conversions, a strong signal enhancement with respect to the electron background is still achieved.

4.6.1 Run-by-Run Check of Impact Parameter Distributions

In order to guarantee a consistent effect of the impact parameter selection for all partial data sets, the mean value of the d_0 distribution and the standard deviation from this value were determined for each run within the LHC periods LHC10d ($\sqrt{s} = 7$ TeV) and LHC11a ($\sqrt{s} = 2.76$ TeV). Strong deviations of the mean value from zero and large differences in the widths of the d_0 distributions of separate runs can hint to a miscalibration of the impact parameter measurement and lead to an exclusion of the corresponding runs from further analysis.

The runs included in this part of the analysis have undergone the selection described in Section 4.4; four of the runs (see Appendix C) that are included in Figures 4.11 and 4.12 have been rejected for not corresponding to different quality requirements after the present checks have been made. For most checks described in this section, the tracks had to fulfil all selection criteria described in Section 4.5 and some or all of the electron identification requirements described in Section 4.7. While the focus of this part of the analysis is on the behaviour of electrons concerning the measurement of their impact parameter, it has however been found

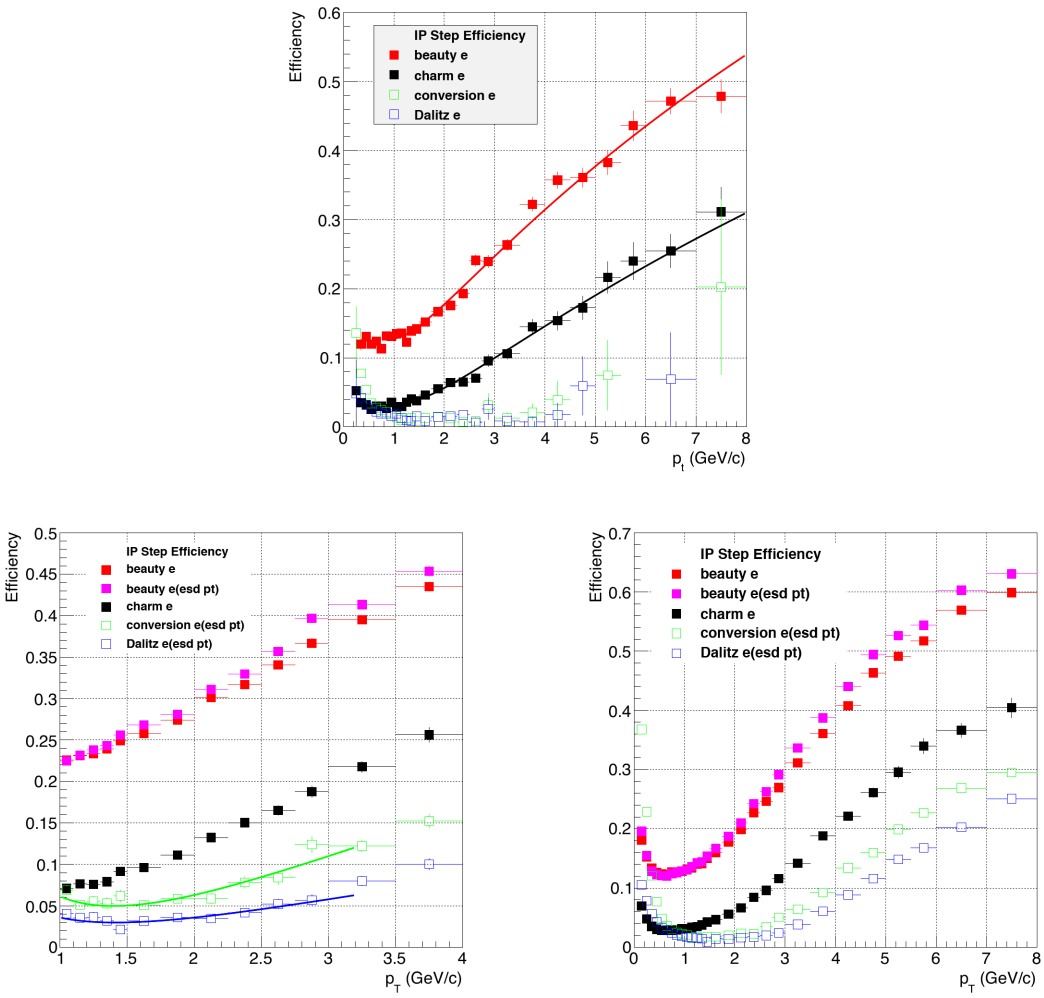

Figure 4.10: Efficiencies of the impact parameter selection for electrons from different sources for pp collisions at $\sqrt{s} = 7$ TeV (upper panel, [Ave12]). For $\sqrt{s} = 2.76$ TeV [Ave13a], the lower left panel shows the corresponding efficiencies for the analysis using TPC and TOF PID (left) and for TPC-only PID (right). For electrons from beauty decays, efficiencies are shown depending on the reconstructed (magenta) and the true simulated p_{T} (red). For all other sources and for the analysis at $\sqrt{s} = 7$ TeV, efficiencies refer to the reconstructed p_{T}. Where fit curves are shown, their values have been used instead of the data points in order to smoothen the statistical fluctuations of the efficiencies.

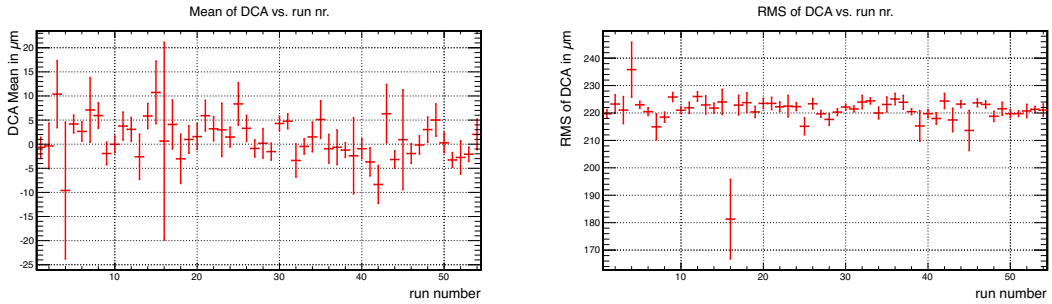

Figure 4.11: Run-by-run quality assurance checks for the impact parameter measurement of electrons in run period LHC10d (pass2) [Ave12]: mean (left panel) and standard deviation (right panel) of the d_0 distributions.

necessary for some purposes to use a larger track sample than the one provided by the selected electron sample. Thus, a wider track selection excluding PID requirements was performed, resulting in an analysis based on a sample mostly consisting of pion tracks, which allowed for spotting finer differences in the global tracking performance within specific runs.

pp Collisions at $\sqrt{s} = 7$ TeV

The electron sample that has been analysed for Figure 4.11 has been selected with the PID requirements by TPC and TOF as described in Section 4.7.1. To minimize the influence of statistical outliers on the mean and standard deviation values of the distributions, only tracks with $|d_0| < 800$ μm have been considered in the checks for run period LHC10d.

In the left panel of Figure 4.11, the mean values of the electron d_0 distributions are plotted versus the run indices of period LHC10d. The run numbers which correspond to the indices used for the figures are listed in Appendix C. Deviations from zero are of the order of ~ 5 μm and can mostly be explained assuming statistical fluctuations. The standard deviation values, shown in the right panel of Figure 4.11, reveal a high degree of homogeneity of the width of the impact parameter distributions throughout run period LHC10d. Two outliers (runs 125023 and 125844) represent very small data samples and have not been excluded based on their d_0 distribution.

One of these two runs, however, was finally rejected on the basis of another check: if no PID cut is applied and the track-by-track d_0 significance distributions of a larger sample are analysed, run 125023 exposes an anomalous behaviour, compared to the other runs (Figure 4.12). Even though the value of $d_0/\sigma(d_0)$ has finally not been considered as a criterion for the track selection, this run has been rejected as a measure of caution, since it does not fulfil the requirement of stable track reconstruction properties for all data sets.

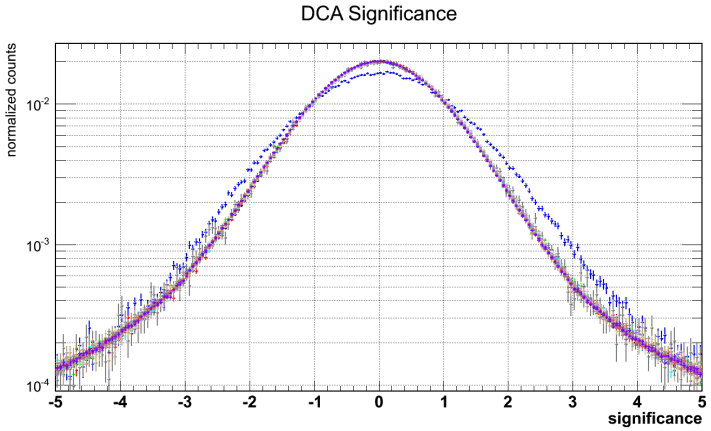

Figure 4.12: d_0/σ_{d_0} distributions for all particle species in individual runs of period LH10d (pass2) [Ave12]. Run 125023 (blue) shows a different behaviour with respect to the bulk of the runs.

pp Collisions at $\sqrt{s} = 2.76$ TeV

A similar series of checks has been performed for the 16 runs of period LHC11a, at a collision energy of 2.76 TeV. In this case, the electron identification for the track sample has been restricted to the TPC selection criteria described in Section 4.7.2, in order to check all runs of period LHC11a based on the same criteria.[6] In order to guarantee a sufficiently pure electron sample, only tracks with $p_{\mathrm{T}} > 1.5$ GeV/c were considered, owing to the limitations of TPC PID at low momenta (see Section 4.7). Tracks with $|d_0| > 500$ μm were rejected, so that the mean and width of the distribution were stable against outliers.

In the same manner as presented above for collisions at $\sqrt{s} = 7$ TeV, the mean and standard deviation values of d_0 were evaluated for all runs, as shown in Figure 4.13. Again, the run numbers corresponding to the indices in the plots are listed in Appendix C. The mean of the single-run d_0 distributions differs from 0 only up to 3 μm, and the standard deviations show no clear outliers, except for run 146807. However, the value for this run suffers from its small data set (0.24M selected events) and the resulting large uncertainty.

Even if the deviations between different runs visible from Figure 4.13 are small compared to the d_0 resolution and the decay length of the B meson, it is difficult to judge if they have a measurable impact on the final result of the analysis. The relevant quantities in this respect are the signal and background efficiencies of the impact parameter selection that have to be corrected for. They are determined via simulations in which the conditions in all runs of period LHC11a are emulated.

[6] In Section 4.4, it has been explained that the data taken in some runs of the period LHC11a do not provide TOF PID information.

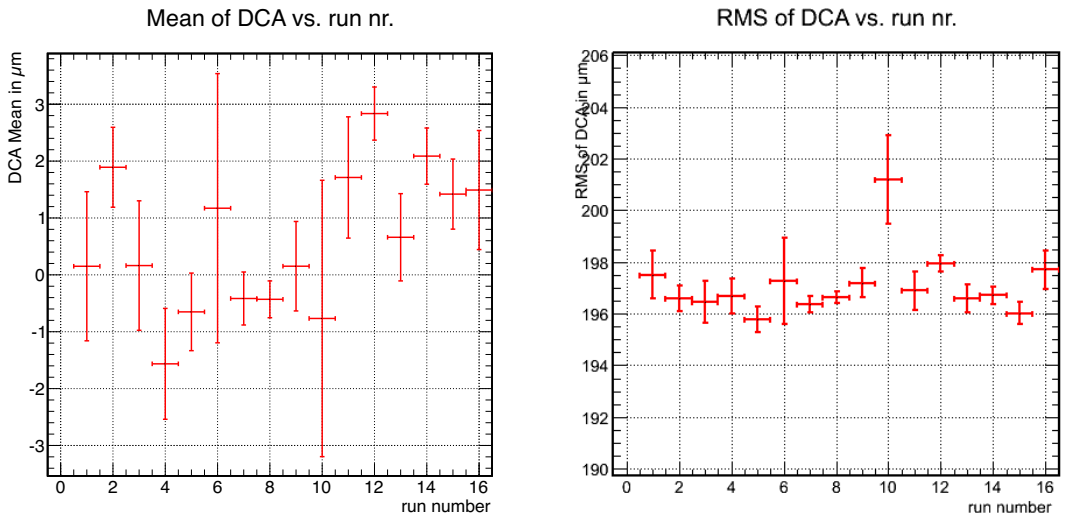

Figure 4.13: Run-by-run quality assurance checks for the impact parameter measurement of electrons in run period LHC11a (pass2) [Ave13a]: mean (left panel) and standard deviation (right panel) of the d_0 distributions.

Therefore, a deviating impact parameter efficiency in simulations for single runs can only be estimated via comparisons of simulated to measured data samples.

As signal and background electrons cannot be distinguished in ALICE measurements, one approach is the comparison of the measured electron d_0 distributions to their counterparts from simulations. However, the size of the respective electron samples have shown to be insufficient for any significant conclusions. Instead, tracks from all particle species without application of particle identification criteria were considered.

For the comparison of efficiencies in simulated and measured data samples, it has to be taken into account that the p_{T} dependence of the particle spectra from different sources is not exactly reproduced in PYTHIA simulations (cf. Section 4.8). Since the impact parameter efficiencies depend on p_{T} and on the particle source, differences in the p_{T} shape and composition of the samples are likely to produce non-negligible deviations of the efficiencies, despite the fact that only minimum-bias simulations have been taken into account. In order to minimize the influence of these deviations on the results of the checks, only the relative deviations in impact parameter efficiency of single runs with respect to the average efficiency of all runs have been compared. In this sense, the checks presented in Figure 4.14 give an estimate of the reproduction accuracy for the run-by-run calibration of period LHC11a in simulations. The track samples used for the plots in this figure have a p_{T} range from 1 GeV/c up to 8 GeV/c, and the presented efficiencies refer to the impact parameter selection criterion as applied for the analysis at 1 GeV/c $< p_{\mathrm{T}} <$ 2 GeV/c (cf. Figure 4.9 and Table 4.9).

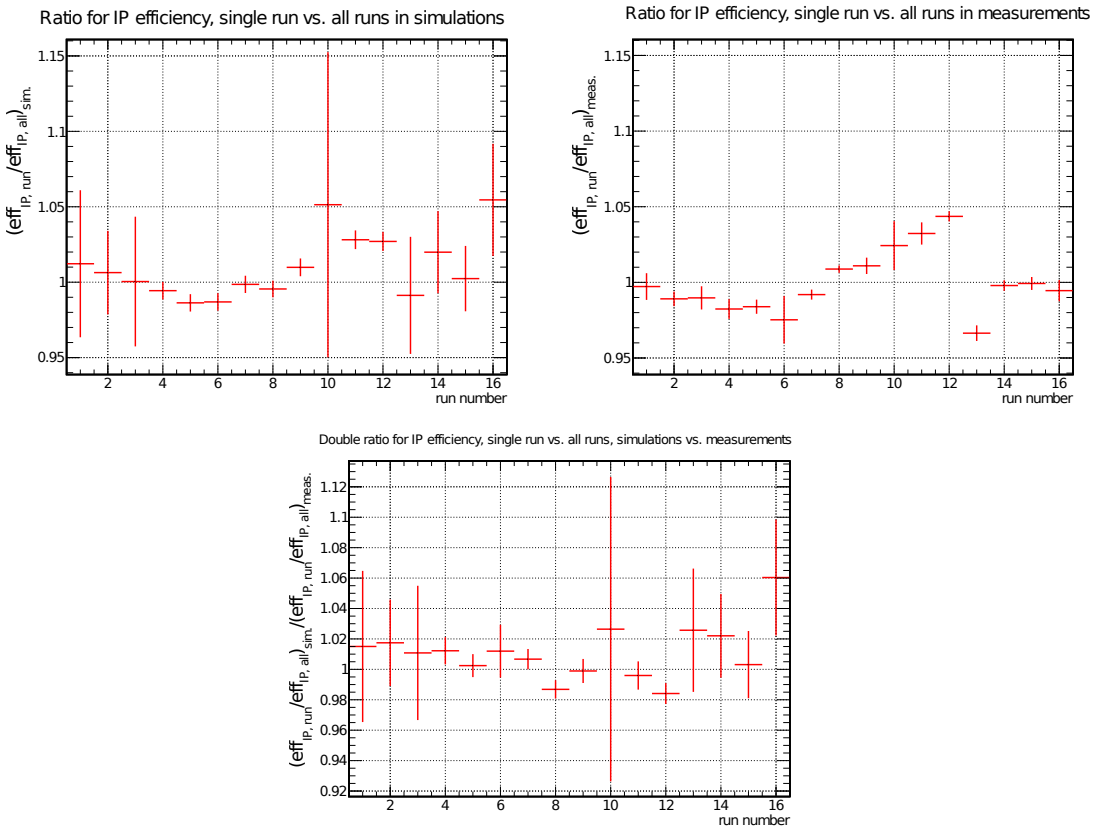

Figure 4.14: Run-by-run quality assurance checks for the impact parameter measurement of electrons in run period LHC11a (pass2) [Ave13a]: ratio of of the impact parameter selection efficiency in single runs to the overall run period efficiency in simulations (upper left) and measurements (upper right), and ratio of both plots (lower panel).

The upper panels of Figure 4.14 show the ratio of the impact parameter selection efficiency in single runs to the average efficiency in the run period for simulated (left) and measured events (right). In the lower panel, the ratio between the two upper plots is presented. No relative deviations of single run efficiencies larger than 6% for simulations or measurements are observed, and the trend in the measured run-specific differences is well reproduced by simulations, as can be seen from the flat ratio between both. Similar results have been obtained by analogous checks using the impact parameter selection as applied for $p_{\mathrm{T}} > 2$ GeV/c, where statistical uncertainties are slightly larger, owing to the stricter requirement. As a result of the homogeneous behaviour of both measured and simulated runs in period LHC11a, no data sets had to be excluded from further analysis.

A comparison of the upper left and right panel of Figure 4.14 shows that eight of the simulated runs suffer from large statistical uncertainties, whereas the uncertainties of the real measurements are of similar magnitude for all runs. The reason for

this difference lies in the fact that the largest part of the simulated minimum-bias events considered in this analysis (25.7M) was produced only for runs in which TOF PID was usable (see Section 4.4), while a much smaller set of simulations (1.67M events) represents the full range of runs considered in this section. As a consequence, all parts of the analysis that are based on simulations do not take into account the conditions of the different runs according to their true relative amount of events. Runs with valid TOF PID are accorded a significantly higher weight, e.g. for the efficiency correction described in Section 4.9 and the determination of the electron background (Section 4.8). For some parts of the analysis, this imbalance is reduced, but not compensated, by the additional usage of 4.68M events from simulations enriched with decays of heavy-flavoured hadrons, π^0, and η, produced for all 16 runs. It can be shown, however, that the effect on the results presented in this work is small. The relative deviation of the overall impact parameter selection efficiency of the statistically underrepresented runs from the overall efficiency measured in all minimum-bias samples is only about 1%, with a statistical uncertainty of similar magnitude. It will therefore be neglected in the following.

4.6.2 Dependence of the Impact Parameter Selection on the Pseudorapidity η

In a similar way as the checks for run-by-run dependences described above, the η dependence of the impact parameter selection efficiency can be investigated. For the analysis of pp collisions at $\sqrt{s} = 2.76$ TeV, efficiencies for $\eta > 0$ and $\eta < 0$ have been compared for different p_{T} bins in simulations and measurements. Ideally, efficiencies for both halves of the pseudorapidity distribution should be equal, since the pp collisions at the LHC and the geometry of the ALICE central-barrel detectors used for this measurement represent symmetric systems in η. Differences in the impact parameter selection efficiencies between positive and negative η can be caused by irregularities in the detector performance that have an effect on the measurement of d_0. The comparison of the double ratio between efficiencies at positive and negative η on the one hand and simulated and measured efficiencies on the other hand provides a test of the reproduction of η dependences in the impact parameter measurements.

Figure 4.15 shows the ratio between the impact parameter efficiency for positive and negative pseudorapidities in simulations (left) and measurements (right), based on the impact parameter requirement as applied for $p_{\mathrm{T}} < 2$ GeV/c. The ratio between these two plots is shown in the lower left panel. Only for the two lowest p_{T} bins below 1.5 GeV/c, a significant difference from unity of the order of 2% is observed. The lower right panel of Figure 4.15 shows the analogous double ratio for the impact parameter criterion applied for $p_{\mathrm{T}} > 2$, in which no significant deviation from unity appears. It is concluded from these checks that η dependences in simulations and measurements are small and consistent enough with each other, so that no dedicated systematic uncertainties have to be assigned.

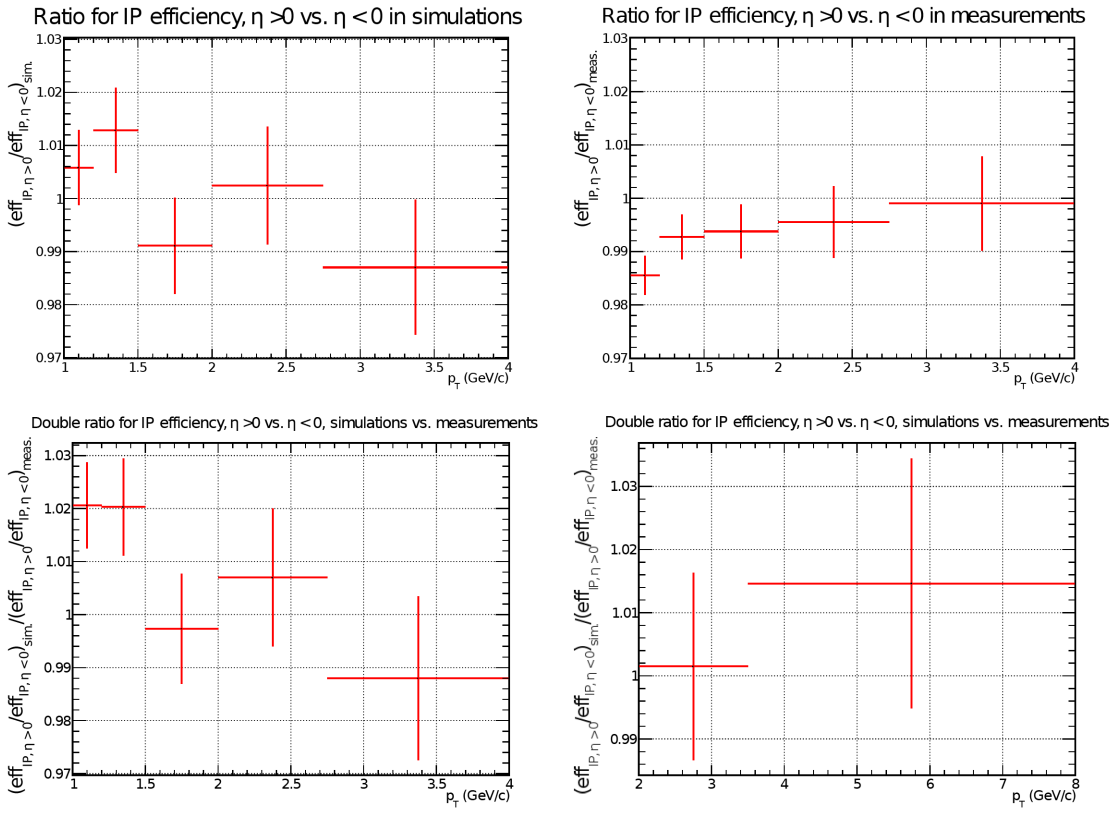

Figure 4.15: Quality assurance checks for the impact parameter measurement at different pseudorapidities in run period LHC11a, at $\sqrt{s} = 2.76$ TeV [Ave13a]: ratio between impact parameter efficiency for $\eta > 0$ and for $\eta < 0$ in simulations (upper left) and measurements (upper right) for the d_0-selection parameters for $p_{\mathrm{T}} < 2$ GeV/c, and ratio of both plots (lower left). The corresponding ratio for the d_0 selection applied at $p_{\mathrm{T}} > 2$ GeV/c is presented in the lower right panel.

4.7 Electron Identification via TPC and TOF

While the analysis dealing with inclusive heavy-flavour electron spectra in collisions at $\sqrt{s} = 7$ TeV either uses TRD in addition to TPC and TOF or combines information from TPC and EMCal (cf. [Abe12g]), it is more convenient for the analysis described in this thesis to use exclusively information from TPC and TOF. This choice has several reasons: first of all, the additional requirement on the impact parameter reduces the amount of signal tracks considerably (cf. Figure 4.10). Requiring particle identification from further detectors would deteriorate this situation, to a degree that would make measurements at transverse momenta as high as 7 or 8 GeV/c statistically insignificant. This is mainly due to the small acceptance of the EMCal and the TRD. During run periods LHC10d and LHC11a, only 7 and

10 of the overall 18 TRD supermodules were installed, respectively. By limiting particle identification to the information provided by TPC and TOF, this analysis therefore sacrifices a significantly better pion rejection at high p_{T} for the sake of smaller statistical uncertainties.

There is, however, an effect of the impact parameter selection which makes up for this loss: since most hadrons are primary particles, their tracks have a relatively small impact parameter to the primary vertex and are consequently rejected (see Figure 4.18, right panel). Therefore, hadron contamination in the remaining raw spectrum is significantly lower than before the impact parameter requirement.

The TOF signal for pp collisions at $\sqrt{s} = 7$ TeV is shown in terms of the relativistic β factor and in terms of the time-of-flight resolution σ in Figure 4.16. Kaons and protons can be reliably separated from electrons up to $p \approx 1.5$ GeV/c and 3 GeV/c, respectively.

The TPC can identify electrons based on their characteristic energy loss per unit of length, $\mathrm{d}E/\mathrm{d}x$, in the detector gas. In the lower left panel of Figure 4.16, the p dependence of the absolute $\mathrm{d}E/\mathrm{d}x$ value for different particle species is shown for collisions at $\sqrt{s} = 7$ TeV, along with the respective parameterization of the energy loss as given by the Bethe formula. The right panel shows the deviation from the parameterization value for electrons in units of the energy-loss resolution $\sigma_{TPC-dE/dx}$.

TOF and TPC provide complementary information for electron identification. At low momenta, for which the TPC cannot distinguish electrons from protons or kaons because of crossing areas between the respective $\mathrm{d}E/\mathrm{d}x$ bands, TOF signals for all three species are well separated. Pions, which also have a β factor close to unity at momenta above 1 GeV/c, are not distinguished from electrons by TOF. However, they deposit far less energy in the TPC gas than electrons in the lower part of the momentum range considered in this analysis. At higher momenta, for which TOF does not provide a sufficient proton and kaon suppression, the TPC rejects both species reliably. Consequently, the only quantitatively non-negligible source of hadron contamination in the selected sample are pions at high momenta.

In the analysis of the inclusive heavy-flavour electron spectrum, it has been found that the TPC $\mathrm{d}E/\mathrm{d}x$ varied significantly with the track pseudorapidity η. The signal is corrected for this effect before the application of selection criteria [Abe12g, Abe14b].

In the following, the specific requirements for electron identification in the analyses at $\sqrt{s} = 7$ TeV and $\sqrt{s} = 2.76$ TeV will be described. Their values are summarized in Table 4.3.

4.7.1 pp Collisions at $\sqrt{s} = 7$ TeV

In this analysis, a band of ± 3 σ around the value for the electron time-of-flight hypothesis (see Figure 4.16, upper right panel) was selected for all momenta. Electron identification with the TPC required a signal within a band from -0.003 σ up to 3 σ from a Gaussian distribution around the mean electron $\mathrm{d}E/\mathrm{d}x$, resulting in an

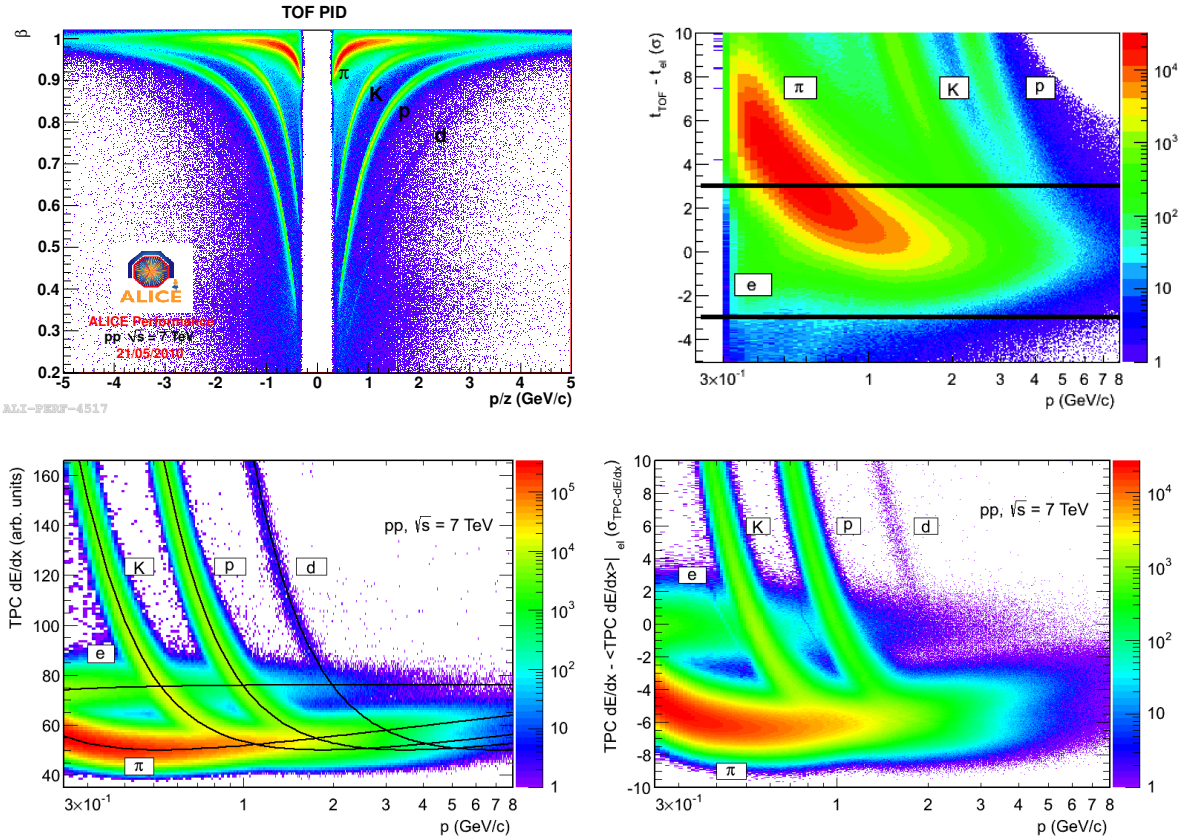

Figure 4.16: Electron selection with the TOF and TPC detectors for proton-proton collisions at $\sqrt{s} = 7$ TeV, run period LHC10d, pass2 reconstruction. Upper left panel: relativistic β factor as measured by TOF vs. signed momentum. The β value for electrons is close to unity at all momenta. Upper right panel: difference between measured time of flight and the value expected for electrons in units of the time-of-flight resolution σ. The horizontal lines mark the ± 3 σ selection band for electron candidates [Abe12g]. Lower left panel: energy deposition per unit of length $\mathrm{d}E/\mathrm{d}x$ in arbitrary units vs. momentum p [Abe12g]. Lower right panel: TPC signal in units of the $\mathrm{d}E/\mathrm{d}x$ resolution $\sigma_{\mathrm{TPC-dE/dx}}$ [Abe12g].

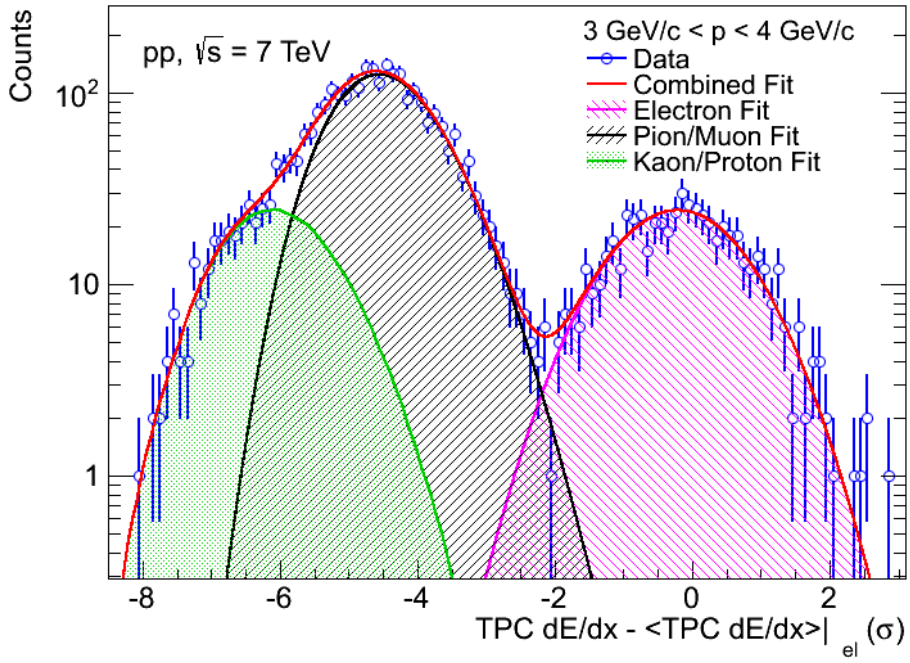

Figure 4.17: TPC $\mathrm{d}E/\mathrm{d}x$ distribution after electron selection with TOF at $3 < p < 4$ GeV/c. The hadron contamination is calculated as the ratio of the hadron and electron fit integrals in the selection range from -0.003 to 3 $\sigma_{\mathrm{TPC-dE/dx}}$ [Abe12g].

electron efficiency of 50% for the whole momentum range.

Hadron contamination

The remaining hadron contamination in the raw spectrum after electron identification and impact parameter selection is estimated in two steps.

First, the relative hadron contribution to the spectrum after electron identification and before the impact parameter requirement is determined. For this, the measured TPC $\mathrm{d}E/\mathrm{d}x$ distributions of electrons and of background hadrons after the application of TOF PID are described by fits for several momentum slices, following the same procedure already applied in the analysis of electrons from inclusive heavy-flavour hadron decays [Abe12g] (Figure 4.17). While the electron signal is well described by a Gaussian in the quantitatively relevant area, the tail of the pion distribution overlapping with the electron peak is better represented by the multiplication of a Landau distribution by an exponential term. This approach was found to be valid for a clean pion sample from K^0_s decays, selected based on the so-called *V0-finder* and a series of requirements on the decay topology [Abe12g]. The fit of the pion distribution also comprises a minor contribution from misidentified muons,

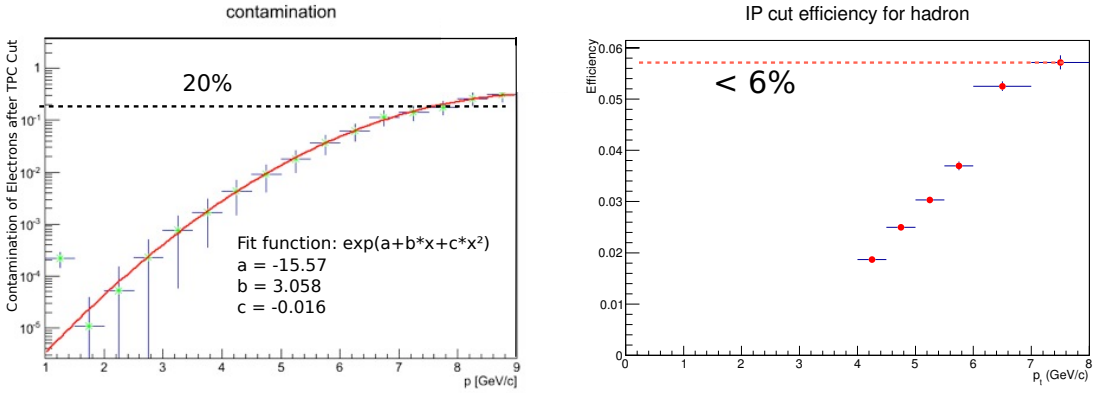

Figure 4.18: Steps for the estimation of hadron contamination after the impact parameter requirement [Ave12]. Left: hadron contamination in the electron spectrum for pp collisions at $\sqrt{s} = 7$ TeV after electron identification by TOF and TPC, without application of the impact parameter requirement. Right: hadron efficiency of the standard impact parameter selection, without application of electron identification criteria.

whose signal in the TPC is very similar to that of pions. Signals from kaons and protons, which are almost completely suppressed by TOF PID at low momenta, can be jointly represented by a slightly skewed Gaussian fit for higher momenta. The relative contamination at this step was calculated as the ratio of the integral of the background fit inside the required TPC $\mathrm{d}E/\mathrm{d}x$ range for electron identification to that of the electron signal fit inside the same range. In the left panel of Figure 4.18, the p dependence of this value is shown. A contamination of less than 20% is achieved up to a momentum of 8 GeV/c.

In a second step, the hadron efficiency of the impact parameter requirement was determined on simulated data, as presented in the right panel of Figure 4.18 [Ave12]. The hadron contamination in the spectrum after the impact parameter requirement was then evaluated based on both plots in Figure 4.18 and on the impact parameter selection efficiency for electrons. It was estimated to be less than 3% up to a transverse momentum of 8 GeV/c. As a cross-check, fits of the hadron background were directly performed on the TPC signal after the impact parameter selection. The result, shown in Figure 4.19 along with the hadron contamination before the impact parameter selection, is very well consistent with the estimation of a hadron contamination below 3% for the complete p_{T} range.

4.7.2 pp Collisions at $\sqrt{s} = 2.76$ TeV

The signal sample for collisions at $\sqrt{s} = 2.76$ TeV is smaller than the one for $\sqrt{s} = 7$ TeV. As already mentioned in Section 4.4, the particle identification criteria have therefore been adapted in order to maximize the statistical significance

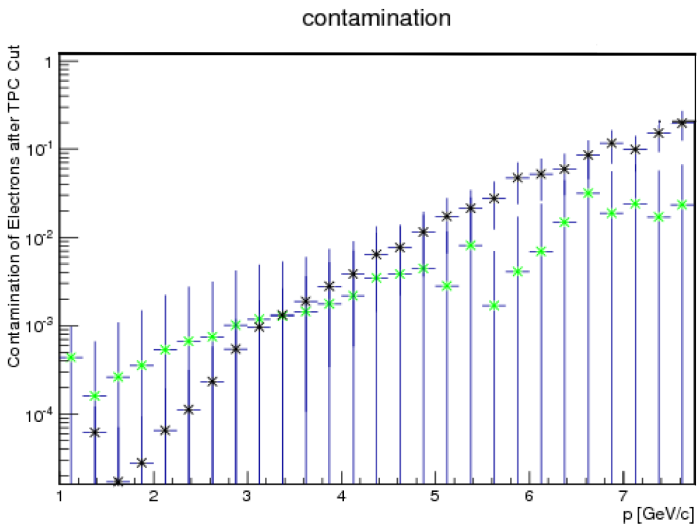

Figure 4.19: Hadron contamination in the inclusive electron spectrum for pp collisions at $\sqrt{s} = 7$ TeV. Black: before impact parameter selection; green: after impact parameter selection [Ave12].

Table 4.3: Electron identification criteria.

Signal for PID	**Accepted signal range**	
	$\sqrt{s} = 7$ TeV	$\sqrt{s} = 2.76$ TeV
TPC dE/dx (TOF-TPC PID)	-0.003 $\sigma <$ dE/d$x <$ 3 σ	-1 $\sigma <$ dE/d$x <$ 3 σ
TPC dE/dx (TPC-only PID)		-0.53 $\sigma <$ dE/d$x <$ 3 σ
Time of Flight t (TOF-TPC PID)	-3 $\sigma < t <$ 3 σ	

of the measurements, above all at high p_{T}.

While TPC and TOF are used to identify electrons from $p_{\mathrm{T}} = 1$ GeV/c up to 2 GeV/c, TOF PID is not applied for higher transverse momenta. For this reason, also runs in which no valid TOF PID was available have been included for $p_{\mathrm{T}} > 2$ GeV/c. Moreover, the TPC was operated at high gain in run period LHC11a, resulting in a better separation of pions from electrons via their TPC dE/dx. This improvement enabled the heavy-flavour electron analyses to extend their TPC electron identification efficiency to 84% for 1 GeV/$c < p_{\mathrm{T}} <$ 2 GeV/c, when combined with TOF PID, corresponding to a selection of a band from -1 σ up to 3 σ around the centre of the electron distribution.

For analysis at $p_{\mathrm{T}} > 2$ GeV/c, only the TPC is used to identify electrons. Here, the selection limits were set to -0.53 σ and 3 σ, with an electron identification efficiency of 70%.

In [Ave13b, Ave13a], the lower electron selection limit for the TPC signal is given as -1.35 $\sigma_{\mathrm{TPC-d}E/\mathrm{d}x}$ and -0.9 $\sigma_{\mathrm{TPC-d}E/\mathrm{d}x}$ for TPC-TOF and TPC-only PID, respec-

tively. It has to be noted that these values refer to the width and centre of the nominal TPC $\mathrm{d}E/\mathrm{d}x$ distribution before correction for the η dependence of the TPC signal. In order to make the connection between the different criteria and their selection efficiencies more obvious to the reader, the final electron signal distribution on which PID requirements are applied will be used as the reference in this thesis.

Hadron contamination

In contrast to the two-step method described in Section 4.7.1, the determination of hadron contamination for pp collisions at $\sqrt{s} = 2.76$ TeV is exclusively based on the TPC $\mathrm{d}E/\mathrm{d}x$ signals after the impact parameter selection.

For 2 GeV/c < p_{T} < 4 GeV/c, the contamination is determined using the same kind of signal and background fits as in Section 4.7.1. As the relative amount of hadron background is found to be negligible in this p_{T} range, the contamination for the TPC-TOF PID below 2 GeV/c, which is supposed to be even significantly lower, does not need to be quantified.

Taking into account the low overall amount of signals at high p_{T} in the data sample from period LHC11a, the number of hadrons at $p_{\mathrm{T}} > 4$ GeV/c is based on the fit for pions only, while the amount of candidate tracks is obtained as the sum of all counts above the electron selection threshold at -1 σ with respect to the mean electron $\mathrm{d}E/\mathrm{d}x$.

In order to minimize the uncertainties due to this low amount of data, the relative contamination value is fitted over a wide momentum range with an error function with the parameters a_0, a_1, a_2, a_3:

$$f(p) = a_0 + a_1 \cdot \mathrm{erfc}(a_2 \cdot p + a_3) \qquad , \tag{4.1}$$

with $\mathrm{erfc}(x) = \frac{2}{\sqrt{\pi}} \int_x^\infty e^{-t^2} dt$.

Figure 4.20 shows the contamination in the different momentum slices and the fit. The subtraction of the contamination from the raw spectrum after the impact parameter selection is done on a statistical basis. Depending on its momentum p, a weight is attributed to each track, representing its probability to be a hadron. These weights are then summed to an overall hadron contamination in bins of the track p_{T}. The resulting hadron contamination p_{T} spectrum is finally subtracted from the raw spectrum [Ave13b].

The subtraction and the propagation of the corresponding uncertainties are handled by the AliRoot Correction Framework (see Section 4.2).

The systematic uncertainties of the final result due to the hadron contamination estimation are shown in Figure 4.21. They were obtained by using the upper and lower limit of the estimation for the calculation of the corrected spectrum. These estimation limits are the results of a variation of the contamination values by their statistical uncertainties and of the upper momentum limit at which 100% of contamination is assumed to be reached (see right panel of Figure 4.20).

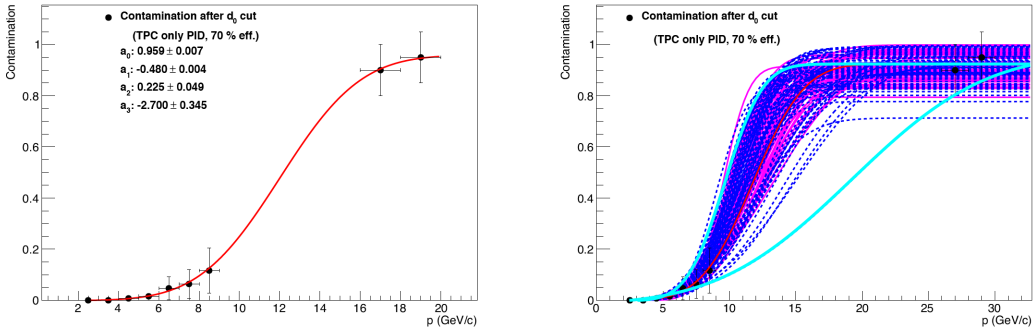

Figure 4.20: Analysis for pp collisions at $\sqrt{s} = 2.76$ TeV with TPC-only PID ($p_{\mathrm{T}} > 2$ GeV/c) [Ave13a]; left: remaining hadron contamination after impact parameter selection. Right: upper and lower limit of the contamination parameterization (light blue), fits from variation of contamination values by their statistical uncertainties (magenta), and fits with different values for the momentum limit at which a contamination of 100% is reached (dark blue).

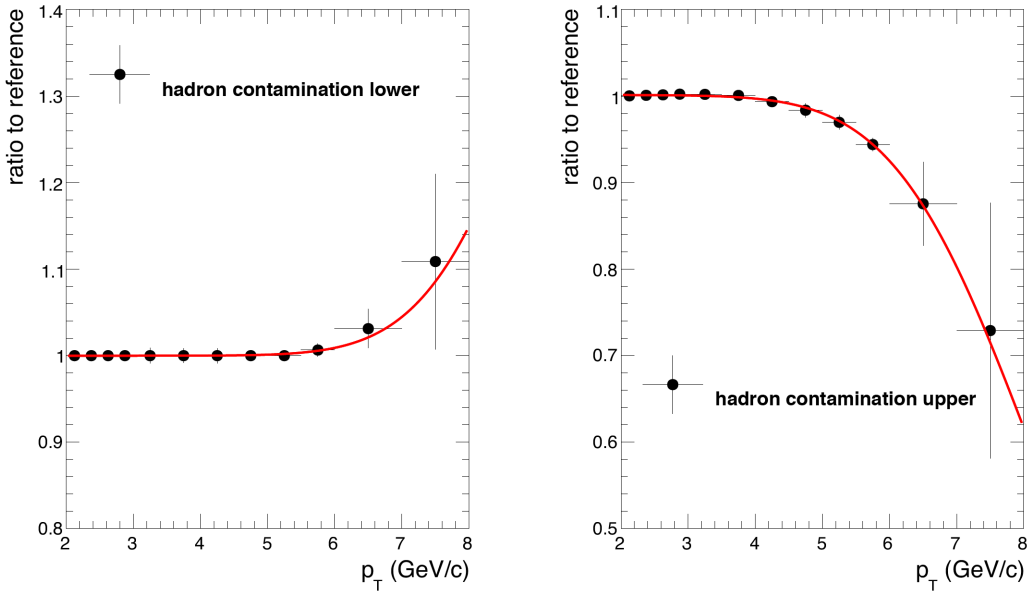

Figure 4.21: Analysis for pp collisions at $\sqrt{s} = 2.76$ TeV with TPC-only PID ($p_{\mathrm{T}} > 2$ GeV/c) [Ave13a]: systematic uncertainties of hadron contamination estimation.

4.8 Electron Background

One of the key challenges of the method chosen for this analysis is the quantification of the electron background within the measured inclusive electron spectrum. Unlike in the analysis of exclusive hadron decay channels, where a requirement on the invariant mass of decaying particles is made, no such tool for an almost complete background elimination is available in this approach. As described in Section 4.6, the impact parameter selection achieves a certain enhancement of the beauty signal, without being able to provide a track-by-track identification of electrons from beauty decays.

The resulting inclusive electron spectrum is therefore at low p_{T} dominated by decays of particles other than beauty hadrons, and even at high p_{T}, an important fraction of charm-decay electrons remains in the selected sample. This background has to be subtracted based on the knowledge of the electron spectra from the decays of different species of mother particles that are produced in pp collisions at the respective energies, and of the efficiencies of the applied selection criteria for the background electron contributions. While the latter can be determined by GEANT simulations to a good precision and the decay kinematics of the mother particles which produce background electrons are mostly well known, the information about the p_{T}-dependent production of these particles are limited to the accuracy to which their spectra have been measured by ALICE or other experiments. This circumstance makes the electron background the most important source of systematic uncertainties at low momenta (see Section 4.10), where the largest part of the production of beauty-hadron decay electrons takes place. A particularly careful treatment of the electron background estimation is therefore necessary in order to reduce as far as possible the uncertainties of the low-p_{T} and total production cross section of electrons from beauty-hadron decays.

Sources of background electrons can be divided into seven groups:

1. Dalitz and di-electron decays of the light neutral mesons π^0, η, η', ϕ, ω, and ρ,
2. conversions of photons from decays of the mesons listed above,
3. semi-electronic decays of hadrons containing one charm quark or antiquark,
4. di-electron decays of the quarkonia J/ψ and Υ,
5. electrons from hard parton scatterings, which include conversions of real or virtual direct photons and electrons from the Drell-Yan process,
6. semi-electronic kaon decays ($K \to e\pi\nu$, also called "K_{e3}"),
7. electrons from decays of secondary particles and from conversions of their decay photons.

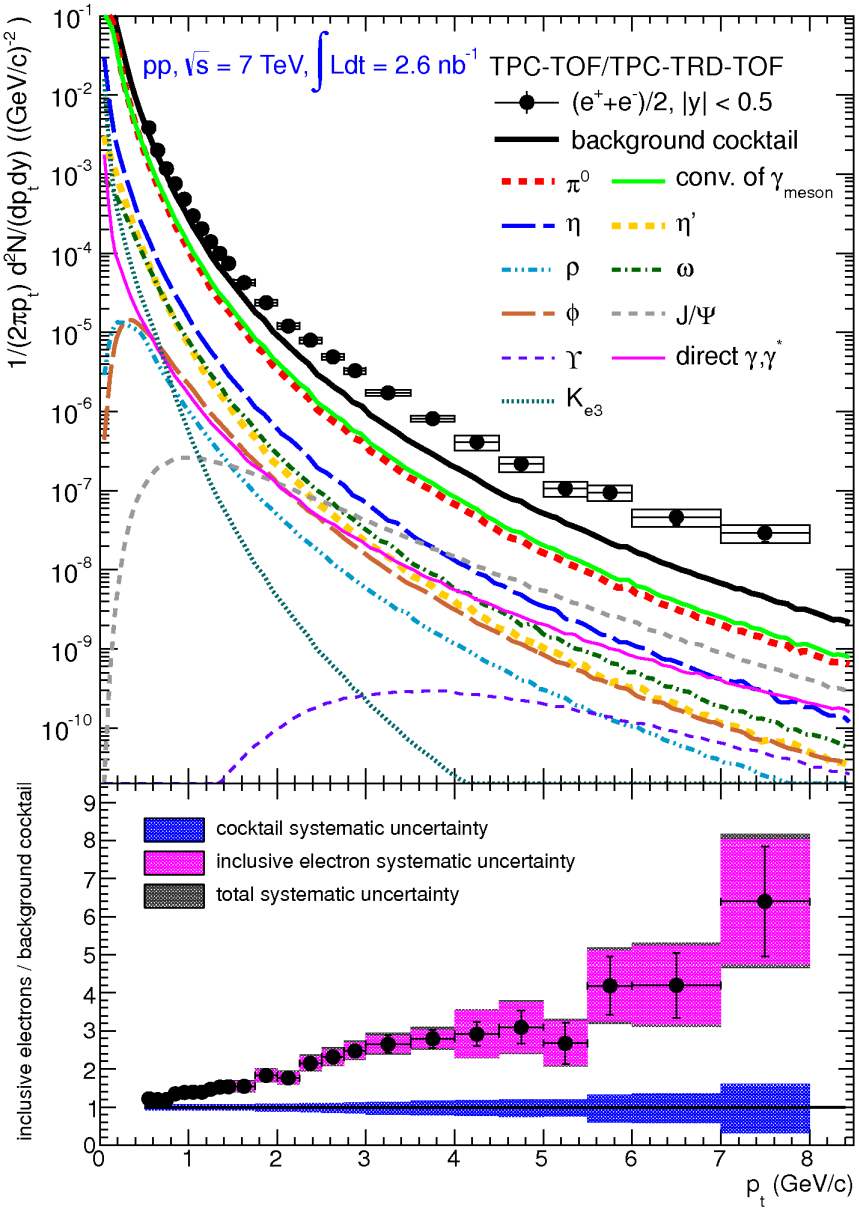

Figure 4.22: Upper panel: p_{T}-differential inclusive electron spectrum measured in ALICE at mid-rapidity in pp collisions at $\sqrt{s} = 7$ TeV [Abe12g]. Contributing electron spectra, apart from open heavy flavour electrons, are represented in coloured curves; their sum, the overall electron background to the inclusive heavy-flavour electron spectrum, is plotted in black. Lower panel: ratio of the measured inclusive electron spectrum to the overall background electron spectrum.

A detailed discussion of the contributions of all these sources to the inclusive electron spectrum is given in [Abe12g, Ave11a]. The measured or calculated p_{T}-dependent production cross sections of electrons from light-flavoured hadrons and quarkonia at mid-rapidity are shown for $\sqrt{s} = 7$ TeV in Figure 4.22, compared to the inclusive electron spectrum measured with ALICE [Abe12g]. For the analyses described in this thesis, only electron sources have been taken into account which, in minimum-bias PYTHIA simulations, contribute to a quantifiable extent to the inclusive electron spectrum at $p_{\mathrm{T}} > 1$ GeV/c after application of the impact parameter requirement. As a consequence, the electron background from decays of quarkonia and kaons as well as from the Drell-Yan process will be neglected. The contribution from conversions of direct photons represented in Figure 4.22 was estimated based on an NLO pQCD calculation. Via multiplication of this spectrum by the p_{T}-dependent impact parameter selection efficiency (see Figure 4.10), it was found to be negligible in the context of this analysis for $p_{\mathrm{T}} > 1$ GeV/c. In principle, the same is true for the backgrounds from ρ, ϕ, ω, and η' decays and the conversions of their daughter photons. They can, however, be estimated in a common procedure with the more abundant electrons of π^0 and η decays and will therefore be included in the following considerations for the estimation of the electron background. Secondary particle decays are no relevant background to beauty-hadron decays in pp collisions. This situation might change for Pb-Pb collisions, as will be discussed in Chapter 6.

The significant contributions of electron sources whose background yields have to be determined are given by the first three items listed above. In this analysis, they are for most purposes treated as only three different sources (e.g. in the determination of the impact parameter efficiency in Section 4.6), although each of them includes several separate components, which will be reflected in the calculation of the corresponding systematic uncertainties. In Appendix D, an overview table of the most important decay channels of light and charmed hadrons contributing to the electron background is given.

The PYTHIA simulations performed to generate the background electron spectra do not reproduce their respective measured p_{T} dependence accurately enough and have therefore to be corrected by attributing weighting factors to the simulated electron track entries before subtracting their sum from the inclusive electron spectrum. This is done in a slightly different way for electrons from light-meson decays and charm decays, as will be explained in the following two sections.

4.8.1 Background from Light-Meson Decays

Decays of light neutral mesons generate electrons in two ways: either they directly produce an electron pair, if the decay is of a Dalitz or di-electron type, or they give rise to one or more photons, which can later convert in the beam pipe or in the detector material.

The most abundant background electron source by far are neutral pions. Their

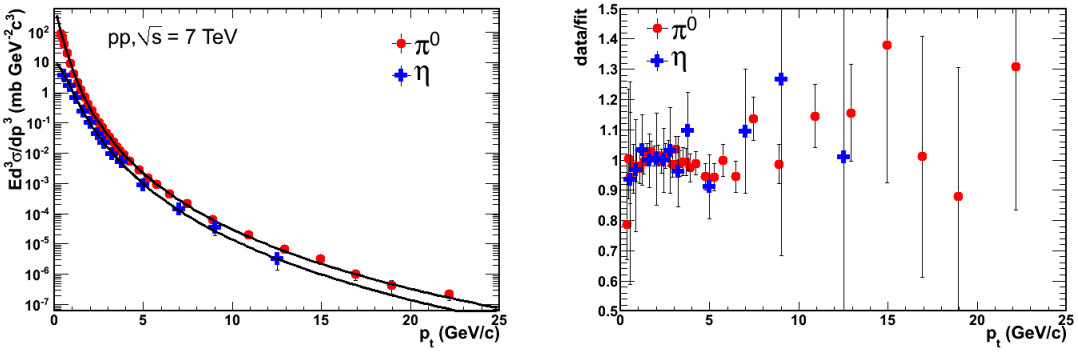

Figure 4.23: Left: measured invariant differential production cross sections of π^0 and η in pp collisions at $\sqrt{s} = 7$ TeV as a function of p_{T} [Abe12j], with fits using Equation 4.2. The right panel shows the ratios of the measured spectra to the corresponding fits. Error bars represent the combined statistical and systematic uncertainties of the measurements.

decays contribute the largest fraction to the electron spectrum from electronic light-meson decays as well as to the photon conversion background. The respective branching ratios are 1.174% ($\pi^0 \to e^+e^-\gamma$) and 98.823% ($\pi^0 \to \gamma\gamma$). Both processes produce a substantial fraction of the measured electron spectrum in this analysis at low p_{T}, and they do so at a very similar magnitude.

Taking into account the material of the beam pipe, air, and (45 ±5)% of the first SPD pixel layer thickness, which is necessary to produce a hit in this detector layer, the effective converter thickness relevant for this analysis was calculated to be (0.77 ± 0.07)% of the photon radiation length [Abe12g], including an uncertainty of the ALICE material budget of 4.5% [Koc11]. The resulting ratio of the corresponding yield of conversion electrons to those of π^0-Dalitz decays is (1.01 ± 0.09)%.

The p_{T}-dependent production cross sections of π^0 and η, the second most abundant light meson, have been measured by ALICE in pp collisions at $\sqrt{s} = 7$ TeV [Abe12j] and $\sqrt{s} = 2.76$ TeV [Abe14c]. The measurements of all four spectra were performed through two complementary approaches to measure $\gamma\gamma$ decays of the mesons, a measurement with the PHOS calorimeter, which provided π^0 spectra up to a p_{T} of 25 GeV/c and 12 GeV/c for $\sqrt{s} = 7$ TeV and 2.76 TeV, respectively, and another one reconstructing photon conversions using TPC and ITS, which was able to extend the π^0 spectra down to 300 MeV/c and 400 MeV/c, respectively.

These spectra are the basis for the weighting of all light-flavour decay and photon conversion electron spectra from PYTHIA simulations that will be explained further

[7]The parameters given for $\sqrt{s} = 2.76$ TeV are based on the preliminary π^0 measurement that was used to produce the results presented in this thesis. In the meanwhile, an updated result for the π^0 measurement has been produced [Abe14c]. The corresponding parameters are $\mathrm{d}N/\mathrm{d}y = 16.67^{+2.38}_{-2.27}$, $T = 0.1393^{+0.0057}_{-0.0048}$ MeV/c^2, and $n = 7.252^{+0.112}_{-0.090}$.

Table 4.4: Parameters[7] of the Tsallis fits from Equation 4.2 to the p_{T}-differential spectra of π^0 and η.

$\sqrt{s}$ (TeV)	Meson	$\mathrm{d}N/\mathrm{d}y$	T (MeV/c^2)	n
7	π^0	2.40 ± 0.15	139 ± 4	6.88 ± 0.07
7	η	0.21 ± 0.03	229 ± 21	7.0 ± 0.5
2.76	π^0	19.75 ± 12.72	0.130 ± 0.017	7.051 ± 0.302

below. For $\sqrt{s} = 7$ TeV, they are shown in Figure 4.23, where they are compared to a fit with the Tsallis function [Tsa88]:

$$E\frac{\mathrm{d}^3\sigma}{\mathrm{d}p^3} = \frac{\sigma_{\mathrm{pp}}}{2\pi}\frac{\mathrm{d}N}{\mathrm{d}y}\frac{(n-1)(n-2)}{nT(nT+m(n-2))}(1+(m_{\mathrm{T}}-m)/(nT))^{-n} \quad . \tag{4.2}$$

$\mathrm{d}N/\mathrm{d}y$, T, and n, the parameters of the fits, are listed in Table 4.4. σ_{pp} is the inelastic pp cross section, and m is the mass of the respective meson. The transverse mass m_{T} is defined as

$$m_{\mathrm{T}} = \sqrt{m^2 + p_{\mathrm{T}}^2} \quad . \tag{4.3}$$

Table 4.5: Ratios of meson yields to π^0 yields at $p_{\mathrm{T}} = 5$ GeV/c in pp collisions at $\sqrt{s} = 7$ TeV and $\sqrt{s} = 2.76$ TeV used for m_{T}-scaling. The η-meson spectrum at $\sqrt{s} = 7$ TeV was determined by ALICE measurements [Abe12j] instead.

$\eta/\pi^0 = 0.48 \pm 0.144$ [Adl07a]
$\rho/\pi^0 = 1.0 \pm 0.3$ [Adl06]
$\omega/\pi^0 = 0.85 \pm 0.255$ [Ada11]
$\eta'/\pi^0 = 0.25 \pm 0.075$ [Adl06]
$\phi/\pi^0 = 0.40 \pm 0.12$ [Adl06]

The spectra of the mesons ρ, ϕ, ω, and η' have not been measured in ALICE. However, they can be estimated based on an approach known as *m_T-scaling* [Alb95, Kha11b]. It uses the empirically established fact that, when expressed in terms of m_{T} instead of p_{T}, the production cross sections of different meson species follow a common shape. Hence, the m_{T}-dependence of the π^0 spectrum will be assumed as a basis for the remaining light mesons in the following. Since, according to Equation 4.3, a similar spectral shape in m_{T} also means that shapes in p_{T} are similar for $p_{\mathrm{T}} \gg m$, the meson spectra are normalized to their absolute values according to

measured or estimated ratios of their yields to the π^0 yield at a p_{T} value that fulfils this condition, in the case of this analysis at 5 GeV/c. These ratios are assumed to be to a good approximation independent of the centre-of-mass energy of the collisions and can therefore be adopted from analyses of other experiments at lower collision energies. Table 4.5 gives an overview over the values used in this thesis. A conservative relative uncertainty of 30% has been assumed for all cross sections determined by m_{T}-scaling. The η meson is treated as a special case in this context: while its spectrum has been determined experimentally for both $\sqrt{s} = 7$ TeV and $\sqrt{s} = 2.76$ TeV, its large systematic uncertainties at the latter collision energy make a calculation via m_{T}-scaling favourable, so that this approach is followed in the corresponding analysis. On its part, the usage of the η measurements at 7 TeV not only bears the advantage of being more exact than the m_{T}-scaling result; ALICE also discovered hints to a deviation of the η/π^0 ratio at low m_{T} from its constant value assumed by m_{T}-scaling at this energy – a behaviour that was not observed for $\sqrt{s} = 2.76$ TeV [Rey11].

The actual background quantities of electrons from light-flavour decays are determined in several steps: first, weighting factors are calculated from the ratio of the normalized yield of their mother mesons – in the case of photon conversions, of their grandmother mesons – to the corresponding simulated meson yield at a given p_{T}. These factors are then applied to all registered entries of electrons from a minimum-bias PYTHIA simulation before the impact parameter selection. In order to minimize the statistical uncertainties of the background estimation, the resulting spectra of electrons from photon conversions and light-meson decays are subsequently multiplied by the impact parameter efficiencies corresponding to these sources, determined using a combination of minimum-bias and signal-enhanced simulations (cf. Sections 4.4 and 4.6). In the following, the calculation of the weighting factors for the electron entries and their systematic uncertainties will be explained in more detail.

To be comparable with the measured or m_{T}-scaled meson spectra, the simulated spectra of light-meson yields are normalized to the number of events, to the width of the respective interval in p_{T}, and to unity in rapidity, where yields are assumed to be flat in the region around mid-rapidity for $|y| < 0.8$:

$$N_{\mathrm{sim,norm}} = \frac{N_{\mathrm{sim}}}{\Delta y N_{\mathrm{evt}} \Delta p_{\mathrm{T}}} \quad , \tag{4.4}$$

with the number N_{sim} of electrons produced in simulations in the relevant rapidity region and p_{T} bin, the width of the rapidity acceptance $\Delta y = 1.6$, the number N_{evt} of analysed pp collisions, and the width Δp_{T} of the p_{T} bin. The resulting meson spectra from ALICE measurements, m_{T}-scaling, and PYTHIA simulations for pp collisions at both centre-of-mass energies are shown in Appendix E. The left panels

[8] The weights that are presented here and used for the subsequent calculations were obtained based on a preliminary π^0 measurement. Spectra and weighting factors determined from an updated π^0 measurement [Abe14c] are shown in Appendix E.

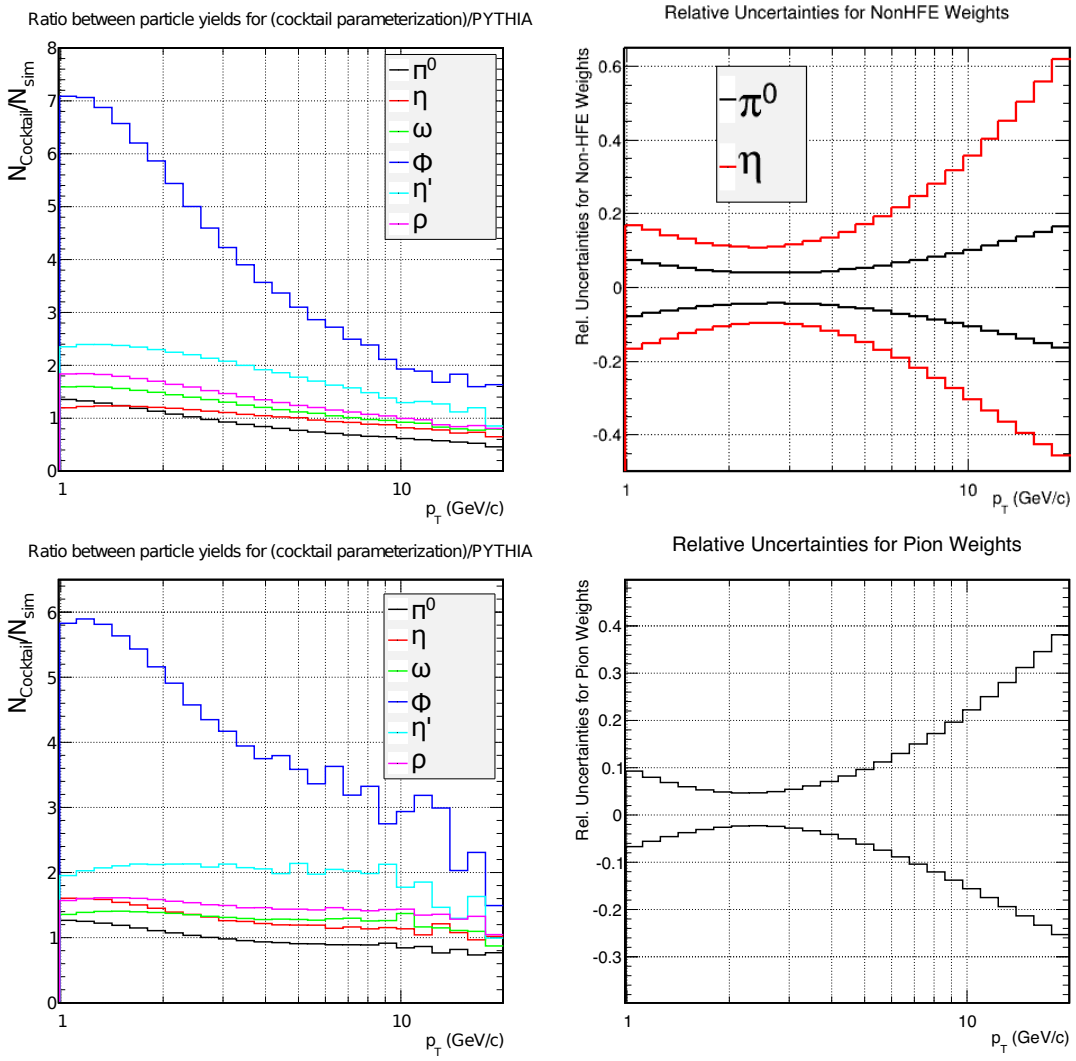

Figure 4.24: Left: weighting factors from ratios of the measured or m_{T}-scaled p_{T}-differential light-meson yields to the yields generated by PYTHIA for pp collisions at $\sqrt{s} = 7$ TeV [Ave12] (upper panel) and $\sqrt{s} = 2.76$ TeV (lower panel) [Ave13a].[8] Right: relative uncertainties of the weighting factors for π^0 and η decays [Ave12] (upper panel) at $\sqrt{s} = 7$ TeV, and for π^0 decays at $\sqrt{s} = 2.76$ TeV (lower panel) [Ave13a]. The uncertainties for all other mesons are composed of the π^0 uncertainty and a scaling uncertainty of 30%. The parameterizations and simulated spectra from which the weights are derived can be found in Figure E.1 in Appendix E.

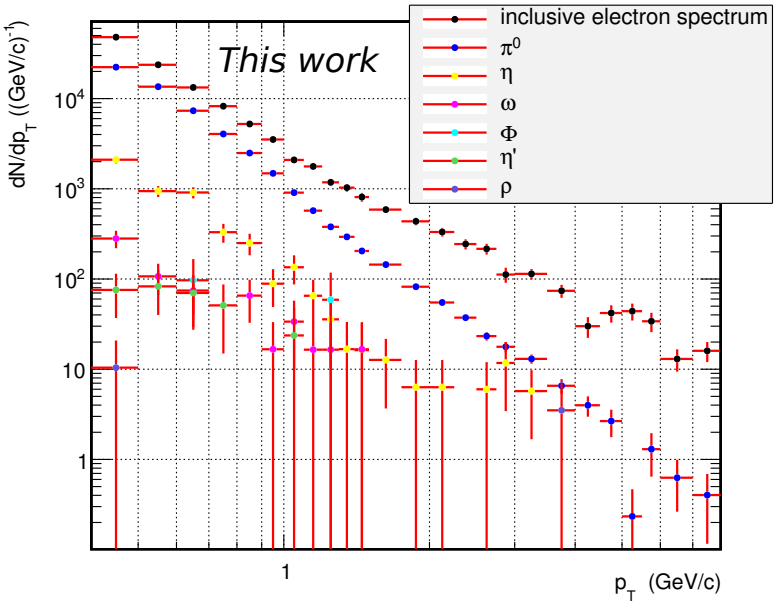

Figure 4.25: Electron background from different meson decays for pp collisions at $\sqrt{s} = 2.76$ TeV, summed over direct meson decays to electrons and conversion of photons from meson decays.

of Figure 4.24 depict the corresponding ratios between the measured or scaled and the simulated meson spectra, while the relative uncertainties of the measured spectra are presented in the right panels.

To make up for the imperfections in the reproduction of the spectral shapes produced by PYTHIA, these ratios are used as weighting factors for the simulated electron entries stored in the `CORRFW` containers (cf. Section 4.2). For each electron, the species and reconstructed transverse momentum of its mother or grandmother meson is determined, according to which the weighting factor taken from the histograms in the left panels of Figure 4.24 is applied.

A Note on the Normalization of the Light-Meson Spectra

The normalization factors for the m_{T}-scaled spectra of ρ, η', and ϕ listed in Table 4.5 have been used in several publications before (e.g. [Adc02, Adl06]), but have not always been quoted consistently in the meantime. A review of the sources of the normalization factors in the course of the preparation of this thesis showed that the values for the ratios of ϕ/π^0 and η'/π^0 were switched in [Ada06c] and propagated to further publications (e.g. [Kha11c]). In other works, far higher values are given for the ratio η'/π^0, e.g. 0.9 and 1.0 in [Dia80] and [Agg00], respectively. Furthermore, the value of 0.4 for the ratio ϕ/π^0 was already determined by measurements from

the first Au-Au collisions at $\sqrt{s} = 130$ GeV at RHIC and seems to be too high, compared to more recent results from ALICE measurements [Ave, Kno13].

As these considerations put into question the adequacy of the representation at least of the spectra of ϕ and η' for the background subtraction in this analysis, it seems necessary to test if possible larger deviations from the true meson-to-pion ratios have any significant impact on the result. Therefore, the simulated electron yields for pp collisions at $\sqrt{s} = 2.76$ TeV with the current weighting factors have been grouped according to the species of the mesons from which they originate, summed over contributions from direct electronic meson decays and conversions of photons from the decay of the respective meson. The selection criteria correspond to the ones used as a reference for the analysis at 1 GeV/$c < p_{\mathrm{T}} < 2$ GeV/c, as listed in Table 4.9.

The result of this test is shown in Figure 4.25. As expected, π^0 decays are the clearly dominating electron source, followed by a small, but still non-negligible contribution by η decays. All other sources are represented by small quantities with very limited statistical significance for $p_{\mathrm{T}} > 1$ GeV/c, and at a far lower level than the electron spectrum after subtraction of all background sources, as represented at a later stage, in Figure 4.38. It can thus be assumed that even a correction of one of these spectra by a factor as large as 4, corresponding to the relative difference between the η'/π^0 ratio used in this analysis and the one given in [Agg00], would not cause a significant difference in the final result. This conclusion notwithstanding, a careful review of the normalization factors for future analyses seems to be in order.

Systematic and Statistical Uncertainties

The relative systematic uncertainties of the parameterizations for the π^0 and η spectra are shown in the right panels of Figure 4.24. They were obtained by Tsallis fits to the spectra that had been shifted up- or downwards by the upper and lower uncertainties of the measured points, respectively. For each electron entry with a central weighting factor w^{cent}, entries with the lower and upper limit of the weighting factor are stored. For the spectra generated by m_{T}-scaling, the systematic uncertainty has two contributions: one from the uncertainty of the pion spectrum from which they are derived, and an additional m_{T}-scaling uncertainty of 30%. When adding up the electron background contributions from one p_{T} bin, these different contributions are taken into account; while the uncertainties from the measured π^0 spectrum for the different meson species are all correlated and therefore added linearly, the m_{T}-scaling contributions and the uncertainties from η-meson measurements are treated as uncorrelated and added to the other uncertainties quadratically. Such a distinction is possible since the relevant quantities for the simulated electrons are stored in a `CORRFW` container along with the information about their mother or grandmother particles.

The overall upper or lower systematic uncertainty limit $u^{light}_{bg,syst}(p_{\mathrm{T}})$ for a given p_{T} bin is therefore calculated as

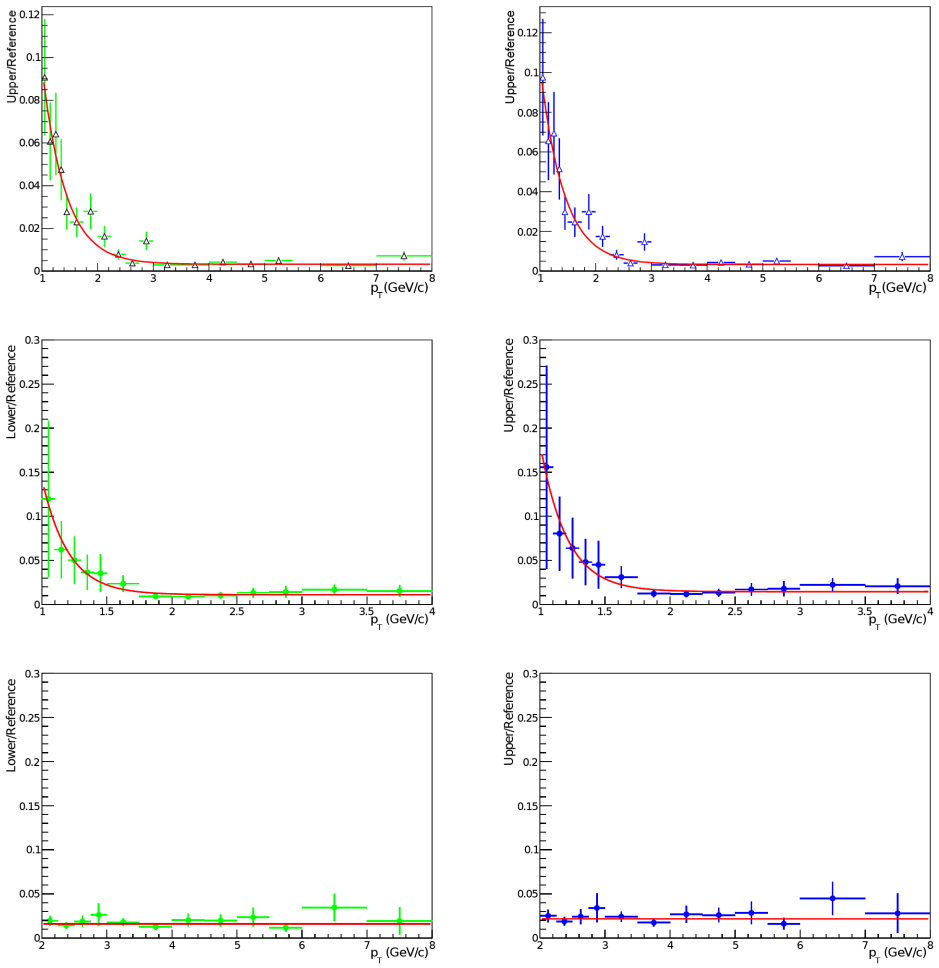

Figure 4.26: Relative systematic uncertainties of the electron yield from the decay of open-beauty hadrons, originating from light-meson yield uncertainties (left panels for upper and right panels for lower uncertainties), for pp collisions at $\sqrt{s} = 7$ TeV [Ave12] (upper panels), and at $\sqrt{s} = 2.76$ TeV [Ave13a] for the analysis using TPC and TOF PID (middle panels) and for TPC-only PID (lower panels).

$$\left(u_{bg,syst}^{light}(p_{\mathrm{T}})\right)^2 = \tag{4.5}$$

$$\left\{\sum_{\substack{i=\pi^0,\\ scaled}}\sum_{j=1}^{N(p_{\mathrm{T}},i)}(w_{i,j}^{lim}-w_{i,j}^{cent})\right\}^2+\left\{\sum_{i=1}^{N(p_{\mathrm{T}},\eta)}(w_{\eta,j}^{lim}-w_{\eta,j}^{cent})\right\}^2+\sum_{\substack{i=\\ scaled}}\left\{\sum_{j=1}^{N(p_{\mathrm{T}},i)}(0.3\cdot w_{i,j}^{cent})\right\}^2,$$

where sums over i are calculated over different electron sources (π^0 decays and mesons whose spectra were obtained by m_{T}-scaling), and sums over j comprise all $N(p_{\mathrm{T}})$ entries from one electron source in a given p_{T} bin. w^{lim} stands either for the upper or the lower limit of the weighting factor, according to the upper or lower uncertainty that is calculated. The second term is not relevant for the analysis at $\sqrt{s} = 2.76$ TeV, where the η spectrum is obtained by m_{T}-scaling and thus covered by the first and third term of the equation.

The uncertainties of the electron background from light-flavour meson decays are finally propagated to the spectrum of electrons from beauty-hadron decays. The resulting relative uncertainties are shown in Figure 4.26 for $\sqrt{s} = 7$ TeV and $\sqrt{s} = 2.76$ TeV, together with fits from which the uncertainty values for the final spectra are taken. For the analysis at $\sqrt{s} = 2.76$ TeV, two separate cases have to be considered for the analyses using TPC and TOF PID, as applied for 1 GeV/c < p_{T} < 2 GeV/c, and using TPC PID alone, as for p_{T} > 2 GeV/c. Owing to the different impact parameter requirements for these two cases (see Section 4.6), different fractions of electron background are present in the selected samples, resulting in slightly different relative uncertainties for the respective beauty-decay electron spectra at the same p_{T}.

The common statistical uncertainties $u_{bg,stat}^{light}(p_{\mathrm{T}})$ resulting from the differently weighted entries in individual p_{T} bins are calculated from the sum of squares of all weights in the considered bin,

$$\left(u_{bg,stat}^{light}(p_{\mathrm{T}})\right)^2 = \sum_{\substack{i=\pi^0,\\ scaled}}\sum_{j=1}^{N(p_{\mathrm{T}},i)}\left(w_{i,j}^{cent}\right)^2 \quad , \tag{4.6}$$

and are propagated to the signal-electron spectrum during the subtraction of electron backgrounds (see Section 4.8.3).

4.8.2 Background from Charm-Hadron Decays

General Procedure

The estimation of the electron background from charm-hadron decays was determined in a similar way as the background from light mesons. It is based on available measurements of the decaying particles, as well as on the simulation of their decays with PYTHIA, and of their transport in the detectors with GEANT.

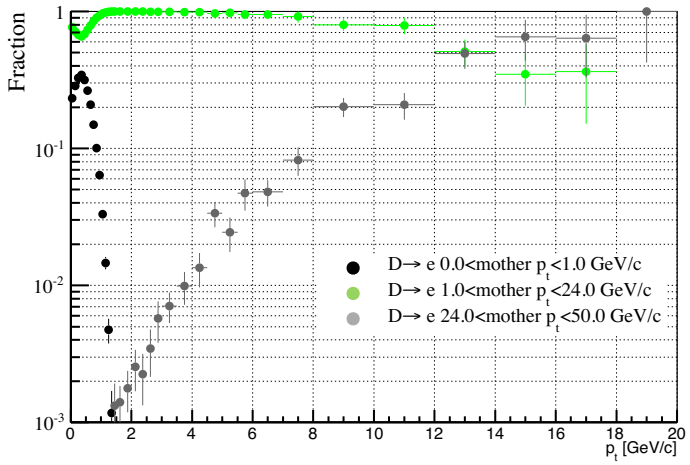

Figure 4.27: Fraction of electrons from decays of D mesons in different p_{T} ranges, simulated with PYTHIA, as a function of the electron p_{T} [Ave12].

For the case of pp collisions at $\sqrt{s} = 7$ TeV, ALICE measurements of D^+, D^0, and D_s [Aam12, Abe12a] at the same centre-of-mass energy were considered; in addition, a ZEUS measurement of Λ_c [Che05] was used. The electron spectra from the contributions of all individual p_{T} bins of each measured charm hadron were obtained by simulating hadron decays with PYTHIA, which takes into account the specific branching ratios to semi-electronic decays. The sum of these contributions, the overall electron background from charm-hadron decays, was compared to the corresponding electron spectrum generated by PYTHIA simulations. The simulated spectrum was reweighted to be consistent with the measurement-based electron distributions. All requirements on the measured electron tracks, up to the impact parameter selection, were applied on the simulated tracks transported via GEANT. The resulting electron background spectrum from charm decays was finally subtracted from the inclusive electron spectrum after the impact parameter requirement.

A similar approach for pp collisions at $\sqrt{s} = 2.76$ TeV proved to suffer from large systematic uncertainties from the charm-hadron measurements at this collision energy. It was therefore decided to determine the charm-decay electron spectrum at $\sqrt{s} = 2.76$ TeV by scaling the spectrum obtained for $\sqrt{s} = 7$ TeV following a FONLL prescription [Ave11b].

Different Contributions

The production cross sections of the D mesons that will be considered for the calculation of the electron spectrum arising from their decays were measured by ALICE [Aam12] within the p_{T} ranges listed in Table 4.6. The electron spectrum measured in the analysis described in this thesis covers a range of 1 GeV/c $< p_{\mathrm{T}} <$ 8 GeV/c.

Table 4.6: p_{T} intervals of ALICE measurements for different D mesons [Ave12].

Species	p_{T} (GeV/c)
D^0	$1 < p_{\mathrm{T}} < 16$
D^+	$1 < p_{\mathrm{T}} < 24$
D_s	$2 < p_{\mathrm{T}} < 12$

Figure 4.27 shows the fraction of electrons from decays of D mesons in different p_{T} ranges, depending on the electron p_{T}, as simulated with PYTHIA. According to these simulations, a significant fraction of the electrons from D-meson decays – about 10% at an electron p_{T} of 8 GeV/c – can be expected to originate from particles with a p_{T} higher than the maximal measured p_{T} of any of the mesons listed in Table 4.6. In order to give a reliable estimate of the electron background from charm decays, the D-meson spectra were therefore extrapolated up to transverse momenta of 50 GeV/c, following a two-step procedure.

Table 4.7: $\mathrm{D}^0/\mathrm{D}^{*+}$ ratios for 16 GeV/c $< p_{\mathrm{T}} <$ 24 GeV/c, determined by the three extrapolation methods shown in Figure 4.28 [Ave12]. $POL0$ corresponds to the fit applied in the lower left panel, $POL1$ to the one in the lower right panel.

Extrapolation method	p_{T} range for fit (GeV/c)	$\mathrm{D}^0/\mathrm{D}^{*+}$ for 16 GeV/c $< p_{\mathrm{T}} <$ 24 GeV/c
$FONLL$	$2 < p_{\mathrm{T}} < 16$	1.72
$POL0$	$2 < p_{\mathrm{T}} < 16$	2.04
$POL1$	$2 < p_{\mathrm{T}} < 16$	1.12

In a first step, the p_{T} range of the D^0 spectrum was extended to 24 GeV/c, exploiting the fact that the D^{*+} spectrum had been measured with ALICE up to this value of p_{T} [Aam12], and that FONLL calculations [Cac12] predict a certain p_{T}-dependent ratio between the production cross sections of D^0 and D^{*+}.[9] As a correction to the ratio from FONLL predictions, a weighting with the ratio of the integrated measured to the integrated FONLL production cross section of the D^0 meson for 2 GeV/c $< p_{\mathrm{T}} <$ 16 GeV/c was applied. Both the D^0/D^{*+} ratios corresponding to the unweighted and the weighted FONLL cross section are shown in the upper panel of Figure 4.28. To determine the systematic uncertainties of this method, two different linear fits were performed, shown in the lower left and lower

[9] The ratio D^0/D^{*+} was chosen as a reference since it was determined with a higher precision than the ratio D^0/D^+, as can be seen from Figure 4.28.

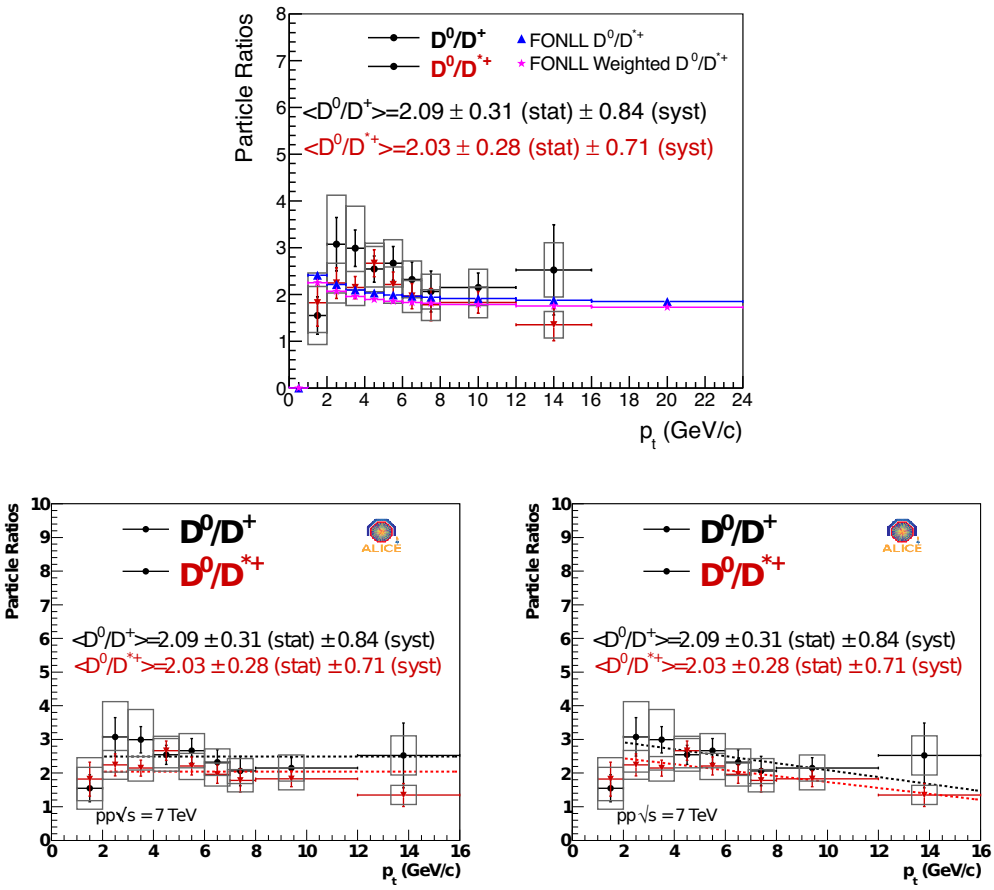

Figure 4.28: Extrapolations of the D^0/D^{*+} ratio up to a p_{T} of 24 GeV/c [Ave12]. Upper panel: based on FONLL; lower panels: alternative extrapolations via two different sets of linear fits for the determination of systematic uncertainties.

right panel of Figure 4.28. The D^0/D^+ ratios resulting from the three different extrapolation methods are listed in Table 4.7.

The spectrum of the D_s meson, measured up to 12 GeV/c, was extrapolated in a similar, albeit more direct way. Here, the D^+ spectrum was multiplied by the ratio of D_s/D^+ measured with ALICE (see Figure 4.29).

An estimate of the p_{T}-differential production cross section of the Λ_c baryon was obtained by multiplying the sum of the ALICE measurements of D^0 and D^+ by the ratio of Λ_c to the sum of D^0 and D^+ measurements by ZEUS [Che05].

In a second step, the extrapolation of the charm-hadron spectra was extended to a transverse momentum of 50 GeV/c. For this purpose, the spectra of D^+ and D^{*+} were fitted in the range 2 GeV/c $< p_{\mathrm{T}} <$ 24 GeV/c as shown in Figure 4.30, using the function

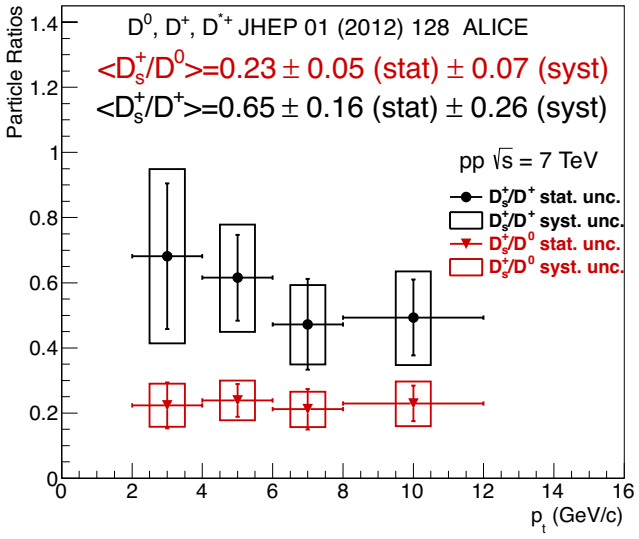

Figure 4.29: D_s/D^+ ratio measured with ALICE (from [Ave12], therein compiled from [Abe12a]).

$$d\sigma/dp_T = p_0 \times p_T/(1 + (p_T/p_1)^{p_3})^{p_2} \quad , \tag{4.7}$$

p_i with $i = 0 - 3$ being parameters of the fit.

The spectra of D^0 and D_s were calculated up to $p_T = 50$ GeV/c based on these fits and the assumption of a constant ratio of their yields to the D^{*+} and D^+ yield, respectively.

Overall Charm-Hadron Decay Electron Spectrum and Weighting of the Simulated Electron Spectrum

After the calculation of the spectra of hadrons containing open charm for the relevant momentum range, the electron spectrum from their decays was determined by means of the decay kinematics simulated via PYTHIA. To achieve this, the yields of D^+, D^0, D_s, and Λ_c were normalized to the calculated quantities discussed above for each hadron and each p_T bin separately. The hadrons were subsequently decayed via PYTHIA simulations, which also provided a correction for the different acceptances of the measurements for D mesons and electrons from $|y_D| = 0.5$ to $|\eta_e| = 0.9$, and the resulting electron yields were finally summed up to an overall charm-hadron decay electron spectrum. Figure 4.31 shows the contributions of single p_T bins for D^0 and D^+ mesons to the electron spectrum, while the summed electron yields for each of the four considered charm hadrons and the overall electron yield from open-charm decays, up to a hadron p_T of 24 GeV/c, are presented in Figure 4.32.

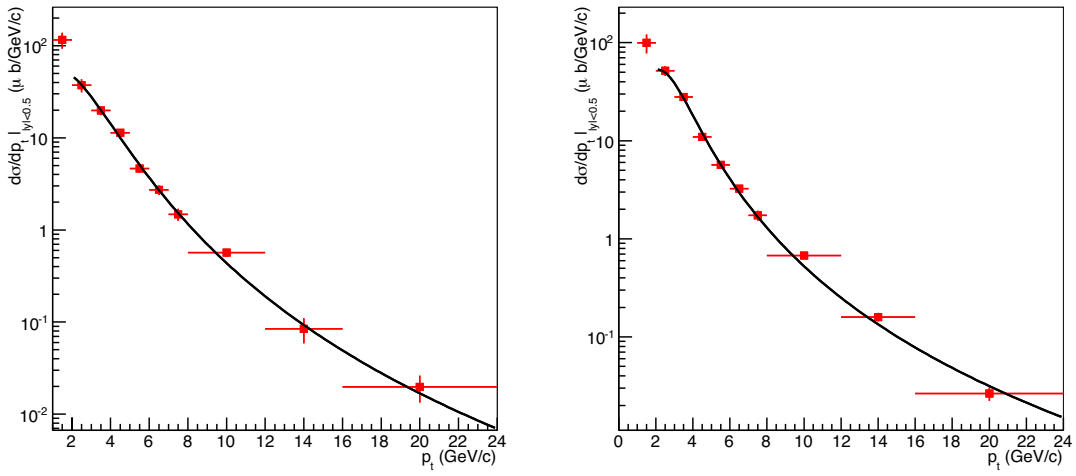

Figure 4.30: Fits to the measured D^+ (left) and D^{*+} spectrum (right). The D^{*+} fit provided the basis for the D^0 extrapolation to a p_{T} of 50 GeV/c [Ave12].

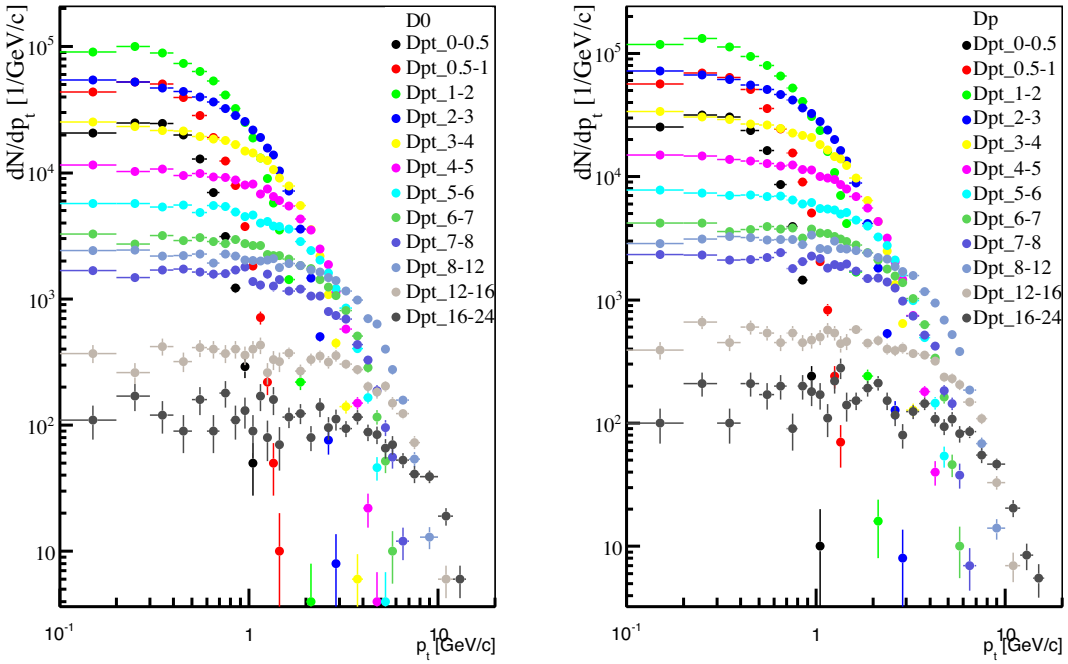

Figure 4.31: Electron spectra from the decays of D^0 (left) and D^+ (right) in given meson-p_{T} bins, obtained via PYTHIA [Ave12].

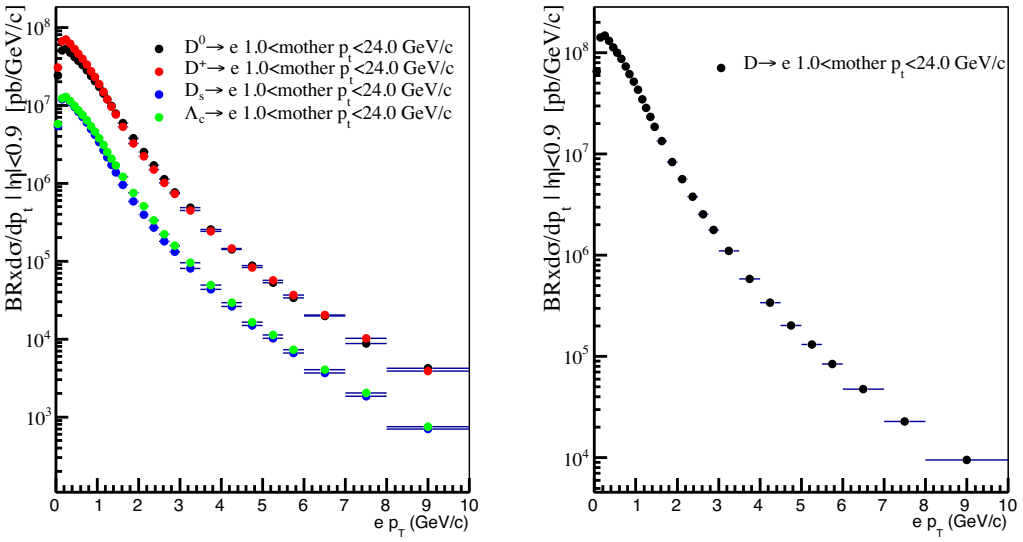

Figure 4.32: Left: p_{T}-differential electron spectra from decays of charm hadrons with $p_{\mathrm{T}} < 24$ GeV/c. Right: overall electron yield from open-charm decays, from the sum of all spectra in the left panel [Ave12].

The inclusion of contributions from decays of charm hadrons with $p_{\mathrm{T}} > 24$ GeV/c, obtained from the extrapolations described above, yields the total spectra of charm-hadron decay electrons, represented in black in Figure 4.33 for both collision energies considered in this analysis. Their ratios to the p_{T} spectra generated by PYTHIA simulations (red) are used as weighting factors by which the simulated charm-decay electron spectra after application of the impact parameter selection criterion are multiplied before being subtracted from the inclusive electron spectra. The weighting factors for $\sqrt{s} = 7$ TeV have been determined using minimum-bias simulations, whose electron spectra from charm decays proved to be significantly harder than those from measurements in ALICE. As a consequence, the ratio between the simulated and the measured spectrum tends to low values with increasing p_{T}. In the case of $\sqrt{s} = 2.76$ TeV, data samples with enhanced production of charm-hadron decays were included (see Section 4.4), which results in a far larger difference between the measured and simulated spectrum. The uncertainties of the measured spectra and of the ratios include statistical and systematic uncertainties, whose calculation will be described in the following section. The description of the electron production from charm decays is limited to transverse momenta above 1 GeV/c in this analysis, since no spectrum of hadrons containing open charm has been measured below this p_{T} value. This restriction also constitutes the main obstacle for an extension of the measurement of beauty-hadron decay electrons to any lower p_{T} than 1 GeV/c.

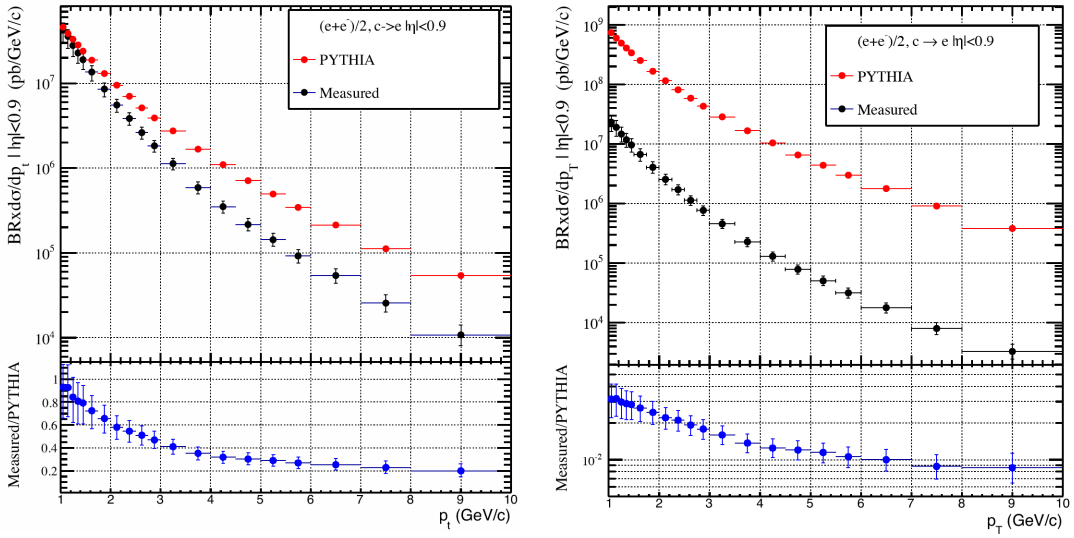

Figure 4.33: Electron spectrum from charm-hadron decays in pp collisions at $\sqrt{s} = 7$ TeV (upper left panel) and at $\sqrt{s} = 2.76$ TeV (upper right panel), estimated from ALICE measurements (black) and PYTHIA simulations (red). The lower panels show the ratios between both, which are used for weighting the PYTHIA-simulated electron spectra from charm-hadron decays [Ave12, Ave13a]. The PYTHIA sample for the analysis at $\sqrt{s} = 2.76$ TeV includes simulations with an enhanced production of charm hadrons.

Statistical and Systematic Uncertainties

Statistical and systematic uncertainties were propagated from the measured and extrapolated hadron spectra to the resulting electron spectrum in different ways. Since statistical uncertainties are uncorrelated for different hadrons or hadron p_{T} bins, their contributions were added quadratically for a given electron p_{T} bin. Systematic uncertainties from different hadron p_{T} bins, however, were considered as correlated, and therefore added linearly in each electron p_{T} bin.

Since the D_s spectrum was determined via the ratio D_s/D^+, the quadratic sum of systematic and statistical uncertainties of this ratio was added to the overall systematic uncertainty. Moreover, a conservative estimate of the systematic uncertainties arising from the Λ_c spectrum was given by varying the ratio $\Lambda_c/(D^+ + D^0)$ by a factor of $1/2$ and 2 for the lower and upper limits, respectively. In a similar way, the systematic uncertainties from the extrapolated hadron spectra above 24 GeV/c were determined by varying their overall production cross section by factors of $1/2$ and 2, comparing it to a FONLL-based extrapolation of the measured electron spectrum from D-meson decays, which is in good agreement with the extrapolation performed in this analysis. Figure 4.34 shows the varied electron spectra along with the FONLL

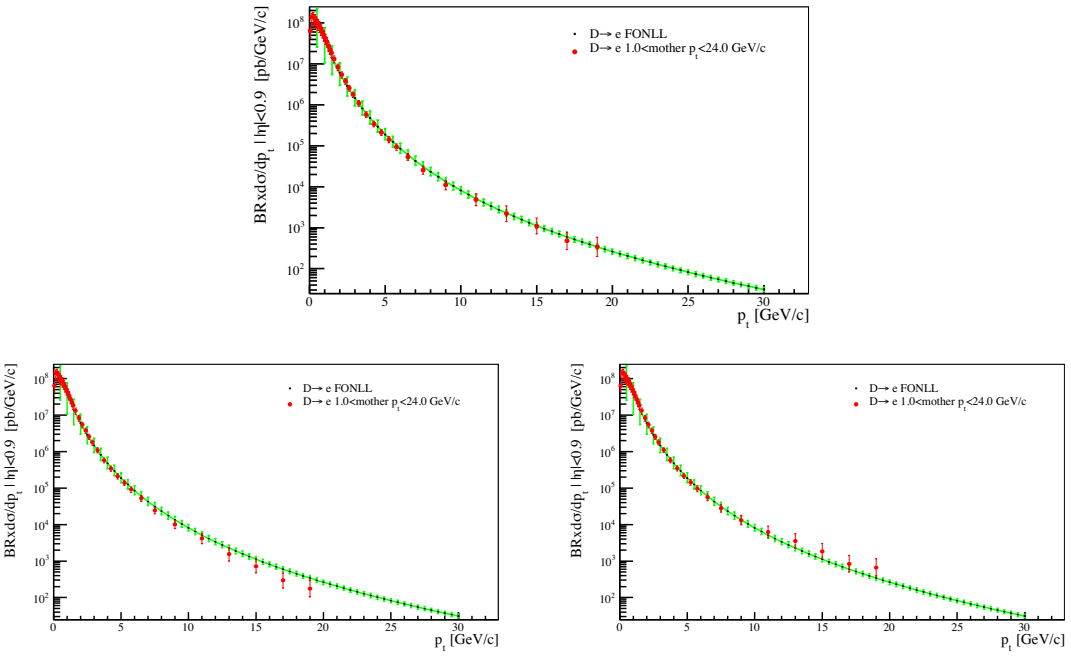

Figure 4.34: Upper panel: comparison of the p_{T}-differential electron spectrum including the contribution from decays of D mesons with 24 GeV/c $< p_{\mathrm{T}} <$ 50 GeV/c to a FONLL prediction. Lower panels: electron spectra from variation of the extrapolated D-meson contribution by a factor of 1/2 (left) and 2 (right). The systematic uncertainties are determined by the variations of these spectra from the FONLL prediction [Ave12].

extrapolation. The systematic uncertainties were calculated as the deviations of the varied extrapolated spectra from the values predicted by FONLL calculations.

In addition to the contributions described above, the systematic uncertainties of the charm-hadron decay electron spectrum at $\sqrt{s} = 2.76$ TeV also account for an additional uncertainty from the FONLL scaling of the spectrum, which is determined by varying the charm-quark mass and the perturbative scales [Ave11b].

Just like the uncertainties of the electron background from light-meson decays, the uncertainties of the charm-decay electron spectrum were propagated to the final spectrum of beauty-decay electrons. Figure 4.35 shows the resulting systematic uncertainties on the final spectrum for $\sqrt{s} = 7$ TeV (upper panels) and $\sqrt{s} = 2.76$ TeV (middle and lower panels).

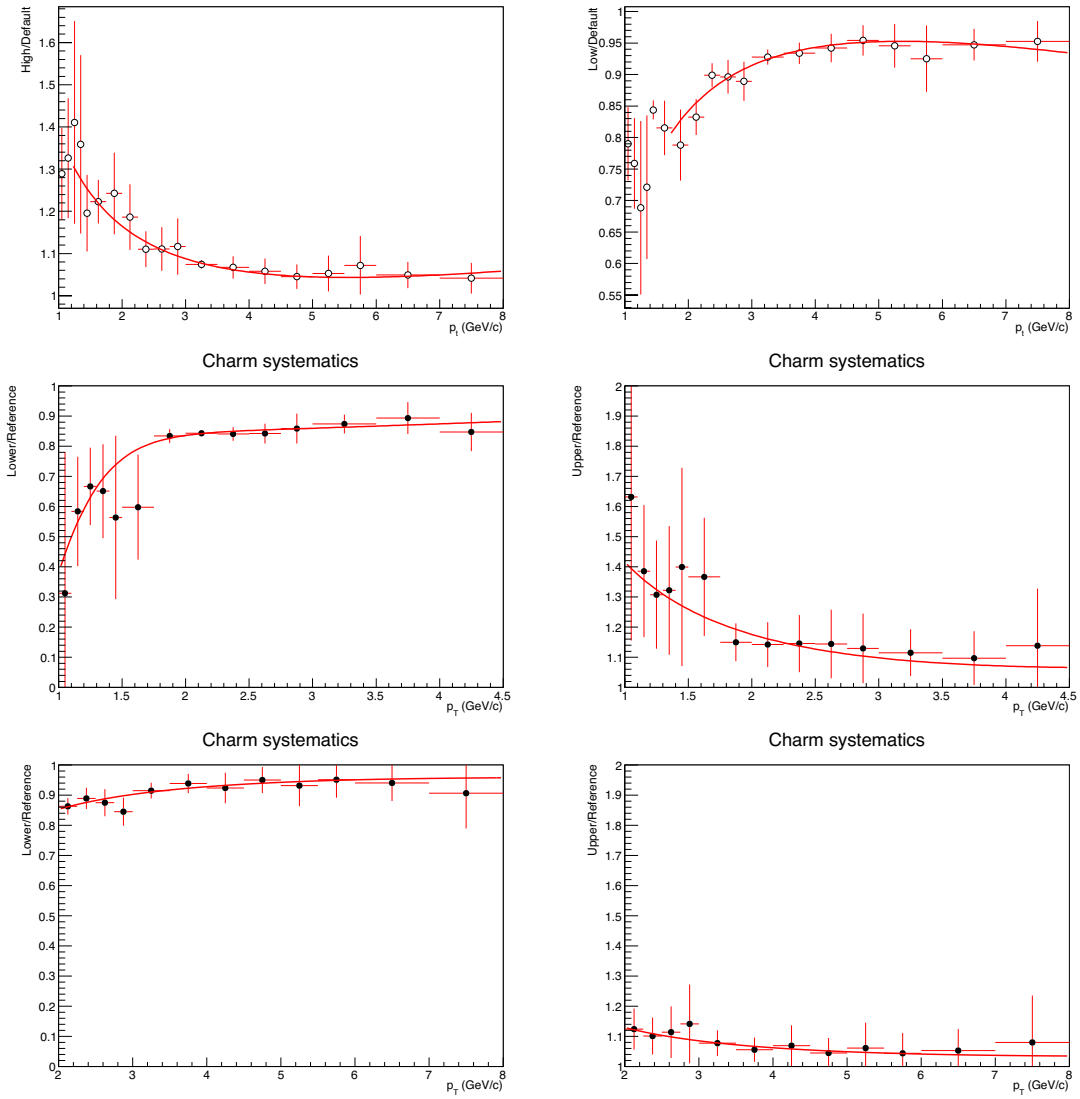

Figure 4.35: Ratio of the production cross section for electrons from beauty-hadron decays, $H_b \rightarrow e$, obtained by the upper (left panels) and lower uncertainty limit (right panels) of the electron background from charm-hadron decays. The deviations from unity are added as relative systematic uncertainties to the $H_b \rightarrow e$ spectrum. The upper panels show the ratios for pp collisions at $\sqrt{s} = 7$ TeV [Ave12], while the middle and lower panels present the ratios for $\sqrt{s} = 2.76$ TeV [Ave13a] for the analysis using TPC and TOF PID and for TPC-only PID, respectively.

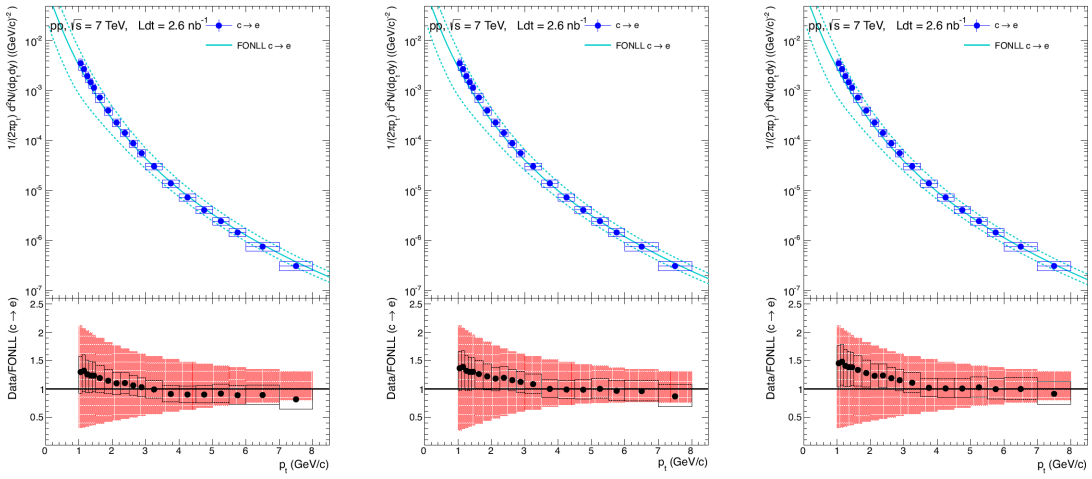

Figure 4.36: Comparison between the p_{T}-differential electron production cross section from hadrons containing open charm, H_c, for pp collisions at $\sqrt{s} = 7$ TeV and FONLL predictions under the assumption of an $H_c \rightarrow e$ branching ratio of 10.3% (left, value given by PDG in 2004 [Eid04]), 9.6% (middle, PDG 2012 [Beh12]), and 9.2% (right, lower uncertainty limit from PDG 2012). Plots from [Ave12].

Comparison of the Electron Spectrum from Charm-Hadron Decays with FONLL Predictions

As a result of the evaluations described in the previous sections, the electron production cross section from charm-hadron decays is shown in the upper panels of Figure 4.36, where the sum of statistical and systematic uncertainties is represented by error boxes. The cross section is compared to predictions from FONLL calculations (plotted as smooth light-blue lines, with dashed lines indicating the corresponding uncertainties) assuming three different branching ratios of open-charm hadrons H_c to electrons. These correspond to the values of 10.3% (left panel), given by the Particle Data Group in the year 2004 [Eid04], a branching ratio of 9.6% (middle), which is the current best estimate, published in 2012 [Beh12], and the current lower uncertainty limit of 9.2% (right). The lower panels depict the ratio of the cross section determined based on measurements to the predicted cross sections. Error boxes represent the overall uncertainties of the measurement-based result, while the red bands around unity describe the uncertainties of the FONLL calculations, which do not include uncertainties of the $H_c \rightarrow e$ branching ratio. The clearly visible variations between the ratio of the measured to the FONLL cross sections demonstrate the significance which the underlying assumption for the semi-electronic branching ratio has for such comparisons. However, under all of the three assumptions, FONLL calculations describe the measured spectrum within uncertainties. The same holds true for the charm-decay electron spectrum for pp collisions at $\sqrt{s} = 2.76$, shown

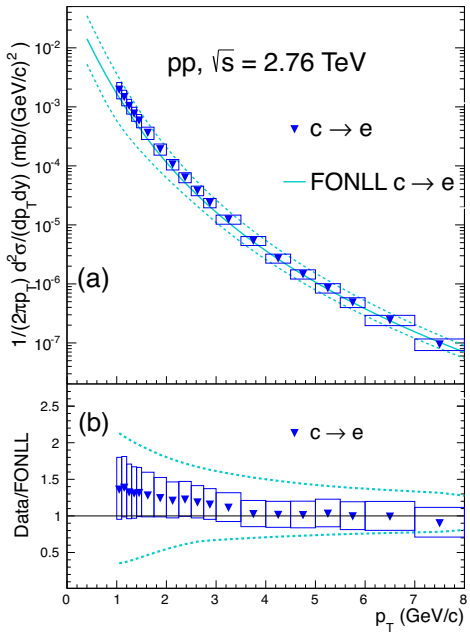

Figure 4.37: Electron spectrum from charm-hadron decays for pp collisions at $\sqrt{s} = 2.76$ TeV, obtained by FONLL-scaling from the spectrum shown in Figure 4.36, in comparison with FONLL calculation [Ave13a].

in Figure 4.37, which was derived from the spectrum at $\sqrt{s} = 7$ TeV by FONLL scaling.

4.8.3 Background Subtraction

For the electron background spectra described in Sections 4.8.1 and 4.8.2, the remaining fractions after the impact parameter requirement were estimated by GEANT simulations (see Section 4.6). By combining this information with the measurement-based weighting of the spectra that were generated in simulations, an estimate of the contribution of each electron source to the overall electron spectrum after the impact parameter selection can be given, as shown in Figure 4.38. While the weighting factors for the background from light-meson decays, which were determined according to the abundances of the decaying mesons, are directly applied to the reconstructed simulated tracks, the procedure for the background from charm decays is slightly different: here, the weighting is performed on the overall electron spectrum from charm decays, based on particle productions that were measured or generated in PYTHIA simulations, without consideration of p_{T} smearing caused by reconstruction and the effects of bremsstrahlung. Therefore, the charm-decay background spectrum is folded with a correlation map relating reconstructed electron momenta

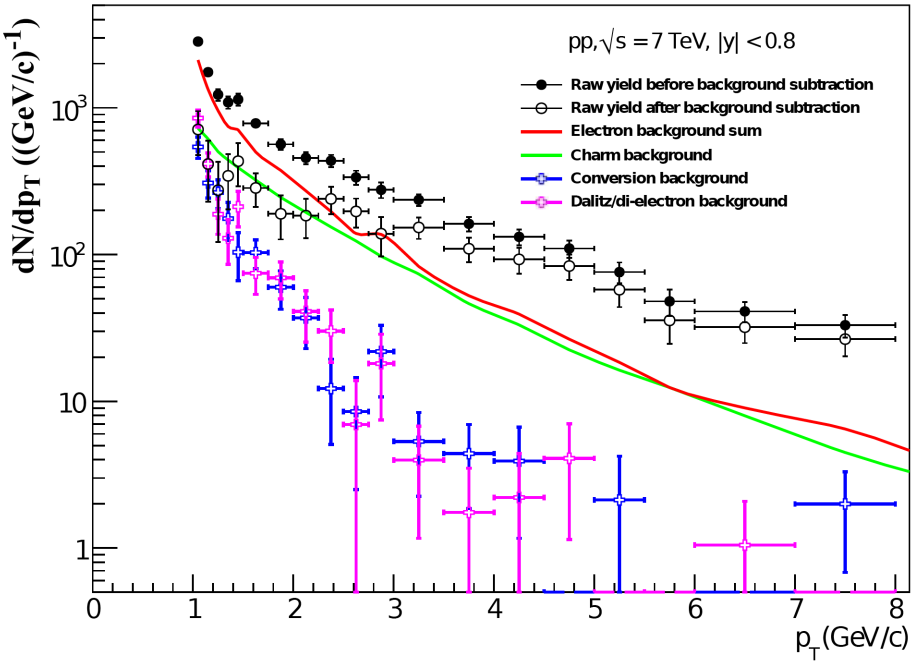

Figure 4.38: Electron yields from signal and background sources after the impact parameter requirement for $\sqrt{s} = 7$ TeV (adapted from [Ave12], upper panel) and for $\sqrt{s} = 2.76$ TeV [Ave13a], in the analysis using TPC and TOF PID (lower left) and using TPC PID only (lower right).

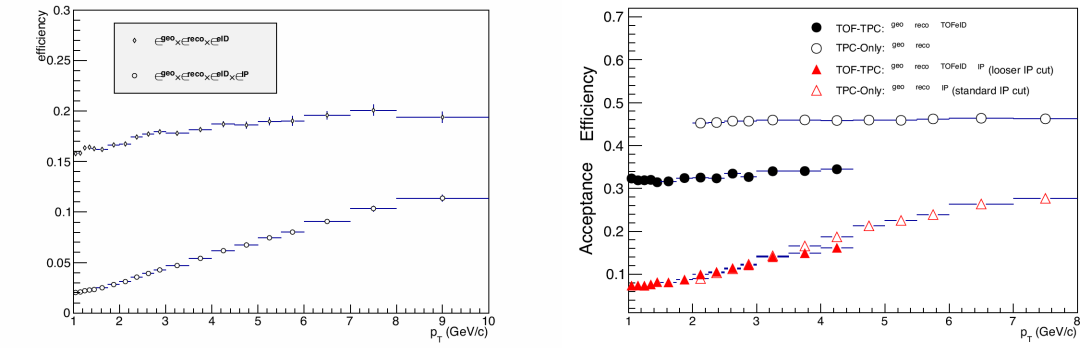

Figure 4.39: Selection efficiency for electrons from beauty-hadron decays, given by acceptance, tracking, particle identification, and impact parameter at mid-rapidity ($|\eta| < 0.8$) in pp collisions at $\sqrt{s} = 7$ TeV [Ave12] (left) and 2.76 TeV [Ave13a] (right). The plot for $\sqrt{s} = 2.76$ TeV does not include the efficiency of the TPC particle identification, which is at a constant value of 70% for the analysis using TPC PID only and of 85% for the combination of TPC and TOF PID.

to those generated by PYTHIA.

The electron background from charm decays, light-meson decays, and photon conversions shown in Figure 4.38 was subtracted from the overall electron spectrum, revealing a raw spectrum of electrons originating from beauty-hadron decays, represented by open circles. From Figure 4.38, it becomes obvious that, even after the impact parameter requirement, the electron spectrum is dominated by background at low momenta, with a charm contribution that exceeds the signal for $p_{\mathrm{T}} \lesssim 2$ GeV/c and an amount of conversion and light-flavour decay electrons that becomes the most important component for the lowest accessible p_{T} bins. As a result, the statistical uncertainties, determined as the quadratical sum of the statistical uncertainties of the overall electron yield and the subtracted background electron yields, increase substantially for low p_{T} as compared to intermediate p_{T} bins. The same is true for the propagated systematic uncertainties, which scale with the ratio of signal to background (see Figures 4.26 and 4.35), so that background-related uncertainties are expected to dominate at low p_{T}, whereas they play only a minor role towards higher transverse momenta (cf. Section 4.10).

4.9 Corrections and Normalization

The total p_{T}-dependent yield of electrons from beauty-hadron decays was obtained via corrections of the measured raw yield after background subtraction for the geometrical detector acceptance ϵ^{geo} and the efficiencies of the track reconstruction ϵ^{reco}, the electron identification ϵ^{eID}, and the impact parameter requirement ϵ^{IP}.

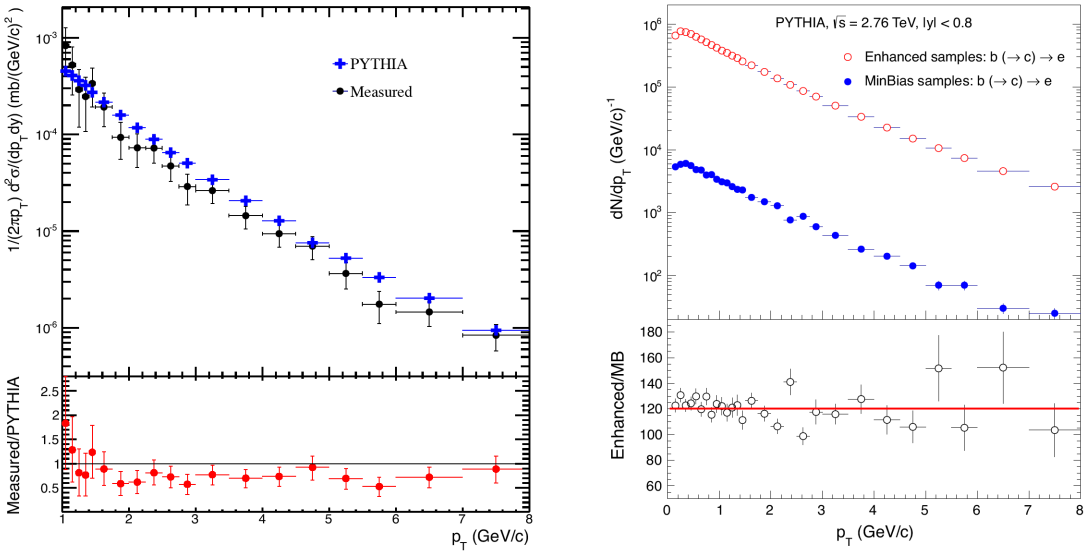

Figure 4.40: Left: p_{T}-differential invariant cross section of electrons from beauty-hadron decays in minimum-bias simulations and ALICE measurements at $\sqrt{s} = 7$ TeV (upper panel), and ratio of both (lower panel) [Ave12]. Right: p_{T}-dependent electron spectra from beauty-hadron decays in minimum-bias and signal-enhanced simulations (upper panel), and ratio of both (lower panel) for $\sqrt{s} = 2.76$ TeV [Ave13a].

A full Monte Carlo simulation of ALICE was employed for the calculation of geometrical acceptance and reconstruction efficiency, including the simulation of pp collisions with the PYTHIA 6.4.21 event generator [Sjo06] using the Perugia-0 parameter tuning [Ska09], and the propagation of generated particles through the detector with GEANT3 [Bru94, Goo95]. The primary vertex distributions of the simulations were the same as in the experiment, and the reconstruction algorithms and selection criteria were identical to those used on experimental data.

The p_{T} distribution of the reconstructed spectrum is distorted by effects of finite momentum resolution and bremsstrahlung. In a correction step contrary to the one described for the p_{T} smearing of the charm background in the previous section, this distortion is corrected by an unfolding procedure in which the reconstructed p_{T} distribution is multiplied with an efficiency map considering the ratio between reconstructed and simulated p_{T}. The validity of this method depends on a good agreement between the p_{T} shapes of the spectra in simulations and experiment, most critically for the large bin widths at high p_{T}. The right panel of Figure 4.40 shows on the example of pp collisions at $\sqrt{s} = 2.76$ TeV that the signal-enhanced simulated data samples used for unfolding in this analysis have a very similar slope to that of minimum-bias samples. These, in turn, proved to represent well the p_{T} dependence of the electron spectrum from beauty-hadron decays found in this

analysis (cf. left panel of Figure 4.40).

Figure 4.39 shows the p_{T}-dependent overall efficiency $\epsilon^{\mathrm{geo}} \times \epsilon^{\mathrm{reco}} \times \epsilon^{\mathrm{eID}} \times \epsilon^{\mathrm{IP}}$ for $\sqrt{s} = 7$ TeV (left) and 2.76 TeV (right), as well as the efficiencies without the factor ϵ^{IP} from the impact parameter requirement. For the case of $\sqrt{s} = 2.76$ TeV, the different sets of requirements for the analysis using TPC and TOF PID, at $p_{\mathrm{T}} < 2$ GeV/c, and for TPC-only PID, at $p_{\mathrm{T}} > 2$ GeV/c, are considered. As a comparison, the efficiency of the former is shown up to 4 GeV/c, where it exhibits a behaviour comparable to that of the TPC-only analysis.

Taking into account these correction factors and the normalization to differentials of rapidity y and transverse momentum, as well as to the number N_{MB} of minimum-bias events, the differential invariant yield of beauty-hadron decay electrons $\frac{e^+ + e^-}{2}$ can be calculated as

$$\frac{1}{2\pi p_{\mathrm{T}}} \frac{\mathrm{d}^2 N^{e^\pm}}{\mathrm{d}p_{\mathrm{T}} \mathrm{d}y} = \frac{1}{2} \frac{1}{2\pi p_{\mathrm{T}}^{\mathrm{centre}}} \frac{1}{\Delta y \Delta p_{\mathrm{T}}} \frac{N_{\mathrm{raw}}^{e^\pm}(p_{\mathrm{T}})}{(\epsilon^{\mathrm{geo}} \times \epsilon^{\mathrm{reco}} \times \epsilon^{\mathrm{eID}} \times \epsilon^{\mathrm{IP}})} \frac{1}{N_{\mathrm{MB}}} \quad , \tag{4.8}$$

with the number $N^{e^\pm}$ of electrons, normalized to $\frac{e^+ + e^-}{2}$, the sum $N_{\mathrm{raw}}^{e^\pm}(p_{\mathrm{T}})$ of measured electrons and positrons in a given p_{T} bin, the central value $p_{\mathrm{T}}^{\mathrm{centre}}$ and the width Δp_{T} of the same bin, and the rapidity interval $\Delta y = 1.6$ of this measurement. From this expression, the differential invariant production cross sections for $\sqrt{s} = 7$ TeV and 2.76 TeV can be inferred immediately via multiplication by the minimum-bias cross sections σ_{MB} for pp collisions at the corresponding centre-of-mass energy, given in Table 4.8. The σ_{MB} values were determined via the V0AND trigger cross sections σ_{V0AND} for both collision energies, measured in van der Meer scans [Abe13b, Mee68]. In doing so, one exploits the fact that the ratios $\sigma_{\mathrm{VOAND}}/\sigma_{\mathrm{MB}}$, corresponding to the ratios of the V0AND and the minimum-bias trigger efficiencies, equal 0.873 and 0.861 for $\sqrt{s} = 7$ TeV and 2.76 TeV, respectively. Variations of these ratios are only of 1% within the considered data samples. The V0AND trigger condition is a coincident signal in both V0 detectors (see Section 3.2). The uncertainties to the σ_{V0AND} values given in Table 4.8 arise from uncertainties concerning the bunch intensities and the beam profiles measured in the van der Meer scans [Abe13b, Ali11].

Table 4.8: Results from van der Meer scans used for the determination of the pp collision cross sections [Abe13b].

$\sqrt{s}$ (TeV)	σ_{V0AND} (mb)	$\sigma_{\mathrm{VOAND}}/\sigma_{\mathrm{MB}}$	σ_{MB} (mb)
7	54.3 ± 1.9	0.8727 ± 0.0001	62.2 ± 2.2
2.76	47.7 ± 0.9	0.8613 ± 0.0006	55.4 ± 1.0

4.10 Systematic Uncertainties

Most of the track reconstruction steps, electron identification criteria, and requirements on the impact parameter give rise to non-negligible uncertainties to the electron production cross section from beauty-hadron decays. In order to quantify these uncertainties, the analysis was performed on the same data sets with requirements deviating from the criteria chosen as a standard. The relative deviations from unity that were consequently produced in the ratio between the fully corrected beauty-hadron decay electron spectrum applying the varied criterion and the standard criterion were considered as the respective systematic uncertainties.

Sources of systematic uncertainties taken into account for this procedure are the efficiencies of the ITS, TPC, and TOF tracking, of the particle identification with TPC and TOF, and of the impact parameter selection. Further uncertainties originate from the unfolding of the p_{T} distribution and the absolute normalization. The variations of the criteria applied to define the systematic uncertainties related to each of them are summarized in Table 4.9. The estimation of the systematic uncertainties from hadron contamination and from electron background sources has been described in Sections 4.7 and 4.8. An additional uncertainty of 2% was attributed to the track matching between ITS and TPC, as a result of dedicated analyses [Otw]. From the relative difference between the unfolded spectra resulting from a Bayesian unfolding procedure on the one hand and from the unfolding via multiplication by the ratio of simulated to reconstructed p_{T} spectra, the standard method in this analysis, on the other hand, the unfolding uncertainty was estimated to be of 5% for $\sqrt{s} = 7$ TeV. For the analysis at $\sqrt{s} = 2.76$ TeV, the influence of the unfolding method, and thus the related systematic uncertainty, was negligible. Systematic uncertainties due to variations for different signs in charge and η were attributed based on the relative difference between the fully corrected p_{T} spectra of positrons and electrons, and of tracks for $\eta > 0$ and $\eta < 0$, respectively.

All systematic uncertainties of the analyses at $\sqrt{s} = 7$ TeV and 2.76 TeV are summarized in Table 4.10. The individual contributions are summed quadratically to an overall systematic uncertainty, as shown in Figure 4.41.

Table 4.9: Varied selection requirements for the determination of systematic uncertainties for the analyses at $\sqrt{s} = 7$ TeV and 2.76 TeV [Ave12, Ave13a]. Selection ranges given in terms of σ refer to the corresponding detector resolution, while percentages indicate the PID signal efficiency.

	$\sqrt{s}$ (TeV)	**Loose criterion**	**Reference criterion**	**Tight criterion**
N. of TPC tracking clusters	7	≥ 100	≥ 120	≥ 140
	2.76	≥ 100	≥ 110	≥ 120
N. of TPC PID clusters	7		≥ 80	≥ 100 ≥ 120
	2.76	60	≥ 80	≥ 100 ≥ 120
DCA to primary vertex in xy (z)	7	< 2 cm (< 4 cm)	< 1cm (< 2 cm)	< 0.5 cm (< 1 cm) < 0.3 cm (< 0.5 cm)
	2.76	< 2 cm (< 4 cm)	< 1cm (< 2 cm)	< 0.5 cm (< 1 cm) < 0.3 cm (< 0.5 cm)
N. of ITS hits	7	≥ 3	≥ 4	≥ 5
	2.76	≥ 2	≥ 3	≥ 4
TOF deviation from e hypothesis	7	$\leq 4\ \sigma$	$\leq 3\ \sigma$	$\leq 2\ \sigma$
(for TPC-TOF PID)	2.76	$\leq 4\ \sigma$	$\leq 3\ \sigma$	$\leq 2\ \sigma$
TPC dE/dx	7	$-0.254 < \sigma < 3$ (60%) $-0.126 < \sigma < 3$ (55%)	$0 < \sigma < 3$ (50%)	$0.126 < \sigma < 3$ (45%) $0.254 < \sigma < 3$ (40%)
(for TPC-TOF PID)	2.76	$-1.289 < \sigma < 3$ (90%)	$-1.042 < \sigma < 3$ (85%)	$-0.847 < \sigma < 3$ (80%) $-0.679 < \sigma < 3$ (75%) $-0.528 < \sigma < 3$ (70%) $-0.389 < \sigma < 3$ (65%)
(for TPC-only PID)	2.76	$-0.847 < \sigma < 3$ (80%) $-0.679 < \sigma < 3$ (75%)	$-0.528 < \sigma < 3$ (70%)	$-0.389 < \sigma < 3$ (65%) $-0.257 < \sigma < 3$ (60%)
Minimal impact parameter d_0	7	$0.0044 + 0.078 \times e^{-0.56 \times p_{\mathrm{T}}}$	$0.0064 + 0.078 \times e^{-0.56 \times p_{\mathrm{T}}}$	$0.013 + 0.077 \times e^{-0.65 \times p_{\mathrm{T}}}$
(for TPC-TOF PID)	2.76	$0.0054 + 0.050 \times e^{-0.66 \times p_{\mathrm{T}}}$	$0.0064 + 0.048 \times e^{-0.56 \times p_{\mathrm{T}}}$	$0.012 + 0.088 \times e^{-0.65 \times p_{\mathrm{T}}}$
(for TPC-only PID)	2.76	$0.0054 + 0.057 \times e^{-0.66 \times p_{\mathrm{T}}}$	$0.0054 + 0.078 \times e^{-0.56 \times p_{\mathrm{T}}}$	$0.012 + 0.088 \times e^{-0.65 \times p_{\mathrm{T}}}$

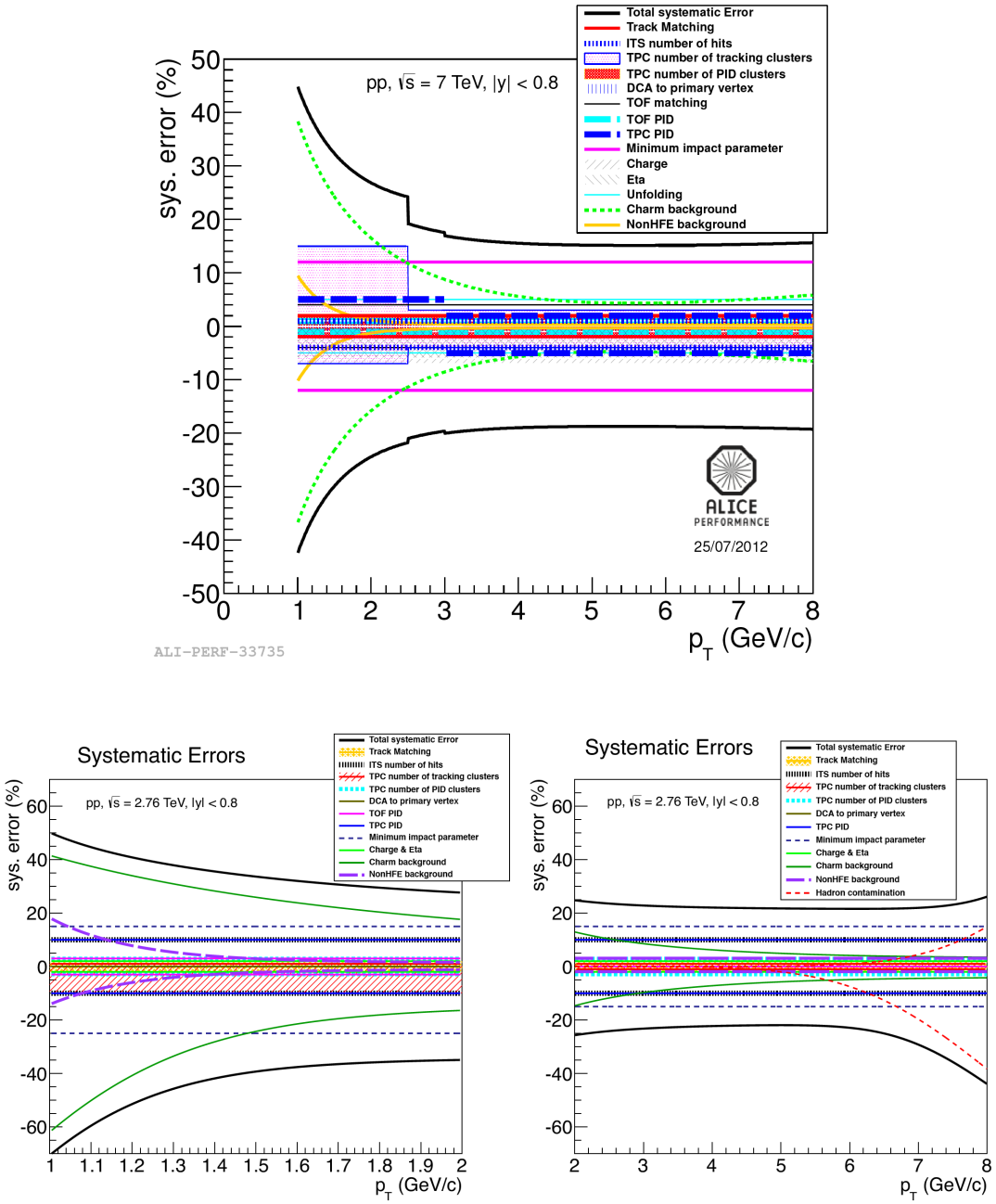

Figure 4.41: Relative systematic uncertainties to the electron spectrum from beauty-hadron decays at $\sqrt{s} = 7$ TeV (upper panel) [Kwe], and at $\sqrt{s} = 2.76$ TeV [Ave13a], for the analysis using TPC-TOF PID (left) and TPC-only PID (right).

Table 4.10: Contributions to the systematic uncertainties [Ave12, Ave13a].

$\sqrt{s}$ (TeV)	**7**	**2.76**	
p_{T} **range** (GeV/c)	**1 − 8**	**1 − 2**	**2 − 8**
	Systematic uncertainty [%]		
ITS-TPC track matching	±2		
N. of ITS hits	+1, -4	±10	
N. of TPC tracking clusters	$p_{\mathrm{T}} < 2.5$ GeV/c: +15, -7 $p_{\mathrm{T}} > 2.5$ GeV/c: +3, -4	+1, -10	±1
N. of TPC PID clusters	±2	±3	
DCA to primary vertex	±1	negligible	
TOF matching	±4	negligible	
TOF PID	±1	±3	–
TPC PID	$p_{\mathrm{T}} < 3$ GeV/c: +5 $p_{\mathrm{T}} > 3$ GeV/c: +2, -5	±10	
Hadron contamination	negligible		see Section 4.7
Impact parameter selection	±12	+15, -25	±15
η **and charge**	η: -6; charge: +1, -7	±2	
Unfolding	±5	negligible	
Light-meson decay electron background	see Subsection 4.8.1		+3, -2
Charm-decay electron background	see Subsection 4.8.2		

5 The Production Cross Section of Electrons from Beauty-Hadron Decays

5.1 p_{T}-Differential Cross Section at $\sqrt{s} = 7$ TeV

The fully corrected and normalized production cross section of electrons from beauty-hadron decays ($H_b \to e$) at $\sqrt{s} = 7$ TeV is shown in panel a) of Figure 5.1. Within uncertainties, the measured and predicted cross section agree throughout the measured p_{T} range from 1 to 8 GeV/c. For comparison, the electron production cross section and corresponding FONLL prediction for charm-hadron decays ($H_c \to e$), already shown in the left panel of Figure 4.38, are drawn in panel a). The ratios between measured and predicted values for electrons from beauty and charm decays are presented in panels b) and c). While the uncertainties of the FONLL predictions for beauty-decay electrons are of the order of 20-40%, predictions for their charm-decay counterparts become much less precise towards low p_{T}. Panel d) shows the p_{T}-dependent ratio between the $H_b \to e$ and $H_c \to e$ cross section for the measured results and the central values of the FONLL predictions. A rise of this ratio towards high p_{T} is visible in both, and the predicted values agree with the measured ones within the uncertainties of the measurements. Since the FONLL values have been obtained directly from the ones given in panels a) and b), no uncertainties to their ratio can be given by the author of this thesis. Such information would have to be determined from dedicated calculations, disentangling correlated and uncorrelated uncertainties of the predictions for beauty and charm decays. In measurements as well as in FONLL predictions, beauty decays take over as the most important source of electrons for $p_{\mathrm{T}} \gtrsim 4$ GeV/c.

Comparisons of the measurement presented in this thesis to more recently published results of pQCD calculations are summarized in Figure 5.2. The p_{T}-differential invariant spectra determined by the k_{T}-factorization framework, based on two different models for the unintegrated gluon distribution functions (UGDFs) [Mac13a], and by the GM-VFN scheme [Bol13] (cf. Section 2.2) all describe well the p_{T} shape of the measured spectrum. The large uncertainties of the GM-VFN scheme calculations show a considerable increase towards the lowest measured p_{T}, where the authors of the paper chose to consider only measurements at transverse momenta above 1.5 GeV/c. Within these uncertainties, GM-VFNS describes the measurements in a satisfactory manner throughout the presented p_{T} range. The cross sections resulting from the two calculations of the k_{T}-factorization framework show a difference of the

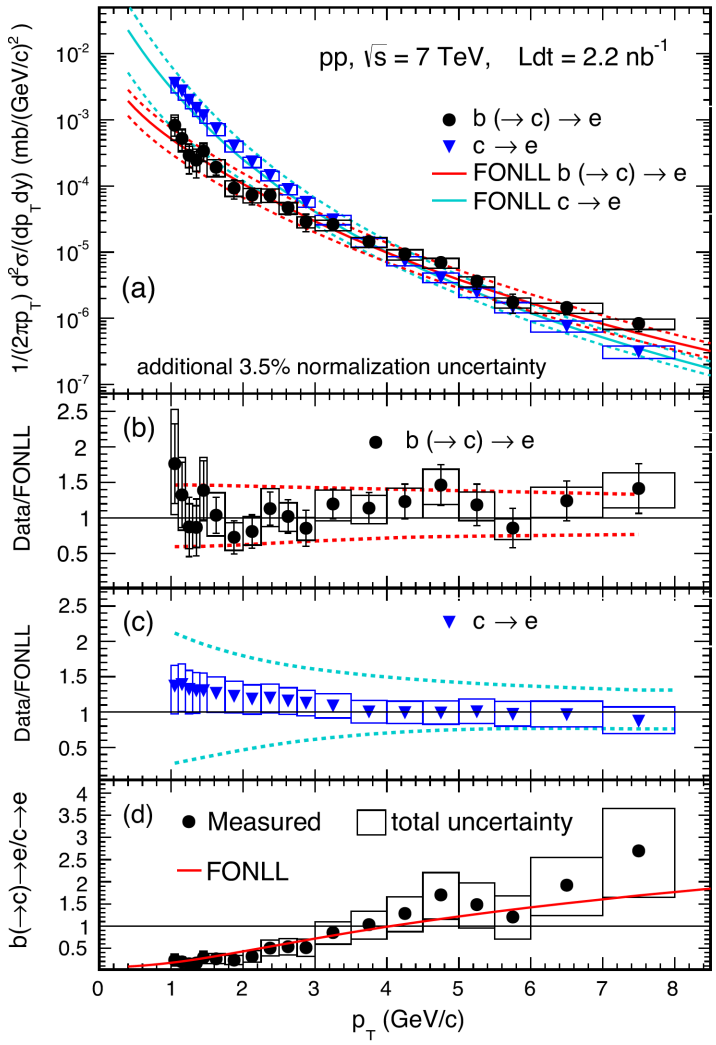

Figure 5.1: Panel a): electron production cross section from beauty (black) and charm decays (blue) with corresponding FONLL predictions (red and light blue, respectively) for pp collisions at $\sqrt{s} = 7$ TeV. Systematic uncertainties are indicated by empty boxes, while statistical uncertainties are represented as thin vertical lines. Predictions by a FONLL pQCD calculation [Cac98, Cac12] are drawn as a smooth red/blue line, with upper and lower uncertainty limits depicted as dashed lines. b) and c): ratio between measured values and FONLL calculation for beauty and charm-decay electrons, respectively. Uncertainties from the FONLL calculations are not included in the error boxes around the data points, but indicated as dashed red/blue lines around unity. Panel d) shows the ratio between the beauty and charm-decay electron cross section, compared to the corresponding ratio resulting from the central values of the FONLL predictions shown in panel a) (adapted from [Ave12]).

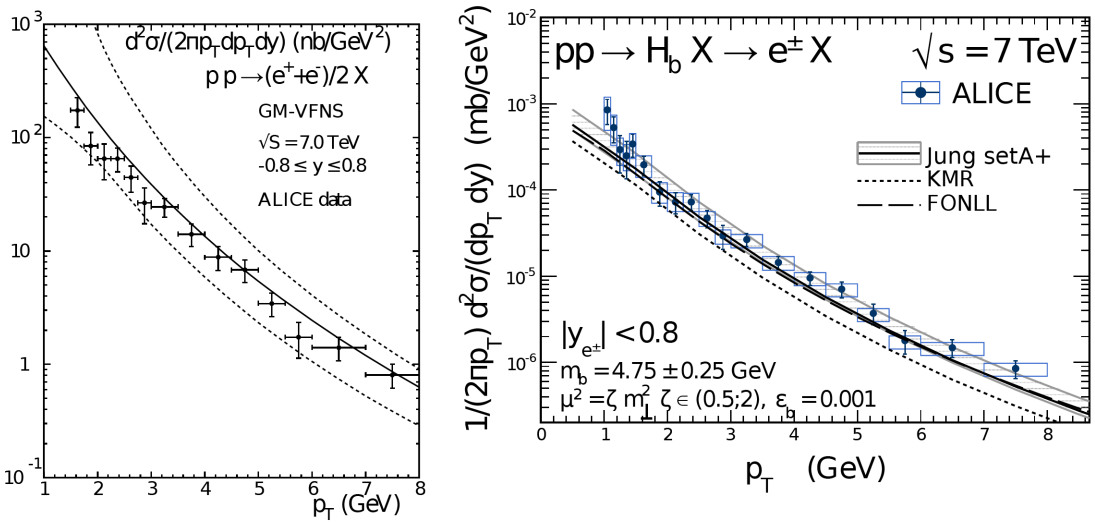

Figure 5.2: Comparison of the result of this analysis for pp collisions at $\sqrt{s} = 7$ TeV to a prediction by the GM-VFN scheme [Bol13] (left, considering measurements for $p_{\mathrm{T}} > 1.5$ GeV/c only) and to calculations from the k_{T}-factorization framework, based on two different models of unintegrated gluon distribution functions, *KMR* and *Jung setA+* [Mac13a] (right). In the right panel, the FONLL prediction is also shown as a reference.

order of 50% over the whole p_{T} range, which is due to the high susceptibility of this method to the choice of the UGDFs. While the *KMR* UGDFs, for which no uncertainties are shown, underestimate the electron yield from beauty-hadron decays, the result based on *Jung setA+* UGDFs almost coincides with the FONLL prediction and gives a good description of the measured spectrum [Mac13a].

As a cross-check for the result of this analysis, an alternative method can be applied to determine the beauty-hadron decay electron spectrum: the charm-decay electron spectrum shown in Figure 4.38 is subtracted from the electron spectrum from inclusive heavy-flavour hadron decays, published in [Abe12g]. By definition, the difference between both should yield the beauty-decay electron spectrum. The result of this subtraction is presented in Figure 5.3, compared to the beauty-electron spectrum obtained via the impact parameter method. The results from both methods are consistent within uncertainties for all considered transverse momenta. From the uncertainties shown in Figure 5.3, it is obvious that the measurement via the impact parameter selection yields clearly more precise results for the whole p_{T} range. This underlines not only the self-consistency of the method chosen in this analysis and the adequacy of the estimates with respect to the charm-electron background (see Section 4.8.2), but also the effectiveness of the impact parameter approach in minimizing the uncertainties and maximizing the signal-to-background ratio.

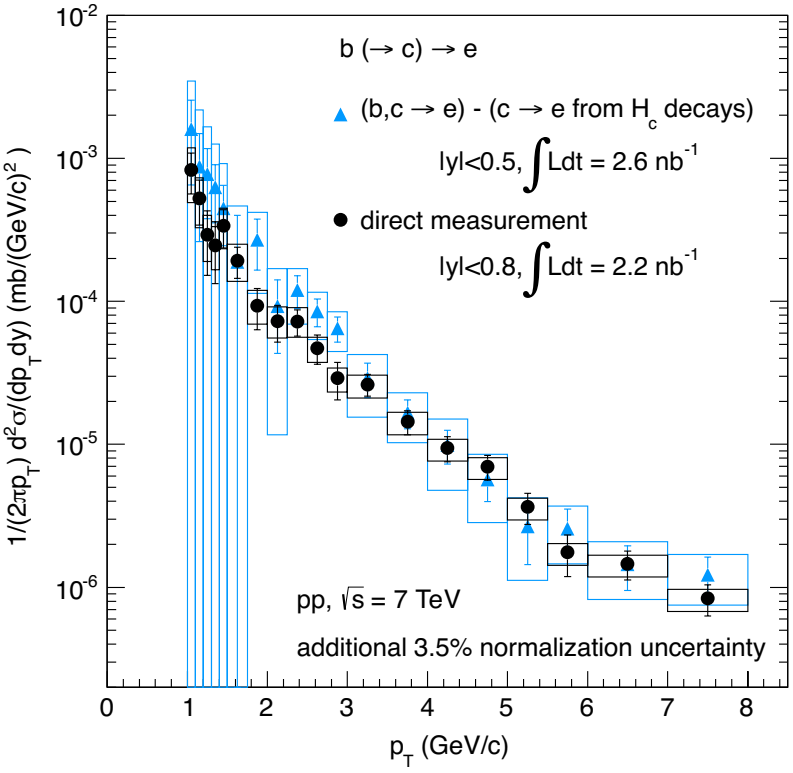

Figure 5.3: Comparison between the results for the beauty-hadron decay electron spectrum at $\sqrt{s} = 7$ TeV determined by subtraction of the charm-decay electron spectrum shown in Figure 4.38 from the inclusive heavy-flavour electron spectrum (light blue) and the corresponding result from the impact parameter approach (black).

5.2 p_{T}-Differential Cross Section at $\sqrt{s} = 2.76$ TeV

In most aspects, the analysis of beauty-hadron decays at $\sqrt{s} = 2.76$ TeV has been performed via a procedure analogous to the one at $\sqrt{s} = 7$ TeV. There are, however, two separate approaches applying different electron identification methods for complementary transverse momentum ranges, and disposing of different amounts of data, as described in Sections 4.4 and 4.7. The results from these two approaches shall therefore be considered separately before combining them to a common spectrum. The left side of Figure 5.4 shows the beauty-hadron decay electron production cross section measured with the TPC-TOF PID approach for the p_{T} range from 1 GeV/c up to 4 GeV/c, while the corresponding result for the analysis using only TPC PID is depicted on the right side of the same figure. The charm-decay electron spectrum and the ratios of the beauty and charm-decay measurements to the respective FONLL predictions, as well as the ratio between the beauty and the

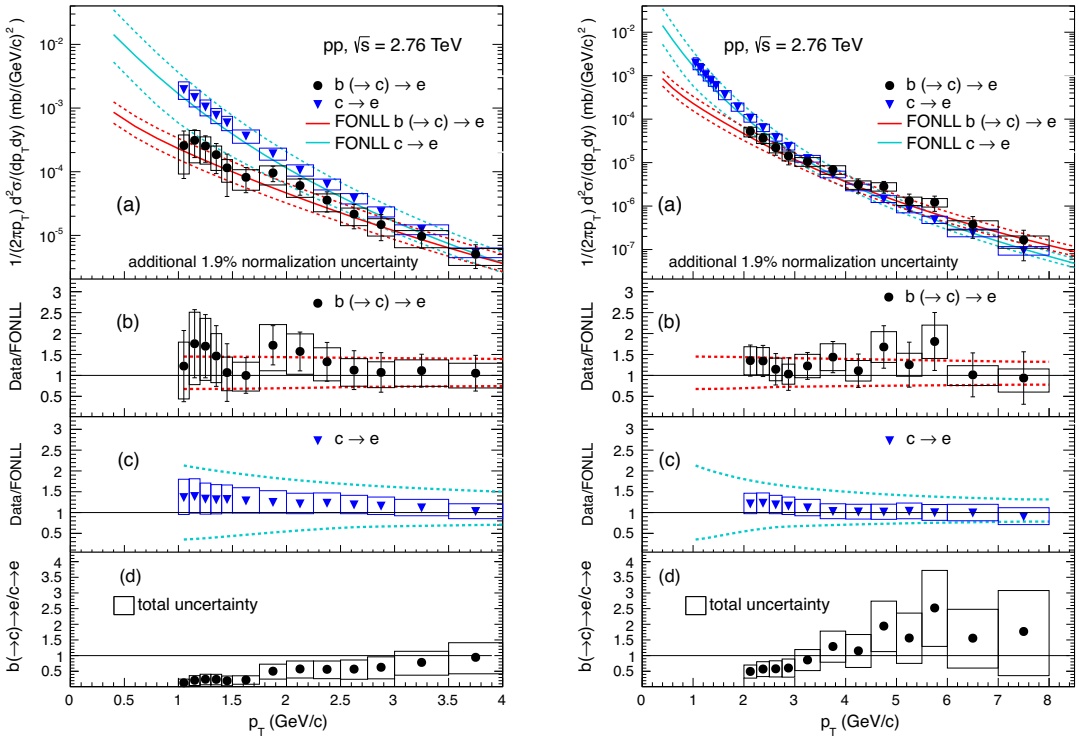

Figure 5.4: Electron production cross section from beauty and charm decays with the corresponding FONLL predictions, represented as in Figure 5.1, for the analysis at $\sqrt{s} = 2.76$ TeV [Ave13a]. The left panel shows the result from the analysis using TPC and TOF PID, while the result from the analysis using TPC-only PID is presented in the right panel. Both are comparable within their common p_{T} range of 2 GeV/c $< p_{\mathrm{T}} <$ 4 GeV/c. Panels b) and c) show the ratio between measured values and FONLL calculation for electrons from beauty and charm decays. Panel d) depicts the ratio between the beauty and charm-decay electron cross section.

charm-electron cross section are presented in the same way as in Figure 5.1 for the $\sqrt{s} = 7$ TeV case. For both methods, and for beauty as well as for charm-decay electrons, FONLL calculations are very well consistent with the results of the measurements. In their overlapping p_{T} region between 2 GeV/c and 4 GeV/c, both results are in good agreement. Since they represent two analyses that have neither been performed on two entirely disjunct data sets nor using completely independent methods, it is not easily possible to combine both measurements to a common result by calculating a weighted average in the p_{T} overlap region. Instead, it was decided to consider only the result obtained with the TPC-only PID method from 2 GeV/c upwards, as its systematic and statistical uncertainties are smaller than those of the complementary result from the TPC-TOF PID approach.

The combined beauty-hadron decay electron cross section, obtained from the

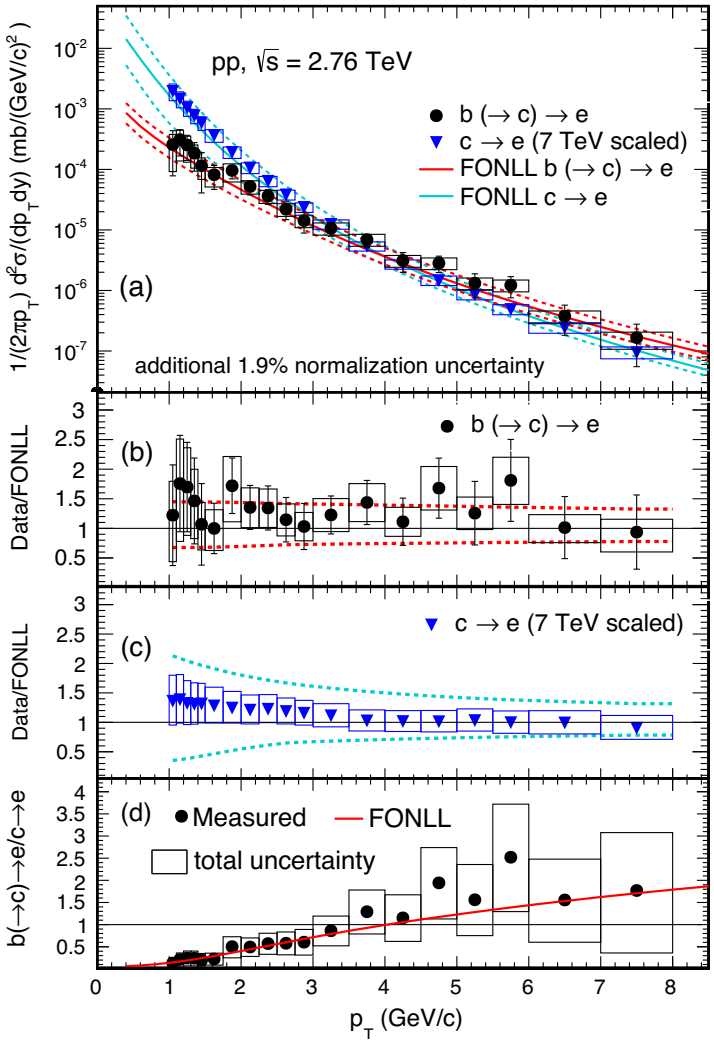

Figure 5.5: p_{T}-differential electron production cross section from beauty-hadron decays for pp collisions at $\sqrt{s} = 2.76$ TeV, combined from both panels of Figure 5.4: for 1 GeV/c < p_{T} < 2 GeV/c, the measurement using TPC and TOF PID was taken into account, while for $p_{\mathrm{T}} > 2$ GeV/c, the results from the analysis using TPC-only PID were used. Panel d) shows a comparison of the ratio between the production cross sections of electrons from beauty and charm decays to the corresponding ratio predicted by FONLL calculations. Figure adapted from [Ave13a].

TPC-TOF PID measurement for 1 GeV/c < p_{T} < 2 GeV/c and from the TPC-only PID measurement for p_{T} > 2 GeV/c is shown in Figure 5.5. From panel d), it is visible that the relative amounts of beauty and charm-decay electrons and their p_{T} dependences are very similar to those at $\sqrt{s}$ = 7 TeV and equally well described by FONLL calculations. Also here, beauty decays become the dominant heavy-flavour electron production process for $p_{\mathrm{T}} \gtrsim 4$ GeV/c.

Like in the case of $\sqrt{s}$ = 7 TeV, further predictions from GM-VFNS and the k_{T}-factorization framework are available for pp collisions at $\sqrt{s}$ = 2.76 TeV [Kra, Mac]. Figure 5.6 gives an overview over the results from all three calculation schemes in comparison with the p_{T}-differential invariant spectrum measured in this analysis, extended up to p_{T} = 10 GeV/c by one further measured point from an analysis of beauty-hadron decays via azimuthal angular electron-hadron correlations [Tho12] (see Section 5.7). While the prediction by the k_{T}-factorization framework agrees with the one from FONLL calculations in its spectral shape and has uncertainties of very similar size, it is shifted to higher values by $\approx$ 20%. The result of the calculation from the GM-VFN scheme has larger uncertainties than either of the two other predictions, especially at low p_{T}, but follows the same p_{T} dependence as the FONLL and k_{T}-factorization spectra. Despite these minor differences, all three calculations agree with the measurements within uncertainties over the whole considered p_{T} range.

Compared to the measurement from the analysis at $\sqrt{s}$ = 7 TeV, the result for $\sqrt{s}$ = 2.76 TeV suffers from much larger statistical and systematic uncertainties. It is, however, desirable to provide as a reference for measurements in Pb-Pb collisions at $\sqrt{s_{\mathrm{NN}}}$ = 2.76 TeV a spectrum that does not introduce overly large a priori uncertainties. One method to achieve this has already been presented in Section 4.8.2, where the electron spectrum from charm decays calculated for $\sqrt{s}$ = 7 TeV was scaled down to an energy of 2.76 TeV according to a FONLL prescription [Ave11b]. The same procedure can now be applied for the cross section of beauty-decay electrons.

Panel a) of Figure 5.7 presents the result of this FONLL scaling procedure in blue, compared to the measured spectrum from Figure 5.5 (black). Panels b) and c) show the ratio of the measured spectrum at $\sqrt{s}$ = 2.76 TeV to the prediction by FONLL calculations and of the scaled spectrum to the same prediction, respectively. The statistical uncertainties of the scaled spectrum are significantly smaller and the systematic uncertainties slightly smaller than those of the measured spectrum. The ratio of both cross sections, drawn in panel d), is consistent with unity within statistical and systematical uncertainties for the whole p_{T} range of the measurement.

The facts that pQCD predictions agree with the measured results for electrons from charm and beauty-hadron decays and that the FONLL scaling procedure provides results that are consistent with the measured ones at $\sqrt{s}$ = 2.76 TeV constitute a remarkable success of these calculation schemes. In contrast, NLO calculations for the production of π^0 and η [Rey11] and of jets [Käh14] at the LHC failed to generate results that agree with ALICE measurements for all considered collision energies to

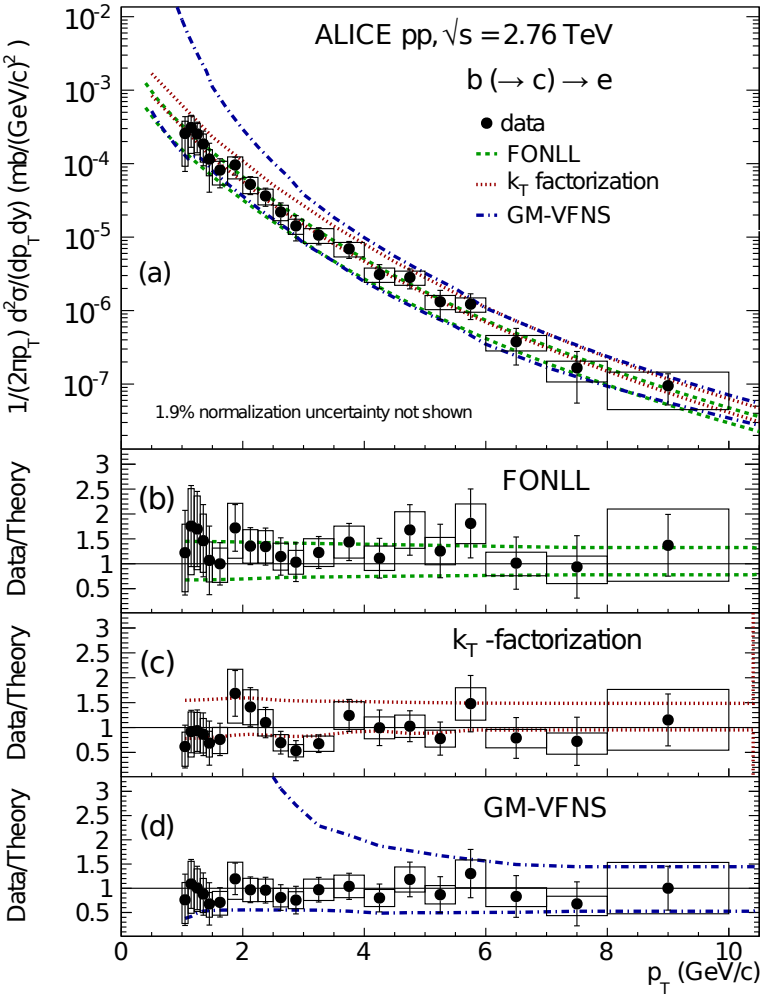

Figure 5.6: The measured p_{T}-differential production cross section of electrons from beauty-hadron decays, compared to different pQCD predictions [Abe14a]. Panel a) shows the measured cross section (black) along with predictions from the FONLL (green), k_{T}-factorization (red), and GM-VFN scheme (blue), whose upper and lower limits are represented by dashed bands. The ratios between the measured spectrum and the central values of the three predictions are shown in panels b), c), and d), respectively.

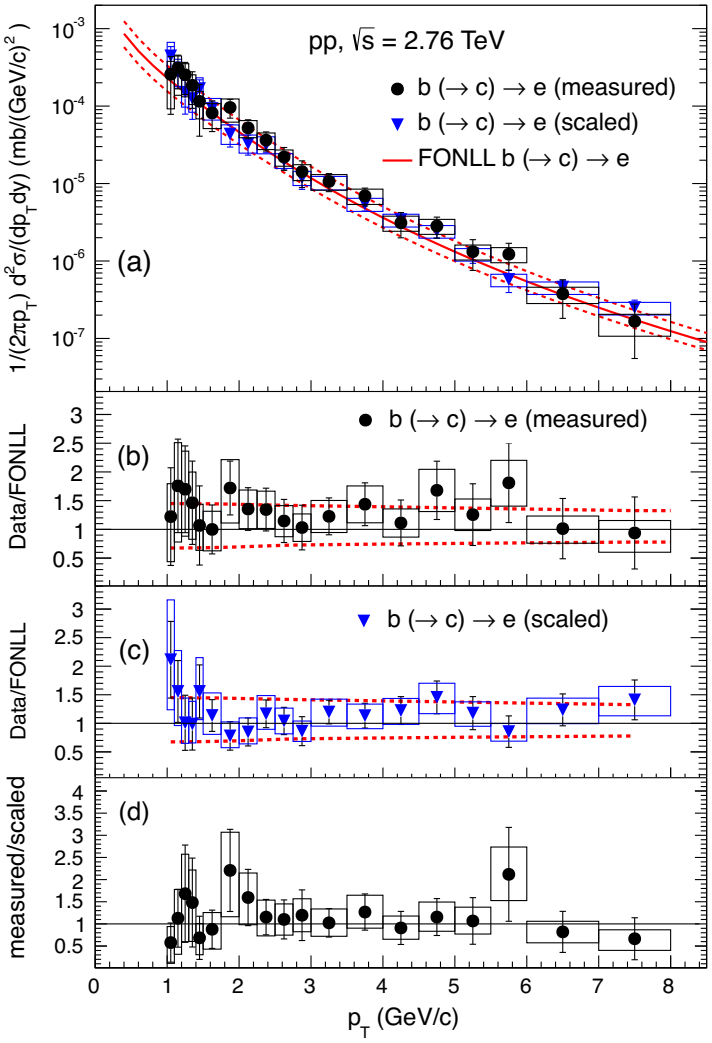

Figure 5.7: Panel a): $H_b \rightarrow e$ production cross sections from measurements at $\sqrt{s} = 2.76$ TeV (black) and scaled from the result at $\sqrt{s} = 7$ TeV using a FONLL prescription (black), compared to FONLL calculations (smooth/dashed red lines). Panel b) shows the p_{T}-dependent ratio of the measured, panel c) that of the scaled spectrum to the FONLL predictions. The ratio between measured and scaled cross section is given in panel d) [Ave13a].

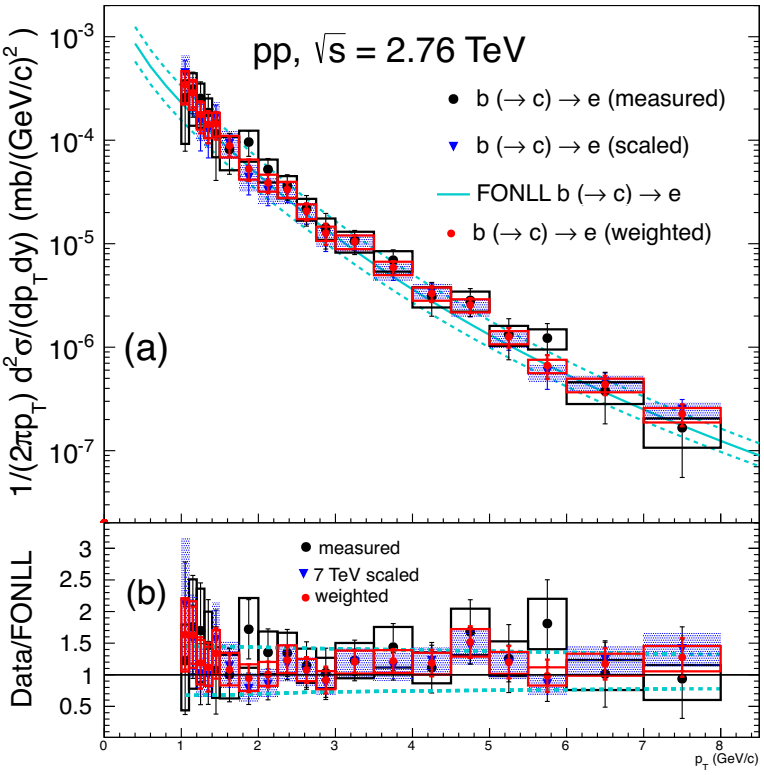

Figure 5.8: Panel a): measured (black) and FONLL-scaled (blue) p_{T}-differential cross section of electrons from beauty-hadron decays at $\sqrt{s} = 2.76$ TeV, with the weighted average of both represented in red. Panel b) shows the ratios of all three spectra to the values predicted by FONLL calculations. Plot taken from [Ave13a].

a similar degree.

In order to obtain a reference spectrum with optimal precision, the measured and the scaled spectrum can be treated as independent measurements and combined by calculating the weighted average of both spectra. The resulting p_{T}-differential cross section, presented in Figure 5.8 in red, has smaller uncertainties than each of the two spectra from which it was calculated and can be used as a reference for investigations in Pb-Pb collisions at $\sqrt{s_{\mathrm{NN}}} = 2.76$ TeV. Also within the reduced uncertainties of the combined result, FONLL calculations show good agreement with the measured cross section.

5.3 The Total Production Cross Section of Beauty Quarks and Beauty-Hadron Decay Electrons

Based on the measured production cross sections of electrons from beauty-hadron and inclusive heavy-flavour hadron decays and on FONLL pQCD calculations, the total production cross section of $b\bar{b}$ pairs can be determined. For this purpose, the integrated *visible* production cross sections of beauty-decay electrons, measured in a rapidity range of $|y| < 0.8$ and for 1 GeV/c < p_{T} < 8 GeV/c, which are determined for $\sqrt{s} = 7$ TeV ($\sigma^{7\,\mathrm{TeV}}_{b\bar{b},vis} = 6.61 \pm 0.54(\mathrm{stat})^{+1.92}_{-1.86}(\mathrm{sys}) \pm 0.23(\mathrm{norm})$ μb) and $\sqrt{s} = 2.76$ TeV ($\sigma^{2.76\,\mathrm{TeV}}_{b\bar{b},vis} = 3.44 \pm 0.41(\mathrm{stat})^{+1.09}_{-1.30}(\mathrm{sys}) \pm 0.07(\mathrm{norm})$ μb), are scaled by the ratio between the corresponding total cross section predicted by FONLL and the FONLL cross section $\sigma^{\mathrm{FONLL}}_{b\bar{b},vis}$ for the same p_{T} and y range as in the measurement, as well as by the branching ratio $\mathrm{BR}(b \to e)$ from beauty quarks to electrons:

$$\sigma_{b\bar{b}} = \frac{\alpha_{b\bar{b}} \cdot \sigma_{b\bar{b},\mathrm{vis}}}{\mathrm{BR}(b \to e)} \quad , \tag{5.1}$$

with

$$\alpha_{b\bar{b}} = \frac{\sigma^{\mathrm{FONLL}}(b \to e, 0 < p_{\mathrm{T}} < \infty, -y_{\mathrm{min}} < y < y_{\mathrm{max}})}{\sigma^{\mathrm{FONLL}}_{b\bar{b},\mathrm{vis}}} \quad . \tag{5.2}$$

$y_{\mathrm{max/min}}$ take on the values $\pm$ 7.2 for $\sqrt{s} = 7$ TeV and $\pm$ 6.3 for $\sqrt{s} = 2.76$ TeV, according to the maximal longitudinal momenta of B mesons produced at these collision energies. The parameter $\alpha_{b\bar{b}}$ contains the information about the FONLL extrapolation to $p_{\mathrm{T}} = 0$, and therefore also the related uncertainties. These are determined by calculating $\alpha_{b\bar{b}}$ for variations of the values of the quark mass, the CTEQ6.6 parton distribution functions [Nad08], and the scale parameters in the FONLL calculations. The relative scaling uncertainty is then obtained from the envelope of the ratios of all varied $\alpha_{b\bar{b}}$ values to the value resulting from the standard FONLL calculation. An additional uncertainty from the branching ratio of beauty-hadron decays into electrons has to be taken into account, according to the current best estimate of $\mathrm{BR}_{H_b \to e} + \mathrm{BR}_{H_b \to H_c \to e} = 0.205 \pm 0.007$ [Beh12].

From an analogous calculation, the beauty-decay electron cross section at mid-rapidity is obtained:

$$\left.\frac{d\sigma(b \to e)}{dy}\right|_{y=0} = \frac{\sigma_{b\bar{b},\mathrm{vis}} \cdot \beta_{b\bar{b}}}{\Delta y} \quad , \tag{5.3}$$

with

$$\beta_{b\bar{b}} = \frac{\sigma^{\mathrm{FONLL}}(b \to e, 0 < p_{\mathrm{T}} < \infty, y_{\mathrm{min}} < y < y_{\mathrm{max}})}{\sigma^{\mathrm{FONLL}}_{b\bar{b},\mathrm{vis}}} \tag{5.4}$$

and $\Delta y = 1.6$, corresponding to the rapidity range from y_{min} = -0.8 to $y_{\mathrm{max}} = 0.8$.

The cross section of beauty-quark production at mid-rapidity is obtained from

$$\left.\frac{d\sigma_{b\bar{b}}}{dy}\right|_{y=0} = \frac{\sigma_{b\bar{b},vis} \cdot \gamma_{b\bar{b}}}{\Delta y \cdot \mathrm{BR}(b \to e)} \quad , \tag{5.5}$$

with

$$\gamma_{b\bar{b}} = \frac{\sigma^{\mathrm{FONLL}}(b\bar{b}, 0 < p_{\mathrm{T}} < \infty, y_{\mathrm{min}} < y < y_{\mathrm{max}})}{\sigma^{\mathrm{FONLL}}_{b\bar{b},\mathrm{vis}}} \quad . \tag{5.6}$$

The results of these calculations for the analyses at $\sqrt{s} = 7$ TeV and 2.76 TeV are summarized in Table 5.1. For $\sqrt{s} = 2.76$ TeV, the total charm production cross section has not been determined since at the time of this thesis, the corresponding inclusive heavy-flavour measurement was not available yet.

Table 5.1: Results of this analysis for the total and mid-rapidity production cross sections of beauty and charm.[1]

cross section	flavour	$\sqrt{s}$ (TeV)	result
σ_{tot}	beauty	7	$280 \pm 23(\mathrm{stat})^{+81}_{-79}(\mathrm{sys})^{+7}_{-8}(\mathrm{extr}) \pm 10(\mathrm{norm}) \pm 10(\mathrm{BR})$ μb
		2.76	$129 \pm 15(\mathrm{stat})^{+41}_{-49}(\mathrm{sys})^{+3}_{-3}(\mathrm{extr}) \pm 2(\mathrm{norm}) \pm 4(\mathrm{BR})$ μb
	charm	7	$10.0 \pm 1.7(\mathrm{stat})^{+5.1}_{-5.5}(\mathrm{sys})^{+3.5}_{-0.5}(\mathrm{extr}) \pm 0.3(\mathrm{norm}) \pm 0.4(\mathrm{BR})$ mb
$\left.\frac{d\sigma}{dy}\right\|_{y=0}$	beauty	7	$42 \pm 3(\mathrm{stat}) \pm 12(\mathrm{sys})^{+1}_{-2}(\mathrm{extr}) \pm 1(\mathrm{norm})$ μb
		2.76	$23.1 \pm 2.7(\mathrm{stat})^{+7.3}_{-8.7}(\mathrm{sys})^{+0.5}_{-0.7}(\mathrm{extr}) \pm 0.4(\mathrm{norm})$ μb
	charm	7	$1.2 \pm 0.2(\mathrm{stat}) \pm 0.6(\mathrm{sys})^{+0.2}_{-0.1}(\mathrm{extr})$ mb
$\left.\frac{d\sigma_{Q\to e}}{dy}\right\|_{y=0}$	beauty	7	$8.4 \pm 0.7(\mathrm{stat}) \pm 2.4(\mathrm{sys})^{+0.2}_{-0.3}(\mathrm{extr}) \pm 0.3(\mathrm{norm})$ μb
		2.76	$4.5 \pm 0.5(\mathrm{stat})^{+1.4}_{-1.7}(\mathrm{sys}) \pm 0.1(\mathrm{extr}) \pm 0.1(\mathrm{norm})$ μb
	charm	7	$110 \pm 19(\mathrm{stat})^{+57}_{-61}(\mathrm{sys})^{+18}_{-4}(\mathrm{extr}) \pm 4(\mathrm{norm})$ μb

[1] Values are rounded to two digits of uncertainties, compared to [Abe13a, Ave13a].

5.4 The Total Production Cross Section of Charm Quarks and Charm-Hadron Decay Electrons at $\sqrt{s} = 7$ TeV

Performing calculations analogous to the ones described in the previous section, the total production cross section of charm quarks and charm-decay electrons for pp collisions at $\sqrt{s} = 7$ TeV can be extracted by combining the result of this analysis with the inclusive heavy-flavour electron production cross section determined in [Abe12g].

Taking into account the different ranges of the inclusive heavy-flavour electron measurement in y and p_{T} ($|y| < 0.5$; $0.5 < p_{\mathrm{T}} < 8$ GeV/c), the visible charm-decay electron production cross section can be determined by scaling the integrated visible beauty-decay electron spectrum by a factor of $\Delta y_{b+c}/\Delta y_b = 1/1.6$ and subtracting it from the visible integrated electron cross section from inclusive heavy-flavour decays. In the p_{T} interval from 0.5 to 1.0 GeV/c, where only a measurement for inclusive heavy-flavour decays is available, the contribution of beauty decays to the inclusive electron yield from heavy-flavour decays is considered as negligible.

Like the results for the beauty production cross sections, the total charm production cross section for $\sqrt{s} = 7$ TeV, determined via the extrapolation method described in Section 5.3, is given in Table 5.1. The uncertainty to the branching ratio of $H_c \rightarrow e$ that was added for this measurement corresponds to a value of $\mathrm{BR}_{H_c \rightarrow e} = 0.096 \pm 0.004$ [Beh12]. The measured total charm production cross section, $\sigma^{7\,\mathrm{TeV}}_{c\bar{c},\mathrm{tot}} = 10.0 \pm 1.7(\mathrm{stat})^{+5.1}_{-5.5}(\mathrm{sys})^{+3.5}_{-0.5}(\mathrm{extr}) \pm 0.3(\mathrm{norm}) \pm 0.4(\mathrm{BR})$ mb, is consistent with the result of a previous, more precise ALICE measurement via D-meson decays [Abe12d], $\sigma_{c\bar{c},tot} = 8.5 \pm 0.5(\mathrm{stat})^{+1.0}_{-2.4}(\mathrm{sys})^{+5.0}_{-0.4}(\mathrm{extr})$ mb. The prediction of this value by FONLL, $\sigma_{c\bar{c},\mathrm{tot}} = 4.76^{+6.44}_{-3.25}$ mb [Cac12], agrees with both measurements within uncertainties.

5.5 Weighted Average of the Total Beauty Cross Section Measurements at $\sqrt{s} = 7$ TeV

The measurement of the total beauty cross section at $\sqrt{s} = 7$ TeV discussed in this thesis is not the only one provided by ALICE for this centre-of-mass energy. In [Abe12h], the fraction of non-prompt J/ψ from B-meson decays in the inclusive J/ψ yield for 1.3 GeV/c $< p_{\mathrm{T}} <$ 10 GeV/c and $|y| < 0.9$ was determined. Combined with the information about the inclusive J/ψ production cross section from [Aam11b], the total beauty cross section was calculated based on a FONLL extrapolation similar to the one applied in Section 5.3, with the result of

$$\sigma_{b\bar{b},\mathrm{tot}} = 282 \pm 74(\mathrm{stat})^{+58}_{-68}(\mathrm{sys})^{+8}_{-7}(\mathrm{extr})\mu\mathrm{b} \quad .$$

In order to present the current best estimate of the total beauty cross section, it is desirable to combine this result with the one of the analysis for $\sqrt{s} = 7$ TeV described in this thesis, in Section 5.3. Both cross section values were obtained using the same FONLL calculations for scaling to the full phase space; the uncertainties of both results are therefore partly correlated. The extraction of a best common estimate under such circumstances is described in [Lyo88]. It is calculated as a weighted average, as

$$\bar{\sigma}_{b\bar{b},\mathrm{tot}} = \sum_{i=0}^{1} \sigma_{b\bar{b},i} w_i \qquad . \tag{5.7}$$

$\sigma_{b\bar{b},i}$ with i =0, 1 are the cross sections from both measurements, and w_i the corresponding weighting factors. These are determined from the equation

$$w = \frac{E^{-1}u}{u^T E^{-1} u} \qquad , \tag{5.8}$$

with the vector u, all of whose elements have the value of 1, and the inverse of the covariance matrix of the uncertainties, E^{-1}. The components of the uncertainties to $\bar{\sigma}_{b\bar{b}}$ result from

$$\delta\sigma^2 = w^T E w \qquad . \tag{5.9}$$

The diagonal terms of the covariance matrix E are the quadratic sum of the statistical uncertainties, the average systematic uncertainties, the branching ratio uncertainties, and the average uncertainties of the FONLL scaling, while the product of both scaling uncertainties constitutes an off-diagonal matrix element.

The weighting factors obtained from these calculations are 0.499 for the measurement of electrons from beauty-hadron decays and 0.501 for the analysis of non-prompt J/ψ from beauty-hadron decays. The uncorrelated uncertainty components are calculated from Equation 5.9, with the squared uncertainties of both measurements as the diagonal matrix elements in E, while all off-diagonal elements are set to 0. The uncertainty from the FONLL scaling to the full phase space, the only correlated uncertainty of both measurements, is determined by setting the off-diagonal elements to the product of the scaling uncertainties of both measurements. The diagonal elements are the same as for the uncorrelated uncertainties. According to this calculation, the weighted average of the total beauty cross section is

$$\sigma_{b\bar{b},\mathrm{tot}} = 281 \pm 34(\mathrm{stat})^{+53}_{-54}(\mathrm{sys})^{+7}_{-8}(\mathrm{extr})\mu\mathrm{b} \qquad .$$

In comparison with the FONLL prediction of $\sigma_{b\bar{b},\mathrm{tot}} = 259^{+120}_{-96}\mu$b [Cac12], which is consistent with the result of this analysis, the ALICE measurements can set significantly narrower constraints to the total beauty cross section.

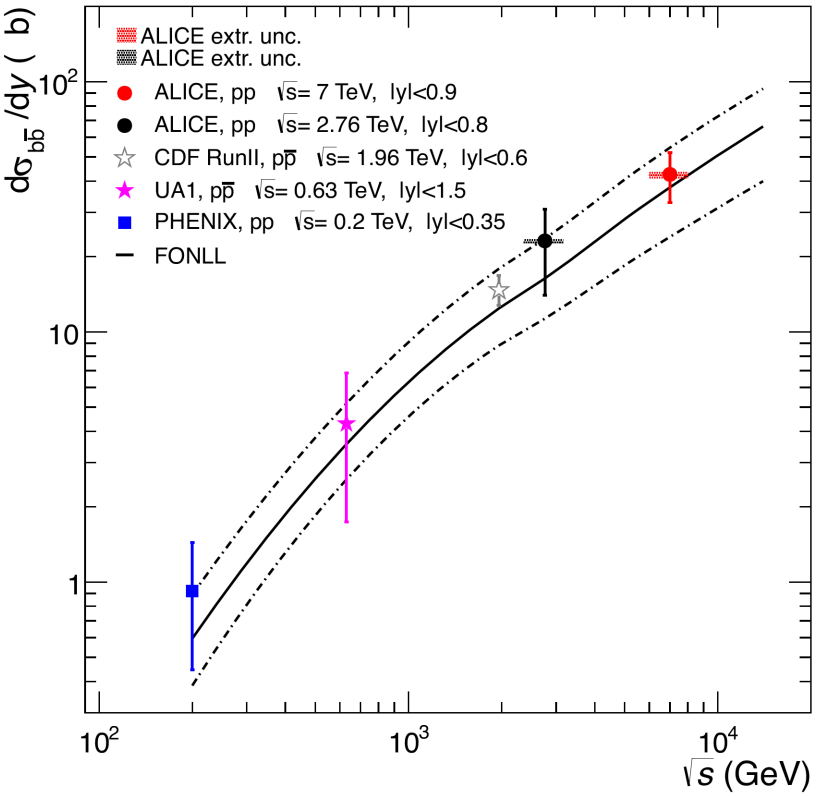

Figure 5.9: Total beauty cross section for different $\sqrt{s}$; same as right panel of Figure 2.6, updated with the results of this analysis for $\sqrt{s} = 2.76$ TeV and 7 TeV [Ave13a].

5.6 Energy Dependence of the Total Beauty Cross Section

Figure 5.9 shows the dependence of $\mathrm{d}\sigma_{b\bar{b}}/\mathrm{d}y$ at mid-rapidity on the centre-of-mass energy in pp and p$\bar{\mathrm{p}}$ collisions. It is an update to Figure 2.6, including the result of this analysis at $\sqrt{s} = 2.76$ TeV and the weighted average of the pre-existing ALICE measurement on non-prompt J/ψ decays [Abe12h] and the measurement described in this thesis for $\sqrt{s} = 7$ TeV.

The range of measurements in $\sqrt{s}$ has been extended substantially by ALICE. The energy dependence of beauty production at mid-rapidity is well described by FONLL predictions within the whole $\sqrt{s}$ range.

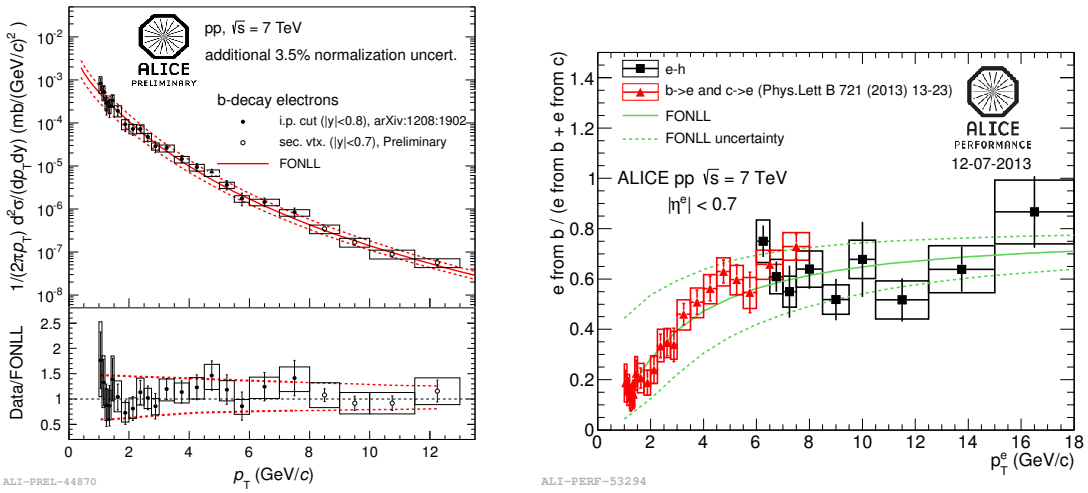

Figure 5.10: Left: cross section of beauty-hadron decay electrons for $\sqrt{s} = 7$ TeV from Figure 5.1, combined with the result of a measurement via displaced secondary vertices (see text) for $p_{\mathrm{T}} > 8$ GeV/c [Aro12]. Right: results for the ratio between the electron yield from beauty-hadron decays and from inclusive heavy-flavour hadron decays, measured via azimuthal angular electron-hadron correlations (black) [Maa13], and as a ratio of the results for the p_{T}-differential cross section from beauty-hadron decays (Figure 5.1) and from inclusive heavy-flavour decays [Abe12g] (red). Both results are well described by FONLL calculations [Cac98, Cac]. Both figures taken from [Hei13].

5.7 Additional Measurements of the $H_b \rightarrow e$ Cross Section in ALICE

For pp collisions at both centre-of-mass energies considered in this thesis, complementary approaches to the analysis of beauty-decay electrons have been made in the ALICE collaboration. During the time in which this analysis was performed, several of them have produced results that provide important cross-checks for those presented in Sections 5.1 and 5.2 and extend the range of beauty-hadron decay measurements to higher transverse momenta, enabled by the usage of the Electromagnetic Calorimeter for triggering on fast electrons. Corresponding to the limits of the EMCal acceptance, the rapidity range of these measurements is $|y| < 0.7$.

By reconstructing electron-hadron vertices that are displaced with respect to the primary vertex, the p_{T}-differential invariant spectrum has been measured up to a transverse momentum of 13 GeV/c in pp collisions at $\sqrt{s} = 7$ TeV, as shown in the left panel of Figure 5.10 [Aro12]. The requirement of a minimum displacement of the reconstructed vertex is based on the same principle as the impact parameter selection described in this work. The analysis applies further requirements on the invariant

mass of the reconstructed electron-hadron pair, in order to reject background from photon conversions and decays of charm hadrons and light mesons, and on the transverse momentum of the hadronic partner of the electron.

Another analysis, described in [Tho12, Maa13, Abe14a], focusses on azimuthal angular electron-hadron correlations to determine the relative amount of electrons from beauty decays, as compared to the inclusive heavy-flavour electron yield. The angular distribution of the associated hadrons around the electron tracks has a two times wider near-side peak for beauty-hadron decays than for charm-hadron decays, as can be shown in simulations. The relative contribution of both to the measured distribution is estimated via fits with PYTHIA templates. Photonic background is rejected by excluding track pairs with small invariant masses. In the right panel of Figure 5.10, the resulting ratio between the electron yields of beauty and inclusive heavy-flavour hadron decays for $\sqrt{s} = 7$ TeV is shown in black for 6 GeV/c < p_{T} < 18 GeV/c. For the p_{T} range from 1 GeV/c to 8 GeV/c, the corresponding ratio extracted from the p_{T}-differential yields of beauty-hadron decays presented in this thesis and from the analysis of inclusive heavy-flavour hadron decays [Abe12g] is plotted in red. The upper left panel of Figure 5.11 shows the analogous measurements for $\sqrt{s} = 2.76$ TeV, where the result via azimuthal angular electron-hadron correlations covers a p_{T} range from 1.5 GeV/c to 10 GeV/c. In the lower left panel of Figure 5.11, the corresponding p_{T}-differential cross sections determined by both methods are shown. In addition, the ratios in the upper panel are compared to the ones resulting from the three pQCD predictions represented in Figure 5.6. The upper (lower) limits of the predictions given in this figure were determined by dividing the upper (lower) limit of a beauty-decay electron spectrum by the lower (upper) limit for a spectrum of inclusive heavy-flavour decay electrons [Abe14a]. No account was taken of uncertainty components that are correlated for the production of charm and beauty electrons. Therefore, the presented uncertainties should significantly overestimate the ones that would result from dedicated pQCD calculations.

A p_{T}-differential cross section of electrons from beauty-hadron decays, shown in the right panel of Figure 5.11, has been calculated for 3 GeV/c < p_{T} < 9 GeV/c by combination of a preliminary result of the ratio obtained via the electron-hadron correlation analysis with a p_{T}-differential heavy-flavour electron spectrum measurement in ALICE, described in [Hic12].

All of the measurements in Figures 5.10 and 5.11 agree well with the results presented in this thesis inside the overlapping p_{T} ranges, where the impact parameter approach provides more accurate results in all cases. Consequently, they are equally well described by FONLL calculations, as depicted in both figures, and by the alternative pQCD descriptions within the GM-VFN scheme [Bol13,Kra] and the k_{T}-factorization approach [Mac13a, Mac].

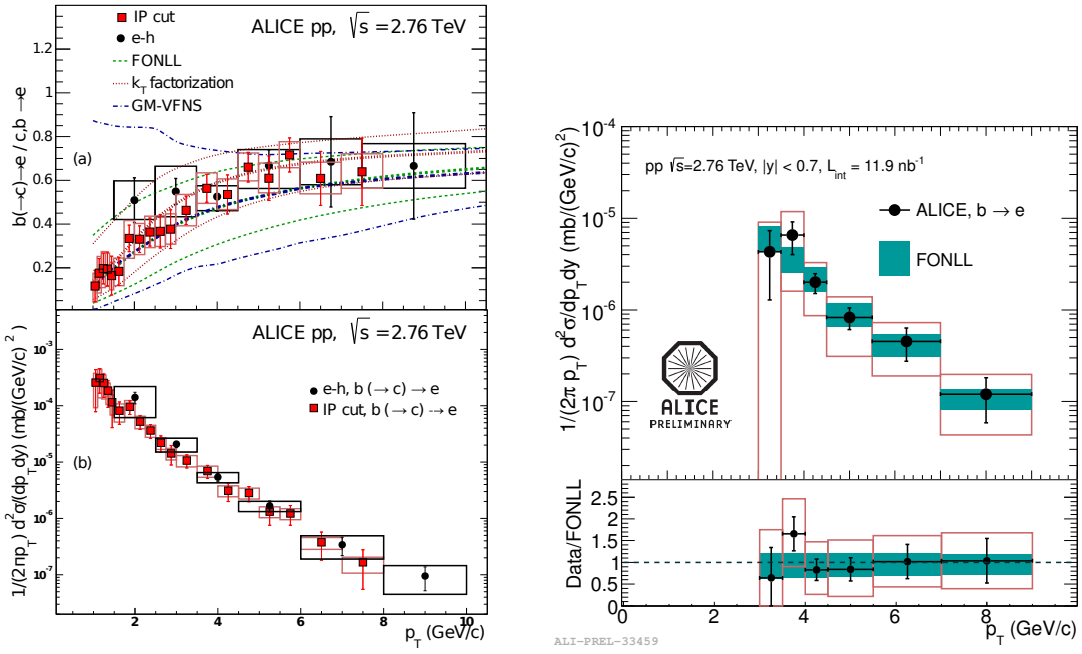

Figure 5.11: Left: p_{T}-dependent ratio of electrons from beauty to inclusive heavy-flavour hadron decays in pp collisions at $\sqrt{s} = 2.76$ TeV (upper panel) from the impact parameter analysis (red) and from an analysis based on azimuthal angular electron-hadron correlations (black) with the corresponding p_{T}-differential invariant production cross sections of electrons from beauty-hadron decays (lower panel) [Abe14a]. The measurements of the ratio in the upper panel are compared to pQCD predictions from FONLL, GM-VFNS, and the k_{T}-factorization framework, whose central values, upper, and lower limits are depicted. Right: p_{T}-differential invariant cross section of electrons from beauty-hadron decays, extracted from a preliminary version of the ratio from the electron-hadron correlation analysis shown in the left panel and a measurement of the cross section of electrons from inclusive heavy-flavour hadron decays [Hic12]. The result is shown in comparison with FONLL predictions. Figure taken from [Hei13].

6 Outlook: Electron Background from Light-Meson Decays and Photon Conversions in the Measurement of Electrons from Beauty-Hadron Decays in Pb-Pb Collisions at $\sqrt{s_{\mathrm{NN}}} = 2.76$ TeV

In parallel to the analysis of semi-electronic beauty-hadron decays in pp collisions presented in the previous chapters, some preliminary, simulation-based work has been performed for the electron background subtraction in the analysis of Pb-Pb collisions at $\sqrt{s_{\mathrm{NN}}} = 2.76$ TeV, whose results will be of particular interest for the investigation of the properties of the QGP (see Section 2.4).

The investigations were carried out on HIJING simulations of Pb-Pb collisions [Gyu94], among them 2.01 $\cdot 10^6$ minimum-bias events and 1.37 $\cdot 10^6$ events with enhanced electron production from charm and beauty decays. In an approach analogous to the procedure described in Section 4.8.1, the electron spectra produced by HIJING are weighted on a track-by-track basis by factors determined according to the preliminary measured π^0 spectra [Ave], presented in Figure 6.1. No contribution of thermal photons is included in the spectrum yet. Their influence on the electron background is expected to be substantial for $p_{\mathrm{T}} \lesssim 3$ GeV/c and will have to be included in the future. The spectra from HIJING and from the parameterization obtained from measurements and m_{T}-scaling from which these weighting factors were calculated can be found in Appendix E.

There are six centrality classes for which such weights are available (0-10%, 10-20%, 20-40%, 40-50%, 50-60%, 60-80%). The percentages classify the events according to their centrality, relative to the total amount of collisions: in the 0-10% centrality class, the 10% of the events with the highest centrality of the collision, corresponding to the smallest impact parameter b (cf. Figure 2.9) are grouped, in the 10-20% centrality class the following 10% most central events, etc. The centrality estimation is based on the charged-particle multiplicities measured by the V0 detector.

The weighting factors for electrons from conversions and light-meson decays have been included in the following investigation of a problem that has already been discussed in the context of the analyses of pp collisions in Section 4.5, but that is expected to be more severe in Pb-Pb events: owing to the high multiplicities achieved in central Pb-Pb collisions, a large number of electron tracks from photon conversions occurring outside the first SPD pixel layer are erroneously combined with

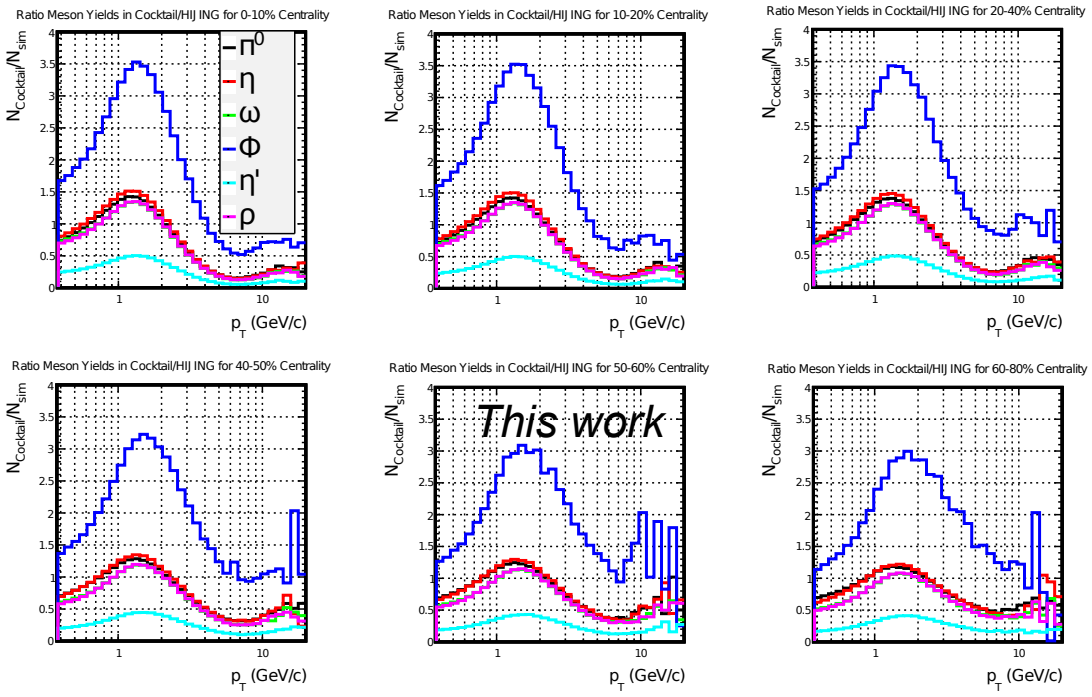

Figure 6.1: Weighting factors from ratios of the measured or m_{T}-scaled p_{T}-differential light-meson yields to the yields generated by HIJING for Pb-Pb collisions at $\sqrt{s_{\mathrm{NN}}} = 2.76$ TeV for six centrality classes.

hits in the inner SPD layer and therefore included in the selected electron spectrum. While this problem has been successfully cured by the requirement of signals in both SPD layers in the analysis of pp collisions, this measure is no longer sufficient for the multiplicities in central Pb-Pb events. In the following, a qualitative estimate will be made concerning the extent of this problem, and a possible strategy for its solution will be discussed.

The fact that the problem of false SPD hit associations to tracks increases with multiplicity can be concluded from Figure 6.2. It shows the ratio between an efficiency-corrected conversion electron spectrum generated by HIJING and transported via GEANT3 and the corresponding spectrum given by a parameterization for the conversion electron yield of tracks that leave a hit in the first SPD layer [Ave]. The simulated spectrum was evaluated after all selection criteria as listed in Table 4.9 for the reference values in pp collisions at $\sqrt{s} = 2.76$ TeV, except for the particle identification and impact parameter criteria. After corrections for the selection efficiencies, the ratio between the simulated and parameterized spectrum for the ALICE inner barrel acceptance should be close to unity, assuming that the conversion probability in the beam pipe and the inner SPD layer is well represented by the calculations for the parameterization and by the GEANT simulation. The fact that the ratios deviate from unity to an increasingly higher level with in-

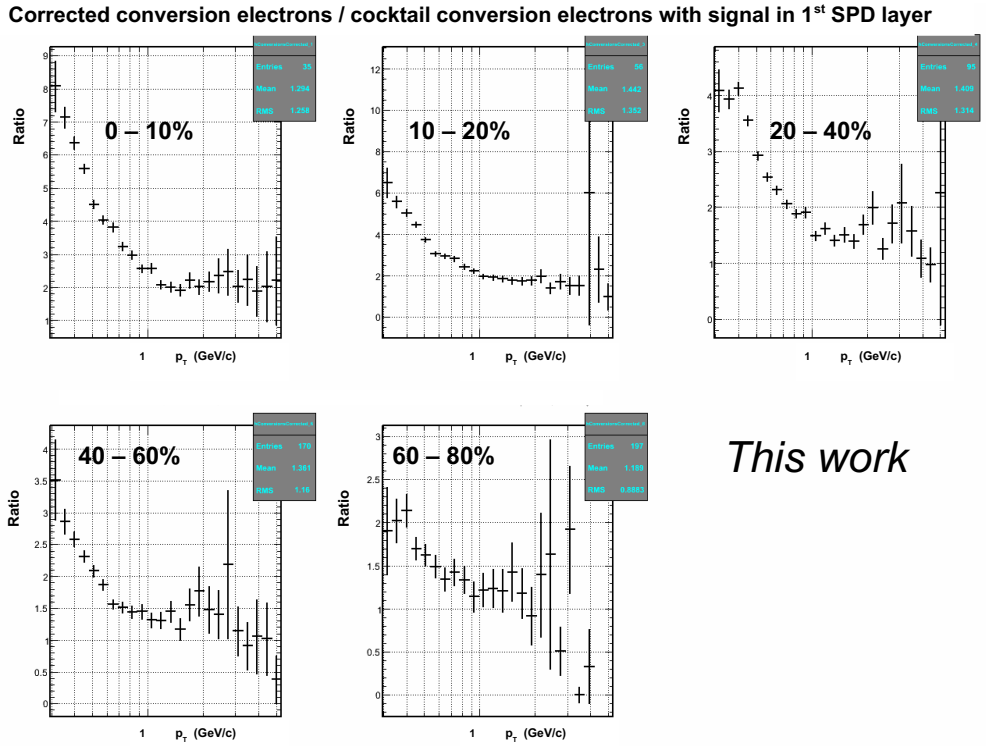

Figure 6.2: Ratio between the HIJING conversion electron spectra after correction from the selected electron spectra (see text) and the spectra calculated for conversion electrons leaving a hit in the first SPD layer, presented for five centrality classes.

creasing centrality hints to a growing amount of wrongly associated hits in the first SPD layer. While for centralities between 60% and 80%, the conversion electron spectra of simulation and parameterization are almost equal for $p_{\mathrm{T}} > 1$ GeV/c, the ratio between them gradually increases to a factor of 2 in most central events, with a steep rise in the p_{T} region below 1 GeV/c.

Since conversions that occur at large distances from the primary vertex have large impact parameters, the situation is expected to be worse for an electron sample after the impact parameter selection. The upper left panel of Figure 6.3 shows the ratio between the simulated spectra of electrons from photon conversions and from light-meson decays in the 0-20% most central Pb-Pb collisions after all track selection criteria as in the analysis for pp collisions at $\sqrt{s} = 2.76$ TeV, this time including the TOF and TPC electron identification criteria and the impact parameter selection. An additional requirement was made for the true production vertex of the respective particle to be at a distance $R < 4.4$ cm from the primary vertex in the $x - y$ plane, corresponding to the maximal distance for a production in the first SPD layer (see

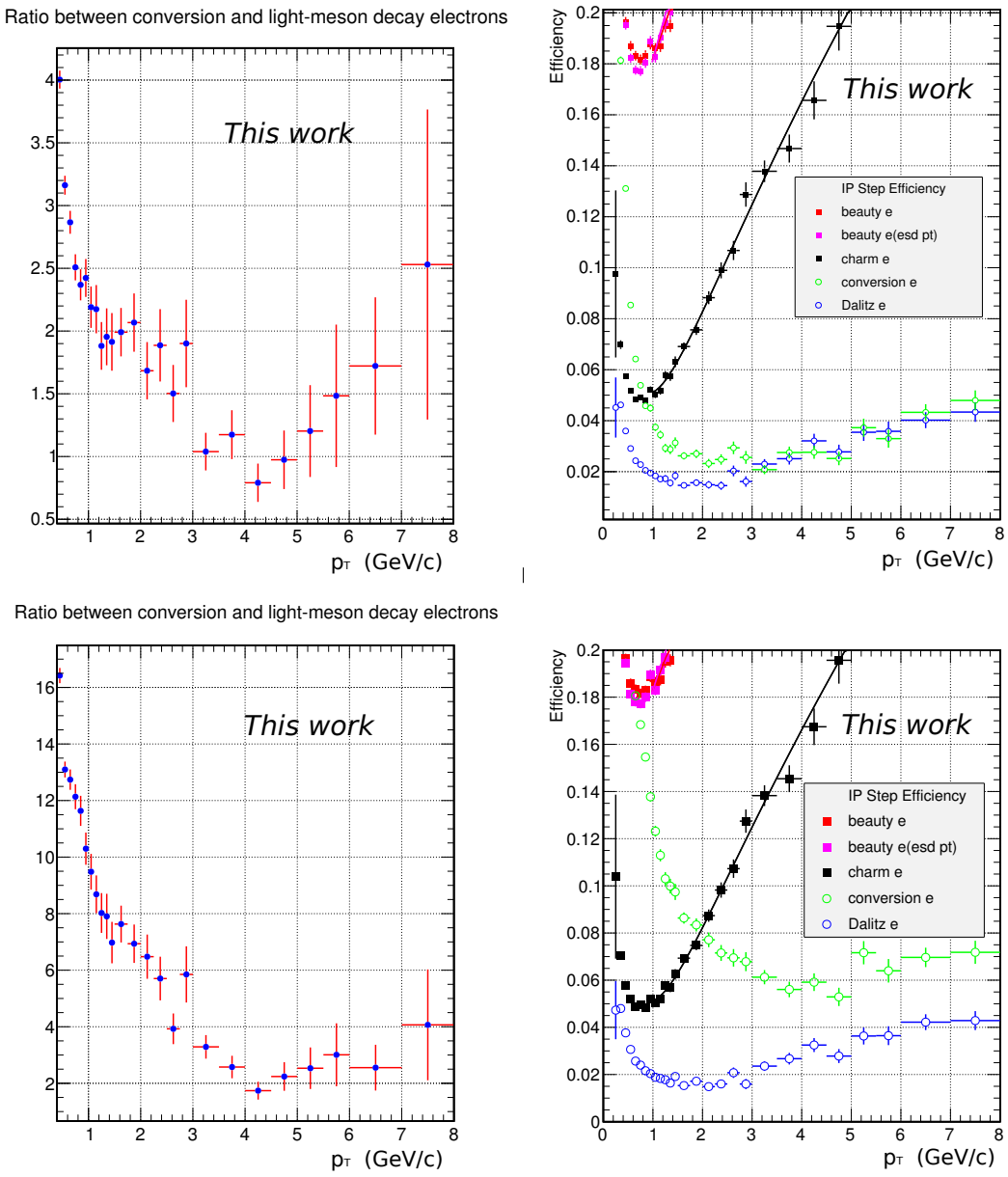

Figure 6.3: Left panels: ratio between electron yields from conversions and light-meson decays after PID and impact parameter selection for electrons produced at $R < 4.4$ cm (top) and at $R < 100$ cm (bottom) in the $x - y$ plane from the primary vertex. Right panels: selection efficiencies of the impact parameter criterion for the same cases.

Section 4.5). Therefore, this ratio can be expected to be close to the one that would be obtained in the uncorrected selected electron sample of this analysis if there were no false combinations of conversions that occur further outside with hits in the inner SPD layer.[1]

The lower left panel shows the same ratio for a more realistic situation – here, all electrons produced up to $R = 100$ cm were included in the analysis, which leads to a large amount of false combinations, above all for the low-p_{T} region, in which conversion background is expected to play an important role. This excess of conversion electrons would reduce the signal-to-background ratio, and thus the significance of possible measurements substantially. It is therefore desirable to minimize the contamination by falsely selected conversions to a degree at which it becomes negligible.

A method that has been considered for this purpose is the application of a modified impact parameter criterion that takes into account the specific d_0 distributions of electrons and positrons from photon conversions, using the information about the charge of the particle. From Figure 4.1, the d_0 distribution of conversion electrons can be seen to differ in shape from the distributions of massive-particle decays. One reason for this is the fact that photons are not subject to an exponential decay in time, but need the presence of matter to convert to electron-positron pairs. As the photon has no mass, the initial momenta of both resulting charged-particle tracks point to the same direction as the momentum of the original photon, radially from the primary vertex. The consequence for the impact parameter of these tracks is visible in Figure 4.5: in their projection on the $x - y$ plane, the extrapolations of tracks from electrons and positrons pass the primary vertex to different sides. Following the definition of the impact parameter given in Section 4.6, this results in opposite signs for the d_0 values of electrons and positrons. In combination with the limited d_0 resolution, two distinct distributions of positron and electron track impact parameters can be identified, each one displaced from zero to a different side.

The displacement of the distributions for tracks of a common p_{T} bin, representing the average absolute value of the impact parameter, depends on the curvature of the tracks and, thus, on the transverse momentum of the particles. At low p_{T}, where conversion background in general and the problem of false track combinations in particular are most significant, the deviation of the mean impact parameter of conversion electrons and positrons from zero is largest. For massive-particle decays, by contrast, a wide angular distribution of the decay products overlays the effects of track curvature and resolution, and no d_0-mean displacement of similar magnitude arises (see Figure 6.4).

These observations suggest the usage of the charge information in order to reject both positrons and electrons from conversions by an adapted criterion that selects for each charge only one side of the d_0 distribution. An elegant possibility to do so is the representation of the impact parameter, multiplied by the sign of the particle

[1] As this is a rough estimate, no account will be taken of electrons that convert in the beam pipe or the first SPD layer, but only leave a hit in the second pixel layer which is then falsely combined with a hit from another track in the inner SPD layer.

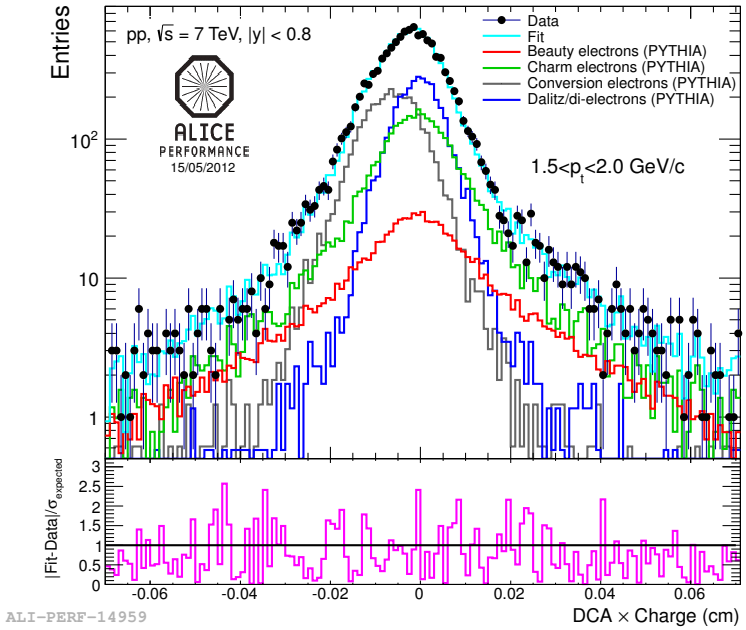

Figure 6.4: Distributions of $d_0 \cdot charge$ for different electron sources by Monte Carlo template fits to data from pp collisions at $\sqrt{s} = 7$ TeV for [Völ12].

charge, so that the electron and positron distribution form a common peak which is displaced from zero. In the case of the investigation described in this chapter, a further multiplication by the sign of the magnetic field in ALICE is necessary, since its polarity was switched during the period LHC10h, and correspondingly also in the data sets that were simulated for this run period. Figure 6.4 shows the resulting distributions for the main electron sources from an alternative analysis approach by Martin Völkl [Völ12, Völ15], which uses Monte Carlo templates for the different d_0 distributions of particle decays and conversions to determine the beauty and charm yields in different p_{T} bins.

An impact parameter selection that only considers the positive side of this distribution is possibly useful for the low-p_{T} regions in which the background by conversion electrons is dominant. The loss in statistical volume at low p_{T} due to this technique may be more than compensated by the improvement of the signal-to-background ratio resulting from a suppression of photon conversions in general and of false track combinations in particular. A quantitative estimate concerning this question can, however, only be given once the inclusive electron spectrum and the electron background from charm decays are known for central Pb-Pb collisions.

The suppression of false combinations by a unilateral impact parameter selection may be even stronger than the overall conversion electron suppression. Figure 6.5 gives a schematic representation of this idea: electron or positron tracks from conversions in the second SPD layer or further outside should have a larger average

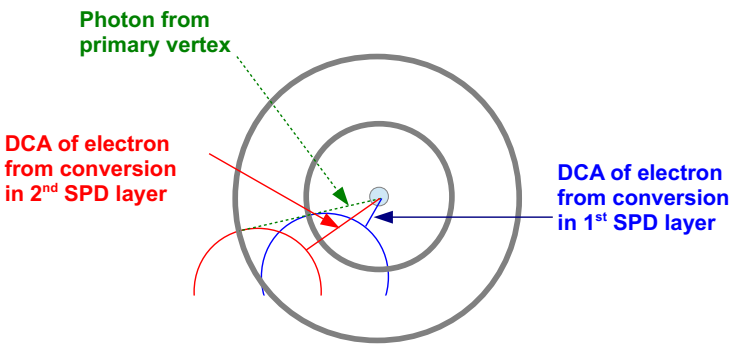

Figure 6.5: Schematic representation of the impact parameter of electrons from photon conversions in the first and second SPD layer. Track curvatures and SPD structures are not to scale.

impact parameter than tracks with comparable p_{T} originating from the beam pipe or the first SPD layer. Consequently, the d_0 distribution of such tracks, shown in Figure 4.2, is wider than the distribution of electrons from conversions occurring closer to the primary vertex, which should correspond to a larger unilateral displacement after multiplication by the particle charge and result in a stronger suppression of falsely associated tracks by a unilateral impact parameter selection.

To test these considerations, analogous checks to the ones shown in Figure 6.3 have been performed with a unilateral d_0 selection, using the same parameterization as the bilateral selection for the sake of comparability. The results are presented in Figures 6.6 and 6.7 and allow two main conclusions:

- From comparison of the upper left and lower left panel of Figure 6.3 to the left panels of Figures 6.6 and 6.7, respectively, it can be seen that the ratio between conversion electrons and electrons from meson decays for $p_{\mathrm{T}} < 3$ GeV/c is reduced by the unilateral impact parameter selection by a factor between 1.5 and 2, which corresponds to an approximate reduction[2] of the conversion electron yield by a factor between 3 and 4.

- No significant difference in conversion suppression by the unilateral impact parameter selection is visible between the cases of conversions at $R < 4.4$ cm and $R < 100$ cm. This observation is equivalent to the statement that no significant additional suppression of falsely combined tracks takes place.

In the probable scenario in which photon conversions generate the dominating or co-dominating background to the signal of electrons from beauty-hadron decays

[2] As an approximation, it can be assumed that the selection efficiencies of the unilateral selection for all other sources are half the efficiencies of the bilateral impact parameter selection. The real efficiencies are slightly lower in the first case, since effects of the track curvature play a certain role.

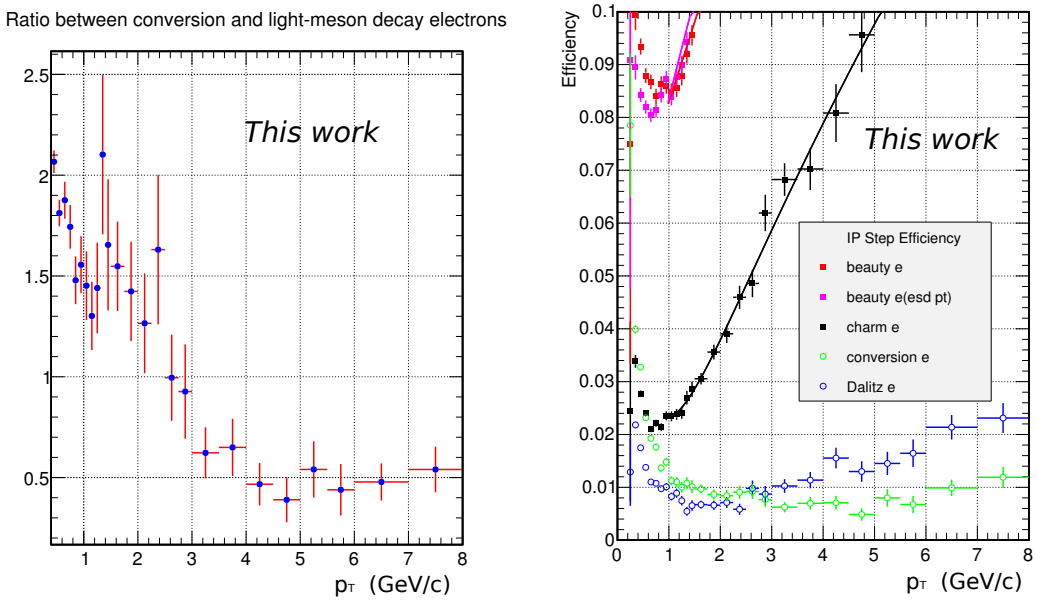

Figure 6.6: Ratio between electron yields from conversions and light-meson decays after unilateral impact parameter selection for electrons produced at $R < 4.4$ cm (left) and efficiencies of the corresponding impact parameter criterion (right).

at low momenta, the proposed unilateral impact parameter selection may therefore help to optimize the signal-to-background ratio. At the time of this thesis, it is being applied and further developed for this purpose in the ongoing analyses of Pb-Pb and p-Pb collisions [Kwe]. The problem of falsely combined conversion electron tracks, however, cannot be solved using the same parameters as in the tests described above.

While this first result is slightly sobering, it has to be emphasized that for a definite conclusion, several alternative parameterizations of impact parameter requirements will have to be tested and related to d_0 distributions for electrons from conversions at radii up to and outside the first SPD layer, as well as to the other signal and background electron distributions.

A further unknown in the analysis of Pb-Pb collisions is the possible background by electron sources that have been hitherto neglected. One component that has already been mentioned in this respect are conversions of thermal photons. In addition, the blue data points in Figure 6.7 hint to a source of light-meson decays that can occur up to rather high radii from the primary vertex. While their quantitative influence on the falsely combined SPD tracks seems to be negligible, it is not obvious that the same is true for the overall electron track sample after the impact parameter selection. A more detailed investigation of the origin of such decays by the author of this thesis points to the decay chain $K^0_s \rightarrow \pi^0 \rightarrow e$ as the main contributor. As

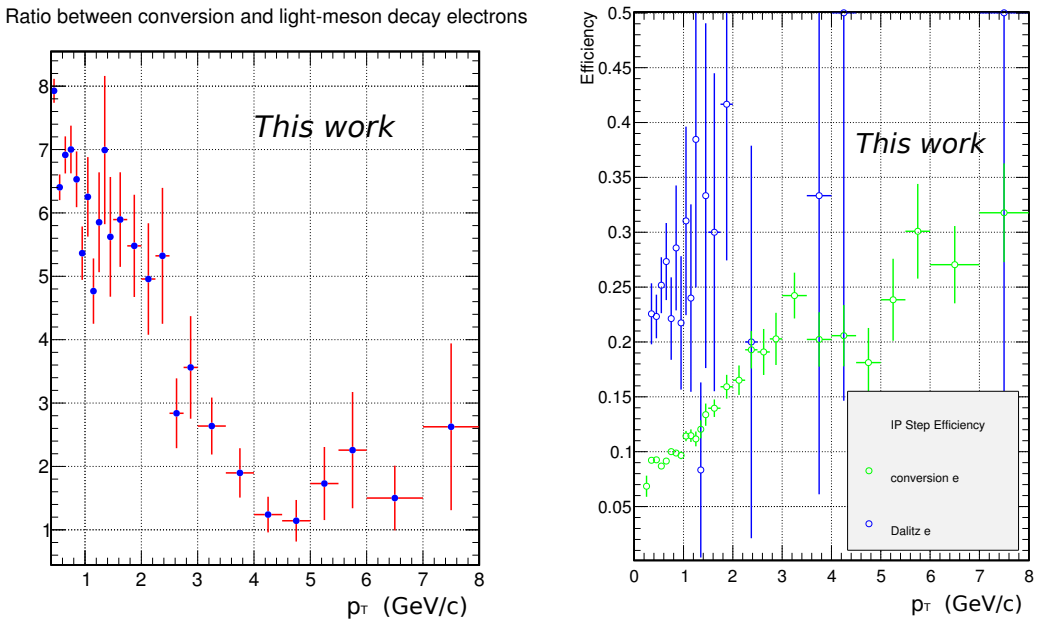

Figure 6.7: Left: same ratio as in Figure 6.6, for electrons produced at $R < 100$ cm. Right: efficiency of the unilateral impact parameter selection for electrons produced outside the first SPD layer, for $R > 4.4$ cm. The entries for electrons from light-meson decays (blue) at such large radii originate mostly from the decays of secondary π^0 from K^0_s decays.

the secondary π^0 from K^0_s decays will also contribute to the conversion background via their subsequent $\pi^0 \to \gamma\gamma$ decays, it will have to be verified if the background from K^0_s decays can still be neglected in central Pb-Pb events.

Summary

The measurement of beauty-hadron decays via the detection of electron tracks that are displaced from the primary vertex can be performed with ALICE, whose capabilities of electron identification and tracking fulfil all requirements for this task. While the large corresponding branching ratios guarantee sufficient yields of beauty-decay electrons at LHC energies, the wide electron impact parameter distribution due to the long lifetime and the decay kinematics of beauty hadrons allows for a separation of electrons from beauty-hadron decays from background electrons on a statistical basis.

This thesis presents the analysis of electrons from beauty-hadron decays in proton-proton collisions at centre-of-mass energies of 7 TeV and 2.76 TeV. Using the ALICE central-barrel detectors ITS, TPC, and TOF, p_{T}-differential electron spectra are measured at mid-rapidity ($|y| < 0.8$) for transverse momenta between 1 and 8 GeV/c.

Information from the TPC and TOF signal is combined to select pure electron samples, whose signal-to-background ratio is subsequently enhanced via the requirement of a minimal impact parameter of the tracks towards the primary vertex in the $x - y$ plane. Tracks from photon conversions occurring outside the innermost ITS layer, which have a wide impact parameter distribution, are rejected via the requirement of hits in both SPD layers of the ITS. The remaining hadron contamination in the selected electron track samples is determined on a statistical basis from the distributions of their energy deposition per unit of length in the TPC.

A crucial challenge of this analysis is the subtraction of the electron background originating from charm decays, photon conversions, and light-meson decays from the measured inclusive electron spectrum. The corresponding electron yields are determined using spectra from PYTHIA simulations that are reweighted based on previous measurements of charmed hadrons, π^0, and η. Minor contributions from other light mesons and, in the case of the analysis for $\sqrt{s} = 2.76$ TeV, from the η meson, are estimated via m_{T}-scaling of the measured π^0 spectra.

The signal-to-background ratio of the selected electron spectra increases towards higher p_{T}, where beauty-hadron decays are the predominant electron source. Electrons from charm-hadron decays constitute the dominating background at high transverse momenta, whereas photon conversions and light-meson decays become more important at low p_{T}. While the measured charm-hadron spectra are the largest source of systematic uncertainties to the measurements for low p_{T}, the background of electrons from light-flavoured sources contributes only moderate additional uncertainties.

For pp collisions at $\sqrt{s} = 7$ TeV as well as at $\sqrt{s} = 2.76$ TeV, the electron production cross section from beauty-hadron decays exceeds the one from charm-hadron decays for electron $p_{\mathrm{T}} \gtrsim 4$ GeV/c. At both collision energies, the measured p_{T}-differential electron spectra from beauty and charm decays are well described by pQCD calculations from FONLL, GM-VFNS, and the k_{T}-factorization scheme. Using the remarkably good description of the $\sqrt{s}$-scaling properties of beauty production by FONLL calculations, the precision of the measured p_{T}-differential electron spectrum from beauty-hadron decays at $\sqrt{s} = 2.76$ TeV, the reference for measurements in Pb-Pb collisions, is improved via combination with the spectrum measured at $\sqrt{s} = 7$ TeV. By extrapolating the measured electron spectra at mid-rapidity to the full rapidity and transverse-momentum range following a FONLL prescription, the total beauty production cross sections for $\sqrt{s} = 2.76$ TeV and $\sqrt{s} = 7$ TeV are calculated. A weighted average for the cross section at $\sqrt{s} = 7$ TeV is determined from the results of this analysis and the measurement described in [Abe12h].

Preliminary analyses are carried out for the weighting of electron background from light-meson decays and photon conversions, and for the suppression of photon conversion background. This last background component is one of the most critical issues in the analysis of electrons from beauty-hadron decays in Pb-Pb collisions, which is in progress from early 2014 on. In parallel, the electron production from beauty-hadron decays in p-Pb collisions at $\sqrt{s_{\mathrm{NN}}} = 5.02$ TeV is being analysed in order to investigate on cold nuclear matter effects [Kwe].

The results presented in this thesis provide not only an important test for perturbative QCD calculations, which describe the beauty and charm production at LHC energies very well, but are also an essential reference for future measurements in Pb-Pb collisions, and thereby help to shed light on the pending questions concerning the mass dependence of the energy-loss mechanisms in the Quark-Gluon Plasma.

Zusammenfassung

Zerfälle von Beauty-Hadronen können durch den Nachweis von Elektronen gemessen werden, deren Spuren räumlich versetzt zum Primärvertex verlaufen. Die von ALICE gebotenen Möglichkeiten zur Elektronenidentifikation und Spurrekonstruktion erfüllen alle Anforderungen für diese Aufgabe. Während die hohen Verzweigungsverhältnisse zu elektronischen Zerfällen einen hinreichenden Ertrag an Elektronen aus Beauty-Zerfällen gewährleisten, gestattet es die breite Stoßparameter-Verteilung aufgrund der langen Lebensdauer und der Zerfallskinematik von Beauty-Hadronen, Elektronen aus deren Zerfällen auf statistischer Grundlage vom Elektronenuntergrund zu trennen.

In der vorliegenden Arbeit wird die Analyse von Elektronen aus Zerfällen von Beauty-Hadronen in Proton-Proton-Kollisionen bei Schwerpunktsenergien von 7 TeV und 2.76 TeV beschrieben. Mithilfe dreier Detektoren des ALICE Central Barrel, ITS, TPC und TOF, werden p_{T}-differentielle Elektronenspektren für mittlere Rapidität ($|y| < 0.8$) und Transversalimpulse zwischen 1 und 8 GeV/c gemessen.

Die Informationen aus den Signalen von TPC und TOF werden miteinander kombiniert, um reine Proben von Elektronen zu identifizieren, deren Signal-zu-Untergrund-Verhältnis anschließend durch die Bedingung eines minimalen Stoßparameters der Spuren gegenüber dem Primärvertex in der $x - y$-Ebene verbessert wird. Spuren aus Photonenkonversionen außerhalb der innersten ITS-Lage, die eine breite Stoßparameter-Verteilung aufweisen, werden durch die Anforderung von Signalen in beiden SPD-Lagen des ITS ausgeschlossen. Die verbleibende Hadronen-Verunreinigung in der gewählten Probe von Elektronenspuren wird auf statistischer Grundlage aus den Verteilungen der Energiedeposition pro Längeneinheit in der TPC bestimmt.

Eine entscheidende Herausforderung für diese Analyse ist die Subtraktion des Elektronenuntergrunds aus Photonenkonversionen sowie Zerfällen von leichten Mesonen und Charm-Hadronen vom gemessenen inklusiven Elektronenspektrum. Um die entsprechenden Elektronenmengen korrekt in ihrer Transversalimpulsverteilung zu reproduzieren, werden Elektronenspektren aus PYTHIA-Simulationen auf Grundlage eines Vergleichs von bereits vorliegenden Messungen von Charm-Hadronen, π^0 und η zu deren Darstellung in Simulationen gewichtet. Kleinere Beiträge anderer leichter Mesonen und, im Falle der Analyse für $\sqrt{s} = 2.76$ TeV, des η-Mesons werden durch m_{T}-Skalierung der gemessenen π^0-Spektren abgeschätzt.

Das Signal-zu-Untergrund-Verhältnis der selektierten Elektronenspektren wächst zu höheren p_{T}, wo Zerfälle von Beauty-Hadronen die vorherrschende Elektronen-

quelle sind. Elektronen aus Charm-Hadronen-Zerfällen stellen den dominierenden Untergrund bei hohen Transversalimpulsen dar, wohingegen Photonenkonversionen und Zerfälle leichter Mesonen bei niedrigeren p_{T} bedeutsamer werden. Während die gemessenen Spektren von Charm-Hadronen die größte Quelle systematischer Unsicherheiten für die Messungen bei niedrigen p_{T} sind, ist der Abzug des Elektronenuntergrundes aus Zerfällen leichter Flavours nur mit geringen zusätzlichen Unsicherheiten verbunden.

Sowohl für pp-Kollisionen bei $\sqrt{s} = 7$ TeV als auch bei $\sqrt{s} = 2.76$ TeV übertrifft der Produktionswirkungsquerschnitt für Elektronen aus Beauty-Hadronen-Zerfällen den von Elektronen aus Charm-Hadronen-Zerfällen für Elektronen-$p_{\mathrm{T}} \gtrsim 4$ GeV/c. Für beide Kollisionsenergien werden die gemessenen p_{T}-differentiellen Elektronenspektren aus Beauty- und Charm-Zerfällen durch pQCD-Rechnungen der Modelle FONLL, GM-VFNS und k_{T}-Faktorisierung gut beschrieben. Durch Nutzung der bemerkenswert exakt zutreffenden Vorhersage bezüglich des $\sqrt{s}$-Skalierungsverhaltens der Beauty-Produktion durch FONLL-Berechnungen wird die Genauigkeit des gemessenen p_{T}-differentiellen Elektronenspektrums aus Beauty-Hadronen-Zerfällen bei $\sqrt{s} = 2.76$ TeV, der Referenz für Messungen in Pb-Pb-Kollisionen, durch Kombination mit dem bei $\sqrt{s} = 7$ TeV gemessenen Spektrum erhöht. Indem die für mittlere Rapidität gemessen Elektronenspektren anhand von FONLL-Berechnungen auf die gesamte Rapiditäts- und Transversalimpulsspanne extrapoliert werden, ergeben sich die Gesamtwirkungsquerschnitte für Beauty-Produktion bei $\sqrt{s} = 2.76$ TeV und $\sqrt{s} = 7$ TeV. Ein gewichteter Durchschnitt für den Wirkungsquerschnitt bei $\sqrt{s} = 7$ TeV wird aus den Ergebnissen der vorliegenden Analyse und der in [Abe12h] beschriebenen Messung ermittelt.

Vorläufige Analysen wurden durchgeführt hinsichtlich der Gewichtung des Elektronenuntergrundes aus Zerfällen leichter Mesonen und aus Photonenkonversionen, sowie bezüglich der Unterdrückung des Untergrundes aus Photonenkonversionen. Die letztere Untergrundkomponente stellt eines der kritischsten Probleme der Analyse von Elektronen aus Beauty-Hadronen-Zerfällen in Pb-Pb-Kollisionen dar, die Anfang 2014 begonnen wurde. Gleichzeitig wird die Elektronenproduktion aus Zerfällen von Beauty-Hadronen in p-Pb-Kollisionen bei $\sqrt{s_{\mathrm{NN}}} = 5.02$ TeV analysiert, um den Einfluss kalter Kernmaterie zu erforschen [Kwe].

Die in dieser Arbeit vorgestellten Ergebnisse eröffnen nicht nur eine bedeutende Möglichkeit zur Überprüfung von Berechnungen der perturbativen QCD, welche die Beauty- und Charm-Produktion am LHC sehr gut beschreiben, sondern sind ebenfalls eine unverzichtbare Referenz für zukünftige Messungen in Pb-Pb-Kollisionen. Somit tragen sie dazu bei, offene Fragen bezüglich der Energieabhängigkeit der Energieverlust-Mechanismen im Quark-Gluon-Plasma zu beantworten.

A The ALICE Global Coordinate System

The global coordinate system of ALICE is defined as a right-handed orthogonal Cartesian system whose origin $x = y = z = 0$ is situated at the nominal beam interaction point. The two sides of ALICE along the beam direction are called *Side A* and *Side C*, defined as depicted in Figure A.1. The definitions of axes x, y, and z, of the azimuthal angle ϕ and the polar angle ϑ are the following [Bet08]:

- x-axis: perpendicular to the beam direction, pointing horizontally towards the accelerator centre.
- y-axis: perpendicular to the beam direction and the x-axis, pointing upward.
- z-axis: perpendicular to the x and y-axis and parallel to the beam direction, pointing towards Side A.
- azimuthal angle ϕ: increasing clockwise from x ($\phi = 0$) to y ($\phi = \pi/2$), with the observer looking towards Side A.
- polar angle ϑ: increasing from the positive part of the z-axis ($\vartheta = 0$) via the $x - y$-plane ($\vartheta = \pi/2$) to the negative part of the z-axis ($\vartheta = \pi$).

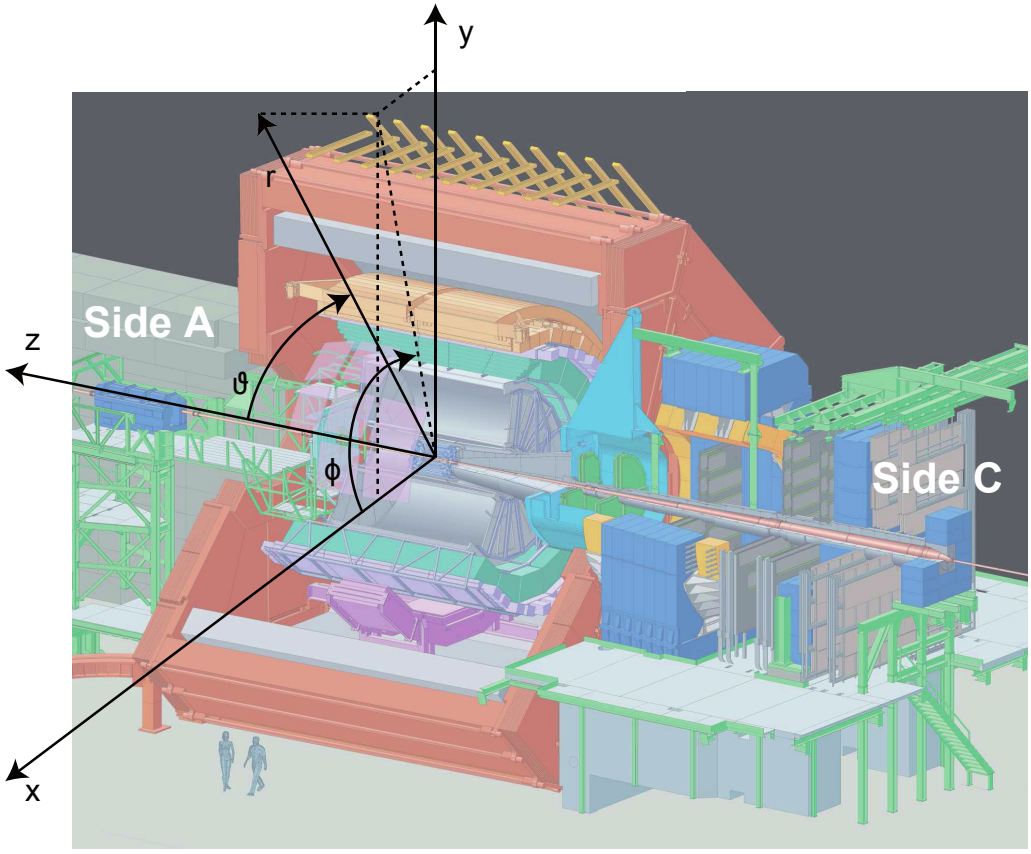

Figure A.1: The ALICE coordinate system. Taken from [Wil10], therein adapted from [Gro09].

B Kinematic Variables

In the following, the definitions of several kinematic variables will be given that are used to describe the physics of ultra-relativistic particle collisions. In this context, it is most favourable to operate with variables that have simple properties under Lorentz transformations. In all equations given in this appendix, the convention $\hbar \equiv c \equiv 1$ will be followed.

A particle is described by its *four-momentum*

$$\vec{P} = (E, p_x, p_y, p_z) \tag{B.1}$$

consisting of the total energy E of the particle and the three components of its momentum $\vec{p}$. The definition of the absolute value of $\vec{P}$ is chosen in such a way that it is equal to the Lorentz-invariant mass m_{inv}, and therefore also to the rest mass m_0 of the particle:

$$P^2 \equiv E^2 - p_x^2 - p_y^2 - p_z^2 = m_{\mathrm{inv}}^2 \qquad \Rightarrow \qquad |P| = m_{\mathrm{inv}} \qquad . \tag{B.2}$$

In the centre-of-mass frame of a particle collision, the energy $\sqrt{s}$ of the collision system is given by the square root of the *Mandelstam variable* s:

$$\sqrt{s} = \sqrt{(P_1 + P_2)^2} = \sqrt{(E_1 + E_2)^2 - (\vec{p}_1 + \vec{p}_2)^2} = E_1 + E_2 \qquad , \tag{B.3}$$

where the indices 1 and 2 stand for the two colliding particles, and $\vec{p}_1 = -\vec{p}_2$.

Furthermore, one distinguishes between the components of the particle momentum parallel to the beam axis (in ALICE the $z-$axis) and transverse to it. The former is the *longitudinal momentum* p_{L}, the latter the *transverse momentum* p_{T}. In the ALICE coordinate system (see Appendix A), they can be given as:

$$\begin{aligned} p_{\mathrm{L}} &= p\cos\theta = p_z \qquad , \\ p_{\mathrm{T}} &= p\sin\theta = \sqrt{(p_x^2 + p_y^2)} \qquad . \end{aligned} \tag{B.4}$$

While p_{T} is by definition invariant under a Lorentz transformation in z-direction, the transformation properties of p_{L} are not simple. Therefore, two dimensionless variables are defined that are more convenient for calculations in high-energy physics: the rapidity y and the pseudo-rapidity η. They are defined as

$$y = \frac{1}{2} \ln \frac{E + p_z}{E - p_z} \tag{B.5}$$

and

$$\eta = -\ln\left\{ tan\left(\frac{\theta}{2}\right)\right\} = \frac{1}{2}\left(\frac{|\vec{p}| + p_z}{|\vec{p}| - p_z}\right) \quad . \tag{B.6}$$

Neither of them is Lorentz-invariant, but the rapidity has the advantage of being additive under a Lorentz transformation in z-direction, as

$$y' = y + atanh(\beta) \quad , \tag{B.7}$$

where y' is the rapidity in a reference frame moving at a velocity β along the z-axis, in relation to the reference frame in which y is defined. For different centre-of-mass frames, distributions in y are shifted by a constant value, but always keep the same shape. A drawback of the variable y is that it depends on the total energy E, which is only known if the particle species has been identified.

For many purposes, the pseudo-rapidity η is therefore used instead, for whose determination only a measurement of the angle θ between the direction of the particle momentum and the z-axis is necessary. At high energies $E \gg m_0$, η is a good approximation of y. Introducing another variable, the *transverse mass* $m_{\mathrm{T}} = \sqrt{m_0^2 + p_{\mathrm{T}}^2}$, the following relations between rapidity, pseudo-rapidity, the momentum components and the total energy of a particle can be established:

$$E = m_{\mathrm{T}} \cosh(y) = p_{\mathrm{T}} \cosh(\eta) \quad , \tag{B.8}$$

$$p_{\mathrm{L}} = m_{\mathrm{T}} \sinh(y) = p_{\mathrm{T}} \sinh(\eta) \quad . \tag{B.9}$$

C Run Numbering for Impact Parameter Quality Assurance

Table C.1: List of runs from the period LHC10d, pass2.

Run Number	Events after Physics and Event Selection	Number in Impact Parameter QA Plots	Comments
122374	3510359	1	
122375	666173	2	
124751	277453	3	
125023	76873	4	rejected run
125085	4048207	5	
125097	3425744	6	
125100	296555	7	
125101	1944499	8	
125134	2812386	9	
125296	4576667	10	
125630	1636307	11	
125632	2357714	12	
125633	619548	13	
125842	2040208	14	
125843	333781	15	
125844	138560	16	rejected run
125847	540171	17	
125848	536805	18	
125849	1684797	19	
125850	1913766	20	
125851	1387282	21	
125855	2181581	22	
126004	461706	23	
126007	3289784	24	
126008	690621	25	

Run Number	Events after Physics and Event Selection	Number in Impact Parameter QA Plot	Comments
126073	2142711	26	
126078	4347792	27	
126081	1469224	28	
126082	4501806	29	
126088	6203448	30	
126090	5728321	31	
126097	1171200	32	
126158	6039652	33	
126160	1593466	34	
126167	981193	35	rejected run
126168	1721123	36	
126283	1140926	37	
126284	6137589	38	
126285	220624	39	
126351	3412296	40	rejected run
126352	1714345	41	rejected run
126359	1032650	42	
126403	386189	43	
126404	4669674	44	
126405	39104	45	
126406	3568470	46	
126407	4000706	47	
126408	2001562	48	
126409	1269478	49	
126422	3364081	50	
126424	6138320	51	
126425	1171526	52	
126432	6386609	53	
126437	1441493	54	

Table C.2: List of runs from the period LHC11a, *pass2*. All runs are accepted for analysis. For p_{T} below 2 GeV/c, only runs with available TOF PID are used.

Run Number	Events after Physics and Event Selection	Number in Impact Parameter QA Plots	TOF PID Available
146801	1.4M	4	Yes
146802	2.9M	5	Yes
146803	0.2M	6	Yes
146804	6.3M	7	Yes
146805	13.1M	8	Yes
146806	2.2M	9	Yes
146817	1.2M	11	Yes
146824	6.3M	12	Yes
Total	33.8M		Yes
146746	0.80M	1	No
146747	2.75M	2	No
146748	1.06M	3	No
146807	0.24M	10	No
146856	2.34M	13	No
146858	5.63M	14	No
146859	3.63M	15	No
146860	1.23M	16	No
Total	17.7M		No
Sum	51.5M		

D Electron Background: Decay Channels

Table D.1: Light-meson decay channels contributing to the background electron yield via electronic or photonic decays, or by generating particles that subsequently decay through electronic or photonic channels [Beh12].

meson	decay channel	branching ratio
π^0	$2\ \gamma$	$(98.823 \pm 0.034)\%$
	$e^+e^-\gamma$	$(1.174 \pm 0.035)\%$
η	$2\ \gamma$	$(39.41 \pm 0.20)\%$
	$3\pi^0$	$(32.68 \pm 0.23)\%$
	$\pi^+\pi^-\pi^0$	$(22.92 \pm 0.28)\ \%$
	$e^+e^-\gamma$	$(6.9 \pm 0.4)\cdot 10^{-3}$
ρ	$\pi^+\pi^-\gamma$	$(9.9 \pm 1.6)\cdot 10^{-3}$
	e^+e^-	$(4.72 \pm 0.05)\cdot 10^{-5}$
ω	$\pi^+\pi^-\pi^0$	$(89.2 \pm 0.7)\%$
	$\pi^0\gamma$	$(8.28 \pm 0.28)\%$
	$\pi^0e^+e^-$	$(7.7 \pm 0.6)\cdot 10^{-4}$
η'	$\pi^+\pi^-\eta$	$(42.9 \pm 0.7)\%$
	$\rho^0\gamma$	$(29.1 \pm 0.5)\%$
	$\pi^0\pi^0\eta$	$(22.2 \pm 0.8)\%$
	$\pi^+\pi^-e^+e^-$	$2.4^{+1.3}_{-1.0} \cdot 10^{-3}$
Φ	K^+K^-	$(48.9 \pm 0.5)\%$
	$K^0_S K^0_L$	$(34.2 \pm 0.4)\%$
	$\rho\pi + \pi^+\pi^-\pi^0$	$(15.32 \pm 0.32)\%$
	$\eta\gamma$	$(1.309 \pm 0.024)\%$
	e^+e^-	$(2.954 \pm 0.030)\cdot 10^{-4}$
	ηe^+e^-	$(1.15 \pm 0.10)\cdot 10^{-4}$

Table D.2: Charm-hadron decay channels contributing to the background electron yield via electronic or photonic decays, or by generating particles that subsequently decay through electronic or photonic channels [Beh12].

	decay channel	branching ratio
D^0	e^+ semileptonic	$(6.49 \pm 0.11)\%$
	K^- anything	(25.7 ± 1.4) %
	K^0 anything $\bar{K}^0$ anything	$(47 \pm 4)\%$
$D^{+/-}$	e^+ semileptonic	$(16.07 \pm 0.30)\%$
	K^- anything	(54.7 ± 2.8) %
	K^0 anything $\bar{K}^0$ anything	$(61 \pm 5)\%$
$D_s^{+/-}$	e^+ semileptonic	$(6.5 \pm 0.4)\%$
	π^0 anything	$(123 \pm 7)\%$
	η anything	$(29.9 \pm 2.8)\%$
	K^+K^- anything	$(15.8 \pm 0.7)\%$
	$K_S^0K^+$ anything	$(5.8 \pm 0.5)\%$
Λ_c	e^+ anything	$(4.5 \pm 1.7)\%$

E Parameterized and Simulated Light-Meson Spectra for the Calculation of Background Weights

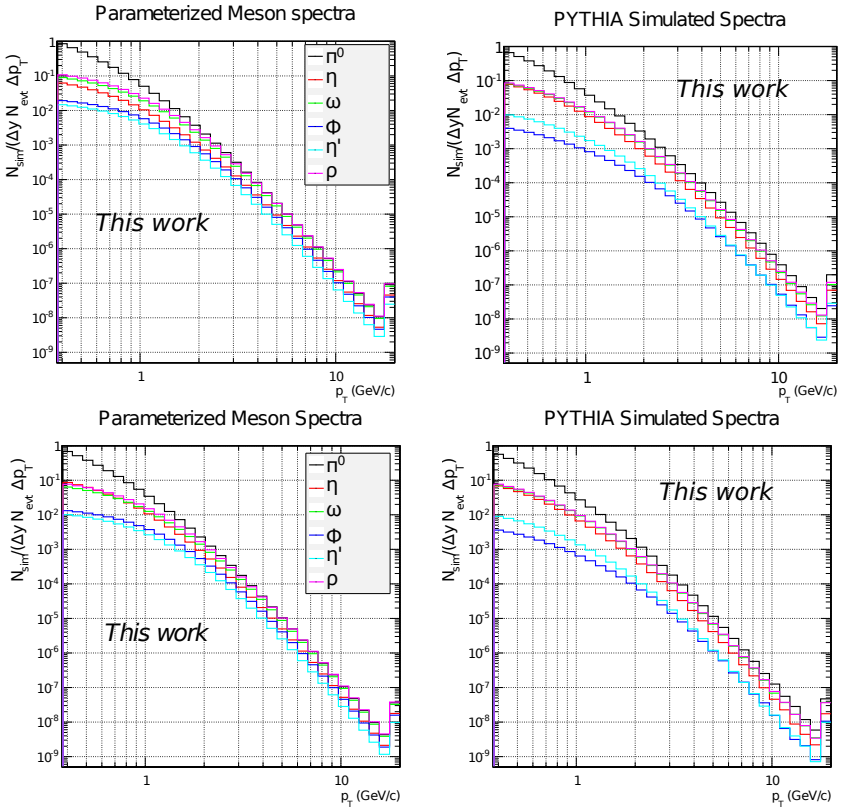

Figure E.1: Left: parameterized light-meson spectra for pp collisions at $\sqrt{s} = 7$ TeV (upper panel) and 2.76 TeV (lower panel; see Section 4.8) used for the calculation of background weights in this work. The π^0 spectra for both centre-of-mass energies and the η spectrum for $\sqrt{s} = 7$ TeV are based on measurements. For π^0 at $\sqrt{s} = 2.76$ TeV, a preliminary measurement is used that will be replaced by the final one from [Abe14c] (see Figure E.2) in the future. All other spectra are obtained by m_{T}-scaling based on the π^0 measurements. Right: corresponding spectra from PYTHIA simulations. In all cases, the highest p_{T} bin sums up all contributions from higher p_{T}, for which one common weighting factor is determined.

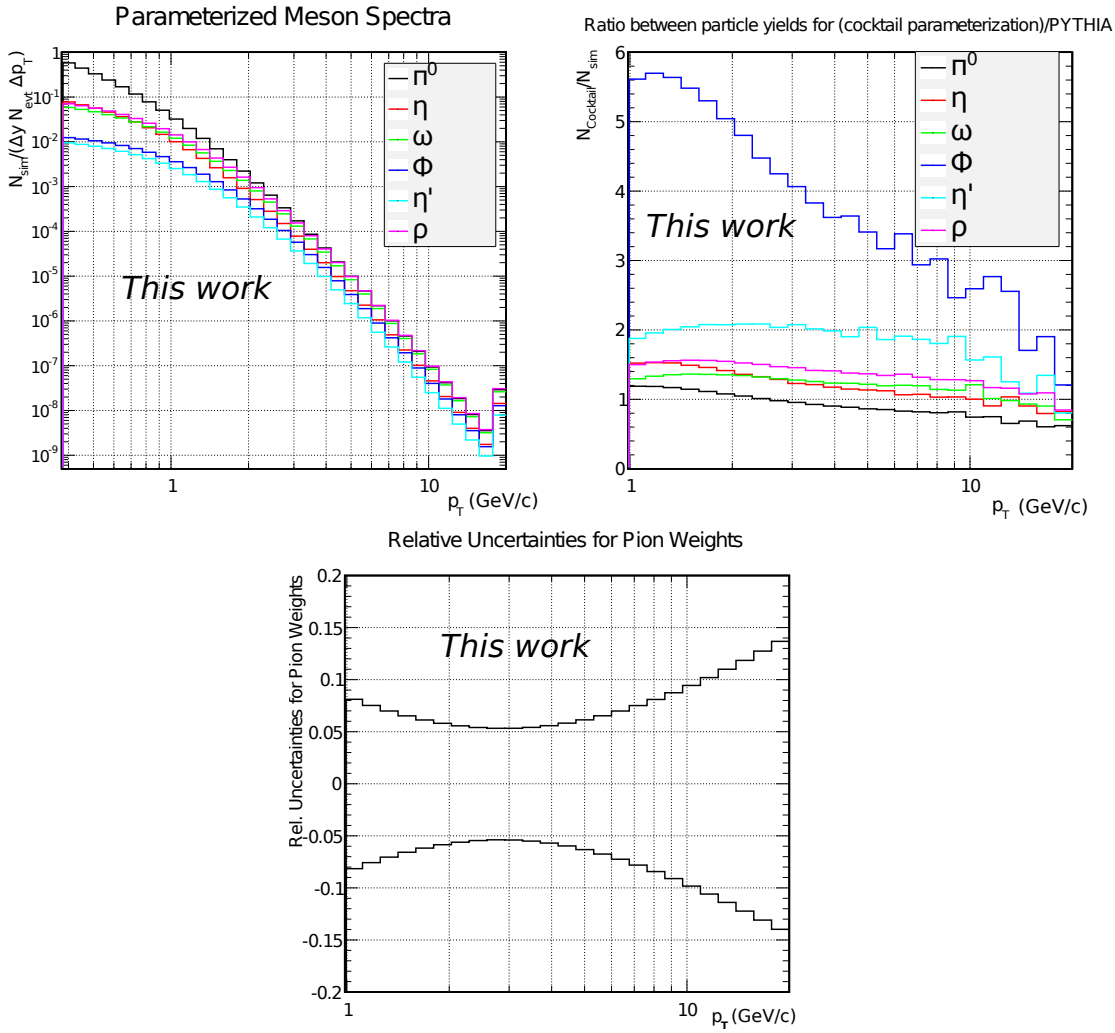

Figure E.2: Upper left: parameterized light-meson spectra for pp collisions at $\sqrt{s} = 2.76$ TeV, based on the π^0 measurement presented in [Abe14c]. Upper right: weighting factors from the ratios of the light-meson yields in the upper left panel to the yields generated by PYTHIA (cf. Figure E.1) for pp collisions at $\sqrt{s} = 2.76$ TeV. Lower panel: corresponding relative uncertainties of the weighting factors for π^0 decays at $\sqrt{s} = 2.76$ TeV.

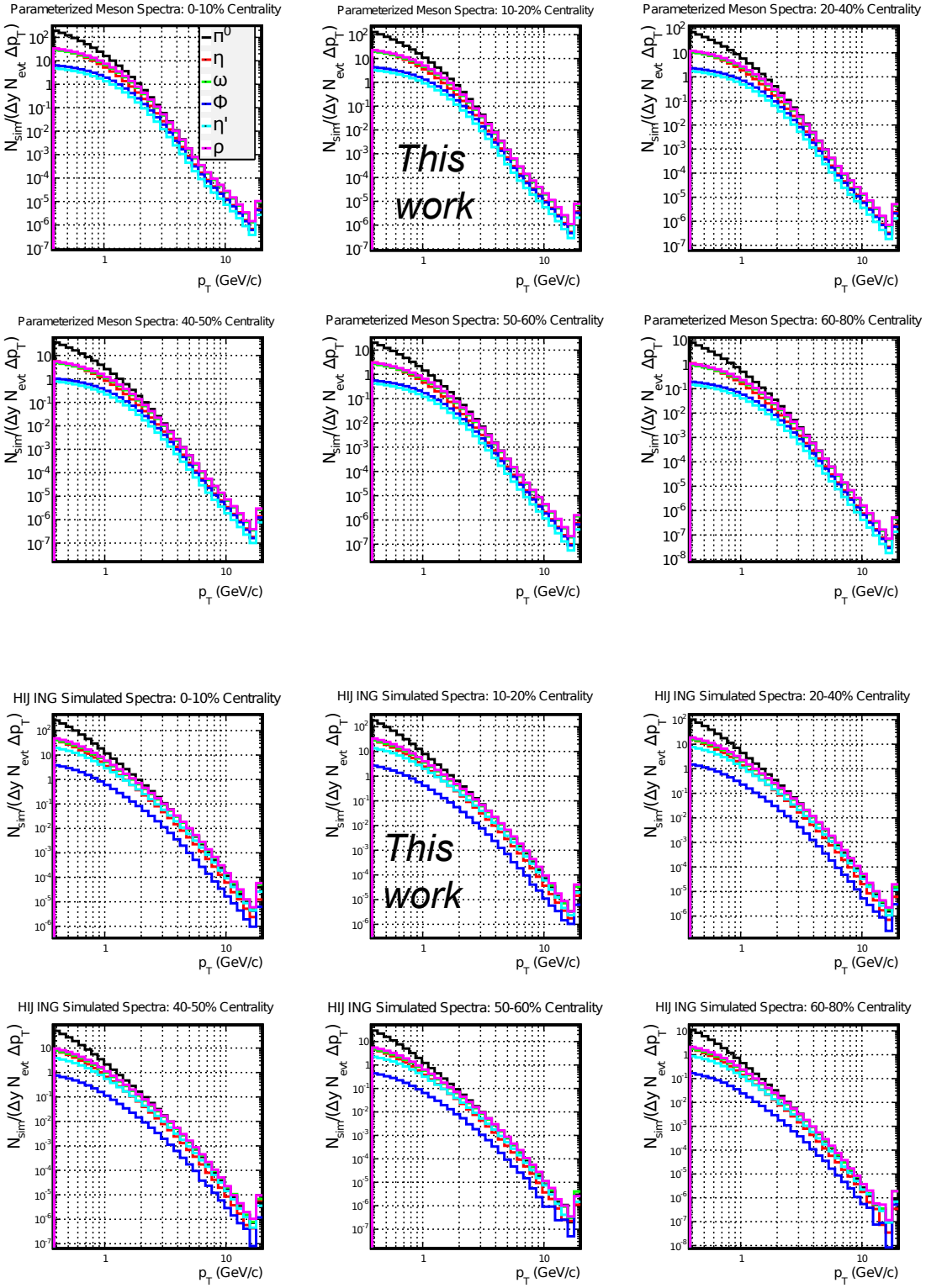

Figure E.3: Parameterized (upper panels) and HIJING-simulated (lower panels) light-meson spectra for different centralities of Pb-Pb collisions at $\sqrt{s_{\mathrm{NN}}} = 2.76$ TeV. The parameterization for the π^0 spectrum has been obtained from measurements, all other spectra by m_{T}-scaling.

F Differential Production Cross Section of Electrons from Beauty-Hadron Decays

F.1 pp Collisions at $\sqrt{s} = 7$ TeV

Table F.1: p_{T}-differential invariant production cross section for electrons from beauty-hadron decays for $\sqrt{s} = 7$ TeV. The cross section normalization uncertainty of 3.5% is not included in the systematic uncertainties.

p_{T} (GeV/c)	$\frac{1}{2\pi p_{\mathrm{T}}} \frac{\mathrm{d}^2\sigma}{\mathrm{d}p_{\mathrm{T}}\mathrm{d}y} \pm \mathrm{stat} \pm \mathrm{sys}$ (nb/(GeV/c ^{2}))
1.00 - 1.10	$(8.2 \pm 2.6^{+3.6}_{-3.4}) \cdot 10^2$
1.10 - 1.20	$(5.2 \pm 1.8^{+2.1}_{-2.0}) \cdot 10^2$
1.20 - 1.30	$(2.9 \pm 1.4^{+1.1}_{-1.0}) \cdot 10^2$
1.30 - 1.40	$(2.5 \pm 1.1^{+0.9}_{-0.8}) \cdot 10^2$
1.40 - 1.50	$(3.4 \pm 1.0^{+1.1}_{-1.0}) \cdot 10^2$
1.50 - 1.75	$192 \pm 47^{+59}_{-54}$
1.75 - 2.00	$93 \pm 30^{+26}_{-24}$
2.00 - 2.25	$73 \pm 21^{+19}_{-17}$
2.25 - 2.50	$72 \pm 15^{+18}_{-16}$
2.50 - 2.75	$47 \pm 11^{+9}_{-10}$
2.75 - 3.00	$29.0 \pm 8.5^{+5.2}_{-5.8}$
3.00 - 3.50	$26.2 \pm 4.5^{+4.3}_{-5.2}$
3.50 - 4.00	$14.4 \pm 2.8^{+2.3}_{-2.8}$
4.00 - 4.50	$9.4 \pm 1.9^{+1.4}_{-1.8}$
4.50 - 5.00	$7.0 \pm 1.4^{+1.1}_{-1.3}$
5.00 - 5.50	$3.65 \pm 0.90^{+0.55}_{-0.68}$
5.50 - 6.00	$1.76 \pm 0.57^{+0.27}_{-0.33}$
6.00 - 7.00	$1.46 \pm 0.33^{+0.22}_{-0.27}$
7.00 - 8.00	$0.84 \pm 0.21^{+0.13}_{-0.16}$

F.2 pp Collisions at $\sqrt{s} = 2.76$ TeV

Table F.2: p_{T}-differential invariant production cross section for electrons from beauty-hadron decays for $\sqrt{s} = 2.76$ TeV. The cross section normalization uncertainty of 1.9% is not included in the systematic uncertainties.

p_{T} (GeV/c)	$\frac{1}{2\pi p_{\mathrm{T}}} \frac{\mathrm{d}^2\sigma}{\mathrm{d}p_{\mathrm{T}}\mathrm{d}y} \pm \mathrm{stat} \pm \mathrm{sys}$ (nb/(GeV/c ^{2}))
1.00 - 1.10	$(2.6 \pm 1.8^{+1.2}_{-1.7}) \cdot 10^2$
1.10 - 1.20	$(3.1 \pm 1.4^{+1.3}_{-1.7}) \cdot 10^2$
1.20 - 1.30	$(2.5 \pm 1.4^{+1.0}_{-1.2}) \cdot 10^2$
1.30 - 1.40	$185 \pm 92^{+68}_{-81}$
1.40 - 1.50	$115 \pm 74^{+40}_{-47}$
1.50 - 1.75	$82 \pm 35^{+26}_{-31}$
1.75 - 2.00	$96 \pm 26^{+28}_{-34}$
2.00 - 2.25	$52 \pm 18 \pm 13$
2.25 - 2.50	$36 \pm 13 \pm 9$
2.50 - 2.75	$22.0 \pm 8.9^{+5.1}_{-5.3}$
2.75 - 3.00	$14.2 \pm 6.5 \pm 3.3$
3.00 - 3.50	$10.6 \pm 3.4 \pm 2.4$
3.50 - 4.00	$6.9 \pm 2.1^{+1.5}_{-1.6}$
4.00 - 4.50	$3.1 \pm 1.2 \pm 0.7$
4.50 - 5.00	$2.8 \pm 1.1 \pm 0.6$
5.00 - 5.50	$1.32 \pm 0.89 \pm 0.29$
5.50 - 6.00	$1.22 \pm 0.66^{+0.26}_{-0.27}$
6.00 - 7.00	$0.38 \pm 0.26^{+0.08}_{-0.09}$
7.00 - 8.00	$0.17 \pm 0.15^{+0.04}_{-0.06}$

Bibliography

[Aad08] G. Aad *et al.*. *JINST* **3**(08) (2008) S08003.

[Aad12a] G. Aad *et al.*. *Nucl. Phys.* **B864**(3) (2012) 341 .

[Aad12b] G. Aad *et al.*. *Phys. Lett.* **B707**(5) (2012) 438 .

[Aad12c] G. Aad *et al.*. *Phys. Lett.* **B716** (2012) 1.

[Aad13] G. Aad *et al.*. *JHEP* **1310** (2013) 042.

[Aai12] R. Aaij *et al.*. *JHEP* **1204** (2012) 093.

[Aai13a] R. Aaij *et al.*. *JHEP* **1308** (2013) 117.

[Aai13b] R. Aaij *et al.*. *Nucl. Phys.* **B871** (2013) 1.

[Aam08] K. Aamodt *et al.*. *JINST* **3**(08) (2008) S08002.

[Aam11a] K. Aamodt *et al.*. *Eur. Phys. J.* **C71**(6) (2011) 1.

[Aam11b] K. Aamodt *et al.*. *Phys. Lett.* **B704** (2011) 442.

[Aam12] K. Aamodt *et al.*. *JHEP* **01** (2012) 128.

[Aba98] A. Abada and M. C. Birse. *Phys. Rev.* **D57** (1998) 292.

[Abb00] B. Abbott *et al.*. *Phys. Lett.* **B487**(3-4) (2000) 264 .

[Abe07] B. Abelev *et al.*. *Phys. Rev. Lett.* **98** (2007) 192301.

[Abe11] B. Abelev *et al.*. *Phys. Rev. Lett.* **106** (2011) 159902.

[Abe12a] B. Abelev *et al.*. *Phys. Lett.* **B718**(2) (2012) 279 .

[Abe12b] B. Abelev *et al.*. *Phys. Lett.* **B708**(3-5) (2012) 265 .

[Abe12c] B. Abelev *et al.*. *JHEP* **2012**(7) (2012) 1.

[Abe12d] B. Abelev *et al.*. *JHEP* **2012**(7) (2012) 1.

[Abe12e] B. Abelev *et al.*. *JHEP* **2012**(1) (2012) 1.

[Abe12f] B. Abelev *et al.*. *JHEP* **1201** (2012) 128.

[Abe12g] B. Abelev *et al.*. *Phys. Rev.* **D86** (2012) 112007.

[Abe12h] B. Abelev *et al.*. *JHEP* **1211** (2012) 065.

[Abe12i] B. Abelev *et al.*. *JHEP* **2012**(11) (2012) 1.

[Abe12j] B. Abelev *et al.*. *Phys. Lett.* **B717** (2012) 162.

[Abe12k] B. Abelev *et al.*. *Phys. Rev. Lett.* **109** (2012) 112301.

[Abe12l] B. Abelev *et al.*. *JHEP* **1209** (2012) 112.

[Abe13a] B. Abelev *et al.*. *Phys. Lett.* **B721** (2013) 13.

[Abe13b] B. Abelev *et al.*. *Eur. Phys. J.* **C73** (2013) 2456.

[Abe14a] B. Abelev *et al.* URL `https://aliceinfo.cern.ch/ArtSubmission/node/166`.

[Abe14b] B. Abelev *et al.* ALICE Analysis Note, URL `https://aliceinfo.cern.ch/ArtSubmission/node/159`.

[Abe14c] B. Abelev *et al.* ALICE Analysis Note, URL `https://aliceinfo.cern.ch/ArtSubmission/node/153`.

[Abe14d] B. Abelev *et al.* (ALICE Collaboration) `1402.4476`.

[Abl13] M. Ablikim *et al.*. *Phys. Rev. Lett.* **110** (2013) 252001.

[Acc07] A. Accardi. *Phys. Rev.* **C76** (2007) 034902.

[Aco02] D. Acosta *et al.*. *Phys. Rev. D* **65** (2002) 052005.

[Aco03] D. Acosta *et al.*. *Phys. Rev. Lett.* **91** (2003) 241804.

[Aco05] D. Acosta *et al.*. *Phys. Rev. D* **71** (2005) 032001.

[Ada06a] J. Adams *et al.*. *Phys. Lett.* **B637** (2006) 161.

[Ada06b] A. Adare *et al.*. *Phys. Rev. Lett.* **97** (2006) 252002.

[Ada06c] A. Adare *et al.*. *Phys. Rev. Lett.* **97** (2006) 252002.

[Ada07] A. Adare *et al.*. *Phys. Rev. Lett.* **98** (2007) 172301.

[Ada09] A. Adare *et al.*. *Phys. Rev. Lett.* **103** (2009) 082002.

[Ada11] A. Adare *et al.*. *Phys. Rev.* **C84** (2011) 044902.

[Ada12] A. Adare *et al.*. *Cold-nuclear-matter effcts on heavy-quark production in d+Au collisions at* $\sqrt{s_{NN}} = 200$ *GeV*. 2012. 1208.1293.

[Ada13] A. Adare *et al.*. *Phys. Rev.* **C88** (2013) 024906.

[Adc02] K. Adcox *et al.*. *Phys. Rev. Lett.* **88** (2002) 192303.

[Adl06] S. S. Adler *et al.*. *Phys. Rev. Lett.* **96** (2006) 032301.

[Adl07a] S. S. Adler *et al.*. *Phys. Rev.* **C75** (2007) 024909.

[Adl07b] S. S. Adler *et al.*. *Phys. Rev. D* **76** (2007) 092002.

[Aga11] H. Agakishiev *et al.*. *Phys. Rev. D* **83** (2011) 052006.

[Agg00] M. Aggarwal *et al.*. *Direct photon production in 158-A-GeV Pb-208 + Pb-208 collisions*. 2000. nucl-ex/0006007.

[Agg10] M. Aggarwal *et al.*. *Phys. Rev. Lett.* **105** (2010) 202301.

[Ago03] S. Agostinelli *et al.*. *Nucl. Instrum. Meth.* **A506** (2003) 250.

[Alb95] R. Albrecht *et al.*. *Phys. Lett.* **B361** (1995) 14.

[Ale06] B. Alessandro *et al.*. *Journal of Physics G: Nuclear and Particle Physics* **32**(10) (2006) 1295.

[Alia] *AliRoot tag v5-03-27-AN*. URL http://alisoft.cern.ch/viewvc/tags/v5-03-27-AN/?root=AliRoot.

[Alib] *AliRoot tag v5-03-42-AN*. URL http://alisoft.cern.ch/viewvc/tags/v5-03-42-AN/?root=AliRoot.

[ALI95] *ALICE: Technical proposal for a Large Ion collider Experiment at the CERN LHC*. LHC Tech. Proposal. CERN, Geneva, 1995.

[Ali11] A. Alici *et al.*. *LHC Bunch Current Normalisation for the October 2010 Luminosity Calibration Measurements*, 2011. CERN-ATS-Note-2011-016 PERF.

[Alv08] J. Alves, A. Augusto *et al.*. *JINST* **3** (2008) S08005.

[ARO] *ALICE Off-line project*. URL http://aliweb.cern.ch/Offline/.

[Aro12] T. Aronsson ALICE Analysis Note, URL https://aliceinfo.cern.ch/Notes/node/131.

[Ars13] I.-C. Arsene. *J. Phys. Conf. Ser.* **426** (2013) 012023.

[ASV] *AliRoot SVN repository.* URL `http://alisoft.cern.ch/viewvc/?root=AliRoot`.

[Ave] R. Averbeck. Private communication.

[Ave11a] A. Averbeck *et al.* ALICE Analysis Note, URL `https://twiki.cern.ch/twiki/pub/ALICE/InternalAnalysisNotes/HFEnote.pdf`.

[Ave11b] R. Averbeck *et al.*. *Reference Heavy Flavour Cross Sections in pp Collisions at $\sqrt{s}$ = 2.76 TeV, using a pQCD-Driven $\sqrt{s}$-Scaling of ALICE Measurements at $\sqrt{s}$ = 7 TeV*. 2011. `1107.3243`.

[Ave12] R. Averbeck *et al.*. *Measurement of electrons from beauty hadron decays in pp collisions at $\sqrt{s} = 7$ TeV*, 2012. ALICE Analysis Note, URL `https://aliceinfo.cern.ch/Notes/node/79`.

[Ave13a] R. Averbeck *et al.*. *Measurement of electrons from beauty hadron decays in pp collisions at $\sqrt{s} = 2.76$ TeV*, 2013. ALICE Analysis Note, URL `https://aliceinfo.cern.ch/Notes/node/135`.

[Ave13b] R. Averbeck *et al.*. *Measurement of electrons from semi-leptonic decays of charm and beauty hadrons in proton-proton collisions at $\sqrt{s}$=2.76 TeV with TPC and TOF*, 2013. ALICE Analysis Note, URL `https://aliceinfo.cern.ch/Notes/node/122`.

[Bai97a] R. Baier, Y. L. Dokshitzer, A. H. Mueller, S. Peigne, and D. Schiff. *Nucl. Phys.* **B484** (1997) 265.

[Bai97b] R. Baier, Y. L. Dokshitzer, A. H. Mueller, S. Peigne, and D. Schiff. *Nucl. Phys.* **B483** (1997) 291.

[Bat12] B. Bathen. *Jet Measurements and Reconstruction Biases in Proton-Proton and Pb-Pb Collisions with ALICE at the LHC*, 2012. Ph.D. thesis, Westfälische Wilhelms-Universität Münster.

[Beh12] J. Behringer *et al.*. *Phys. Rev.* **D86** (2012) 010001.

[Ben87] Bengtsson, H-U and Sjöstrand, T. *Comput. Phys. Commun.* **46**(1) (1987) 43 .

[Bet08] L. Betev and P. Chochula. *Definition of the ALICE Coordinate System and Basic Rules for Sub-detector Components Numbering*, 2008. ALICE Internal note, ALICE-INT-2003-038.

[Bil84] P. Billoir. *Nucl. Instrum. Meth.* **225**(2) (1984) 352 .

[Bjo82] J. D. Bjorken. *FERMILAB-PUB-82-059-THY, FERMILAB-PUB-82-059-T* .

[Bjo83] J. D. Bjorken. *Phys. Rev. D* **27** (1983) 140.

[Bla10] D. Blaschke, F. Sandin, V. Skokov, and S. Typel. *Acta Phys. Polon. Supp.* **3** (2010) 741.

[BM07] P. Braun-Munzinger and J. Stachel. *Nature* **448** (2007) 302 .

[Bol13] P. Bolzoni and G. Kramer. *Nucl. Phys.* **B872** (2013) 253.

[Bor10] S. Borsanyi *et al.*. *JHEP* **1011** (2010) 077.

[Bro90] S. J. Brodsky and H. J. Lu. *Physical Review Letters* **64**(12) (1990) 1342.

[Bru94] R. Brun *et al.*. *GEANT Detector Description and Simulation Tool*, 1994. CERN Program Library Long Write-up, W5013.

[Cac] M. Cacciari. Private communication.

[Cac98] M. Cacciari, M. Greco, and P. Nason. *JHEP* **9805** (1998) 007.

[Cac12] M. Cacciari *et al.*. *JHEP* **1210** (2012) 137.

[Caf13] D. Caffarri. *Nucl. Phys.* **A904–905**(0) (2013) 643c .

[CER08] *CERN FAQ - LHC the guide*. CERN-Brochure-2008-001-Eng, 2008.

[CER12] CERN press office. *The first LHC protons run ends with new milestone*, 2012. URL `http://press.web.cern.ch/press-releases/2012/12/first-lhc-protons-run-ends-new-milestone`.

[Cha08] S. Chatrchyan *et al.*. *JINST* **3** (2008) S08004.

[Cha12a] S. Chatrchyan *et al.*. *Phys. Lett.* **B716** (2012) 30.

[Cha12b] S. Chatrchyan *et al.*. *JHEP* **1205** (2012) 063.

[Che05] S. Chekanov *et al.*. *Eur. Phys. J.* **C44** (2005) 351.

[Col98] J. C. Collins. *Phys. Rev.* **D58** (1998) 094002.

[COR] *Documentation for CORRFW*. URL `http://aliweb.cern.ch/Offline/Activities/Analysis/CORRFW.html`.

[Cor01] P. Cortese. *ALICE transition-radiation detector: Technical Design Report*. Technical Design Report ALICE. CERN, Geneva, 2001.

[Cor02] P. Cortese *et al.*. *ALICE: Addendum to the technical design report of the time of flight system (TOF)*. 2002.

[Cor04] P. Cortese *et al.*. *ALICE forward detectors: FMD, TO and VO: Technical Design Report*. Technical Design Report ALICE. CERN, Geneva, 2004.

[Cor06] T. Cormier, C. W. Fabjan, L. Riccati, and H. de Groot. *ALICE electromagnetic calorimeter: addendum to the ALICE technical proposal. Technical Report*, CERN, Geneva, 2006.

[Cro73] J. W. Cronin *et al.*. *Phys. Rev. Lett.* **31** (1973) 1426.

[Dai] A. Dainese. Private communication.

[Dai03] A. Dainese. *Charm production and in-medium QCD energy loss in nucleus-nucleus collisions with ALICE. A performance study.*, 2003. Ph.D. thesis, Universitá degli Studi di Padova.

[Del99a] G. Dellacasa *et al.*. *ALICE technical design report of the inner tracking system (ITS)*. CERN, Geneva, 1999.

[Del99b] G. Dellacasa *et al.*. *ALICE technical design report: Photon multiplicity detector (PMD)*. CERN, Geneva, 1999.

[Del00] G. Dellacasa *et al.*. *ALICE time projection chamber: Technical Design Report*. Technical Design Report ALICE. CERN, Geneva, 2000.

[Dia80] M. Diakonou *et al.*. *Phys. Lett.* **B89**(3-4) (1980) 432 .

[Dok01] Y. L. Dokshitzer and D. Kharzeev. *Phys. Lett.* **B519** (2001) 199.

[Eid04] S. Eidelman *et al.*. *Phys. Lett.* **B592** (2004) 1.

[Eva08] L. Evans and P. Bryant. *JINST* **3**(08) (2008) S08001.

[Fab03] C. W. Fabjan, Y. P. Viyogi, and H. de Groot. *ALICE Photon Multiplicity Detector (PMD): addendum to the Technical Design Report*. Technical Design Report ALICE. CERN, Geneva, 2003.

[Fas03] A. Fasso *et al.*. *eConf* **C0303241** (2003) MOMT005.

[Fas12] M. Fasel. *Single-electron analysis and open charm cross section in proton-proton collisions at* $\sqrt{s} = 7$ *TeV*, 2012. Ph.D. thesis, Technical Unversity Darmstadt.

[Fie02] R. Field. *Phys. Rev.* **D65** (2002) 094006.

[Fra12] A. Frawley. *Cold Nuclear Matter Effects and Heavy Quark Production in PHENIX*, 2012. `1209.1159`.

[Gal99] M. Gallio *et al.*. *ALICE Zero-Degree Calorimeter (ZDC): Technical Design Report. Technical Report*, Geneva, 1999.

[Gla70] R. Glauber and G. Matthiae. *Nucl. Phys.* **B21** (1970) 135.

[Goo95] M. Goossens *et al.*. *GEANT detector description and simulation tool*. CERN program library long write-up W5013, 1995. URL `http://cdsweb.cern.ch/record/1073159`.

[Gre04] V. Greco, C. Ko, and R. Rapp. *Phys. Lett.* **B595**(1-4) (2004) 202 .

[Gre13] A. Grelli. *Nucl. Phys.* **A904-905**(0) (2013) 635c .

[Gro09] Grosse-Oetringhaus, J F. *Measurement of the Charged Particle Multiplicity in Proton-Proton Collisions with the ALICE Detector*, 2009. Ph.D. thesis, Westfälische Wilhelms-Universität Münster.

[Gyu94] M. Gyulassy and X.-N. Wang. *Computer Physics Communications* **83**(2-3) (1994) 307 .

[Han01] S. Hands. *Contemporary Physics* **42**(4) (2001) 209.

[Har96] J. W. Harris and B. Muller. *Ann. Rev. Nucl. Part. Sci.* **46** (1996) 71.

[He12] M. He, R. J. Fries, and R. Rapp. *Phys. Rev. C* **86** (2012) 014903.

[Hei13] M. Heide. *Measurement of electrons from heavy-flavour hadron decays in pp and p-Pb collisions with ALICE*, 2013. `1309.1642`.

[HFE] *HFE software package*. URL `http://alisoft.cern.ch/viewvc/tags/v5-04-16-AN/PWGHF/hfe/?root=AliRoot`.

[Hic12] B. Hicks ALICE Analysis Note, URL `https://aliceinfo.cern.ch/Notes/node/99`.

[Hor13] W. Horowitz. *Nucl. Phys.* **A904-905** (2013) 186c.

[Jo13] M. Jo. *Nucl. Phys.* **A904–905**(0) (2013) 657c .

[Käh14] P. Kähler. *Jet Production in Proton-Proton Collisions at LHC Energies*, 2014. Master thesis in preparation, Westfälische Wilhelms-Universität Münster.

[Kal12] A. Kalweit. *Production of light flavor hadrons and anti-nuclei at the LHC*, 2012. Ph.D. thesis, Technical Unversity Darmstadt.

[Kha11a] V. Khachatryan *et al.*. *Eur. Phys. J.* **C71**(3) (2011) 1.

[Kha11b] P. Khandai, P. Shukla, and V. Singh. *Phys. Rev.* **C84** (2011) 054904.

[Kha11c] P. Khandai, P. Shukla, and V. Singh. *Phys. Rev.* **C84** (2011) 054904.

[Kim01] M. Kimber, A. D. Martin, and M. Ryskin. *Phys. Rev.* **D63** (2001) 114027.

[Kle04] Klein-Bösing, C. *Production of Neutral Pions and Direct Photons in Ultra-Relativistic Au+Au Collisions*, 2004. Ph.D. thesis, Westfälische Wilhelms-Universität Münster.

[Kni08] A. Kniehl *et al.*. *Phys. Rev.* **D77** (2008) 014011.

[Kno13] A. Knospe ALICE Analysis Note, URL `https://aliceinfo.cern.ch/Notes/node/42`.

[Koc97] V. Koch. *Int. J. Mod. Phys.* **E6** (1997) 203.

[Koc11] K. Koch. *Nucl. Phys.* **A855** (2011) 281.

[Kra] G. Kramer. Private communication.

[Kwe] M. Kweon. Private communication.

[KY05] T. H. K. Yagi and Y. Miake. *Quark-Gluon Plasma*. Cambridge University Press, 2005.

[Liu13] Z. Q. Liu *et al.*. *Phys. Rev. Lett.* **110** (2013) 252002.

[Lyo88] L. Lyons, D. Gibaut, and P. Clifford. *Nucl. Instrum. Meth.* **A270** (1988) 110.

[Maa13] J. van der Maarel, D. Thomas, and A. Mischke ALICE Analysis Note, URL `https://aliceinfo.cern.ch/Notes/node/198`.

[Mac] R. Maciula and A. Szurek. Private communication.

[Mac11] R. Maciula, A. Szczurek, and G. Slipek. *Int. J. Mod. Phys.* **A26** (2011) 549.

[Mac13a] R. Maciula and A. Szczurek. In *Proc. XXI. Int. Workshop on Deep-Inelastic Scattering and Related Subjects DIS 2013 (Marseille)*. 2013 .

[Mac13b] R. Maciula and A. Szczurek. *Phys. Rev. D* **87**.

[Man99] V. I. Manko *et al.*. *ALICE Photon Spectrometer (PHOS): Technical Design Report*. Technical Design Report ALICE. CERN, Geneva, 1999.

[Man05] M. L. Mangano. *AIP Conf.Proc.* **753** (2005) 247.

[Mat86] T. Matsui and H. Satz. *Phys. Lett.* **B178** (1986) 416.

[McL07] L. McLerran and R. D. Pisarski. *Nucl. Phys.* **A796** (2007) 83.

[Mee68] S. van der Meer. *Calibration of the effective beam height in the ISR*, 1968. CERN-ISR-PO-68-31, ISR-PO-68-31.

[Mua00] *ALICE dimuon forward spectrometer: addendum to the Technical Design Report*. Technical Design Report ALICE. CERN, Geneva, 2000.

[Mue05] B. Mueller. *Nucl. Phys.* **A750** (2005) 84.

[Muo99] *ALICE technical design report of the dimuon forward spectrometer*. Technical Design Report ALICE. CERN, Geneva, 1999.

[Mup96] *The forward muon spectrometer of ALICE: addendum to the technical proposal for a Large Ion Collider experiment at the CERN LHC*. LHC Tech. Proposal. CERN, Geneva, 1996.

[Nad08] P. Nadolsky *et al.*. *Phys. Rev.* **D78** (2008) 013004.

[Otw] J. Otwinowski. Private communication.

[Per00] D. H. Perkins. *Introduction to High Energy Physics*. Cambridge University Press, 2000.

[Pes94] A. Peshier *et al.*. *Phys. Lett.* **B337** (1994) 235.

[Phi12] O. Philipsen. *Acta Phys. Polon. Supp.* **5** (2012) 825.

[Pic12] A. Pich. *Review of α_S determinations*. PoS. 2012. 1303.2262.

[Piu98] F. Piuz *et al.*. *ALICE high-momentum particle identification: Technical Design Report*. Technical Design Report ALICE. CERN, Geneva, 1998.

[Pov09] B. Povh, K. Rith, C. Scholz, and F. Zetsche. *Teilchen und Kerne. Eine Einführung in die physikalischen Konzepte*. Springer-Verlag GmbH, eighth edition, 2009.

[Ren11] T. Renk. *Phys. Rev. C* **84** (2011) 067902.

[Rey11] K. Reygers. *J. Phys.* **G38** (2011) 124076.

[Roe00] S. Roesler *et al.* 1033 – 1038.

[ROO] *ROOT website*. URL http://root.cern.ch/drupal/.

[Sak13] S. Sakai. *Nucl. Phys.* **A904-905**(0) (2013) 661c .

[Sal12] C. A. Salgado *et al.*. *Journal of Physics G: Nuclear and Particle Physics* **39**(1) (2012) 015010.

[Sav91] F. Savatier. *J. Math. Phys.* **32**(10) (1991) 2666.

[Sjo06] T. Sjostrand, S. Mrenna, and P. Skands. *JHEP* **0605** (2006) 026.

[Ska09] P. Z. Skands FERMILAB-CONF-09-113-T, arXiv:0905.3418 [hep-ph].

[Sto09] R. Stock. *PoS* **CPOD2009** (2009) 001.

[Tak87] F. Takagi. *Phys. Rev.* **D35** (1987) 2226.

[Tho12] D. Thomas *et al.* ALICE Analysis Note, URL `https://aliceinfo.cern.ch/Notes/node/130`.

[TOF00] *ALICE Time-Of-Flight system (TOF): Technical Design Report*. Technical Design Report ALICE. CERN, Geneva, 2000.

[Tsa88] C. Tsallis. *J. Statist. Phys.* **52** (1988) 479.

[Uph12] J. Uphoff *et al.*. *Phys. Lett.* **B717** (2012) 430.

[Vit07] I. Vitev. *Phys. Rev. C* **75** (2007) 064906.

[Vog02] R. Vogt. In *Proc. 18th Winter Workshop on Nuclear Dynamics*. 2002 253.

[Völ12] M. Völkl. *Study of the Transverse Momentum Spectra of Semielectronic Heavy Flavor Decays in pp Collisions at $\sqrt{s}$ = 7 TeV and Pb-Pb Collisions at $\sqrt{s_{NN}}$ = 2.76 TeV with ALICE*, 2012. Master thesis, University of Heidelberg.

[Völ15] M. Völkl. *Charm and Beauty from Heavy Flavor Electrons*, 2015. Ph.D. thesis in preparation, University of Heidelberg.

[Wil74] K. Wilson. *Phys. Rev.* **D10** (1974) 2445.

[Wil10] Wilk, A. *Particle Identification Using Artificial Neural Networks with the ALICE Transition Radiation Detector*, 2010. Ph.D. thesis, Westfälische Wilhelms-Universität Münster.

[Wil13] M. Wilde. *Nucl. Phys.* **A904-905** (2013) 573c.

[Wil14] Wilde, M. *Production of Direct Photons in pp and Pb-Pb Collisions in ALICE*, 2014. Ph.D. thesis, Westfälische Wilhelms-Universität Münster.

[Won94] C.-Y. Wong. *Introduction to High-Energy Heavy-Ion Collisions*. World Scientific, 1994.

[Zha07] Zhang, Y. *Measurement of charm production cross-section and leptons from its semileptonic decay at RHIC*, 2007. Ph.D. thesis, University of Science and Technology of China, Hefei.

Acknowledgements/Danksagung

There are many people who deserve my gratitude for the support, sympathy, patience, and friendship which I had the opportunity to experience in the past few years.

Für die Betreuung meiner Arbeit und die Themenstellung bedanke ich mich bei Herrn Dr. Johannes P. Wessels, der mir, obgleich Lehramtsstudent, das Vertrauen entgegenbrachte, an einem großen internationalen Experiment wie ALICE mitzuarbeiten, einschließlich der wiederholten Gelegenheit zur Teilnahme an Konferenzen im Ausland. Seine immer faire, ermutigende und konstruktive Art ermöglichte ein durchweg angenehmes Arbeitsklima in Münster, das es sicherlich nicht nur mir erleichterte, auch in schwierigeren Zeiten durchzuhalten.

Mein Dank geht ebenso an PD Dr. Christian Klein-Bösing, von dessen Erfahrung und Rat ich sehr oft profitieren konnte. Ohne ihn sähen nicht zuletzt viele Kapitel dieser Arbeit anders aus. Zu letzterem hat auch Dr. Bastian Bathen beigetragen, der mir half, meiner Dissertation ihren letzten Schliff zu verleihen.

I would like to express my gratitude to the members of the Heavy-Flavour Electron working group, from whom I learned a lot in the last four years, and whose patience I hope I didn't overstrain in the beginning; this is especially true for PD Dr. Silvia Masciocchi, who despite many other obligations always found the time for PhD committee meetings, answering to my questions, and even to step in as the second examiner of this work. A very big thanks goes to Dr. MinJung Kweon, to whom I am deeply indebted for her advice regarding many aspects of this work, and without whose expertise and tireless effort the analysis presented in this thesis would not have been possible. Besides her, Dr. Markus Fasel deserves a special mention for frequently helping out with all questions concerning the HFE software. These and the other HFE members I had the privilege to work with, Dr. Ralf Averbeck, Dr. Raphaëlle Bailhache, Andrea Dubla, Dr. Yvonne Pachmayer, Elienos Pereira, Theodor Rascanu, Dr. Shingo Sakai, Dr. Deepa Thomas, and Martin Völkl, made our collaboration a very pleasant experience to me.

Dr. Daša Kaliská und Dr. Matúš Kaliský mit Tereza, Dr. Tom Dietel, Dr. Melanie Klein-Bösing und PD Dr. Christian Klein-Bösing mit Maria Josefa, sowie Swannet Wilk und Dr. Alexander Wilk mit Kolja, Frederik und Moritz möchte ich für ihre Unterstützung und Aufmunterung danken, und dafür, dass ich immer auf sie zählen konnte, auch und gerade außerhalb des rein Fachlichen.

Allen weiteren Mitarbeitern der Arbeitsgruppe Wessels, Björn Albrecht, Dr. Anton Andronic, Jonas Anielski, Dr. Christoph Baumann, Cyrano Bergmann, Jen-

nifer Bersch, Stephan Dyba, Dr. David Emschermann, Linus Feldkamp, Alexandre de Figueiredo, Henriette Gatz, Dr. Holger Gottschlag, Helge Grimm, Norbert Heine, Philipp Kähler, Thomas Keuter, Sebastian Klamor, Martin Kohn, Stefan Korsten, Daniel Mühlheim, Annika Passfeld, Friederike Poppenborg, Henrik Poppenborg, Markus Rammler, PD Dr. Klaus Reygers, Dr. Baldo Sahlmüller, Prof. em. Dr. Rainer Santo, Dr. Eva Sicking, Markus Tegeder, Wolfgang Verhoeven, Don Vernekohl, Matthias Walter, Uwe Westerhoff, Martin Wilde, Dr. Svenja Wulff und Markus Zimmermann, danke ich für die angenehme Zusammenarbeit und Gesellschaft. Dasselbe gilt für die Mitglieder der AGs Khoukaz, Weinheimer und Frekers.

Herrn PD Dr. Khoukaz danke ich dafür, dass er sich als Zweitbetreuer meiner Arbeit zur Verfügung gestellt hat, vor allem aber für den stets entgegenkommenden und freundlichen Umgang bei der Koordination der Praktikumsbetreuung. In letzterem Zusammenhang war mir insbesondere Dr. Volker Hannen häufig bei technischen Schwierigkeiten eine Hilfe. Michael Papenbrock schließlich verdient meinen Dank, da er jahrelang ein zuverlässiger und immer hilfsbereiter Partner bei der Leitung des Praktikums war.

Zu guter Letzt sollen auch die Menschen Erwähnung finden, bei denen ich abseits der Arbeit stets Halt und Verständnis fand: meine Eltern Agnes und Martin Heide, denen ich nicht nur die Möglichkeit meiner Ausbildung verdanke, sowie meine Tante Barbara Drebs und mein Onkel Edmund Heide, die mich während meines gesamten Studiums unterstützten. Der größte Dank gebührt jedoch meiner geliebten Frau Noelia dafür, dass sie mich fern ihrer Heimat auf diesem Weg begleitet, in guten und in schwierigen Momenten zu mir steht und so allen Anstrengungen einen Sinn gibt.